



## Agglomeration Mechanisms during Fluidized Bed Combustion of Biomass

Anicic, Bozidar

*Publication date:*  
2018

*Document Version*  
Publisher's PDF, also known as Version of record

[Link back to DTU Orbit](#)

*Citation (APA):*  
Anicic, B. (2018). *Agglomeration Mechanisms during Fluidized Bed Combustion of Biomass*. Technical University of Denmark.

---

### General rights

Copyright and moral rights for the publications made accessible in the public portal are retained by the authors and/or other copyright owners and it is a condition of accessing publications that users recognise and abide by the legal requirements associated with these rights.

- Users may download and print one copy of any publication from the public portal for the purpose of private study or research.
- You may not further distribute the material or use it for any profit-making activity or commercial gain
- You may freely distribute the URL identifying the publication in the public portal

If you believe that this document breaches copyright please contact us providing details, and we will remove access to the work immediately and investigate your claim.

# Agglomeration Mechanisms during Fluidized Bed Combustion of Biomass

Božidar Aničić

*PhD thesis*

*July 2018*

Supervisors    Kim Dam-Johansen (DTU, Chemical and Biochemical Engineering)  
                     Hao Wu (DTU, Chemical and Biochemical Engineering)  
                     Weigang Lin (DTU, Chemical and Biochemical Engineering)  
                     Wei Wang (CAS, Institute of Process Engineering)  
                     Bona Lu (CAS, Institute of Process Engineering)



## PREFACE AND ACKNOWLEDGEMENTS

---

This thesis is the results of the three years research, from 2015 to 2018, performed in the Combustion and Harmful Emission Control (CHEC) research center, at department of Chemical and Biochemical Engineering, Technical University of Denmark (DTU), in collaboration with Institute of Process Engineering, Chinese Academy of Sciences (CAS). The research is conducted within framework of Sino-Danish Center (SDC) for Education and Research, and it is partially funded by Danish Innovation Fond under the Development and Application of Circulating Fluidized Bed Gasification of Biomass (DANCNGAS) project. The PhD project was supervised by Professor Kim Dam-Johansen, Assistant Professor Hao Wu, Associate Professor Weigang Lin, Professor Wei Wang, and Assistant Professor Bona Lu.

Firstly, I would like to thank my supervisors for their guidance and support during these three years. I am sincerely thankful to Weigang Lin and Hao Wu for being available all the time, for all help and useful discussion (sometimes on the daily bases), and for guiding me in the right direction through-out the project. I am grateful to Kim Dam-Johansen for all of his support, and for being the source of enthusiasm and encouragement. I am also really thankful to my supervisors from China, Wei Wang and Bona Lu, for all of the professional help, as well as for making my external stays in China easier.

I would also like to thank all CHEC technicians and the technician from the workshop for their support with using, construction, commissioning, and troubleshooting of experimental setups. I was also fortunate to be a part of CHEC group surrounded by motivated PhD students and researchers.

Above all I would like to thank my brother Nemanja, my parents Milan and Vesna, as well as all of my friends from Serbia, Slovenia, Denmark, and China for their support, motivation, and encouragement.

Bozidar Anicic

July 2018



## SUMMARY

---

Biomass, as a carbon neutral and renewable fuel, has a potential to partially replace coal for heat and power production. Fluidized bed combustion is a promising technology for utilization of biomass due to its fuel flexibility and high efficiency. However, bed agglomeration is one of the main operating problems in fluidized bed combustion. Formation of agglomerates may change the hydrodynamics and influence the stability of fluidized bed boilers. The severe agglomeration may cause defluidization, leading to an unscheduled shut down of a power plant. Therefore, understanding the mechanisms of agglomeration and developing the effective countermeasures are of essential importance.

This PhD project aims to achieve and improved understanding of the agglomeration mechanisms, as well as to evaluate effective measures for reducing agglomeration problems. The agglomeration phenomena are investigated by: 1) evaluating the interactions between model potassium compounds and silica sand in a lab-scale fluidized bed reactor; 2) examining the reaction mechanisms between  $K_2CO_3$  and silica sand; 3) performing combustion experiments of biomass and K-compounds doped biomass under different temperature and air staging conditions in the lab-scale fluidized bed reactor. For reducing the agglomeration problems, various solid additives and different dosing methods are evaluated. In addition, the segregation phenomena of bed material caused by formation of agglomerates are simulated by Computational Fluid Dynamics (CFD) modelling.

The studies of agglomeration mechanisms by using potassium model compounds, such as KCl,  $K_2SO_4$ ,  $K_2CO_3$  and  $K_2Si_4O_9$ , and their mixtures indicate two interaction mechanisms between model K-compounds and silica sand particles: without reaction and with reaction occurring. When KCl and a eutectic mixture of KCl/ $K_2SO_4$  are applied, defluidization occurs near KCl melting temperature and KCl/ $K_2SO_4$  eutectic temperature, respectively. Such defluidization is caused by the formation of liquid phase in form of low viscous melting salts, with limited reaction between K-species and silica sand. The minimal amount of salt required for defluidization occurring depends on the hydrodynamics, particularly the  $U_g/U_{mf}$  ratio. However, the defluidization temperature appears to be independent of the amount of K-salts in the bed for this type of agglomeration. On contrary, the addition of  $K_2CO_3$  results in defluidization well below its melting point, and it is induced by reaction between  $K_2CO_3$  and silica sand. The defluidization

temperature decreases with increasing amount of  $K_2CO_3$  loaded, by using coarser sand particles, and by reduced gas velocity. Finally, unique behavior is observed when  $K_2Si_4O_9$  is added, since defluidization is not observed up to 850 °C, even for a very high amount of  $K_2Si_4O_9$  added to bed. However, large number of agglomerates is observed because high-viscous  $K_2Si_4O_9$  particles act as nuclei for binding several sand particles, and the interaction is localized at contact point between particles.

The reaction mechanism between  $K_2CO_3$  and silica sand is further studied by thermogravimetric analysis (TGA). It is showed that the reaction occurs in a solid-solid phase already at temperatures around 700 °C. The reaction rate increases with increasing temperature, but decreases in presence of  $CO_2$ . The reaction is enhanced by using smaller particle size and by mixing of solid reactants. It is observed that the reaction is initiated at the contact points between  $K_2CO_3$  and silica sand, forming a thin product layer. The layer acts as a reactive media further reacting with  $K_2CO_3$  and silica sand.

For different type of biomass, the appearance of potassium may vary. In order to investigate the transformation of K-compounds and their interaction with bed material during biomass combustion, KCl,  $K_2CO_3$ , KCl/ $K_2CO_3$  and KOH doped pine wood and washed straw are continuously burned in lab-scale fluidized bed reactor. It is observed that KCl and KOH might be transferred to  $K_2CO_3$  during combustion process, which further reacts with silica sand and causes defluidization. The transformation of KCl to  $K_2CO_3$  depends on fuel properties, for example, the transformation is more pronounced for pine wood compared to washed straw. Continuous combustion experiments of wheat straw and sunflower husk are also conducted in order to investigate the influence of fuel type with an emphasis of the impact of stage combustion (widely used for  $NO_x$  emission reduction) on agglomeration tendencies. It is observed that firing the biomass with high content of both, K and Si, results in a short combustion time before defluidization. On the other hand, firing the biomass containing Ca, Mg, S, and Cl, appears to reduce agglomeration and defluidization tendencies. The agglomeration tendency is increasing for lower ratio between primary air and total air ( $\lambda_1/\lambda$ ), and the trend is particularly pronounced for sunflower husk. However, no defluidization is observed when pyrolysis condition is applied in the dense bed, *i.e.*  $\lambda_1/\lambda$  ratio equal to 0, probably due to the fact that the presence of char hinders the interaction between the biomass ash and the silica sand particles. A fast defluidization occurs during char combustion at very low oxygen level.

Different additives, as well as dosing methods are examined as a countermeasure to reduce the agglomeration tendency during combustion of wheat straw and sunflower husk. The additives can either react with potassium present in biomass ash and reduce the amount of potassium reacting with silica

sand, or they can increase the viscosity of formed melts, thus reducing their stickiness and agglomeration tendency. The results show that kaolin is the most efficient additive, followed by magnesium carbonate, lime, ammonium sulphate, coal fly ash, and clay. It is also showed that mixing of the additives with fuels is more effective than direct feeding of additives to the bed.

Formed agglomerates may segregate from the bed material particles, which accelerates further agglomeration. Computational Fluid Dynamics (CFD) modeling is applied to investigate the segregation process due to the agglomerates formation. Segregation data of the binary particle system in literature are used for the CFD simulations. It was found that the EMMS drag model coupled with Ma-Ahmadi radial distribution and solid pressure models predicted more reasonable axial distribution of solid phases compared to commonly used Syamlal O'Brian drag model coupled with Lun et al. radial distribution and solid pressure models. An increase in the solid-solid drag further improved the simulation results. Developed and optimized simulation scheme can be further used for simulation of mixing/segregation behaviour of sand/agglomerates mixtures in fluidized bed reactors.



## DANSK RESUMÉ

---

Biomasse, som et kulstofneutralt og vedvarende brændsel, har potentiale til delvis at erstatte kul til varme- og energiproduktion. Fluid bed forbrænding er en lovende teknologi til udnyttelse af biomasse på grund af dets brændstoffleksibilitet samt høje effektivitet. Imidlertid er agglomerering af bed-materialet et af de vigtigste driftsproblemer i fluid bed forbrænding. Agglomerater kan ændre hydrodynamikken og påvirke stabiliteten af fluid-bed reaktorer. I værste fald kan agglomerering forårsage defluidisering og dermed driftstop. Forståelse af agglomerationsmekanismer og udvikling af effektive modforanstaltninger er derfor vigtig.

Dette ph.d.-projekt sigter mod at forbedre forståelse af agglomerationsmekanismerne samt at evaluere effektive foranstaltninger til begrænsning af agglomerationsproblemer. Agglomereringsfænomener er blevet undersøgt ved: 1) evaluering af interaktioner mellem modelkaliumforbindelser og silikatsand i en laboratorieskala fluid-bed reaktor; 2) undersøgelse af reaktionsmekanismerne mellem  $K_2CO_3$  og silikatsand; 3) udførelse af forbrænding af biomasse og K-forbindelser tilført biomasse under forskellige temperatur- og luftstrømsbetingelser i en laboratorieskala fluid-bed reaktor.

For at reducere agglomerationsproblemerne blev forskellige additiver og additiv doseringsmetoder undersøgt. Desuden blev adskillelsesfænomenerne af bed-materialet forårsaget af dannelse af agglomerater simuleret ved brug af Computational Fluid Dynamics (CFD) modellering.

Undersøgelserne af agglomerationsmekanismer ved anvendelse af kaliummodelforbindelser, såsom KCl,  $K_2SO_4$ ,  $K_2CO_3$  and  $K_2Si_4O_9$ , og deres blandinger indikerer to interaktionsmekanismer mellem model K-forbindelser og silikatsandpartikler: uden og med tilstedeværelsen af reaktion. Når KCl og en eutektisk blanding af KCl/ $K_2SO_4$  benyttes, forekommer defluidisering nær henholdsvis KCl-smeltetemperatur og KCl/ $K_2SO_4$ -eutektisk temperatur. En sådan defluidisering skyldes dannelsen af en væskefase i form af lavviskøse smeltede salte med begrænset reaktion mellem K-forbindelser og silikat sand. Den minimale mængde salt, der kræves til defluidisering, afhænger af hydrodynamikken, især  $U_g/U_{mf}$  -forholdet. Imidlertid forekommer defluideringstemperaturen at være uafhængig af mængden af K-salte i beden for denne type agglomerering. Til gengæld resulterer tilsætning af  $K_2CO_3$  i defluidisering langt under

smeltepunktet, og den induceres ved reaktion mellem  $K_2CO_3$  og silikat sand. Defluidiseringstemperaturen falder med stigende mængde  $K_2CO_3$ , ved anvendelse af grovere sandpartikler og ved reduceret gashastighed. Endelig observeres en unik adfærd, når  $K_2Si_4O_9$  tilsættes, da defluidisering ikke observeres op til 850 °C, selv ved addering af en meget stor mængde  $K_2Si_4O_9$ . Dog observeres et stort antal agglomerater, fordi højviskøse  $K_2Si_4O_9$  partikler agerer som kerner til binding af flere sandpartikler, og interaktionen er lokaliseret ved kontaktpunkterne mellem partiklerne.

Reaktionsmekanismen mellem  $K_2CO_3$  og silikatsand blev undersøgt yderligere ved termogravimetrisk analyse (TGA). Det blev påvist, at reaktionen forløber i en fastof-faststof fase allerede ved temperaturer omkring 700 °C. Reaktionshastigheden forøges med stigende temperatur, men falder ved tilstedeværelse af  $CO_2$ . Reaktionshastigheden øges ved anvendelse af mindre partikelstørrelse og ved blanding af de faste reaktanter. Det blev observeret, at reaktionen initieres ved kontaktpunkterne mellem  $K_2CO_3$  og silikatsand, der danner et tyndt produktlag. Laget virker som et reaktivt medium, der reagerer yderligere med  $K_2CO_3$  og silikatsand.

For forskellige typer biomasse kan kemien af kalium variere. For at undersøge transformationen af K-forbindelser og deres interaktion med bedmaterialet under biomasseforbrænding er KCl,  $K_2CO_3$ , KCl/ $K_2CO_3$  og KOH doseret fyrretræ og vasket hvedestrå blevet forbrændt kontinuerligt i en laboratorieskala fluid-bed reaktor. Det observeres, at KCl og KOH kan reagere til  $K_2CO_3$  under forbrændingsprocessen, hvilket yderligere reagerer med silikatsand og forårsager defluidisering. Omdannelsen af KCl til  $K_2CO_3$  afhænger af brændselsegenskaber, for eksempel er reaktionen mere markant for fyrretræ end vasket strå. Kontinuerte forbrændingseksperimenter af hvedestrå blev udført for at undersøge indflydelsen af brændslet med speciel fokus på virkningen af trinvis forbrænding (i vid udstrækning brugt til reduktion af  $NO_x$ -emissioner) på agglomereringstendensen. Det bemærkes, at affyring af biomasse med et højt indhold af både K og Si resulterer i en kort forbrændingstid før defluidisering. På den anden side fremgår det fra forbrænding af biomasse indeholdende Ca, Mg, S og Cl at agglomerings- og defluidiseringstendensen blev reduceret. Agglomereringstendensen øges for et lavere forhold mellem primærluft og total luft ( $\lambda_1/\lambda$ ), og tendensen er særligt klar for solsikkefrøskaller. Imidlertid observeres ingen defluidisering, når primærluften reduceres til 0, sandsynligvis på grund af tilstedeværelsen af koks som kan forhindre samspillet mellem biomasseaske og silikatsandpartikler. En hurtig defluidisering forekom under den efterfølgende koksforbrænding selv ved meget lavt iltniveau.

Forskellige tilsætningsstoffer samt doseringsmetoder blev undersøgt for at reducere agglomereringstendensen under forbrænding af hvedestrå og solsikkefrøskaller. Tilsætningsstofferne kan enten reagere med kalium fra biomasseasken og reducere mængden af kalium, der kan reagere med silikatsand, eller de kan øge viskositeten af de dannede smeltefaser, hvilket reducerer deres klæbeevne og agglomereringstendens. Resultaterne har vist, at kaolin er det mest effektive additiv efterfulgt af magnesiumkarbonat, kalciumoxid, ammoniumsulfat, kulflyveaske og ler. Det blev desuden vist, at blanding af tilsætningsstoffer med brændstoffer er mere effektiv end direkte tilførsel af additiver til fluid bedden.

Allerede dannede agglomerater kan adskilles fra resten af bed-materialet, hvilket yderligere kan accelerere agglomereringen. Computational Fluid Dynamics (CFD) modellering er blevet anvendt til at undersøge segregeringsprocessen på grund af agglomeratdannelse. Segregationsdata fra litteraturen er anvendt til sammenligning med CFD-simuleringerne. Det blev fundet, at "EMMS drag modellen" kombineret med Ma-Ahmadi radialfordeling og "solid pressure model" bedre forudsagde den aksiale fordeling af faste faser i sammenligning med den almindeligt anvendte Syamlal O'Brian "drag model" kombineret med Lun et al. radialfordeling og "solid pressure model" modeller. En forøgelse i "solid-solid drag" forbedrede yderligere simuleringresultaterne. Et udviklet og optimeret simuleringsskema kan anvendes til simulering af blanding/adskillelsesadfærd af sand/agglomerat blandinger i fluid bed reaktorer.



# CONTENTS

---

Preface and Acknowledgements.....	i
Summary.....	iii
Dansk resumé.....	vii
Contents .....	xi
Abbreviations and Symbols .....	xv
<b>1 Introduction.....</b>	<b>1</b>
1.1 Project objectives.....	2
1.2 Structure of this thesis.....	2
<b>2 Literature survey.....</b>	<b>5</b>
2.1 Fluidized bed boilers.....	5
2.2 Fluidized bed combustion.....	6
2.2.1 Bed agglomeration.....	6
2.2.2 Biomass composition.....	7
2.3 Mechanisms of bed agglomeration.....	9
2.3.1 Potassium release .....	9
2.3.2 Form of K-species during biomass combustion .....	12
2.3.3 Interaction between biomass ash and bed material .....	14
2.4 Impact of operating parameters.....	16
2.4.1 Operating temperature.....	17
2.4.2 Bed material size .....	17
2.4.3 Gas velocity.....	17
2.5 Countermeasures.....	17
2.5.1 Alternative bed material .....	18
2.5.2 Additives .....	19

2.5.3	Co-Combustion .....	20
2.5.4	Pretreatment.....	21
2.6	Modeling.....	21
2.6.1	CFD modeling .....	22
2.7	Summary.....	24
<b>3</b>	<b>Potassium induced agglomeration in a high temperature lab-scale fluidized bed.....</b>	<b>27</b>
3.1	Introduction .....	27
3.2	Experimental .....	27
3.2.1	Experimental setup.....	27
3.2.2	Materials .....	29
3.2.3	Experimental procedures and conditions .....	29
3.2.4	Analysis of the samples.....	30
3.3	Results and discussion.....	31
3.3.1	Critical amount of K-compounds and defluidization temperature .....	31
3.3.2	Agglomeration mechanisms .....	37
3.3.3	Melting behaviour .....	41
3.4	Conclusions.....	43
<b>4</b>	<b>Reaction between potassium carbonate and silica sand .....</b>	<b>45</b>
4.1	Introduction .....	45
4.2	Experimental.....	45
4.2.1	Materials .....	45
4.2.2	Experimental setup.....	46
4.2.3	Analytical methods.....	47
4.2.4	Thermodynamic equilibrium calculations.....	47
4.3	Results and discussion.....	47
4.3.1	Equilibrium distribution of potassium species.....	47
4.3.2	TGA results .....	49
4.3.3	SEM-EDX analyses .....	54
4.3.4	Plausible reaction mechanism .....	57
4.3.5	Practical implication .....	58

4.4	Conclusions .....	58
<b>5</b>	<b>Biomass combustion in fluidized bed reactor .....</b>	<b>59</b>
5.1	Introduction .....	59
5.2	Experimental .....	60
5.2.1	Fluidized bed reactor .....	60
5.2.2	Materials .....	61
5.2.3	Experimental procedure .....	63
5.2.4	Solid samples analysis .....	64
5.2.5	Thermodynamic equilibrium calculations .....	65
5.3	Results and discussion .....	66
5.3.1	Combustion under $\lambda_1/\lambda = 1$ .....	66
5.3.2	Stage combustion .....	75
5.4	Conclusion .....	80
<b>6</b>	<b>Effect of additives during fluidized bed combustion of biomass fuels .....</b>	<b>81</b>
6.1	Introduction .....	81
6.2	Experimental .....	81
6.2.1	Materials .....	82
6.2.2	Experimental procedure .....	83
6.2.3	Solid samples analysis .....	84
6.3	Results and discussion .....	84
6.3.1	Kaolin addition .....	85
6.3.2	Lime addition .....	87
6.3.3	Ammonium sulphate addition .....	89
6.3.4	Magnesium carbonate addition .....	91
6.3.5	Coal fly ash .....	92
6.3.6	Clay soil .....	93
6.3.7	Interaction mechanism .....	93
6.4	Conclusion .....	94
<b>7</b>	<b>CFD simulation of mixing and segregation of binary solid mixtures .....</b>	<b>95</b>
7.1	Introduction .....	95

7.2	Mathematical models and simulation set-up .....	95
7.2.1	Experimental data .....	95
7.2.2	Hydrodynamic model .....	96
7.2.3	Simulations settings .....	98
7.3	Simulation results .....	100
7.3.1	Base case simulation .....	100
7.3.2	Comparison of 2D and 3D geometry .....	101
7.3.3	Impact of specular coefficient .....	102
7.3.4	Effects of gas-solid drag model .....	103
7.3.5	Impact of solid pressure and radial distribution models .....	104
7.3.6	Impact of solid-solid drag model .....	105
7.4	Conclusion .....	107
<b>8</b>	<b>Concluding remarks .....</b>	<b>109</b>
8.1	Summary of Conclusions .....	109
8.2	Suggestions for future work .....	113
	<b>References .....</b>	<b>115</b>
	<b>Appendix A .....</b>	<b>125</b>
	<b>Appendix B .....</b>	<b>127</b>
	<b>Appendix C .....</b>	<b>129</b>
	<b>Appendix D .....</b>	<b>133</b>

## ABBREVIATIONS AND SYMBOLS

---

### Abbreviations

AS	Ammonium Sulphate
BFB	Bubbling Fluidized Bed
CFB	Circulating Fluidized Bed
CFD	Computational Fluid Dynamics
CFA	Coal Fly Ash
DP	Defluidization Point
DT	Defluidization Temperature
EDX	Energy-dispersive X-ray Spectroscopy
ICP	Inductive Coupled Plasma
KTGF	Kinetic theory of granular flow
OES	Optical Emission Spectrometry
PBM	Population Balance Model
SEM	Scanning Electron Microscopy
SFH	Sunflower Husk
SL	Silicon Lean fuels
SR	Silica Rich fuels
SS	Solid-solid drag model modification constant
TGA	Thermogravimetric Analysis
XRD	X-ray Diffraction

### Symbols

$C_{fr,ki}$	Coefficient of friction between solid phases
$\varepsilon_g$	Voidage (gas volume fraction)
$\varepsilon_{s,i}$	Solid volume fraction of phase $i$
$e_{ss}$	Solid restitution coefficient
$H_b$	Heterogeneity index
$g_0$	Radial distribution of solid phases

$I$	Second invariant of the solid deviatoric stress tensor
$\nabla p$	Pressure gradient
$p_s$	Solid pressure
$\boldsymbol{\tau}_g$	Stress tensors of gas phase
$\boldsymbol{\tau}_{s,i}$	Stress tensors of solid phases
$\mathbf{u}$	Velocity vector
$u_t$	Terminal velocity
$U_g$	Superficial gas velocity
$U_{mf}$	Minimal fluidization velocity

### **Greek**

$\beta_i$	Drag force coefficient between gas and solid phase
$\gamma_s$	Energy generation by solid stress tensor
$\phi$	Angle of internal friction
$\lambda_s$	Granular bulk viscosity of solid phases
$\lambda$	Actual air/fuel ratio compared to stoichiometric ratio
$\lambda_1$	Amount of primary air
$\zeta_{ki}$	Drag coefficient between solid phases
$\mu_g$	Viscosity of gas phase
$\mu_s$	Viscosity of solid phases
$\mu_{s,col}$	Collisional viscosity of solid phases
$\mu_{s,kin}$	Kinetic viscosity of solid phases
$\mu_{s,fr}$	Frictional viscosity of solid phases
$\varphi$	Specularity coefficient
$\rho$	Density
$\theta_s$	Granular temperature of solid phases

# 1

---

## INTRODUCTION

Utilization of biomass, as carbon neutral fuel, does not contribute to the net CO<sub>2</sub> emission, which is one of the main greenhouse gases. That is why; it is an ideal candidate for replacing coal used for heat and power production, since Danish government set regulative with purpose of excluding coal from energy production by 2030 <sup>1</sup>. Wood pellets, wood chips, and wheat straw are principle biomass resources in Denmark. More than 90 % of woody biomass is imported to Denmark, while wheat straw is domestically produced <sup>2</sup>. In order to increase the share of wheat straw in energy production, and to reduce Danish dependence on imported biomass, it is necessary to eliminate operating problems associated with wheat straw utilization (for example bed agglomeration in fluidized bed boilers).

Fluidized bed combustion of biomass is promising technology since it ensures high fuel flexibility, energy efficiency and low emission. On the other hand, bed agglomeration is one of the main operating problem, especially pronounced for herbaceous biomass such as wheat straw due to the its inorganic composition <sup>3</sup>. Bed agglomeration is mainly related to the interaction between ash containing elements (primarily potassium) and bed material (*i.e.* silica sand), which leads to the formation of melts. The melts act as glue to bind bed material particles, leading to the formation of coarser particles (agglomerates). Consequentially, system hydrodynamics can be changed (poor mixing, occurrence of hot spots), and in most severe cases the agglomeration can lead to the bed defluidization <sup>4</sup>. The phenomena have been studied for many years, but the detailed mechanism is still unclear. An important step in further understanding is to identify compounds (mainly potassium formed during biomass combustion) that are interacting with bed material and investigate mechanisms of the interaction under different operating conditions. Beside potassium, the impacts of other elements (Si, Mg, Ca, S, Cl) on the agglomeration phenomena have to be considered.

Improved understanding of agglomeration phenomena should enable us to propose effective and cheap countermeasures. Numerous countermeasures are already proposed in literature, and they include biomass pretreatment, co-combustion, additive addition, and alternative bed materials <sup>5</sup>. All of them are associated with additional cost or environmental problems, and it seems that these countermeasures

cannot completely eliminate agglomeration problems during combustion of most troublesome fuels, such as wheat straw <sup>5</sup>. That is why; the identification of effective additive, even for most troublesome fuels, is needed, and usage of cheap additives (wastes, largely available minerals, etc.) is desirable.

Bed agglomeration is usually treated experimentally and limited number of models is available. Recent development of computational fluid dynamics (CFD) makes it applicable for fluidized bed systems. More detailed simulation of agglomeration phenomena is currently not possible, due to the extreme process complexity and computational power needed, but CFD can be used for investigating bed hydrodynamics, and influence of formed agglomerates.

## **1.1 Project objectives**

The main goal of this PhD thesis is to further investigate agglomeration mechanisms and to propose effective and cheap countermeasures. Laboratory scale setups, various characterization methods, as well as modeling tools are used. Specifically, following topics are addressed in this PhD project:

- Bed agglomeration phenomena with special emphasis on interaction between potassium compounds and silica sand, as well as the impact of operating conditions (bed temperature, and air staging) and fuel properties on bed agglomeration during continuous combustion in fluidized bed reactor.
- Effective countermeasures for reducing agglomeration problems during combustion of most troublesome fuels such as wheat straw.
- Modeling tools (CFD based) to be used in order to investigate segregation phenomena of formed agglomerates

## **1.2 Structure of this thesis**

The thesis is divided into 8 chapters, including introduction.

### **Chapter 2: Literature review**

This chapter provides the overview on agglomeration phenomena in biomass fired fluidized beds, potassium transformation during combustion, and interaction between potassium compounds and silica sand.

### **Chapter 3: Interaction between model K-species and silica sand**

This chapter focuses on systematic investigation of the interactions between model potassium compounds (KCl,  $K_2CO_3$ , and  $K_2Si_4O_9$ ) and their mixtures ( $KCl/K_2SO_4$  and  $KCl/K_2CO_3$ ) with silica sand in a lab-scale fluidized bed reactor. SEM-EDX and optical dilatometry analyses are carried out to understand the defluidization mechanism taking place at high temperatures. The critical amount of model potassium species, needed to cause bed defluidization, is evaluated for different gas velocity and sand size conditions.

### **Chapter 4: Reaction between $K_2CO_3$ and silica sand**

In this chapter the reaction between  $K_2CO_3$  and the silica sand is investigated using thermogravimetric analysis (TGA). The influence of the important parameters, such as temperature,  $CO_2$  partial pressure, mixing of solid particles, and particle size on the reaction rate is examined. SEM-EDX analyses of the reaction products, as well as thermodynamic calculations of the reaction systems, are carried out in order to understand the reaction and to propose plausible reaction mechanism.

### **Chapter 5: Biomass combustion in lab-scale fluidized bed reactor**

In this chapter the results of continuous combustion experiments of wheat straw, sunflower husk, as well as fuels (pine wood and washed wheat straw) doped with the model potassium compound (KCl, KOH,  $K_2CO_3$ ,  $KCl/K_2CO_3$ ), in lab scale fluidized bed reactor are presented. The impacts of air staging and fuel properties, as well as bed temperature and material, are examined.

### **Chapter 6: Effect of additive addition during fluidized bed combustion of wheat straw and sunflower husk**

In this chapter fuel additives (kaolin, lime, magnesium carbonate, coal fly ash, clay, and ammonium sulphate) are used in order to reduce agglomeration and defluidization tendencies during continuous combustion of wheat straw and sunflower husk in fluidized bed reactors. The impacts of additive dosing method (mixing with fuel or addition of the bed), additives composition, and interaction mechanisms are evaluated.

### **Chapter 7: CFD modeling of mixing and segregation of binary solid mixture**

In this chapter CFD simulations of two binary solid mixtures are performed and the results are compared to the experimental data from Joseph et al.<sup>6</sup>. The impact of reactor geometry, specular coefficients, radial distribution function and solid pressure, gas-solid and solid-solid drag models is evaluated. Optimal

combination of simulation settings and a reasonable scheme that can successfully reproduce both axial distribution profiles are proposed.

### **Chapter 8: Concluding Remarks**

Summary of main conclusions, as well as suggestion for future work are presented in this chapter.

# 2

This chapter provides the overview of agglomeration in biomass fired fluidized bed boilers. It focuses on potassium release and its interaction with silica sand, agglomeration mechanisms, impact of operating parameters and countermeasures on agglomeration and defluidization tendency, as well as on the modelling tools (mainly CFD).

### 2.1 Fluidized bed boilers

Fluidized bed boilers are widely applied in heat and power generation<sup>3</sup>. Several types of fluidized boilers are commercially available, among which bubbling fluidized bed (BFB) and circulating fluidized bed (CFB) are the most commonly used<sup>3</sup>. A schematic representation of the two types of fluidized boilers are shown in Figure 2-1<sup>3</sup>.

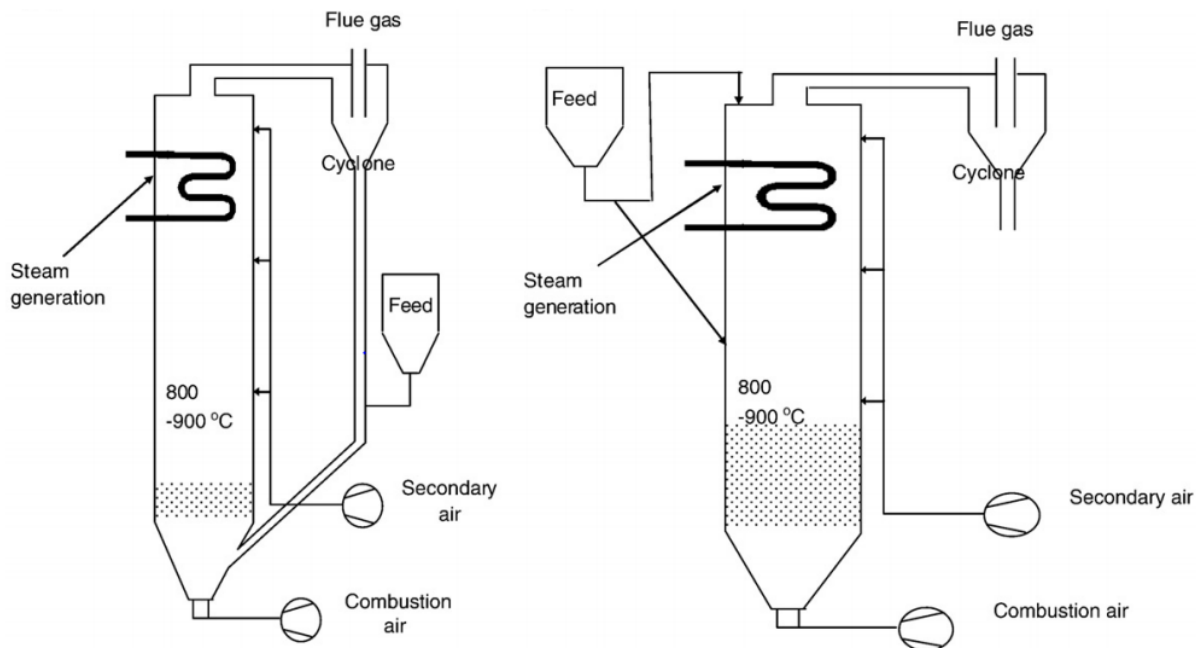


Figure 2-1: A circulating fluidized bed boiler (left) and a bubbling fluidized bed boiler (right)<sup>3</sup>.

In both, CFB and BFB boilers, the solid bed material is fluidized with the flow of the primary combustion air supplied through an air distributor. The main difference between the two systems is the superficial gas velocity. It is significantly lower in the BFB systems, resulting in smaller entrainment of solid particles to the freeboard of the boiler. The entrainment rate of the CFB systems is much higher, meaning that the entrained particles have to be recycled to the main combustion chamber by a cyclone. Secondary air (in some case also tertiary air) is usually injected in the section above the bed in order to ensure a complete burnout of the fuel. The fuel can be fed either directly to the bed (usually for particles with a small size and a low moisture content) or above the bed (usually for particles with a large size and a high moisture content)<sup>7</sup>. The temperature in the bed typically varies between 800 and 900 °C<sup>3</sup>.

## **2.2 Fluidized bed combustion**

Fluidized bed combustion is a widely used technology for heat and electricity production from biomass<sup>3,8</sup>. It provides a good heat transfer, a uniform combustion temperature, and a high energy efficiency<sup>3,8</sup>. On the other hand, bed agglomeration, ash deposition, and erosion of reactor's walls are the most common operational problems<sup>3,9,10</sup>. Utilization of woody biomass in the fluidized bed boilers is usually not accompanied with serious operational problems. On the other hand, herbaceous biomass is more problematic, due to their higher ash content and ash composition, which promote bed agglomeration and defluidization<sup>11-14</sup>.

### **2.2.1 Bed agglomeration**

During combustion of biomass in fluidized bed boilers, formation of melt can take place due to the melting of ash particles, or in the reaction between biomass ash (e.g. potassium species) and bed material (e.g. silica sand)<sup>14-16</sup>. The melts can act as a binder for several silica sand particles, which causes formation of coarse particles (agglomerates). Due to the different size and density of the agglomerates, segregation at the bottom of fluidized bed can occur, as illustrated in Figure 2-2<sup>4</sup>. After some time, partial bed segregation occurs, inducing significant changes in bed hydrodynamics. In most severe cases, complete bed defluidization can occur, which causes unscheduled boiler shut down. On the other hand, melt can coat surface of bed particles, which increases the dissipation of kinetic energy between colliding bed particles. At critical conditions, related to the coating layer thickness and viscosity, particles rebounding is not possible anymore and defluidization occurs<sup>17</sup>.

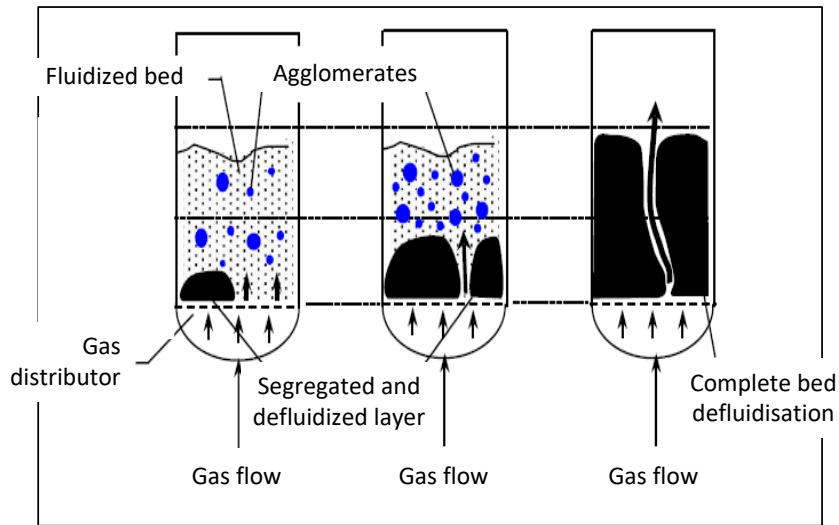


Figure 2-2: Impact of agglomerates formation of bed hydrodynamics and bed defluidization<sup>4</sup>

### 2.2.2 Biomass composition

Biomass fuels can be divided into several groups: wood and woody biomass, forest residues, herbaceous biomass, aquatic biomass, animal and human biomass wastes, etc.<sup>18</sup>. The organic composition (i.e. O, C, N, H, S) of all biomass fuels is comparable, while the ash content and the inorganic composition vary significantly<sup>18</sup>. The ash content of herbaceous biomass, especially straw, is higher compared to the woody biomass. An average inorganic composition of different types of biomass is given in Figure 2-3<sup>19,20</sup>.

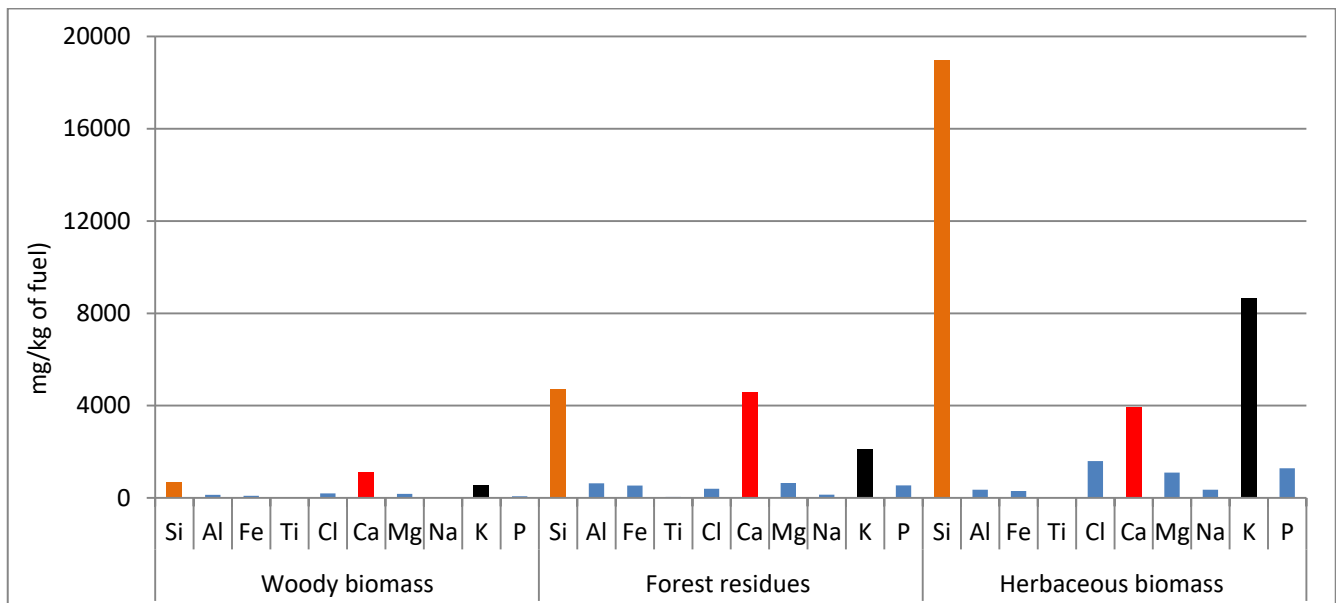


Figure 2-3: Inorganic composition of various biomass fuels<sup>19,20</sup>

It can be seen that woody biomass contains significantly smaller amounts of Si and K, compared to that of herbaceous biomass (straw, grass, etc.).

### 2.2.2.1 Potassium in the biomass

Potassium present in biomass contributes significantly to the agglomeration and defluidization problems. Potassium can be present in the form of salts, organic compounds and minerals<sup>21</sup>. The association of potassium in biomass has been studied by a stepwise leaching method schematically represented in Figure 2-4<sup>22</sup>.

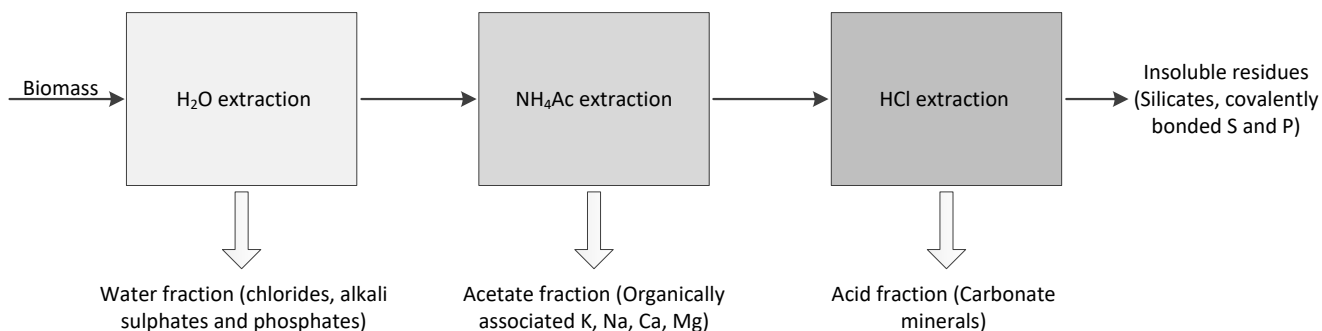


Figure 2-4: Stepwise leaching method for determination of biomass combustion<sup>23</sup>

The biomass is firstly dissolved in water in order to remove all water soluble salts such as chlorides, sulphates, carbonates, and phosphates. The solid fraction from water extraction is further dissolved in  $\text{NH}_4\text{Ac}$  solution in order to remove organically associated elements such as K, Na, Ca and Mg, which are usually bonded to the organic matrix in biomass<sup>23</sup>. In the third step of the leaching process, the solid fraction from the  $\text{NH}_4\text{Ac}$  extraction is further dissolved in HCl in order to remove minerals. The remaining solid fraction from HCl extraction contains primarily silica and silicates<sup>23</sup>. Figure 2-5 represents the amount of potassium dissolved in each leaching step, as well as the non-leachable amount for different fuels<sup>22,24</sup>. As shown in Figure 2-5, the results of the stepwise leaching process are comparable even though the initial potassium content differs significantly for these fuels, ranging from 3 to 19 g per kg of fuel<sup>22,24</sup>. The majority of potassium is leached in the first step, which indicates that potassium is primarily present in the form of water soluble salts. The amount of the potassium leached in the second step is generally smaller; meaning that amount of organically bounded potassium is smaller. The amount of potassium originally present in mineral and silicates forms is also small.

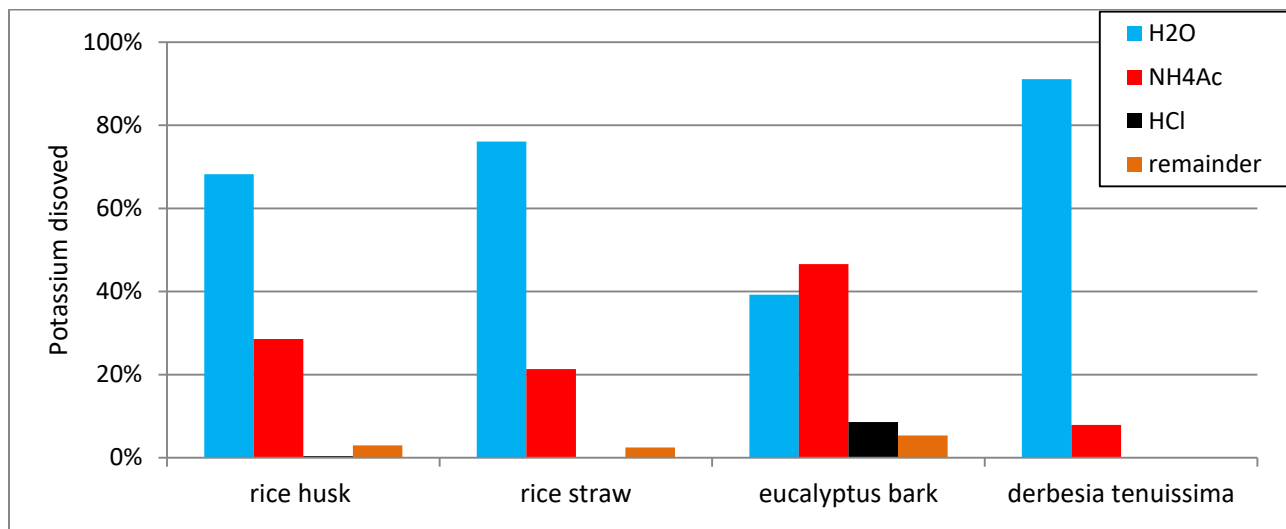


Figure 2-5: Percentage of potassium dissolved in each leaching step for different biomass<sup>22,24</sup>

## 2.3 Mechanisms of bed agglomeration

High temperature bed agglomeration in biomass combustion is a complex phenomenon. It is related to the particle interactions within the bed and ash transformations taking place during biomass combustion<sup>9</sup>. For bed agglomeration in biomass fired boilers, release and transformation of potassium species in biomass play an important role.

### 2.3.1 Potassium release

During combustion, the potassium species in biomass can be either released to the gaseous phase, or retained in the ash. The formation of different potassium species can occur at different stages of combustion, and it is strongly related to the Cl, Si, and S fuel content in biomass<sup>25,26</sup>. It is important to understand the mechanism of potassium release of the herbaceous biomass, due to the significant agglomeration problems related to these fuels<sup>9,11,12</sup>. The potassium release mechanism has been systematically studied in laboratory scale fixed bed reactor between 500 and 1150 °C. The oxygen concentration was varied between 2 vol.% (at the beginning) to 21 vol.% as the burnout was reaching the end. Residual ash was dissolved in 0.1 M HNO<sub>3</sub> and further analyzed by ion chromatography, while the gas phase release was quantify by the mass balance of the system<sup>26</sup>. The potassium release profiles (as a function of temperature) are represented in Figure 2-6 for six herbaceous fuels<sup>26</sup>. The results in Figure 2-6 suggests that a limited amount of potassium is released below 700 °C for all investigated fuels. Above 700 °C, there is significant difference between silica rich (SR) and silica lean (SL) fuels<sup>26</sup>. In the case of SL fuels, K release is almost linear from 750 to 1150 °C. In the case of SR fuel a significant potassium release is observed between 700 and 800 °C, followed by additional release between 900 to 1150 °C<sup>26</sup>. Generally,

more potassium is released for SL fuels up to 1150 °C<sup>26</sup>. The final potassium release is related to the silica content, meaning that in the case of SR fuels, more potassium is retained in the ash in the form of various silicates<sup>26</sup>. The silicates may be originally present in the biomass fuel (see Figure 2-5), while the additional amount can be formed above 900 °C<sup>26</sup>.

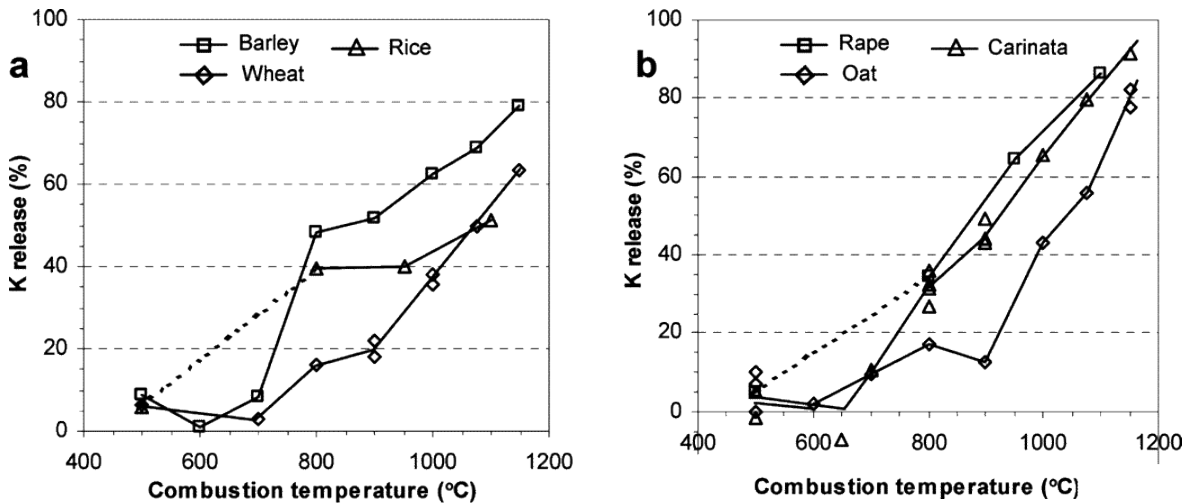


Figure 2-6: Potassium release profiles of herbaceous biomasses as a function of combustion temperature for silica rich fuels (left) and silica lean fuels (right)<sup>26</sup>

The potassium release profiles for woody biomass are obtained using the same methodology and results are presented in Figure 2-7<sup>25</sup>. For woody biomass, a small potassium release is observed below 800 °C, while a significant amount is released between 800 and 1150 °C, with the exception of fiber board which has a significantly different inorganic composition.

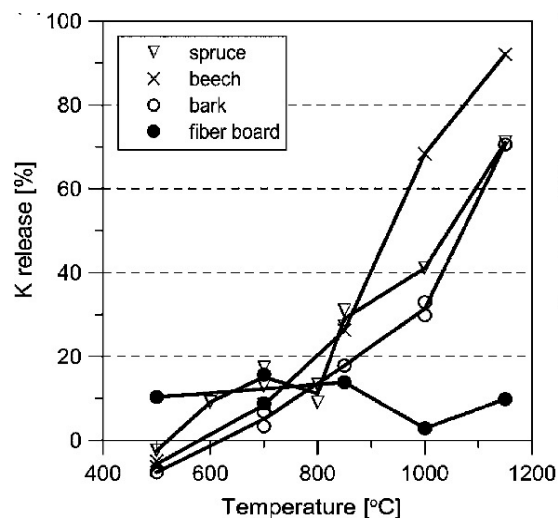


Figure 2-7: Potassium release profiles as function of combustion temperature for different woody biomass fuels<sup>25</sup>





In the presence of water vapor the overall dissociation reaction can be enhanced by formation of KOH:



It is suggested that the salt decomposition is the dominant mechanism above 900 °C<sup>26</sup>. Salt formed during char oxidation stage, as well as the salt initially present in fuel can react with fuel silica to form K-silicates. Silicates are stable below 1150 °C, and the total amount of potassium retained in the ash depends on the Si content, as well as the reactivity of fuel K and Si.

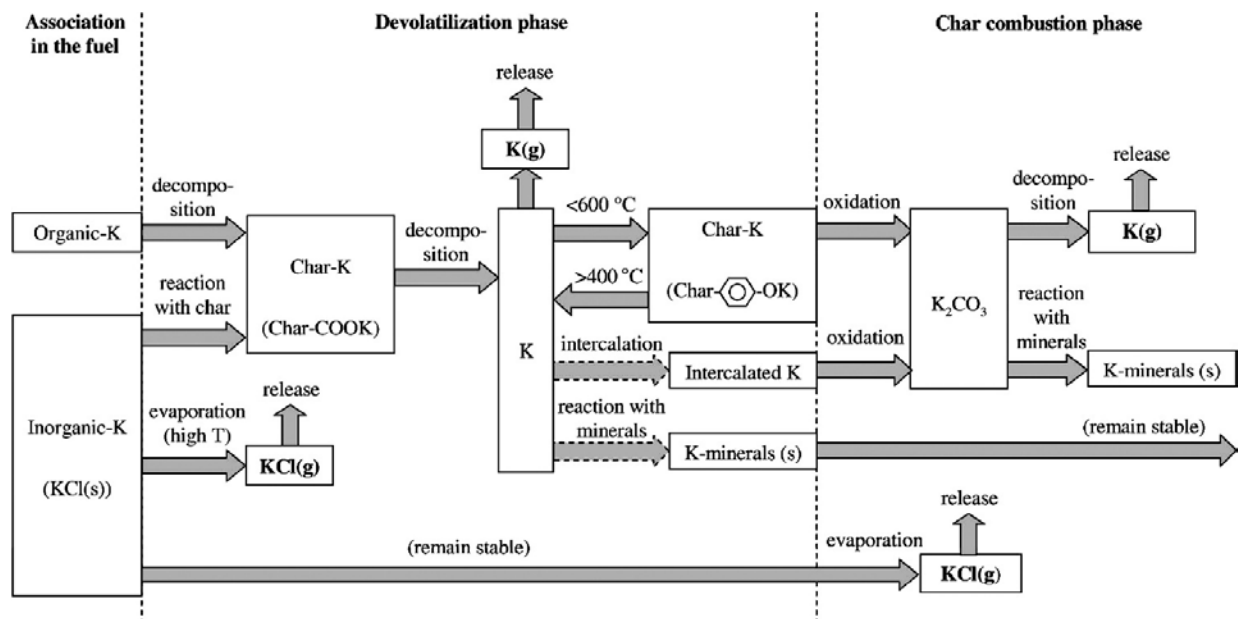


Figure 2-9: Potassium release mechanism and reaction paths for woody biomass<sup>25</sup>

### 2.3.2 Form of K-species during biomass combustion

In biomass combustion, different potassium species can be formed as gaseous products, or retained in the solid phase as a part of biomass ash. The formation of KOH, KCl, K<sub>2</sub>CO<sub>3</sub>, K<sub>2</sub>SO<sub>4</sub> and various K-silicates has been suggested based on thermodynamical calculation<sup>28-30</sup>. Based on these calculations, a hypothesis regarding primary and secondary transformation reactions of potassium are introduced<sup>30</sup>. The primary reactions include formation of KOH and K<sub>2</sub>O via direct interaction with oxygen and water vapor<sup>30</sup>. In later stages (secondary reactions) KOH and K<sub>2</sub>O can be converted to the different K-species

such are potassium phosphates, sulphates, chlorides, carbonates, silicates<sup>30</sup>. These compounds are also experimentally detected using various techniques.

### **KCl**

Potassium chloride is the most commonly identified potassium species in biomass ash<sup>20</sup>. In biomass combustion, it can be found in gaseous phase, in aerosol form, or retained in the ash particles. Potassium chloride is also detected by XRD in various biomass ashes produced at temperatures below 600 °C<sup>31</sup> or at higher temperatures<sup>32</sup>. KCl content in bottom ash decreases with increasing temperature due to its evaporation, and it can be completely eliminated above 1100 °C<sup>32</sup>. KCl is also detected in the fly ash obtained from the grate boiler combustion of agricultural residues<sup>33</sup>.

### **K<sub>2</sub>SO<sub>4</sub>**

Potassium sulphate is detected in the ash from biomass fuels with elevated potassium and sulphur content. It was detected by XRD analysis of the ashes from combustion of rice straw<sup>34</sup>, wood and straw<sup>35</sup>, as well as olive kernel and olive tree wood<sup>36</sup>. Besides K<sub>2</sub>SO<sub>4</sub>, K<sub>2</sub>Ca<sub>2</sub>(SO<sub>4</sub>)<sub>3</sub> is detected in the ash from wood and straw combustion<sup>35</sup>.

### **K<sub>2</sub>CO<sub>3</sub>**

The formation of K<sub>2</sub>CO<sub>3</sub> is thermodynamically favorable when the chlorine, sulphur, and silica contents of the biomass fuel are lower than total potassium content. Potassium carbonate has been detected in the fly ash obtained from a full-scale pulverized wood combustion boiler<sup>37</sup>, and in the ash obtained from combustion of a groundnut shell below 650 °C<sup>31</sup>. In addition, it is suggested that a significant amount of K<sub>2</sub>CO<sub>3</sub> is present in the char from a fast pyrolysis of rice husk in a temperature range of 500–900 °C, based on the measured water soluble potassium and the anions (SO<sub>4</sub><sup>2-</sup>, PO<sub>3</sub><sup>3-</sup>, HCO<sub>3</sub><sup>-</sup>)<sup>38</sup>. Recently, the formation of K<sub>2</sub>CO<sub>3</sub> from char bonded potassium during pyrolysis of KCl doped cellulose samples has been reported<sup>39</sup>. Moreover, formation of mixed carbonate K<sub>2</sub>Ca(CO<sub>3</sub>)<sub>2</sub> is also confirmed by XRD analysis of the ash from wood combustion<sup>30</sup>.

### **K-silicates**

Potassium silicates may be originally present in biomass or they can be formed during combustion process<sup>18,23</sup>. K-silicates can be present either in crystalline or amorphous forms. The formation of

amorphous potassium silicates (e.g.  $K_2Si_4O_9$ ,  $K_2Si_2O_5$ ,  $K_2SiO_3$ ) is suggested in ashes from rapeseed combustion<sup>40</sup>, rice straw combustion<sup>24</sup>, and wheat straw combustion<sup>41</sup> based on SEM-EDX analysis.

On the other hand, the formation of crystalline K-silicates is reported based on XRD analysis of ash.  $K_2CaSiO_4$  is detected in ash from groundnut shell combustion<sup>31,42</sup>, wood and straw combustion<sup>35</sup>, and rice husk combustion<sup>43</sup>.  $KAlSi_3O_8$  is detected in the ash samples from straw combustion<sup>35</sup>, as well as in ash from wood combustion<sup>44,45</sup>.

### 2.3.3 Interaction between biomass ash and bed material

The ash formed during combustion of biomass can interact with bed material in different ways, and these interactions may cause bed agglomeration. Two main agglomeration mechanisms, coating induced and melt induced agglomeration, are usually reported<sup>14,15</sup>. The interaction between biomass species (mainly potassium) and bed material (*i.e.* silica sand) can induce formation of high viscous coating layer around bed particles. The viscosity of the coating layer is related to its stickiness and coating induced bed defluidization can occur due to the viscos flow sintering<sup>16</sup>. The coating induced agglomeration has been observed during fluidized bed combustion of various biomass fuels<sup>10,14</sup>, and the mechanism is schematically presented in Figure 2-10a.

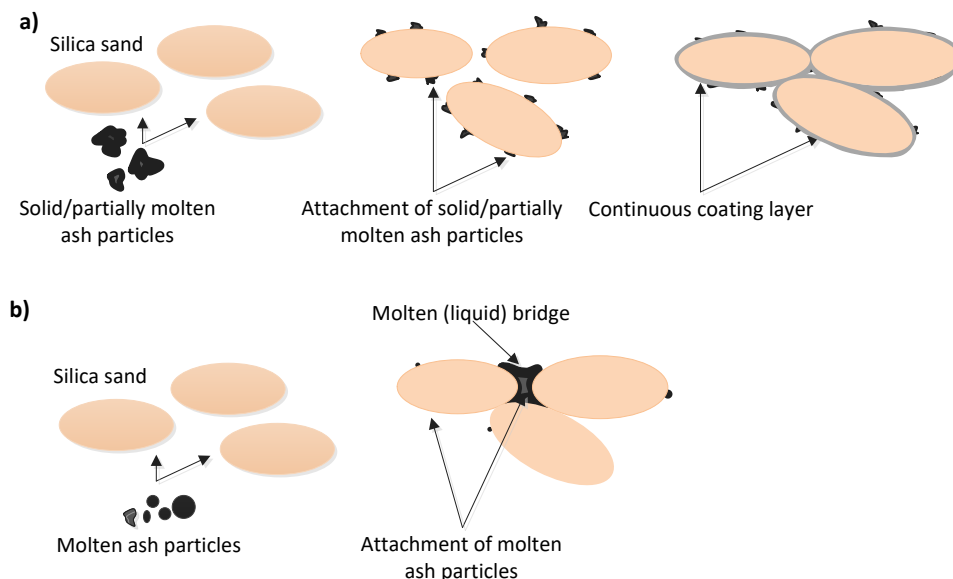


Figure 2-10: a) Coating and b) melt induced agglomeration

The formation of the coating layer can be induced in reaction between potassium released in gaseous phase (KCl and KOH for instance) or aerosols with silica sand to form high viscous K-silicates<sup>46</sup>. Moreover, the interaction between biomass ash and bed material can be initiated by attachment of molten/partially

molten ash particles <sup>12</sup>, or adhesion of solid ash particles <sup>15</sup>. K-species present in attached ash particles (mainly potassium) can invade silica sand surface to form K-silicate that is covering surface of bed material particles. The contribution of each of these mechanisms has been unknown until the recent two-stage experiments, where it is showed that the extent of the gas-solid reaction is negligible <sup>15</sup>.

When an ash particle (molten or solid) is attached to a silica sand particle, the potassium present in the ash particle (the form of potassium is still unknown) can invade silica sand lattice, which results in the formation of a melt consisting of high-viscous K-silicate <sup>15,47</sup>. This mechanism is illustrated in Figure 2-11. If the number of contact points is sufficient, the melt can cover complete silica sand surface to form sticky coating layer. It is suggested that the coating layer grows into two directions: outwards by dissolving the potassium in the ash particle; inwards by dissolving silica sand <sup>16</sup>. After the formation of the melt K-silicate, the calcium present in the ash is further incorporated into the formed layer <sup>16,17,48</sup>. The properties of the formed layer, such as viscosity and thickness, play an important role in defluidization. As soon as a critical layer thickness and viscosity are reached, a complete bed defluidization can occur due to the viscous-flow sintering <sup>17</sup>. Beside the described high viscous coating layer, an additional, solid-like layer is observed <sup>12,15-17</sup>. It is rather heterogeneous, with the composition similar to the global ash compositions apart from K and Ca content. That indicates that the outer coating layer consists on ash particles attached to silica sand surface, followed by the diffusion and reaction of K and Ca with bed material <sup>12,15</sup>.

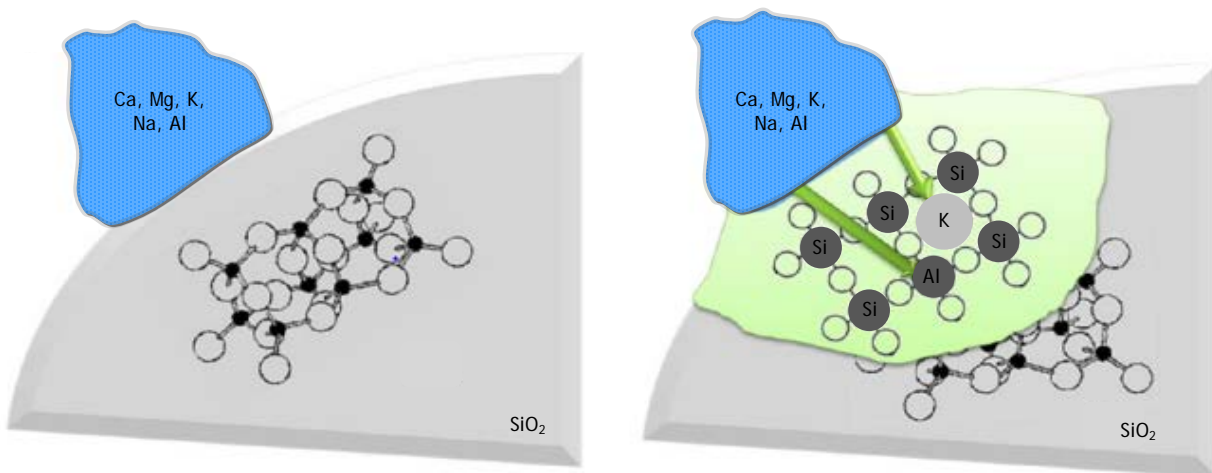


Figure 2-11: Invasion of potassium to silica sand lattice <sup>15</sup>

Melt induced agglomeration is the second agglomeration mechanism related to the formation of molten ash particles observed, for example, during combustion of poultry litter and wheat straw <sup>14,49</sup>. The inorganic composition of these biomass fuels favors the formation of molten ash particles at combustion

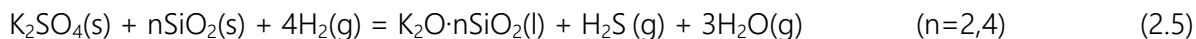
temperature of fluidized bed boilers. The formation of coating layers is limited in this case and the molten ash particles act as a binder of silica sand particles (Figure 2-10b). Molten ash particles are usually generated near the burning particles, due to the high local temperature<sup>15</sup>. Melt induced agglomeration alone cannot cause severe defluidization problems, especially in the large scale boilers<sup>49</sup>, but it can be easily combined with coating induced agglomeration to cause rapid bed defluidization<sup>14</sup>.

### 2.3.3.1 Interaction between model K-species and silica sand

The agglomeration problems in fluidized bed boilers are, to large extent, caused by the interaction between potassium species present in biomass and silica sand bed material. Recently, several studies investigated the interaction between model potassium compounds and silica sand in the fluidized bed system. It was found that potassium species can induce agglomeration in two ways: a) melt induced agglomeration observed in case of KCl and KOH<sup>50-52</sup> addition with limited reaction involved, and b) reaction induced agglomeration observed in case of K<sub>2</sub>CO<sub>3</sub> addition<sup>51,52</sup>. A low viscous liquid is formed above KCl or KOH melting point and smeared over silica sand particles. It acts as a glue to bind sand particles, which causes defluidization. It is observed that the critical amount of melt necessary to cause defluidization is increasing at a higher superficial gas velocity<sup>50</sup>. It should be pointed out that molten ionic species (KOH and KCl) induced defluidization has to be distinguished from molten ash induced agglomeration (Figure 2-10b) since the viscosity of molten ionic species is much lower compared to viscosity of molten ash particles<sup>53,54</sup>. Reaction induced defluidization by K<sub>2</sub>CO<sub>3</sub> occurs in a wide temperature range of 728-900 °C, primarily depending on the K<sub>2</sub>CO<sub>3</sub> content in the silica sand bed. In this case, defluidization is induced by formation of sticky potassium silicates<sup>51,52</sup>.



The reaction between K<sub>2</sub>CO<sub>3</sub> and silica sand occurs below melting point of both species, and it can be monitored by CO<sub>2</sub> release<sup>55</sup>. The formation of potassium silicates is also possible through reaction 2.5, between K<sub>2</sub>SO<sub>4</sub> and silica sand under H<sub>2</sub> rich atmosphere<sup>56</sup>. On the other hand, the reaction does not take place under air atmosphere<sup>51</sup>.



## 2.4 Impact of operating parameters

The extent of bed agglomeration and defluidization is influenced by the operating parameters, such as temperature, gas velocity, sand size, fuel size, etc. The impact of the operating parameters is described below.

### **2.4.1 Operating temperature**

It is commonly suggested that bed agglomeration is pronounced at higher temperatures due to the faster formation of the coating layer, as well as relatively larger amount of molten ash particles<sup>11-13,57</sup>. Besides, the stickiness of the coating layer is increasing with increasing temperatures, thus favoring viscous flow sintering<sup>13</sup>. When the bed temperature is decreased below 650 °C, the defluidization can be avoided, even for problematic fuels such as rice straw<sup>58</sup>. However, in industrial scale boilers, the bed temperature is typically kept about 800-850 °C to facilitate good combustion efficiency.

### **2.4.2 Bed material size**

Different impacts of the bed material size on the defluidization phenomena have been observed. It is reported that a bigger sand size promotes defluidization during combustion of wheat straw<sup>11</sup> and eucalyptus bark<sup>57</sup>. On the other hand, coarser sand size decreased defluidization tendency during combustion of exhausted olive husk, virgin olive husk, pine seeds shells<sup>12</sup>, and dried distillery grains, corn cobs, willow, alder<sup>59</sup>. The impact of a bigger sand size on agglomeration can be attributed to two parameters: total surface area of the sand particles, and the ratio between gas velocity and minimal fluidization velocity ( $U_g/U_{mf}$ ). The total surface area of bigger sand particles is smaller; meaning that thickness of the coating layer is higher. The  $U_g/U_{mf}$  ratio for bigger sand particles is smaller, resulting in a poorer mixing and, consequentially, a higher defluidization tendency<sup>11</sup>. On the other hand, kinetic energy of bigger sand particles is higher; meaning that the breakage of the formed agglomerates is easier, therefore defluidization is prolonged<sup>12</sup>. Besides that, the porosity of formed agglomerates is higher for bigger sand particles, which also inhibits partial segregation and, consequentially, decreases defluidization tendency<sup>12</sup>.

### **2.4.3 Gas velocity**

A higher gas velocity reduces defluidization tendency<sup>11-13</sup>, due to a better bed mixing that inhibits both, bed segregation and hot spots formation<sup>11</sup>. Furthermore, higher gas velocity increases the kinetic energy carried by bed particles, thus promoting agglomerates breakage<sup>11,13</sup>. A higher gas velocity can prolong defluidization time up to 30 %, but the defluidization cannot be avoided<sup>11,13</sup>.

## **2.5 Countermeasures**

The bed agglomeration and defluidization tendencies can be partially reduced by manipulating operating conditions, but usually bed defluidization cannot be completely avoided. That is why; implementation of effective counteractions for preventing defluidization is necessary in order to ensure stable operation

<sup>5,9,60</sup>. Numerous countermeasures are proposed in literature such as alternative bed materials <sup>30,35,61,62</sup>, additives <sup>63–67</sup>, co-combustion <sup>40,58,68,69</sup>, and biomass pretreatment <sup>70</sup>.

### 2.5.1 Alternative bed material

Agglomeration related problems are mainly caused by interaction between ash containing species and silica sand, which is usually used as a bed material <sup>5</sup>. Consequentially, it is considered that replacing the bed material with more inert compounds (such as alumina, olivine, speiolite, etc.) can reduce agglomeration problems and prevent defluidization.

Alumina ( $\text{Al}_2\text{O}_3$ ) is a suitable bed material, since the reaction between ash species (mainly potassium) and  $\text{Al}_2\text{O}_3$  is limited in the temperature range commonly used in fluidized bed systems. Eucalyptus bark is combusted in a fluidized bed consisting of both, silica sand and alumina, and agglomeration extent is significantly reduced when using alumina <sup>57</sup>. When using alumina as bed material no agglomeration problems are observed in a pilot scale conical bubbling fluidized bed during 30h combustion of peanut shells and palm kernel shells <sup>61,71</sup>. Similarly, no agglomeration is observed during lab-scale fluidized bed combustion of cedar pellets <sup>62</sup>, as well as of cypress pellet and cypress sawdust <sup>72</sup>. Olivine ( $(\text{Mg}, \text{Fe})_2\text{SiO}_4$ ) is also used as a bed material in the lab-scale combustion of various biomass fuels including willow, logging residues, wheat straw, and wheat distiller's dried grain with soluble (wheat DDGS) <sup>73</sup>. On contrary to silica sand bed material, no agglomeration problems are observed during combustion of willow and logging combustion when using olivine as bed material. On the other hand, agglomeration problems are observed during combustion of wheat straw and DDGS when using both, olivine and silica sand bed material. The problems are related to molten ash particles that causes bed agglomeration <sup>73</sup>. When iron blast-furnace slag is used as a bed material during combustion of five biomass fuels included bark, olive residue, peat, wheat straw, and reed canary grass <sup>74</sup>. Compared to silica sand, agglomeration tendency is significantly reduced for most of the fuels, except for the wheat straw. In the case of wheat straw, formation of molten ash particles is observed, which results in the formation of agglomerates <sup>74</sup>. Recently, ilmenite ( $\text{FeTiO}_3$ ) is proposed as effective bed material for combustion of wood chips in a large scale circulating fluidized bed, when mixed with silica sand up to 40 wt. % <sup>75</sup>. Ilmenite is capable of capturing potassium, released during combustion, in the non-soluble  $\text{KTi}_8\text{O}_{16}$  form. In such way potassium associated problems, such are agglomeration and deposition, can be significantly reduced <sup>75</sup>. The comparison between different bed materials (silica sand, bone ash, and magnesite) for combustion of different biomasses (sawdust, meat and bone meal, straw, and willow) is performed in a lab-scale pressurized fluidized bed <sup>65</sup>. It was concluded that performance of different bed materials is related to

both, their compositions and the biomass K and Si content. Agglomeration problems can be reduced by using alternative bed materials for most of the biomasses, except the straw with high K and Si content <sup>65</sup>. Besides that, the cost of alternative bed material is higher compared to commonly used silica sand, and some problems can occur during disposal of alternative bed materials (olivine for examples) <sup>76</sup>.

### 2.5.2 Additives

Additives are used to change ash chemistry and reduce potassium, as well as chlorine and silica related problems. Different types of additives have been used during fluidized bed combustion of biomass and, according to their chemical compositions, they can be grouped into Al-Si based, Ca based, S based, and P based additives.

Kaolin ( $\text{Al}_2\text{Si}_2\text{O}_5(\text{OH})_4$ ) is one of the Al-Si-based additives. Up to 10 wt.% of kaolin is added to silica bed during combustion of wheat straw and bark in a bench scale fluidized bed reactor <sup>63</sup>. Kaolin was transformed to meta-kaolin during combustion process, which is capable of capturing potassium effectively through reaction with potassium released in gaseous phase <sup>77</sup>. Consequentially, the formation of K-Al-silicates with relatively high melting point takes place, and thereby the formation of low melting point K-silicates is inhibited. That is also the reason why addition of kaolin increased defluidization temperature from 739 to 886 °C in the case of wheat straw, and from 988 to 1000 °C in the case of bark <sup>63</sup>. Kaolin is also used during co-combustion of wood and straw pellets in a 12 MW circulating fluidized bed <sup>78</sup>. It is shown that kaolin is capable for capturing gaseous potassium species, such as KCl <sup>78</sup>. Kaolin is also successfully applied in a 35 MW fluidized bed boiler firing forestry residues <sup>64</sup>, and it reduced agglomeration problems as well as ash deposition problems <sup>64</sup>. Beside kaolin, mulite ( $3\text{Al}_2\text{O}_3 \cdot 2\text{SiO}_2$  or  $2\text{Al}_2\text{O}_3 \cdot \text{SiO}_2$ ) and clay are also Al-Si-based additives, which are used during pressurized fluidized bed combustion of various biomass fuels <sup>65</sup>. It is shown that mulite cannot reduce agglomeration tendency of sawdust, while the clay can slightly reduce agglomeration tendency during combustion of meat and bone meal <sup>65</sup>.

Another group of commonly used additives are Ca-based additives.  $\text{CaCO}_3$ ,  $\text{Ca}(\text{NO}_3)_2$ , and  $\text{CaO}$  are used during fluidized bed combustion of artificial solid waste (sawdust, polypropylene, metal solution, and polyethylene) <sup>79</sup>.  $\text{CaO}$  played a significant role in prolonging defluidization, mainly due to the interaction with formed alkali-silicates, which resulted in formation of Ca-alkali-silicates with higher melting point. It is also shown that addition of calcium in a form of aqueous solutions, as in case of  $\text{Ca}(\text{NO}_3)_2$  addition, has been the most effective way for prolonging defluidization time due to the enhanced contact area between fuel and additives particles <sup>79</sup>.  $\text{CaCO}_3$  is also successfully applied in the large scale fluidized bed

combustion of poultry litter <sup>66</sup>. It is observed that both, coating and melt induced agglomeration problems are reduced, mainly due to the formation of Ca-alkali-silicates-phosphates with relatively higher melting temperature <sup>66</sup>.

Phosphorous rich additives have also been used for solving agglomeration problems.  $H_3PO_4$  is added in bench scale fluidized bed combustion of logging residues and wheat straw <sup>67</sup>. Formation of amorphous potassium silicates (usually responsible for agglomeration) is significantly reduced in this case, due to the formation of crystalline Ca-K-phosphates. KCl emission is decreased simultaneously, which reduces deposition problems <sup>67</sup>.

Sulphur base additives (e.g. S and  $(NH_4)_2SO_4$ ) are tested in the 12 MW circulating fluidized bed during co-combustion of wood and straw pellets <sup>78</sup>. Addition of ammonium sulphate slightly reduces agglomeration problems, but the impact of elemental sulphur is negligible <sup>78</sup>.

### 2.5.3 Co-Combustion

Co-combustion of problematic biomass fuels (e.g. wheat straw) with fuels rich in Ca, Al, and S may be as effective as usage of additives. For example, sulfur present in sewage sludge is capable of effective potassium capture in form of stable K-sulphates, as observed during combustion of wheat straw in a 12 MW circulating fluidized <sup>69</sup>. Moreover, it is suggested that Al, Ca, Fe, and P present in the sludge ash are also involved in potassium capture <sup>69</sup>. Wheat straw is co-combusted with sewage sludge in a lab scale bubbling fluidized bed, and it is shown that co-pelletization is more effective compared to co-combustion of separate fuel particles due to close contact between the fuel particles <sup>80</sup>. High sulphur and phosphorous content in the sewage sludge favors the formation of K-phosphates and K-sulphates <sup>80,81</sup>. Besides that, alumina-silicates present in sewage sludge are capable of gaseous potassium capture through formation of K-Al-silicates <sup>80</sup>. Beside co-combustion with straw, sewage sludge is successfully fired together with guar stalks, mustard husk, Prosopis Juliflora wood in a 20 kW bubbling fluidized bed boiler under both, air and oxygen-enriched atmosphere <sup>82</sup>.

Coal is also commonly used for co-combustion with biomass fuels. Co-combustion of coal with wheat straw, olive cake, and wood pellets in a pilot scale fluidized bed, resulted in reduced agglomeration and fouling tendency due to the higher S and Ca content of coal <sup>68</sup>. It is suggested that the sulphur present in coal promotes the formation of potassium sulphate through the sulphation of KCl and KOH <sup>83</sup>. Furthermore, the positive effect of coal addition can be related to presence of alumina silicates, which can react with potassium to form K-Al-silicates <sup>83</sup>. Co-combustion of coal and rice straw can significantly

reduce agglomeration problems, and it has been shown that if coal content is kept above 50 wt. % bed defluidization can be avoided in bench-scale vortexing fluidized bed <sup>58</sup>.

Fuels rich in phosphorous such as rapeseed cake <sup>40,84</sup> and animal manure <sup>85</sup>, are also co-combusted with other fuels in order to reduce agglomeration problems. Rapeseed is very problematic fuel (due to the high K and P content), but when up to 18 wt.% of rapeseed is mixed with wood pellets, the mixture can be burned without agglomeration problems in a 12 MW circulating fluidized bed <sup>40</sup>. If the wood pellets are replaced with bark, stable combustion can be achieved for the rapeseed content up to 40 wt.%, since Ca present in bark limits formation of low-melting point K-P-silicates <sup>84</sup>. On the other hand, animal manure is not as problematic as rapeseed cake and it is successfully co-combustion with olive pruning in a lab scale bubbling fluidized bed under various operating conditions <sup>85</sup>.

#### **2.5.4 Pretreatment**

Significant agglomeration problems caused by high alkali content of biomass can be potentially solved by biomass pre-treatment. Water leaching (washing) is usually applied to troublesome fuels such as olive residues and straw <sup>70</sup>. Formation of agglomerates is not observed during combustion of water washed olive kernel (at 80 °C for 2h) since chlorine and potassium content are significantly reduced during the leaching process, but leaching is not successful for avoiding agglomeration related problems in the case of wheat straw <sup>70</sup>. Beside controlled leaching process, it is suggested that natural leaching process (occurring at land field during rainy days) can significantly improve combustion performance of rice straw and eliminate agglomerates formation in a bench scale fluidized bed <sup>86</sup>.

Recently, torrefaction is applied as a biomass pretreatment method to increase energy density of the fuel, and it is showed that torrefaction can also reduce ash related during combustion of willow, due to the significant reduce of chlorine content <sup>87</sup>. This significantly reduced ash deposition problems, but the impact on agglomeration is unclear <sup>87</sup>. Torrefied willow is also successfully co-combusted with coal in a lab scale bubbling fluidized bed <sup>88</sup>.

### **2.6 Modeling**

Even though bed agglomeration has been extensively studied by experiments for many years, there is very limited number of models, which can describe the agglomeration phenomena. One of such models is coalesce model for two colliding particles and it can be used to estimate defluidization time under various operating conditions <sup>11</sup>. The adhesive force that can hold two particles together is defined by following equation:

$$F_{ad} = \pi b^2 \sigma$$

2.6

The binding radius ( $b$ ) depends on the coating layer thickness and it is related to the amount of ash retained within bed<sup>11</sup>. The binding stress ( $\sigma$ ) is associated with the visco-plastic force and it is inversely proportional to the viscosity of the coating layer<sup>11</sup>. The force opposing to adhesion force is the breakage force, which is proportional to the superficial gas velocity. Beside adhesive and breakage force, the model contains several parameters that needs to be determined by fitting to experimental data<sup>11</sup>. The model can be used to predict defluidization time, but it cannot describe rate of agglomeration as well as size distribution of formed agglomerates. The model has been recently modified in order to consider the reaction between fuel potassium and silica sand<sup>52</sup>, and the interphase momentum transfer is also considered via implementation of drag force. The model can predict defluidization temperature under different operational conditions and the model accuracy is estimated to 80 %<sup>52</sup>.

### 2.6.1 CFD modeling

Beside the described chemical engineering models, computation fluid dynamics (CFD) modeling is a promising approach that might be used in order to simulate bed agglomeration in fluidized bed boilers. For CFD simulation of multiphase system, the Eulerian and Lagrangian approaches are commonly used<sup>89</sup>. Lagrangian approach is also known as discrete element modeling or discrete particle modeling. The gaseous phase is treated as continuous media, while the solid particles are traced individually. Eulerian approach is also known as two-fluid or multi-fluid model (depending on the number of solid phases) where both, solid and gaseous phases, are considered as continuous media<sup>90,91</sup>. Lagrangian approach is more reliable, but computationally more expensive, which limits its usage to dilute systems such as freeboard region of fluidized bed<sup>92</sup>. The Eulerian approach is, on the other hand, less stable and it demands several empirical correlations in order to describe the interaction between phases. Due to the lower computational price, it is more suitable for systems with high number of smaller particles, such as bubbling fluidized bed reactors or dense part of circulating fluidized beds<sup>93,94</sup>.

#### 2.6.1.1 CFD simulation of agglomeration phenomena

CFD modeling of agglomeration phenomena is usually applied to granulation systems (i.e. cold processes involving gas/liquid/solid phases) due to the process simplicity, which does not require comprehensive heat and mass transfer correlations as in fluidized bed combustion of biomass. Modeling of agglomeration formation processes in granulators is based on Lagrangian approach, due to the relatively big solid particles size and, consequentially, reasonable low number of particles. Beside gas and solid phase, a liquid phase, which acts as a binder for solid particles, is present in such systems. That is why;

these systems can be related to fluidized bed combustion where a formation molten ash particles, which act as binder to solid particles, is taking place.

The introduction of liquid phase in granulation processes induces particles agglomeration due to the formation of liquid bridges. The liquid bridge formation is usually simulated using wet-restitution coefficient, describing collision between wet solid particles<sup>95,96</sup>. In order to correctly reproduce experimental data, wet restitution coefficients should be related to liquid amount<sup>95</sup>, as well as to liquid viscosity and gas velocity<sup>96</sup>. The usage of wet restitution coefficients is only an approximate way for evaluation of wet particles collisions<sup>97</sup>. The other possibility is usage of well-defined force models for simulation of liquid bridge formation. These models are based on capillary force since the viscosity of liquid phases used in granulation processes is low (in an order of  $10^{-4}$  Pa·s)<sup>98,99</sup>.

One of the promising approaches for evaluation of agglomeration process and consequential change of particle size distribution along the bed is population balance method (PBM), which can be incorporated within CFD code. The approach is successfully used for modeling of ethylene polymerization in a fluidized bed<sup>100</sup>. The core of PBM model is the agglomeration kernel, which represents the rate coefficient for particles agglomeration<sup>100</sup>. PBM coupled with CFD simulations can successfully reproduce particle growth due to the agglomeration and possible defluidization during fluidized bed granulation<sup>101</sup>. On the other hand, PBM demands accurate kinetic models for determination of agglomeration kernels, which means that the usage is limited to well-defined systems.

Application of existing approaches for CFD simulation of fluidized bed agglomeration during biomass combustion is complex, and it may be extremely computationally expensive. Usage of wet restitution coefficient is limited since physical properties of molten ash particles are not well-defined, and Lagrangian approach may not be suitable due to the very high number of solid particles. On the other hand, agglomeration kinetics is not investigated in detail, which limits the applicability of PBM approach.

#### **2.6.1.2 CFD simulation of bed hydrodynamics**

CFD modeling is an effective tool for investigating hydrodynamics in fluidized bed systems. CFD may not be used for modeling of bed agglomeration during fluidized bed biomass combustion, but it is possible to investigate the impact of formed agglomerates on bed hydrodynamics, for example, the segregation phenomena<sup>4</sup>. Agglomerates formed during biomass combustion have different density and size compared to initial bed material. The investigation of mixing and segregation behaviors of such multiphase systems (with two or more solid phases, for example sand and agglomerates) can be related

to defluidization tendency and possible ways to avoid it. Mixing and segregation behaviors of solid phases have been extensively investigated by experiments using particles of different size and/or density<sup>6,102–108</sup>. It is commonly observed that heavier and larger (jetsam) particles tend to accumulate at the bottom of the bed, while the lighter and smaller (flotsam) particles are concentrated in the upper part of the bed<sup>6,104</sup>. The extent of phase segregation is increased with a lower gas velocity<sup>103,104</sup>, an intermediate mass ratio of the jetsam and flotsam phases<sup>6,106</sup>, and a larger difference in size and density of the solid phases (density being more important)<sup>104</sup>. Recently, the mixing and segregation of binary solid phases in fluidized beds have been evaluated by CFD<sup>109–113</sup>. Eulerian approach is usually used due to the significantly lower computation cost, which makes it applicable for dense fluidized beds<sup>91</sup>. Eulerian multi-fluid simulation of mixing and segregation of solid phases is influenced significantly by the solid-solid drag model<sup>114</sup>, the gas-solid drag model<sup>110,111</sup>, and the particle-wall interaction model<sup>112,113</sup>. It has been shown that an empirical modification of the standard Syamlal O'Brien symmetric solid-solid drag model, proposed by Chao et al.<sup>114,115</sup>, performed better than other solid-solid drag models in simulating a binary solid mixture of glass particles with different diameters<sup>111,114</sup>. For gas-solid drag models, the EMMS-based drag model predicted better mixing and segregation behaviors of a binary solid mixture with different size but same density particles, compared to other gas-solid drag models included in Ansys® Fluent software<sup>111</sup>. However, a universal gas-solid drag model applicable to a wide range of operation conditions is still not available<sup>110</sup>. For particle-wall interaction, the commonly used model is the Johnson-Jackson model, where the specular coefficient ( $\varphi$ ) is a key parameter for representing the degree of tangential momentum transfer of solid phase ( $\varphi = 1$  represents a no-slip boundary condition and  $\varphi = 0$  is corresponding to a free-slip condition)<sup>116</sup>. It was found that a smaller specular coefficient promoted the particle movement along walls, thus enhancing mixing of two solid phases in simulation<sup>113</sup>. The specular coefficient is not measurable in experiments, and is specified by empiricism in practice based on wall roughness, physical properties of particles, the collision velocity, etc.<sup>116</sup>. Even though CFD simulations of binary solid mixtures have been extensively studied, a universal set of simulation parameters and constitutive relations, which can successfully reproduce experimental data for a wide range of operating parameters, is still not available. Therefore, it is hard to choose an optimal set of simulation parameters in the cases where no experimental data is available for model validation.

## 2.7 Summary

Bed agglomeration, as one of the main operational problems in fluidized bed boilers, has been studied for many years. It is commonly agreed that bed agglomeration is mainly caused by the interactions between potassium present in the biomass and silica sand bed material. Recently, the interaction

between model potassium salts and silica sand has been investigated in fluidized bed systems, and two defluidization mechanisms are identified: melt induced and reaction induced agglomeration. Melt induced agglomeration occurs due to the melting of KCl and KOH, which are further acting as glue to bind silica sand particles (limited reaction between K-species and silica sand). On the other hand, it was showed that  $K_2CO_3$  is reacting with silica sand to form K-silicates that potentially cause bed defluidization above their softening temperature. Among all K-species, it seems that only  $K_2CO_3$  is reacting with silica sand under oxidizing conditions, and there is a possibility to follow the reaction rate due to the mass loss associated to  $CO_2$  release.

The extent of bed agglomeration can be reduced by using higher gas velocity, smaller sand size, or reducing operating temperature. The extent can be only decreased, but agglomeration cannot be completely avoided by manipulation of operating parameters. In order to more efficiently deal with agglomeration, numerous countermeasures (pre-treatment, co-combustion, alternative bed materials, and additives) are proposed over the years. They can be very effective for most of the fuels, except for most troublesome fuel, such as wheat straw. Besides that, all of the countermeasures are associated with additional costs.

Bed agglomeration is usually treated experimentally, and there is limited number of precise chemical engineering models. On the other hand, recent development of Computational Fluid Dynamics models enables its implementation to agglomeration problems. CFD models for bed agglomeration process already exist and they are mainly related to cold processes. Its implementation to fluidized bed combustion may not be possible due to the extreme process complexity and relatively limited knowledge about the kinetics of agglomeration, but CFD can be used to evaluate the change in bed hydrodynamics after formation of agglomerates.



# 3

## POTASSIUM INDUCED AGGLOMERATION IN A HIGH TEMPERATURE LAB-SCALE FLUIDIZED BED

---

This chapter has been written in a manuscript format. A slightly modified version of this chapter will be submitted to the peer-reviewed journal, *Energy & Fuels*, very soon.

### 3.1 Introduction

It is commonly agreed that the agglomeration is, to large extent, caused by interactions between the potassium species present in biomass ash and bed materials, which lead to melts formation<sup>11,14,15</sup>. To evaluate the impact of different potassium species on agglomeration, interactions between model potassium compounds and the typical bed material, silica sand, have been investigated as already described in Chapter 2<sup>50-52,117,118</sup>. Most studies on the model potassium compounds focused primarily on the interactions between single potassium compound with silica sand<sup>50-52</sup>. However, different potassium compounds may co-exist during biomass combustion in a fluidized bed<sup>30,31</sup>. Thus, it is important to understand the interactions of mixed potassium compounds with silica sand. Moreover, the interactions between potassium silicates (formed from biomass ash) and sand may also play a role on agglomeration<sup>11,16</sup> and the phenomena from such interaction have not been studied.

This chapter presents the results of a systematic investigation of the interactions of model potassium compounds (KCl, K<sub>2</sub>CO<sub>3</sub>, K<sub>2</sub>Si<sub>4</sub>O<sub>9</sub>) and the mixtures (KCl/K<sub>2</sub>SO<sub>4</sub> and KCl/K<sub>2</sub>CO<sub>3</sub>) with silica sand. The experiments are performed in a lab-scale fluidized bed reactor in term of defluidization temperature. The solid samples are analysed by SEM-EDX, and optical dilatometry in order to further understand the agglomeration mechanisms.

### 3.2 Experimental

#### 3.2.1 Experimental setup

The experimental studies are carried out in a setup illustrated in Figure 3-1. The setup consists of four parts: a gas dosing system, a fluidized bed reactor, a gas analysis system, and a data acquisition system. The gas flow rate to the reactor is controlled by mass flow controller. Fluidizing gas is heated in the preheating section just below a perforated gas distributor. Above the distributor is a bubbling fluidized

bed reactor with an inner diameter of 62 mm. In freeboard, the inner diameter is increased to 100 mm to minimize elutriation of fine particles. The preheater and reactor sections are electrically heated by four independent controllers to obtain the required heating rate and a temperature profile in the reactor. The gas from the reactor enters a cyclone to remove the fines and is sent to the ventilation system. A small part of gas is sampled to an infrared gas analyser (Fischer-Rosemount NGA) to measure CO<sub>2</sub> in some of the experiments. The setup is equipped with 4 temperature sensors: T<sub>1</sub> - right before air distributor; T<sub>2</sub> - right above air distributor; T<sub>3</sub> - in the freeboard; T<sub>4</sub> - 5 cm above the air distributor (used to monitor bed temperature). Moreover, pressure sensor P<sub>1</sub> is used to monitor the pressure right below the air distributor, while pressure sensor P<sub>2</sub> measures differential pressure between points located just above the air distributor and in the freeboard (used to monitor the pressure drop over the bed and detect bed defluidization). The output of temperature and pressure sensors, as well as the outlet gas concentration is recorded by a data acquisition system with frequency of 1 Hz.

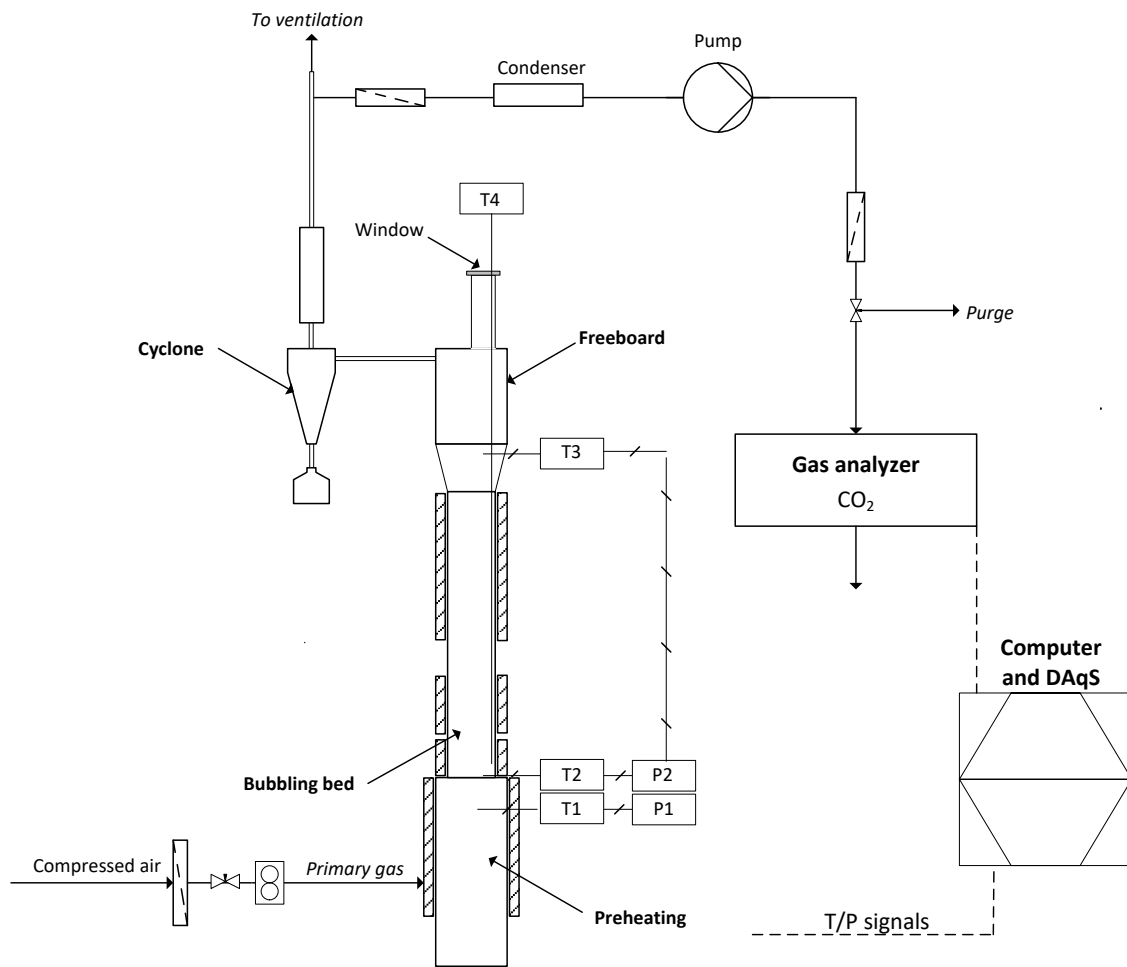


Figure 3-1: A schematic diagram of the lab-scale fluidized bed reactor.

### 3.2.2 Materials

Different potassium compounds (KCl,  $K_2CO_3$ ,  $K_2SO_4$  and  $K_2Si_4O_9$ ), with high purity (>99.9 %), were used for the experimental study. The KCl/ $K_2SO_4$  and KCl/ $K_2CO_3$  mixtures were used as model compounds to understand the effect of co-existing of different potassium forms on agglomeration phenomena. The mixtures were mixed in a ball mill for 15 min at 350 rpm, followed by pelletization, grinding and sieving. Two weight ratios of KCl/ $K_2SO_4$  mixtures were examined: KCl/ $K_2SO_4$  = 46/54 % (eutectic mixture) and KCl/ $K_2SO_4$  = 11/89 %. An eutectic mixture of KCl/ $K_2CO_3$  with a weight ratio of 49/51 % was prepared. The potassium silicate was heated to 850 °C in order to be homogenized, and subsequently grinded and sieved. All model potassium compounds were sieved to a size range of 180-350  $\mu\text{m}$ . The melting points of the model potassium compounds and their mixture are listed in Table 3-1. Two size ranges of silica sand particles were used: 250-300  $\mu\text{m}$  (mean diameter of 273  $\mu\text{m}$ , hereafter denoted as reference sand particles) and 425-500  $\mu\text{m}$  (mean diameter of 473  $\mu\text{m}$ , hereafter denoted as coarse sand particles).

Table 3-1: Melting/eutectic points of K compounds used in the experiments<sup>119</sup>

Salt/mixtures	Melting/eutectic point*
KCl	771 °C
$K_2CO_3$	901 °C
$K_2SO_4$	1069 °C
KCl/ $K_2CO_3$ =49/51 wt.% (eut.)	629 °C
KCl/ $K_2SO_4$ =46/54 wt.% (eut.)	690 °C
KCl/ $K_2SO_4$ =11/89 wt.%	960 °C

### 3.2.3 Experimental procedures and conditions

Silica sand and model potassium compound particles were premixed and loaded to the reactor at ambient temperature. Half kilogram of sand particles were mixed with different amount of potassium salts in each run, corresponding to a static bed height of approximately 10 cm. The fluidizing air was turned on before particles were loaded with a flow rate of 23.5 NL/min. Then, the reactor was heated at a ramp of 10 °C/min up to either the moment of defluidization or to 850 °C. The temperature, at which defluidization occurred, indicated by a sudden decrease of the pressure drop, was defined as defluidization temperature (DT) as already used by Ma et al.<sup>56</sup>. A typical defluidization diagram is illustrated in Figure 3-2. The potassium to sand ratios were varied from 0.25 to 3 wt.% to determine the critical amount of each potassium compound or mixture needed for defluidization in the tested temperature range. Majority of experiments were performed at a constant air flow rate of 23.5 NL/min, meaning that the ratio of superficial gas velocity ( $U_g$ ) to the minimum fluidization velocity ( $U_{mf}$ ) increases

during the heating up stage. In order to study the effect of  $U_g/U_{mf}$  ratio on the critic amount of potassium compounds, the gas flow rate was reduced every three minutes during heating up period to maintain the value of  $U_g/U_{mf}$  equal to 3. The coarser sand particles were also used to examine the influence of  $U_g/U_{mf}$  ratio at the constant air flow of 23.5 NL/min. In some experiment with  $K_2CO_3$ , a low heating rate of 2.5 °C/min was applied after heating up to 650 °C, to examine the effect of heating rate based on our previous work<sup>120</sup>. The variation of the parameters in the study is summarized in Table 3-2.

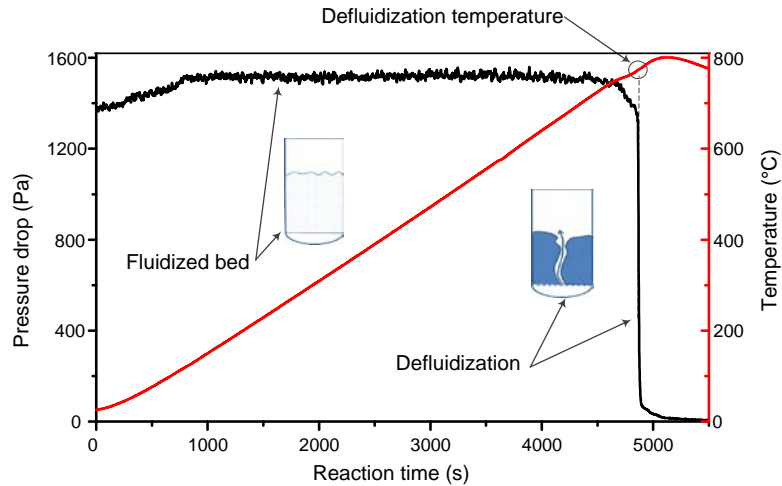


Figure 3-2: A typical defluidization diagram and the identification of defluidization temperature (DT). The experiment is performed for KCl-silica sand system under reference conditions, with a potassium to sand ratio of 0.75 wt.%.

A few experiments were duplicated, showing a good repeatability, with deviations in defluidization temperatures within 1 °C.

Table 3-2: Summary of parameter variation

	Reference parameters	Varying parameters
Mean sand particle size	273 $\mu\text{m}$	473 $\mu\text{m}$
Gas flow rate	23.5 NL/min	Decreased stepwise to maintain $U_g/U_{mf}$ ratio of 3
Heating rate	10 °C/min	2.5 °C/min after 650 °C

### 3.2.4 Analysis of the samples

Particles were sampled from the bed after each experiment. Selected samples were analysed by Scanning Electron Microscopy equipped with Energy dispersive X-ray (JEOL JSM-5910 and JEOL JSM-7001F). A few samples were imbedded in epoxy resin and gradually polished for analysis of the cross section. A Fraunhofer TOMMI optical dilatometry analyser was used to study the melting behaviour of KCl/ $K_2SO_4$  mixture and  $K_2Si_4O_9$ .

### 3.3 Results and discussion

#### 3.3.1 Critical amount of K-compounds and defluidization temperature

##### 3.3.1.1 KCl and mixtures of KCl-K<sub>2</sub>SO<sub>4</sub>

The experimental conditions and results for the KCl and the mixtures of KCl-K<sub>2</sub>SO<sub>4</sub> with sand are summarized in Table 3-3 and Table 3-4, respectively.

Table 3-3: Summary of experimental conditions and results from KCl-silica sand system

Exp. No	Potassium to sand ratio (wt.%)	Salt to sand ratio (wt.%)	Operating parameters	Final Temp. (°C)*	Defluidization
1.	0.25	0.47	Reference	850	No
2.	0.375	0.72	Reference	850	No
3.	0.5	0.94	Reference	773	Yes
4.	0.75	1.44	Reference	773	Yes
5.	0.25	0.47	Low gas vel.	850	No
6.	0.375	0.72	Low gas vel.	769	Yes
7.	0.375	0.72	Coarse sand	774	Yes

\*Corresponding to either defluidization temperature of highest possible reactor's temperature

Table 3-4: Summary of experimental conditions and results from KCl-K<sub>2</sub>SO<sub>4</sub>-silica sand system

Exp. No	KCl:K <sub>2</sub> SO <sub>4</sub> ratio	K to sand ratio (wt.%)	Salt to sand ratio (wt.%)	Operating parameters	Final Temp. (°C)*	Defluidization
1.	46:54 wt.%	0.25	0.50	Reference	850	No
2.	46:54 wt.%	0.5	1.01	Reference	850	No
3.	46:54 wt.%	0.75	1.53	Reference	675	Yes
4.	46:54 wt.%	2	4.04	Reference	675	Yes
5.	11:89 wt.%	0.75	1.56	Reference	850	No
6.	11:89 wt.%	2.92	5.78	Reference	713	Yes
7.	46:54 wt.%	0.25	0.50	Low gas vel.	850	No
8.	46:54 wt.%	0.375	0.76	Low gas vel.	686	Yes
9.	46:54 wt.%	0.375	0.76	Coarse sand	691	Yes

\*Corresponding to either defluidization temperature of highest possible reactor's temperature

Under reference conditions (listed in Table 3-2), the critical amount of potassium, for KCl-silica sand system, is around 0.5 wt.% of the bed material. When a low gas flow rate is applied, the minimal potassium to sand ratio, necessary to cause defluidization, decreases from 0.5 wt.% to 0.375 wt.%. The same phenomenon is observed when coarse sand particles are used. The relation between the potassium to sand weight ratio and defluidization temperature is plotted in Figure 3-3.

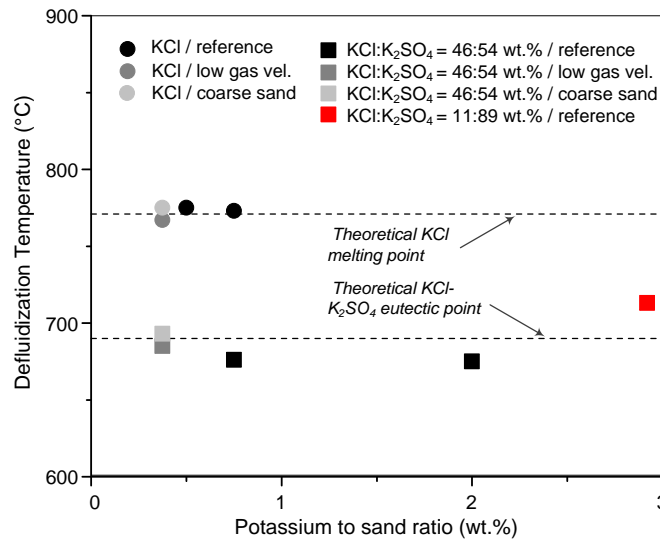


Figure 3-3: Defluidization behavior ( $DT$  as a function of  $K$  content) of  $KCl$ -silica sand and  $KCl$ - $K_2SO_4$ -silica sand systems; experiments performed under reference conditions, and under a low gas velocity ( $U_g/U_{mf} = 3$ ) and coarse sand ( $d_{50} = 473 \mu m$ ) conditions.

It is shown that defluidization occurs near  $KCl$  melting point ( $771^\circ C$ ) almost independent of the amount of potassium in the bed. For the eutectic mixture of  $KCl$ - $K_2SO_4$  under reference condition, the critical value of the potassium to sand ratio is  $0.75$  wt. %, which is higher compared to  $KCl$  case, probably due to non-perfect mixing of two solid salts. The corresponding defluidization temperature is  $675^\circ C$ , which is close to the eutectic point of  $KCl$ - $K_2SO_4$ , even slightly lower than the theoretical of  $690^\circ C$ , as shown in Table 3-4<sup>119</sup>. The defluidization temperature as a function of potassium to sand ratio for the mixture of  $KCl$ - $K_2SO_4$  is also plotted in Figure 3-3. Again, the same trend as for  $KCl$  is observed: when the value of potassium to sand ratio is higher than the critical value, a further increase of the ratio has little effect on the defluidization temperature. For the non-eutectic mixture of  $KCl$ - $K_2SO_4$  ( $11$ - $89$  wt.%), potassium sulphate crystals co-exists with the melt in a temperature interval from  $690^\circ C$  to  $960^\circ C$ , as schematically illustrated by the phase diagram of  $KCl$ - $K_2SO_4$  system represented in Figure 3-4<sup>119</sup>. For such system, no defluidization occurs with potassium to sand ratio of  $0.75$  wt. % up to  $850^\circ C$ . When the potassium to sand ratio is increased to  $2.92$  wt. %, defluidization occurs at  $713^\circ C$ . The impact of gas velocity and coarse sand particles on the defluidization caused by  $KCl$  and  $KCl$ - $K_2SO_4$  eutectic mixture is also investigated. In both cases,  $U_g/U_{mf}$  ratio is equal to  $3$ . For the  $KCl$ -silica sand system, under the lower gas velocity, same minimal potassium to sand ratio ( $0.375$  wt. %) is necessary to cause defluidization as when using coarser sand particles and keeping other reference conditions. In the case when sand is mixed with  $KCl$ - $K_2SO_4$  eutectic the minimal potassium to sand ratio necessary to cause defluidization decreased from  $0.75$  to  $0.375$  wt. %, when using lower gas velocity. Same potassium content ( $0.375$  wt. %) caused

defluidization when using coarser sand. Obtained results indicate that defluidization temperature corresponds to either KCl melting or KCl/K<sub>2</sub>SO<sub>4</sub> eutectic temperature. The impact of potassium to sand ratio (above the critical value), gas velocity, and silica sand size on defluidization temperature is minor.

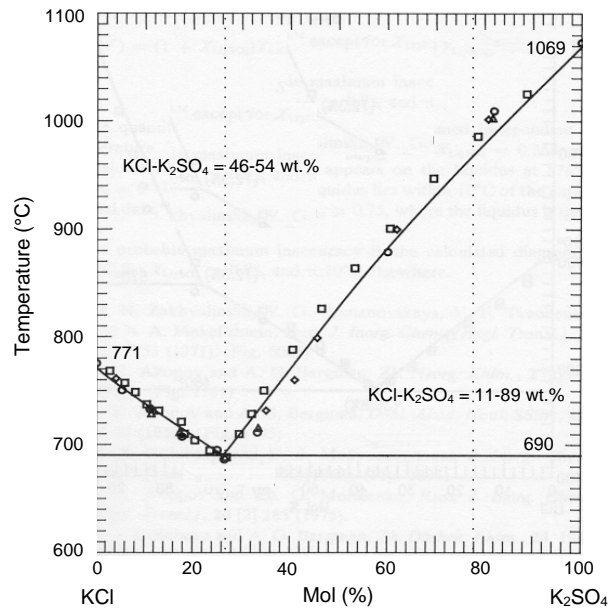


Figure 3-4: KCl-K<sub>2</sub>SO<sub>4</sub> diagram with marked KCl-K<sub>2</sub>SO<sub>4</sub> mixtures used in experiments<sup>119</sup>

### 3.3.1.2 K<sub>2</sub>CO<sub>3</sub> and mixture of K<sub>2</sub>CO<sub>3</sub>-KCl

The experimental conditions and results for K<sub>2</sub>CO<sub>3</sub>-silica sand system are summarized in Table 3-5. It is reported in literature that potassium carbonate reacts with silica sand to form potassium silicates below K<sub>2</sub>CO<sub>3</sub> melting point<sup>51,52,118</sup>. The reactions mechanisms were investigated in our previous study<sup>120</sup>. The reaction between K<sub>2</sub>CO<sub>3</sub> and silica sand during heating up is monitored by analysing CO<sub>2</sub> concentration in the outlet gas at reference conditions for potassium to sand ratio of 0.75 wt.%. It is found that defluidization occurs at 802 °C before a complete conversion (at 830 °C) of K<sub>2</sub>CO<sub>3</sub> at these conditions. Our previous work shows that complete K<sub>2</sub>CO<sub>3</sub> conversion can occur also below 800 °C under sufficiently long reaction time<sup>120</sup>. In order to examine the defluidization behaviour after the complete conversion of K<sub>2</sub>CO<sub>3</sub>, a low heating rate of 2.5 °C/min is applied. Figure 3-5 shows the effect of heating rate on the reaction and defluidization in the K<sub>2</sub>CO<sub>3</sub>-silica sand system. It is shown that the reaction between K<sub>2</sub>CO<sub>3</sub> and silica sand starts at 600 °C. Under the low heating rate, a full conversion of K<sub>2</sub>CO<sub>3</sub> is observed at around 760 °C (based on CO<sub>2</sub> curve) and defluidization occurs at 785 °C. In order to eliminate the influence of incomplete conversion of K<sub>2</sub>CO<sub>3</sub> on the critical K to sand ratio, the low heating rate of 2.5 °C/min has been used in most of the K<sub>2</sub>CO<sub>3</sub>-silica sand experiments, as shown in Table 3-5. The

correlation between the potassium to sand ratio and defluidization temperature is shown in Figure 3-6. Under the low heating rate, the critical K to sand ratio is 0.375 wt. % with a defluidization temperature of 822 °C. Unlike the cases for KCl and KCl- K<sub>2</sub>SO<sub>4</sub> mixtures, the defluidization temperature decreases to 785 °C with an increase of the potassium to sand ratio to 0.75 wt. %, as shown in Figure 3-6.

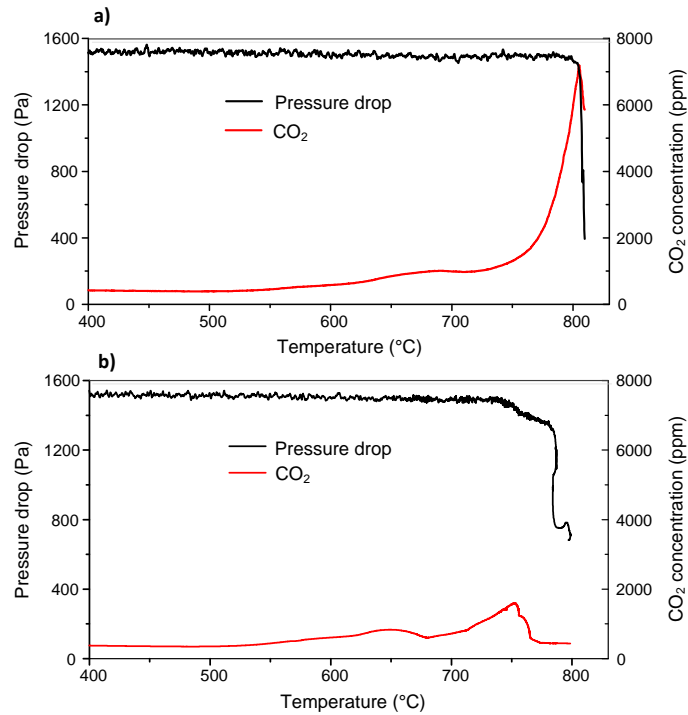


Figure 3-5: Pressure drop and outlet gas CO<sub>2</sub> concentrations as a function of temperature for the K<sub>2</sub>CO<sub>3</sub>-silica sand system. a) Experiment performed under reference conditions and a potassium to sand ratio of 0.75 wt.%; b) Same potassium to sand ratio as in a) but with the heating rate changed to 2.5 °C/min after 650 °C.

Table 3-5: Summary of experimental conditions and results from K<sub>2</sub>CO<sub>3</sub>-silica sand system

Exp. No	K to sand ratio (wt.%)	Salt to sand ratio (wt.%)	Operating parameters	Final Temp. (°C)*	Def.
1.	0.75	1.44	Reference	802	Yes
2.	0.25	0.48	Stepwise heating after 650 °C	850	No
3.	0.375	0.72	Stepwise heating after 650 °C	822	Yes
4.	0.5	0.96	Stepwise heating after 650 °C	802	Yes
5.	0.75	1.44	Stepwise heating after 650 °C	785	Yes
6.	0.5	0.96	Stepwise heating after 650 °C/ Low gas vel.	765	Yes
7.	0.5	0.96	Stepwise heating after 650 °C/ Coarse sand	740	Yes

\*Corresponding to either defluidization temperature of highest possible reactor's temperature

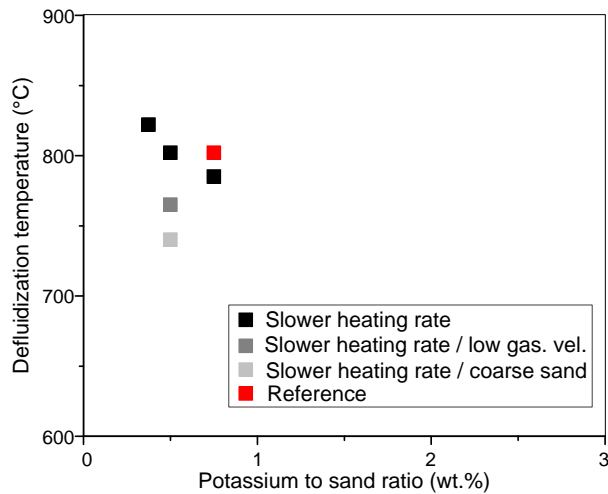


Figure 3-6: Defluidization temperature as function of K content for  $K_2CO_3$ -silica sand system; experiments performed under reference heat rate of  $10\text{ }^\circ\text{C}/\text{min}$ , a slow heating rate of  $2.5\text{ }^\circ\text{C}/\text{min}$  after  $650\text{ }^\circ\text{C}$ , and under a low gas velocity ( $U_g/U_{mf} = 3$ ) and coarse sand ( $d_{50} = 473\text{ }\mu\text{m}$ ) conditions.

The effect of gas velocity and sand particle size can be also seen in Table 3-5 and Figure 3-6. When the low gas flow is applied, the defluidization temperature is decreased to  $765\text{ }^\circ\text{C}$  compared to  $802\text{ }^\circ\text{C}$  at high gas flow with the other parameters keeping the same. When the coarse sand particles are used, the defluidization temperature is as low as  $740\text{ }^\circ\text{C}$ . The results suggest that the defluidization temperature is not the same by varying gas velocity and particle size when keeping the  $U_g/U_{mf}$  ratio constant as in case of KCl and KCl/ $K_2SO_4$  mixtures. The results indicate that defluidization temperature is not related to  $K_2CO_3$  melting point ( $901\text{ }^\circ\text{C}$ ) but rather to the amount of potassium, gas velocity and sand particle size, as well as the reaction time.

The experiments using KCl- $K_2CO_3$  eutectic mixture are performed under reference condition, and summarized in Table 3-6.

Table 3-6: Summary of experimental conditions and results from KCl- $K_2CO_3$ -silica sand system

Exp. No	K to sand ratio (wt.%)	Salt to sand ratio (wt.%)	Operating parameters	Final Temp. ( $^\circ\text{C}$ )*	Defluidization
1.	0.5	0.96	Reference	850	No
2.	0.75	1.37	Reference	771	Yes
3.	2	3.68	Reference	626	Yes

\*Corresponding to either defluidization temperature of highest possible reactor's temperature

The  $CO_2$  concentration in the outlet gas has been continuously monitored to follow the progress of the reaction between  $K_2CO_3$  and silica sand. The pressure drop and the  $CO_2$  concentration as a function of bed temperature for two potassium to sand ratios are shown in Figure 3-7. The results show that reaction

starts at 580 °C, and completes around 700 °C. By comparing Figure 3-5a and Figure 3-7, it can be observed that presence of KCl enhances the reaction between  $K_2CO_3$  and silica sand, resulting in significant shift of the reaction to a lower temperature.

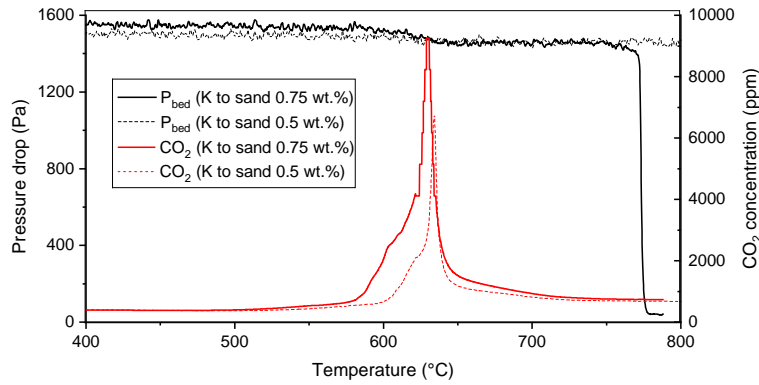


Figure 3-7: Pressure drop and outlet gas  $CO_2$  concentration for the  $KCl-K_2CO_3$ -silica sand systems. Reference conditions, initial potassium to sand ratio of 0.5 and 0.75 wt. %.

Figure 3-8 schematically represents the relation between the potassium content and defluidization temperature for the  $KCl-K_2CO_3$  eutectic mixture. No defluidization is observed, up to 850 °C, if the potassium to sand ratio is kept below 0.5 wt. %. When the potassium to sand ratio is increased to 0.75 wt. %, defluidization is observed at 771°C, which corresponds to  $KCl$  melting point. When the potassium to sand ratio is increased further to 2 wt. %, defluidization occurs at 626 °C, which is close to  $KCl-K_2CO_3$  eutectic point.

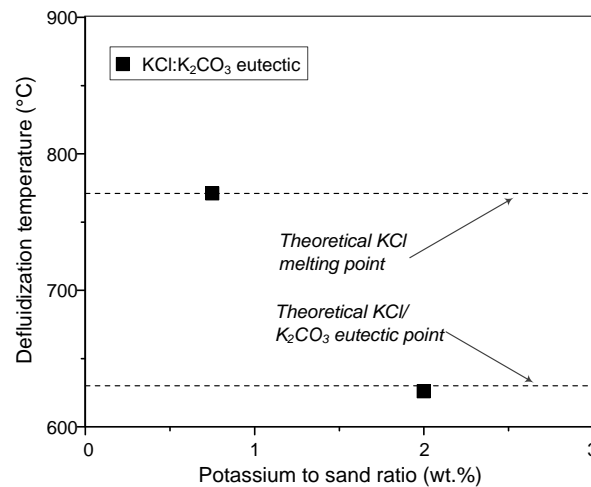


Figure 3-8: Experimental results for  $KCl-K_2CO_3$ -silica sand system under reference conditions

### **3.3.1.3 $K_2Si_4O_9$**

The interaction between  $K_2Si_4O_9$  and silica sand is investigated with two potassium to sand ratios of 0.75 and 2.5 wt.%, the later one corresponds to a potassium silicate to sand weight ratio of 9.68 wt.%. No defluidization is observed for both cases at the reference conditions up to 850 °C and keeping this temperature for 2 h. Only a small decrease in the pressure drop is detected, indicating the formation of agglomerates.

### **3.3.2 Agglomeration mechanisms**

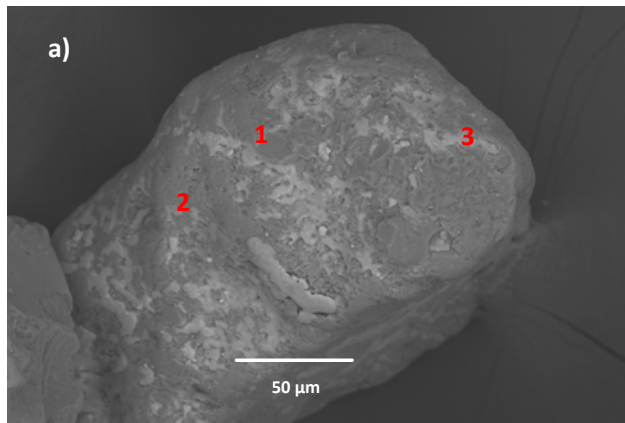
The experimental results clearly show that defluidization induced by the interactions between the model potassium compounds and silica sand particles in fluidized bed at the high temperature can be divided into two categories: melting of the salts and their mixtures without chemical reaction with sand particles and melting resulting from the chemical reactions between the potassium compounds and sand particles. In the first case, defluidization temperature is close to the melting point of the salt or the eutectic point of the salt mixture, independent of the amount of potassium compounds when it is higher than the critical amount. The minimum amount of potassium compounds required for defluidization depends on the flow regime of the fluidized bed (e.g. gas velocity, particle size). In the second case, the defluidization temperature decreases with an increase of the potassium amount, and is dependent of many parameters, such as reaction time, particle size and gas velocity. The agglomeration and defluidization mechanisms are further discussed based on SEM-EDX analysis of the bed material sampled during heating up and after defluidization.

#### **3.3.2.1 *Morphology and composition of the surfaces of agglomerates***

##### **KCl and KCl- $K_2SO_4$ mixture**

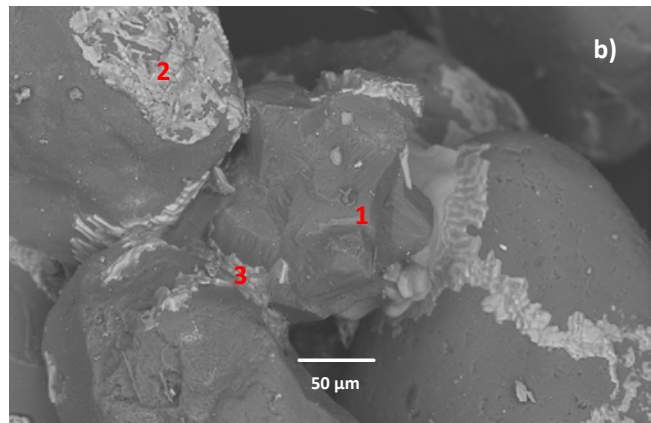
SEM-EDX results (Figure 3-9) reveal that melts only cover part of silica sand surfaces in both systems. The melts glue silica sand particles, and subsequently cause defluidization. The Si concentration in the coating layers is low, which indicates limited reaction between K-salts and silica sand. Moreover, the layer appears to be thin. Thus, the EDX beam may penetrate the coating layer and analyse both, the coating layer and the silica sand surface. Figure 3-9b shows that the composition of the coating layer is not uniform, implying the KCl- $K_2SO_4$  mixture may not be ideally mixed. Additional analysis can be found in Appendix A. Behaviour of KCl-silica sand and KCl- $K_2SO_4$ -silica sand system can be related to melt-induced defluidization observed in literature<sup>50</sup>, showing that a critical amount of melt is needed to induce defluidization and that the DT is always close to the melting temperature of the materials<sup>50,52</sup>. The similar impact of a reduced gas velocity on critical amount of melt needed for defluidization was already

observed in the KOH-silica sand systems<sup>50</sup>. Our study shows, that the critical amount of KCl and KCl-K<sub>2</sub>SO<sub>4</sub> eutectic depends primary on U<sub>g</sub>/U<sub>mf</sub> ratio, and it is decreasing for reduced ratio. The lower ratio can be related to either lower superficial gas velocity (reducing total air flow) or coarser sand particles (keeping total gas flow constant).



Spot	O	Si	Cl	K
1	77.9	21.2	0.02	0.19
2	69.7	28.3	0.06	0.52
3	31.2	3.5	32.1	30.6

All values are given in atomic %



Spot	O	Si	Cl	K	S
1	63.2	36.8			
2	21.7	1.5	18.9	43.6	14.2
3	20.2	1.3	38.6	38.5	1.4

All values are given in atomic %

Figure 3-9: SEM-EDX analysis: a) KCl-silica sand system; reference conditions; initial potassium to sand ratio 0.5 wt.%; sampled from cold reactor. b) KCl-K<sub>2</sub>SO<sub>4</sub>-silica sand system; reference conditions; initial potassium to sand ratio 0.75 wt.%; sampled from cold reactor.

### K<sub>2</sub>CO<sub>3</sub>-silica sand system

SEM-EDX analyses of the agglomerated samples from K<sub>2</sub>CO<sub>3</sub>-silica sand system are shown in Figure 3-10. Figure 3-10a corresponds to the particles sampled at 750 °C, which is before defluidization point, while Figure 3-10b corresponds to the sample taken after the defluidization point (802 °C in this case). The formation of small agglomerates and a coating layer consisting of potassium silicates can already be observed before the defluidization point. As the reaction degree and the temperature further increase, a continuous product layer around the silica sand particles is formed (Figure 3-10b), with a molar ratio of Si/K around 2. The molar ratio is consistent with our previous study, which revealed that K<sub>2</sub>Si<sub>4</sub>O<sub>9</sub> is the main product of reaction between K<sub>2</sub>CO<sub>3</sub> and silica sand<sup>120</sup>. It has been also showed that reaction between K<sub>2</sub>CO<sub>3</sub> and silica sand can occur to some distance from contact point between reactants and the product can cover surface of silica sand<sup>120</sup>. That is the main reason why formation of coating layer around bed material particles is observed. K<sub>2</sub>Si<sub>4</sub>O<sub>9</sub> is a viscous material, with an initial sintering (deformation) temperature of 712 °C<sup>121</sup> and a decreasing viscosity with increasing temperature. Thus, with a fixed

amount of  $K_2Si_4O_9$  in the coating layer, defluidization may occur when a critical viscosity is reached at high temperatures. Besides the viscosity, the thickness of the coating layer also plays an important role<sup>14</sup> and it mainly depends on the amount of product formed. Hence, for a larger amount of  $K_2CO_3$  in the system and a slower heating rate, a thicker product layer is formed, and the critical layer viscosity is reached at lower temperatures. Similar impact of the gas velocity has been reported in the system where high viscous coating layer was formed<sup>14</sup>, observing that DT is influenced by gas velocity if  $U_g/U_{mf}$  ratio was below 4. The dependence on particle size confirms that DT is not only related to  $U_g/U_{mf}$  but also to the layer thickness, which increases when using coarse sand particles.

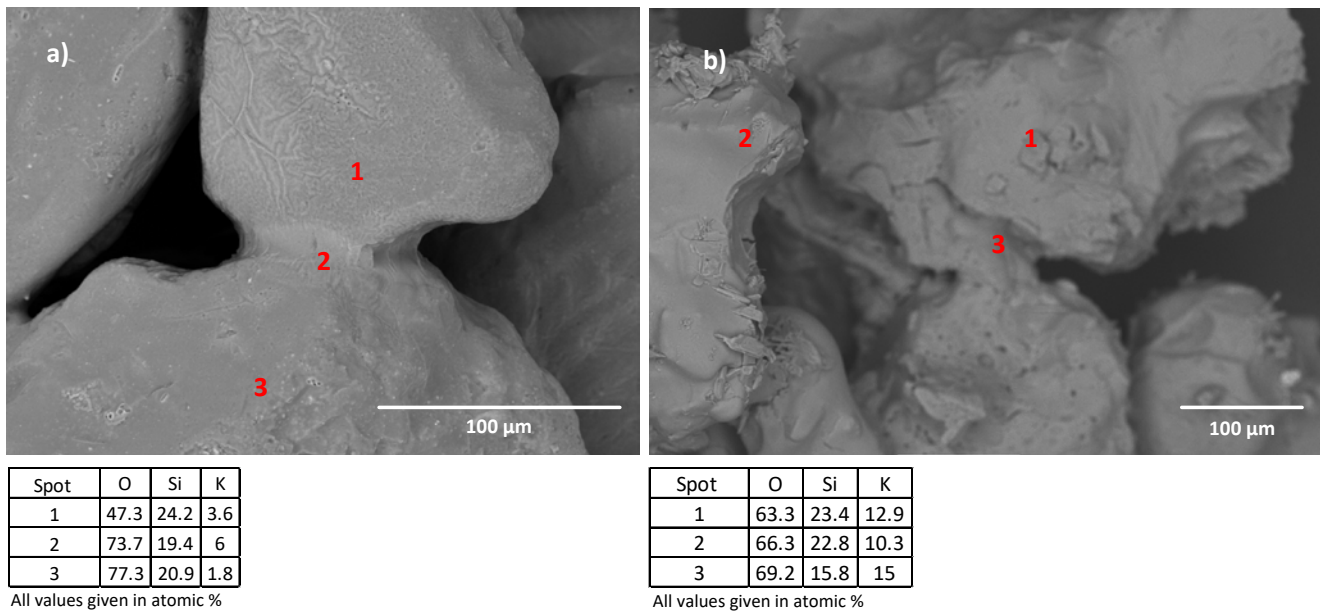
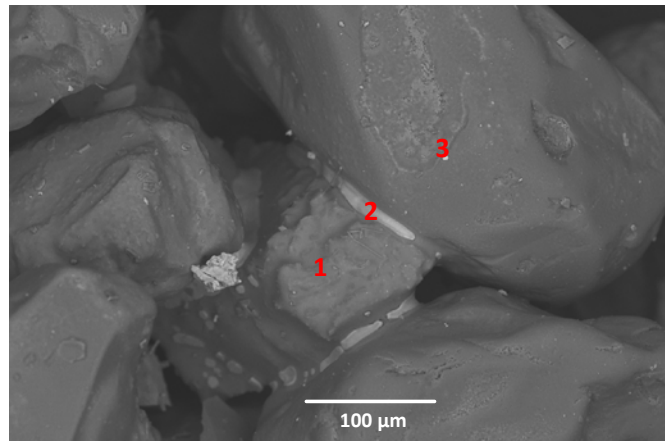


Figure 3-10: SEM-EDX analysis of the samples from  $K_2CO_3$ -silica sand system, with a potassium to sand ratio of 0.5 wt. %, and a heating rate of 2.5 °C/min after 650 °C: a) sampled at 750 °C, b) sampled after defluidization point (802 °C).

### KCl- $K_2CO_3$ -silica sand system

SEM-EDX analysis of the sample with potassium to sand ratio of 0.75 wt. % (Figure 3-11) shows formation of KCl melts together with K-silicate coating layer formed in reaction between  $K_2CO_3$  and silica sand. Additional analysis can be found in Appendix A.

Both of them may contribute to bed defluidization, with KCl melting being a dominant mechanism. When the potassium to sand ratio is increased further to 2 wt. %, defluidization occurs at 626 °C. The defluidization temperature indicates that defluidization is caused by formation of KCl/ $K_2CO_3$  eutectic (theoretical eutectic point is 630 °C)<sup>119</sup>.



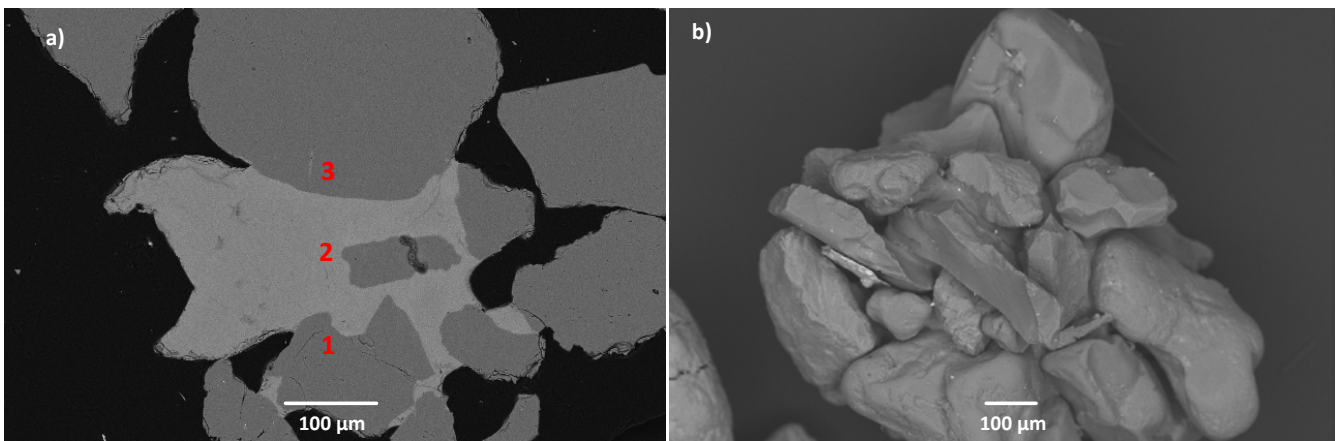
Spot	O	Si	Cl	K
1	72.0	20.5	0.3	6.4
2	37.4	2.7	29.9	29.2
3	67.3	30.1		2.4

All values given in atomic %

Figure 3-11: SEM-EDX analysis of the samples from KCl-K<sub>2</sub>CO<sub>3</sub>-silica sand system: potassium to sand ratio 0.75 wt.%, reference conditions, sampled at defluidization point (771 °C).

### K<sub>2</sub>Si<sub>4</sub>O<sub>9</sub>-silica sand system

SEM-EDX analysis (Figure 3-12) shows formation of molten K<sub>2</sub>Si<sub>4</sub>O<sub>9</sub> particles (spot 2) that act as a glue to physically bind several silica sand.



Spot	O	Si	K
1	64.8	35.2	
2	61.9	27.2	10.9
3	65.2	34.8	

All values given in atomic %

Figure 3-12: SEM-EDX analysis of the sample from K<sub>2</sub>Si<sub>4</sub>O<sub>9</sub>-silica sand system. Potassium to sand ratio 2.5 wt.%; reference conditions; sampled from cold reactor.

The interaction is localized at the contact point between particles, with no reaction. Compared to salt melts, the viscosity of K-silicate is much higher (approximately  $10^4$  Pa·s)<sup>54</sup>, meaning that it cannot be smeared around silica sand surface to form a continuous coating layer. Consequentially, the defluidization is avoided even for very high content of  $K_2Si_4O_9$  in the system.

### 3.3.3 Melting behaviour

The difference of the two types of agglomeration may be attributed to the melting behaviors of the melts. Optical dilatometry analysis is applied to reveal the difference of the melting behavior of salt eutectics and silicates. The melting behavior for the KCl- $K_2SO_4$  = 50-50 wt. % mixture is given in Figure 3-13. It can be observed that when the salts are heated, the melting happens in a small temperature interval, which changes the salts from solid to a low-viscous liquid. The melting of KCl- $K_2SO_4$  can occur even below the theoretical eutectic point (690 °), which can explain observed defluidization temperature (675 °C) for this system.

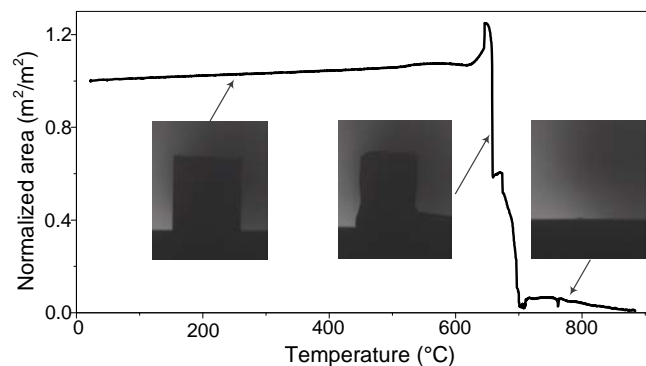


Figure 3-13: Optical dilatometry for KCl- $K_2SO_4$  = 50-50 wt.% mixture, with 1 g sample mass and a heating rate of 5 °C/min.

Generally, the low-viscous liquid can be easily smeared around the sand particles covering part of the sand surfaces as it is schematically represented in Figure 3-14a. The smeared melts cause partial dissipation of kinetic energy between two or more colliding sand particles. At critical conditions, the main part of kinetic energy is adsorbed and particles rebounding is not possible, which leads to bed defluidization<sup>122,123</sup>. Since the viscosity of the molten KCl at 771 °C is  $1 \cdot 10^{-3}$  Pa·s<sup>53</sup>, the dissipation of kinetic energy can be attributed to the surface tension and capillary force, rather than the viscous force<sup>123</sup>. The viscosities of KCl/ $K_2SO_4$  and KCl/ $K_2CO_3$  eutectics are, to the authors' knowledge, not available in literature. However, based on optical dilatometry (Figure 3-13) analysis, it is most likely that the viscosity of the KCl- $K_2SO_4$  eutectic is low, most probably in the same range as molten KCl. Agglomeration caused by low-viscous liquid is widely observed in fluidized bed melt granulation, where liquid phase (water with

comparable viscosity as molten KCl) is added to the gas-solid fluidized bed in order to form granules<sup>101</sup>. If the amount of liquid is not controlled properly, significant agglomeration problems can occur.

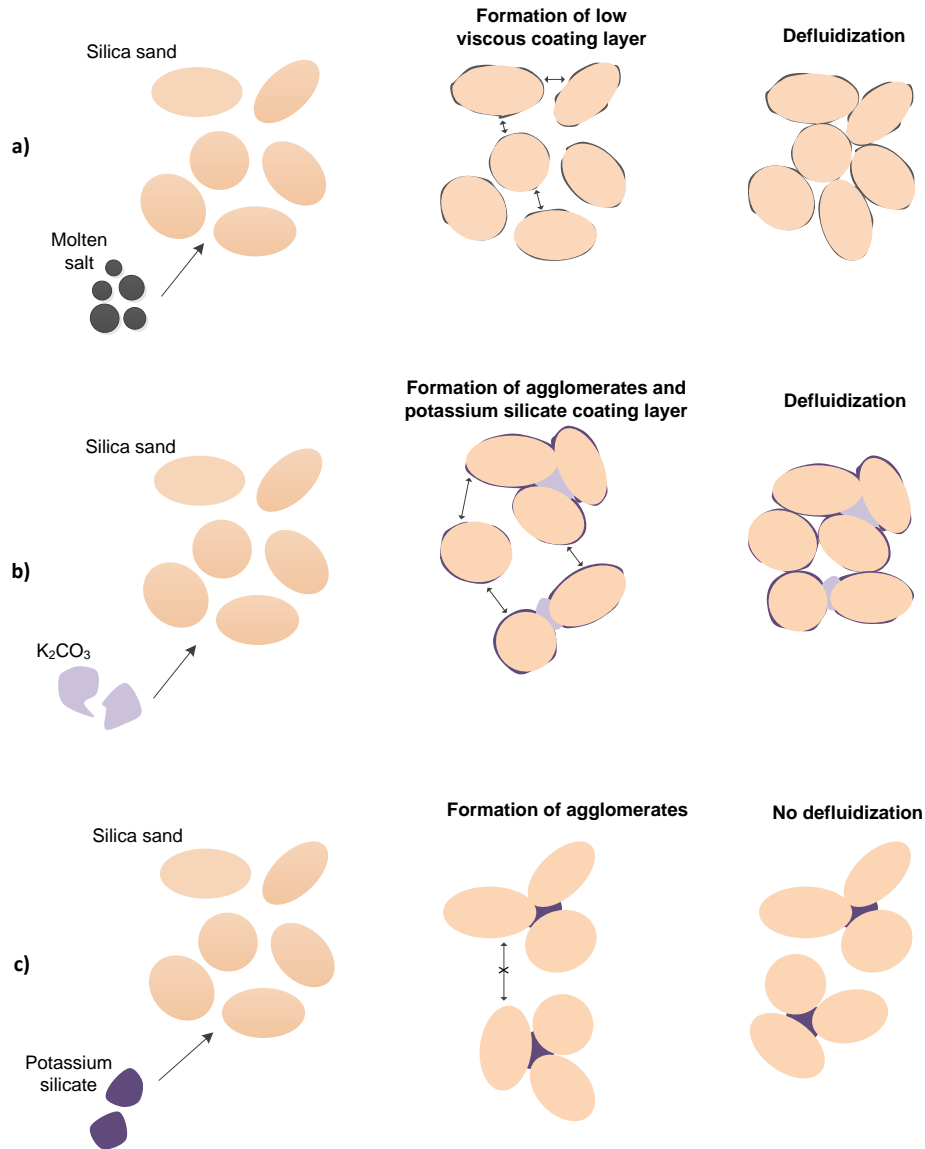


Figure 3-14: Summary of agglomeration and defluidization mechanisms (cross section of sand and agglomerates is considered)

The melting behaviors of  $K_2Si_4O_9$  by optical dilatometry analysis are shown in given at Figure 3-15<sup>121</sup>. In this case transformation from solid to liquid phase is taking place in the wide temperature interval and these materials behave as glass at higher temperature, rather than molten salts.

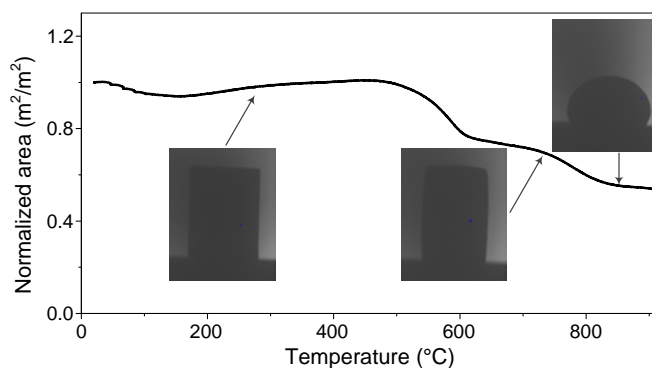


Figure 3-13: Optical dilatometry analysis of  $K_2Si_4O_9$ <sup>121</sup> with 0.96 g sample mass and a heating rate of 5 °C/min.

The viscosity of  $K_2Si_4O_9$  is much higher than viscosity of molten salts, and it cannot be smeared around silica sand particles. On the other hand, such materials becomes sticky above their initial sintering temperature (712 °C)<sup>121</sup>, and they can act as nuclei for binding several silica sand particles, resulting in formation of significant number of small agglomerates (as schematically represented in Figure 3-14c). The interaction between K-silicate and silica sand is purely physical and it is localized at contact points. This indicates that it is difficult to induce a complete bed defluidization by only viscous K-silicates materials from biomass, even though significant number of agglomerates can be formed<sup>49</sup>.

The high-viscous coating layer around bed material particles can be formed in reaction between  $K_2CO_3$  and silica sand since  $K_2CO_3$  can invade silica sand surface and the interaction is not localized at the contact point between reactants as schematically illustrated in Figure 3-14b. The layer mainly consists on  $K_2Si_4O_9$ , which is now smeared around the silica sand surface since it is formed in the reaction between  $K_2CO_3$  and silica sand governed by surface diffusion. It was showed that coating layer is formed continuously during the constant heat up, along with formation of small agglomerates. Besides that, our experiments showed that the reaction is much faster in presence of KCl, implying that the reaction can be promoted by co-existence of KCl and  $K_2CO_3$ . The viscosity of the layer decreases with increasing temperature. In such a case, the dissipation of kinetic energy of colliding particles is related to viscous force<sup>123</sup>, which is dependent both on the viscosity and thickness of the layer. At critical conditions, the majority of the kinetic energy is dissipated by the layer and the defluidization occurs due to the viscous flow sintering, as it is commonly observed during biomass combustion<sup>11,17</sup>.

### 3.4 Conclusions

Based on this work, the following conclusions can be made:

- When adding KCl and a eutectic mixture of KCl/K<sub>2</sub>SO<sub>4</sub>, defluidization is induced by molten salts, with limited reaction between salts and silica sand. DT is close to either KCl melting temperature (770 °C) or KCl/K<sub>2</sub>SO<sub>4</sub> eutectic point (690 °C). Critical potassium to sand ratio mainly depends on  $U_g/U_{mf}$ , and it is increased for higher ratios.
- When adding K<sub>2</sub>CO<sub>3</sub>, defluidization is induced by the formation of a high-viscous coating layer consisting of K-silicates. DT is decreased with increasing amount of K<sub>2</sub>CO<sub>3</sub> added. The reaction between K<sub>2</sub>CO<sub>3</sub> and silica sand is promoted by the presence of KCl.
- In KCl-K<sub>2</sub>CO<sub>3</sub>-silica sand systems, depending on the amount of the KCl/K<sub>2</sub>CO<sub>3</sub> salt mixture, defluidization can occur either near KCl/K<sub>2</sub>CO<sub>3</sub> eutectic point (626 °C) or the KCl melting point (771 °C).
- Molten K<sub>2</sub>Si<sub>4</sub>O<sub>9</sub> particles act as a binder for silica sand particles. Under the investigated conditions, no defluidization is observed up to 850 °C even for a potassium to sand ratio of 2.5 wt.%. Formation of a coating layer is not observed mainly due to the very high viscosity of molten particles.

# 4

## REACTION BETWEEN POTASSIUM CARBONATE AND SILICA SAND

---

This chapter has been written in a manuscript format and a slightly modified form is published in the peer-reviewed journal *Fuel Processing Technology* as:

*B. Anicic, W. Lin, K. Dam-Johansen, H. Wu, Agglomeration mechanism in biomass fluidized bed combustion – Reaction between potassium carbonate and silica sand, Fuel Process. Technol. 2018, 173, 182-190.*

### 4.1 Introduction

In this chapter the results of systematic investigation on the reaction between  $K_2CO_3$  and the silica sand in a TGA is presented. Previous studies, as well as previous chapter indicate that only  $K_2CO_3$  is reacting with silica sand under oxidizing conditions<sup>51,52</sup>. The reaction has been only briefly studied and it is observed that it occurs below melting points of both reactants (around 700 °C) but the detailed mechanisms is not known<sup>55</sup>. In this chapter the influence of the important parameters, such as temperature,  $CO_2$  partial pressure, the mixing of solid particles, and particle size on the reaction rate were examined. SEM-EDX analyses of the reaction products, and thermodynamic calculations of the reaction systems, are carried out to understand the reaction mechanism.

### 4.2 Experimental

#### 4.2.1 Materials

Analytic pure potassium carbonate (CAS 584-08-7, 99.9%) with two particle size ranges, *i.e.* a size range of 2.58 to 224  $\mu m$  (a mean diameter of 18  $\mu m$ , hereafter denoted as powder  $K_2CO_3$ ) and a size range of 146 to 489  $\mu m$  (a mean diameter of 285  $\mu m$ , hereafter denoted as coarse  $K_2CO_3$ ), were used. Moreover, potassium silicate,  $K_2O \cdot nSiO_2$  ( $n=4$ , corresponding to  $K_2Si_4O_9$ ) was melted at 850 °C, and grinded to a narrow size between 180 to 355  $\mu m$ . The silica sand particles used have a size between 255 to 483  $\mu m$  (a mean diameter of 385  $\mu m$ ), which is within the size range commonly used in fluidized bed boilers<sup>124</sup>. The

sand was pretreated at 800 °C under oxidizing conditions for 2h in order to remove potential organic impurities.

The melting temperatures of the  $K_2CO_3$  and  $SiO_2$  are 901 °C and 1710 °C, respectively<sup>119</sup>. Any reaction between  $K_2CO_3$  and  $SiO_2$  occurring below the melting points of both reactants indicates that the reaction is initiated in a solid-solid state<sup>55</sup>. Consequentially, mixing of the reactants may be an important parameter. Thus, three different mixing modes were used in the experiments: well-mixed, two layers (segregated layers of salt and sand with the same surface area), localized two layers (a layer of salt localized at the middle of the sand surface). The well-mixed samples were prepared by manual mixing of the particles for 10 minutes in a cylindrical TGA crucible with a diameter of 16 mm and a height of 20 mm. The two layers samples were prepared by placing the sand at the bottom of the crucible, while the  $K_2CO_3$  was placed above it to completely cover the upper sand surface. The procedure was similar for preparing the localized two layers samples, but in this case the  $K_2CO_3$  was localized at the middle of the sand layer.

#### **4.2.2 Experimental setup**

The experiments were carried out in a high-heating rate thermogravimetric analyzer (TGA, *Netzsch STA 449 F1 Jupiter*), which is capable to heat up the sample up to a maximal heating rate of 1000 °C/min. The uncertainty of the TGA is  $\pm 0.001$  mg, which is several orders of magnitude lower than the mass of samples placed (approximately 0.7 g in each run) in the TGA, indicating that the instrumental error is negligible. Besides that, the results of the repeatability tests showed that the average deviation of the experiments was less than 2% (provided in the Appendix B).

The same temperature program was used for all experiments: the sample was firstly heated to 150 °C and kept for 1 hour to remove moisture. Afterwards, the sample was heated to a final temperature (between 700 and 850 °C) at a heating rate of 500 °C/min and kept for 4 hours. The heating rate was chosen to mimic the rapid heating of particles in a fluidized bed. Due to the high heating rate, the experiments are to a large extent carried out under isothermal conditions. Thus, for presenting the results, the initial time ( $t = 0$  s) is chosen to be the time when the final temperature was reached. A gas flow rate of 50 mL/min was used for all experiments. The experiments were carried out under pure  $N_2$ , pure  $CO_2$ , and a mixture of 50%  $CO_2$  and 50%  $N_2$  conditions. Considering the typical flue gas composition in a fluidized bed boiler, it would be interesting to study the reaction under  $H_2O$  atmosphere. However, our TGA cannot be operated under  $H_2O$  atmosphere. Based on thermodynamic equilibrium calculations, the difference of studying the reaction in  $N_2$  atmosphere and in air atmosphere is negligible. Thus, for the convenience of operating the TGA,  $N_2$  was used instead of air.

### 4.2.3 Analytical methods

The solid samples obtained from the experiments were analyzed by using a Scanning Electron Microscopy with Energy dispersive X-ray (SEM-EDX) analysis (*JEOL JSM-5910*). Some of the samples were imbedded in an epoxy resin and gradually polished using a fine emery paper and an ethanol solution to reveal the cross section of the agglomerated silica sand grains.

Additionally, XRD analysis was performed to identify the products of reaction using a Huber diffractometer with a characteristic Cu K $\alpha$  radiation and operation conditions of 40 kV and 40 mA. The exposure time was 30 minutes.

### 4.2.4 Thermodynamic equilibrium calculations

Thermodynamic equilibrium calculations can provide information about the thermodynamically favored products under different operating conditions. In the present work, equilibrium calculations of the reaction systems were performed in the FACTSAGE 7.0 software. The FToxid and the FactPS databases were chosen for the simulation and the summary of components considered can be found in Appendix D. SlagA model for liquid phase calculation was chosen, since it gave the best fitting between the calculated results of the investigated system and experimentally results reported for a similar K<sub>2</sub>O-SiO<sub>2</sub> system<sup>119</sup>.

The calculations were done for different SiO<sub>2</sub>:K<sub>2</sub>CO<sub>3</sub> molar ratios under pure N<sub>2</sub> and pure CO<sub>2</sub> atmospheres. Calculations were performed in the temperature range 500 and 1500 °C, but the range between 700 and 900 °C is most relevant for the present study. The most common SiO<sub>2</sub>:K<sub>2</sub>CO<sub>3</sub> molar ratio used in experiments was 77 (equal to 100:3 mass ratio), corresponding to the overall (global) ratio. Moreover, since both reactants were present in the solid state, it is expected that the local concentration differs from the global concentration. Thus, a range of SiO<sub>2</sub>:K<sub>2</sub>CO<sub>3</sub> molar ratios, from 77 to 1, were used in equilibrium calculations. 1 mole of SiO<sub>2</sub> was used in all calculations and the amount of K<sub>2</sub>CO<sub>3</sub> was changing in order to obtain specified ratios. The amount of bulk gas was in large excess and it was set to 100 moles for all calculations. Preliminary calculation showed that when in large excess, the exact amount of bulk gas has no impact on the results of equilibrium calculations.

## 4.3 Results and discussion

### 4.3.1 Equilibrium distribution of potassium species

The distributions of potassium species predicted by thermodynamic equilibrium calculations are shown in Figure 4-1. Moreover, the calculation results for the pure K<sub>2</sub>CO<sub>3</sub> in CO<sub>2</sub> and N<sub>2</sub> atmosphere are given in Appendix B.

Thermodynamic equilibrium calculations indicated that at least three different potassium silicates can be formed through the following global reactions:



The results show that the formation of different potassium silicates ( $\text{K}_2\text{SiO}_3$ ,  $\text{K}_2\text{Si}_2\text{O}_5$  and  $\text{K}_2\text{Si}_4\text{O}_9$ ) is already thermodynamically favorable at 600°C. At high temperatures, these potassium silicates are converted to a molten phase slag.

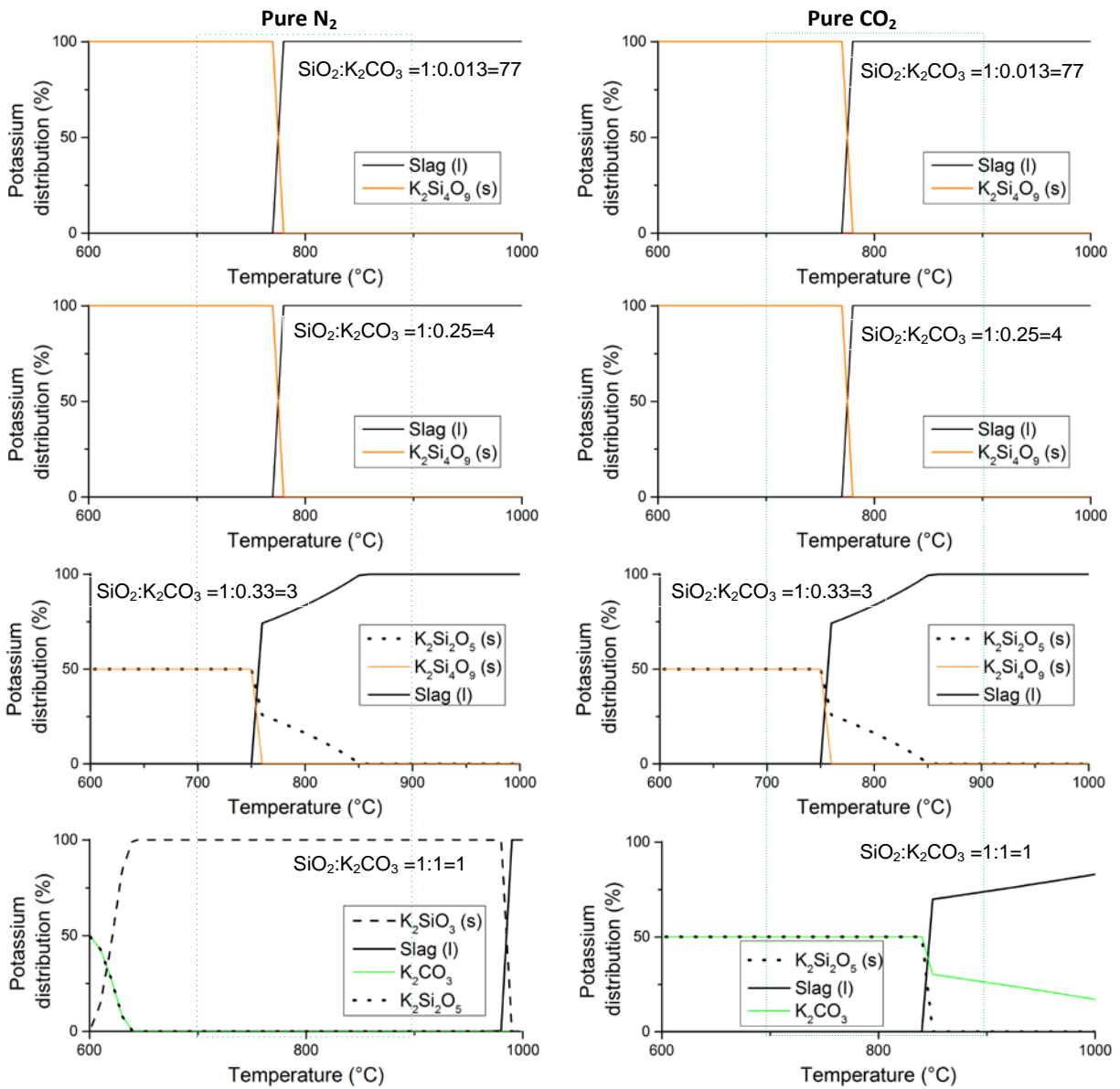


Figure 4-1: Thermodynamic equilibrium calculation for different  $\text{SiO}_2:\text{K}_2\text{CO}_3$  molar ratios under different atmosphere

The formation of the different potassium silicates depends on the molar ratios between the reactants and the gas atmosphere. For high  $\text{SiO}_2:\text{K}_2\text{CO}_3$  molar ratios (4 or above), the formation of  $\text{K}_2\text{Si}_4\text{O}_9$  is favorable, and it converts to a molten slag phase at approximately 770 °C, which is in agreement with the experimentally reported formation of liquid phase for  $\text{SiO}_2:\text{K}_2\text{O}$  systems<sup>119</sup>. For a  $\text{SiO}_2:\text{K}_2\text{CO}_3$  molar ratio of 3, both  $\text{K}_2\text{Si}_4\text{O}_9$  and  $\text{K}_2\text{Si}_2\text{O}_5$  are present at low temperatures, and they convert to a molten slag phase at approximately 750 °C. For  $\text{SiO}_2:\text{K}_2\text{CO}_3$  molar ratios above 3, the impacts of the  $\text{N}_2$  and  $\text{CO}_2$  atmospheres on the equilibrium distribution of potassium species are generally negligible.

The impact of the gas atmospheres is significant when the  $\text{SiO}_2:\text{K}_2\text{CO}_3$  ratio becomes 1. In pure  $\text{N}_2$  atmosphere, the solid phase  $\text{K}_2\text{SiO}_3$  is the only thermodynamically stable species in the temperature range of 700-900 °C. In  $\text{CO}_2$  atmosphere, both  $\text{K}_2\text{Si}_2\text{O}_5$  and  $\text{K}_2\text{CO}_3$  exist at temperatures below 840 °C. Above this temperature, the  $\text{K}_2\text{Si}_2\text{O}_5$  and a part of  $\text{K}_2\text{CO}_3$  convert to a molten slag phase. These results indicate that  $\text{K}_2\text{CO}_3$  conversion is hindered in presence of  $\text{CO}_2$ , probably due to the fact that the equilibrium of reaction (4.1) is shifted to left due to the La Chatelier's principle. Consequentially, as the  $\text{K}_2\text{CO}_3$  amount is increasing the formation of  $\text{K}_2\text{Si}_2\text{O}_5$  is more favorable compared to  $\text{K}_2\text{SiO}_3$ ; meaning that some  $\text{K}_2\text{CO}_3$  remains unconverted.

### **4.3.2 TGA results**

Aforementioned reaction (4.1) indicates that conversion of  $\text{K}_2\text{CO}_3$  can be monitored by the mass loss caused by the release of  $\text{CO}_2$ . Since thermal decomposition of the  $\text{K}_2\text{CO}_3$  is significant only above 1150 °C, all the mass loss below this temperature was attributed to the  $\text{CO}_2$  release, and the  $\text{K}_2\text{CO}_3$  conversion can be calculated accordingly.

#### **4.3.2.1 Influence of reaction temperature**

The conversions of powder  $\text{K}_2\text{CO}_3$  under  $\text{N}_2$  atmosphere, with a  $\text{SiO}_2:\text{K}_2\text{CO}_3$  molar ratio of 1:0.013, are plotted at Figure 4-2. The results show that the reaction rate increased with increasing temperature. The reactants were partially converted before the system reached isothermal condition. The conversion of  $\text{K}_2\text{CO}_3$  in the heating-up stage was increased with increasing reaction temperature. At temperatures above 750 °C,  $\text{K}_2\text{CO}_3$  can be completely converted. However, at 700 °C, the conversion was only approximately 0.8 with a reaction time of 4h. Considering the typical operation temperatures (800-850 °C) of a fluidized bed boiler and the long residence time of bed particles, the results imply that the reaction between  $\text{K}_2\text{CO}_3$  and silica sand can occur to a considerable degree, if the  $\text{K}_2\text{CO}_3$  and silica sand particles are in close contact.

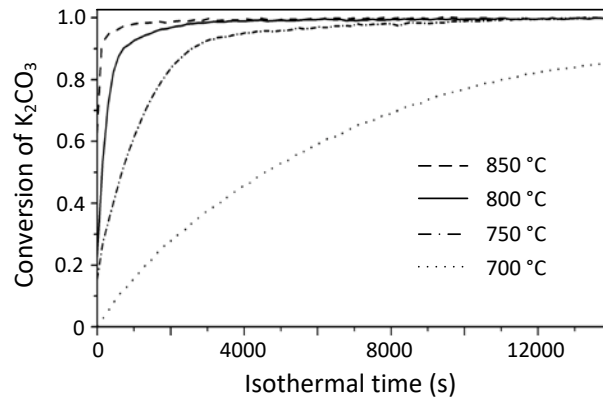


Figure 4-2:  $K_2CO_3$  conversion rates at different temperatures. Pure  $N_2$  environment;  $SiO_2:K_2CO_3$  molar ratio = 1:0.013; well mixed mixtures; powder  $K_2CO_3$ ; total residence time 4h.

The performed thermodynamical calculations revealed that formation of melt phase is possible above 750 °C. Consequentially, above 750 °C, the overall reaction mechanism can be influenced by the change in physical properties of the formed products. That can provide an explanation why the complete conversion was achieved relatively fast above 750 °C, compared to the 700 °C where only 0.8 conversion was reached.

#### 4.3.2.2 Impact of particle size of $K_2CO_3$

Figure 4-3 illustrates the impact of  $K_2CO_3$  particle size (coarse and powder) at two different temperatures (750 °C and 800 °C), with well-mixed  $SiO_2:K_2CO_3$  (molar ratio 1:0.013) samples in the  $N_2$  atmosphere. The results indicate that the  $K_2CO_3$  particle size significantly influenced the initial reaction stages. For the powder  $K_2CO_3$  particles, a complete conversion was achieved at both temperatures. However, the coarse  $K_2CO_3$  particles only reached a stable conversion around 0.8 and 0.9, respectively, at 750 °C and 800 °C.

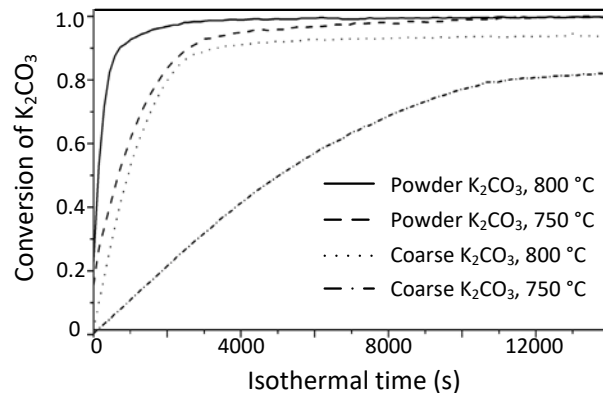


Figure 4-3:  $K_2CO_3$  conversion rates for different sizes of  $K_2CO_3$ . Pure  $N_2$  environment;  $SiO_2:K_2CO_3$  molar ratio = 1:0.013; well mixed mixtures; total residence time 4h.

#### 4.3.2.3 Influence of CO<sub>2</sub> partial pressure

The influence of the gas environment was evaluated by performing experiments under pure N<sub>2</sub>, pure CO<sub>2</sub> and a mixture of 50% N<sub>2</sub> and 50% CO<sub>2</sub>. All experiments were performed at 800 °C, using well-mixed SiO<sub>2</sub> and powder K<sub>2</sub>CO<sub>3</sub> with a molar ratio of 1:0.013. The obtained results are plotted at Figure 4-4. It is shown that the presence of CO<sub>2</sub> strongly inhibited the reaction, especially at the initial stage. However, the difference between 50% CO<sub>2</sub> and 100% CO<sub>2</sub> was insignificant.

Thermodynamic calculations revealed that the impact of atmosphere is significant with low SiO<sub>2</sub>:K<sub>2</sub>CO<sub>3</sub> molar ratio, where the conversion of K<sub>2</sub>CO<sub>3</sub> is less favorable in the presence of CO<sub>2</sub>. We believe the impact of thermodynamics is dominant in our case. However, the presence of CO<sub>2</sub> may also influence CO<sub>2</sub> desorption from the reaction surface, which was observed in the sodium carbonate/silica sand system<sup>125,126</sup>.

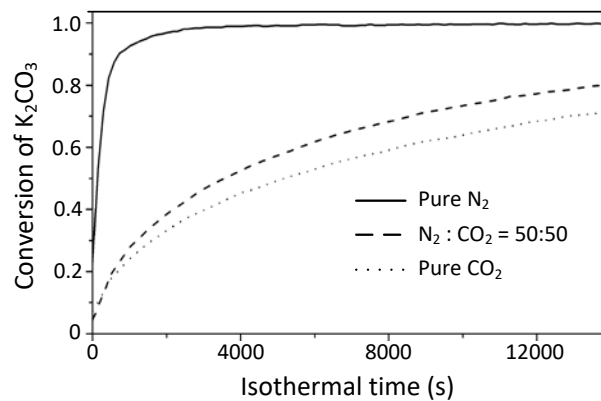


Figure 4-4: K<sub>2</sub>CO<sub>3</sub> conversion rates under different gas atmospheres. T = 800 °C, SiO<sub>2</sub>:K<sub>2</sub>CO<sub>3</sub> molar ratio = 1:0.013; well mixed mixtures; powder K<sub>2</sub>CO<sub>3</sub>; total residence time 4h.

#### 4.3.2.4 Impact of sand to K<sub>2</sub>CO<sub>3</sub> mole ratio

Figure 4-5 shows the impact of molar ratios, for the well-mixed SiO<sub>2</sub> and powder K<sub>2</sub>CO<sub>3</sub> samples at 800°C and the N<sub>2</sub> atmosphere.

A minor effect of the different K<sub>2</sub>CO<sub>3</sub> content can be observed at the initial reaction stage, showing a slightly higher conversion for a lower content of K<sub>2</sub>CO<sub>3</sub>. The difference became negligible after the conversion reached approximately 0.95. Overall, all curves were close to each other, implying an insignificant impact of varying SiO<sub>2</sub>:K<sub>2</sub>CO<sub>3</sub> molar ratio from 1:0.009 to 1:0.022.

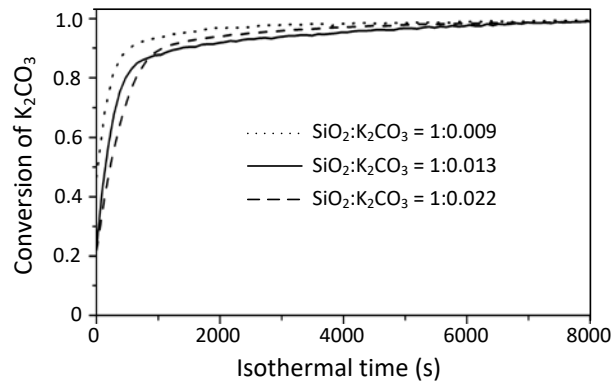


Figure 4-5:  $K_2CO_3$  conversion rates for  $K_2CO_3$ :sand mixtures with different molar ratio.  $T = 800\text{ }^\circ\text{C}$ , Pure  $N_2$ ; well mixed mixtures; powder  $K_2CO_3$ ; total residence time 4h. ( $SiO_2:K_2CO_3 = 1:0.009\text{ mol/mol} = 100:2\text{ wt./wt.}$ ;  $SiO_2:K_2CO_3 = 1:0.013\text{ mol/mol} = 100:3\text{ wt./wt.}$ ;  $SiO_2:K_2CO_3 = 1:0.022\text{ mol/mol} = 100:5\text{ wt./wt.}$ )

#### 4.3.2.5 Impact of mixing

Figure 4-6 illustrates the effect of mixing on the  $K_2CO_3$  conversion, for  $SiO_2$  and powder  $K_2CO_3$  with a mole ratio of 1:0.013 under  $N_2$  atmosphere,  $800^\circ\text{C}$ .

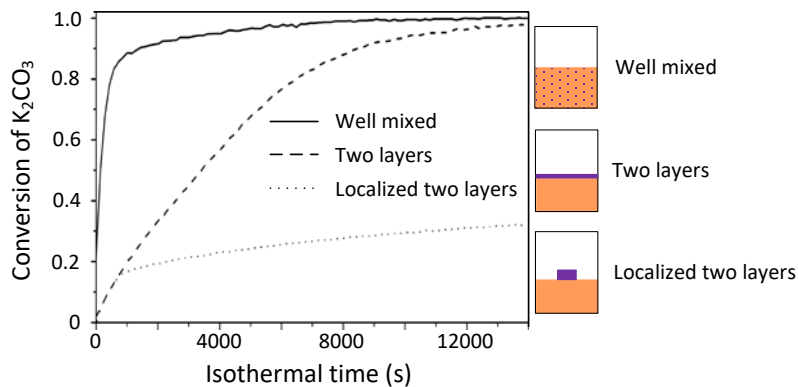


Figure 4-6:  $K_2CO_3$  conversion rates for different mixtures.  $T = 800\text{ }^\circ\text{C}$ ; Pure  $N_2$ ;  $SiO_2:K_2CO_3$  molar ratio = 1:0.013; powder  $K_2CO_3$ ; total residence time 4h.

Initially, the conversions of the two layers and the localized two layers samples were significantly lower compared to the well-mixture sample. The two-layer sample eventually reached an almost complete conversion after a residence time of 4h. On the other hand, the final conversion of  $K_2CO_3$  in the localized two layers sample, was only about 0.3.

#### 4.3.2.6 Comparison of fused glass and silica sand

Figure 4-7 compares the  $K_2CO_3$  conversion with a fused glass and the silica sand. Powder  $K_2CO_3$  was used in both experiments, and it was localized at the middle of the sand/glass surface (localized two layers).

The fused glass was used in order to investigate the impact of the SiO<sub>2</sub> structure on the overall reaction rate. The silica sand has a crystalline structure, while the fused glass is in amorphous phase.

The K<sub>2</sub>CO<sub>3</sub> conversion profiles were similar to each other. The initial conversion (up to about 0.15) was almost the same for the two cases. Then a noticeable change in the K<sub>2</sub>CO<sub>3</sub> conversion rate occurred for both samples, with the fused glass having a slight higher reaction rate. The small difference between the fused glass and silica sand might be associated to the difference in surface smoothness.

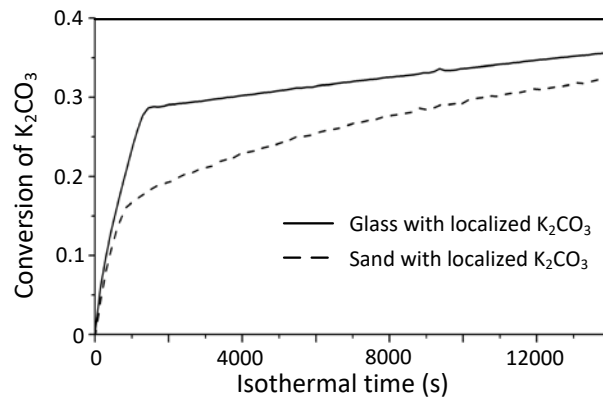


Figure 4-7: K<sub>2</sub>CO<sub>3</sub> conversion rates rate for SiO<sub>2</sub>/K<sub>2</sub>CO<sub>3</sub> and fused glass/K<sub>2</sub>CO<sub>3</sub> samples. T = 800 °C; Pure N<sub>2</sub>; powder K<sub>2</sub>CO<sub>3</sub>; total residence time 4h.

#### 4.3.2.7 Reaction between K-silicate and K<sub>2</sub>CO<sub>3</sub>

Figure 4-8 compares the K<sub>2</sub>CO<sub>3</sub> conversions with potassium silicate (K<sub>2</sub>Si<sub>4</sub>O<sub>9</sub>) and silica sand.

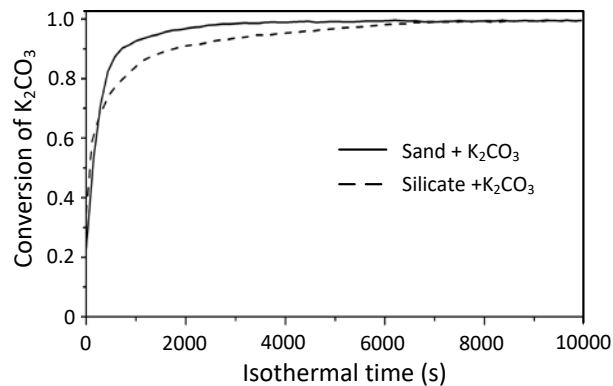


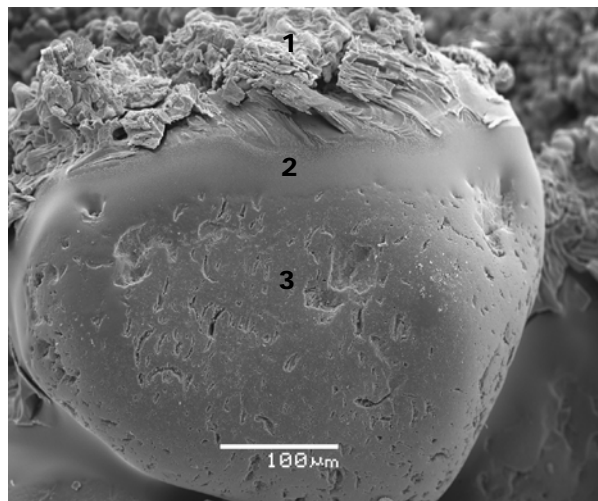
Figure 4-8: K<sub>2</sub>CO<sub>3</sub> conversion rate of SiO<sub>2</sub>:K<sub>2</sub>CO<sub>3</sub> and K<sub>2</sub>Si<sub>4</sub>O<sub>9</sub>:K<sub>2</sub>CO<sub>3</sub> mixtures: T = 800 °C; Pure N<sub>2</sub>; powder K<sub>2</sub>CO<sub>3</sub>; total residence time 4h.

Powder K<sub>2</sub>CO<sub>3</sub> was used in both experiments, with a reaction temperature of 800 °C in N<sub>2</sub> atmosphere. The results indicated that the reaction rate was similar for silica sand and the potassium silicate. At high conversion degrees, the reaction rate was slightly lower for potassium silicate. Since K<sub>2</sub>Si<sub>4</sub>O<sub>9</sub> is a possible

product from the reaction of silica sand and potassium carbonate, the experiments indicate that the formed intermediate potassium silicate product may further react with the potassium carbonate forming different mixtures of potassium silicates.

### 4.3.3 SEM-EDX analyses

SEM-EDX analyses of the reaction products were performed in order to understand the reaction mechanism. Figure 4-9 represents a grain from the two layers mixture under the CO<sub>2</sub> atmosphere with a K<sub>2</sub>CO<sub>3</sub> conversion degree of 0.22.



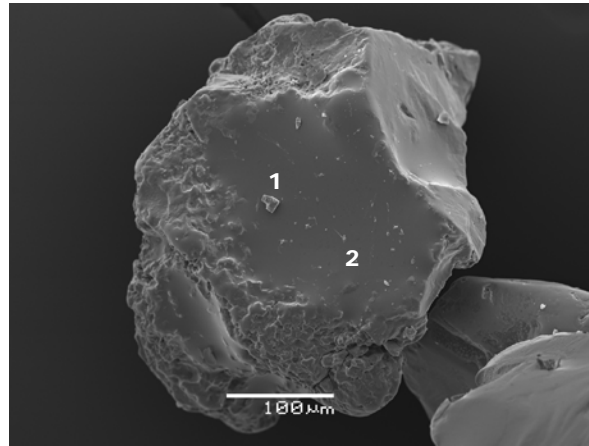
Spot	K	O	Si	Si:K ratio
1	0.17	0.83	0	0
2	0.12	0.67	0.21	1.85
3	0	0.52	0.48	-

All values given in atomic %

Figure 4-9: SEM-EDX analysis of a representative reaction product: 0.22 K<sub>2</sub>CO<sub>3</sub> conversion; SiO<sub>2</sub>:K<sub>2</sub>CO<sub>3</sub> molar ratio = 1:0.013; T= 800 °C; pure CO<sub>2</sub> atmosphere; segregated mixture; powder form of K<sub>2</sub>CO<sub>3</sub>; isothermal reaction time 4h.

Spot 1 characterizes the unreacted K<sub>2</sub>CO<sub>3</sub>, while Spot 3 is the unreacted silica sand surface. Spot 2 represents a layer of produced potassium silicate covering the silica sand surface. The smooth surface implies that the potassium silicate is melted under the experimental temperature (800 °C). Besides, Figure 4-9 indicates that the reaction can proceed away from the initial contact points between K<sub>2</sub>CO<sub>3</sub> and the silica sand, since the formed potassium silicate had invaded the unreacted silica surface. However, at the current conditions, the extent of invasion was limited, since only a part of the sand surface was covered by the product layer.

The observations from Figure 4-9 lead to a hypothesis that formation of a product coating layer around the sand particle is possible at high conversion degrees and sufficient initial contact areas. The hypothesis is supported by Figure 4-10, showing that the sand surface is completely covered by a product layer consisting of potassium silicate. Reacted samples with different  $K_2CO_3$  conversion degrees (0.15/0.55/0.99) were imbedded in an epoxy resin and polished in order to obtain a cross-sectional view of the agglomerated grains.



Spot	K	O	Si	Si:K ratio
1	0.11	0.55	0.34	2.97
2	0.10	0.60	0.30	3.08

All values given in atomic %

Figure 4-10: SEM-EDX analysis of a silica sand grain covered by formed product layer: full  $K_2CO_3$  conversion  $SiO_2:K_2CO_3$  molar ratio = 1:0.013;  $T = 800\text{ }^\circ\text{C}$ ; pure  $N_2$  atmosphere; well mixed sample; powder form of  $K_2CO_3$ ; isothermal reaction time 4h.

Figure 4-11 represents the cross-section SEM images of these samples together with an elemental analysis along the lines, as well as the elemental compositions of selected points (e.g. A1). The elemental analysis along the lines provided the intensity of the EDX emission, showing qualitatively the relative distribution of the elements. Sample A shows the initial stage of the reaction. Spot A1 represents the unreacted potassium carbonate, and Spot A2 represents an initial product layer with a Si:K molar ratio of approximately 1. However, the formed product layer is more heterogeneous compared to the layers in Sample B and Sample C. In Sample B and Sample C, the product layers are quite homogeneous, with more or less constant Si:K molar ratios. The ratio is approximately 2.2 and 2.5, respectively, for Sample B and Sample C, indicating that the product layer consists of a mixture of  $K_2Si_4O_9$  and  $SiO_2$ .

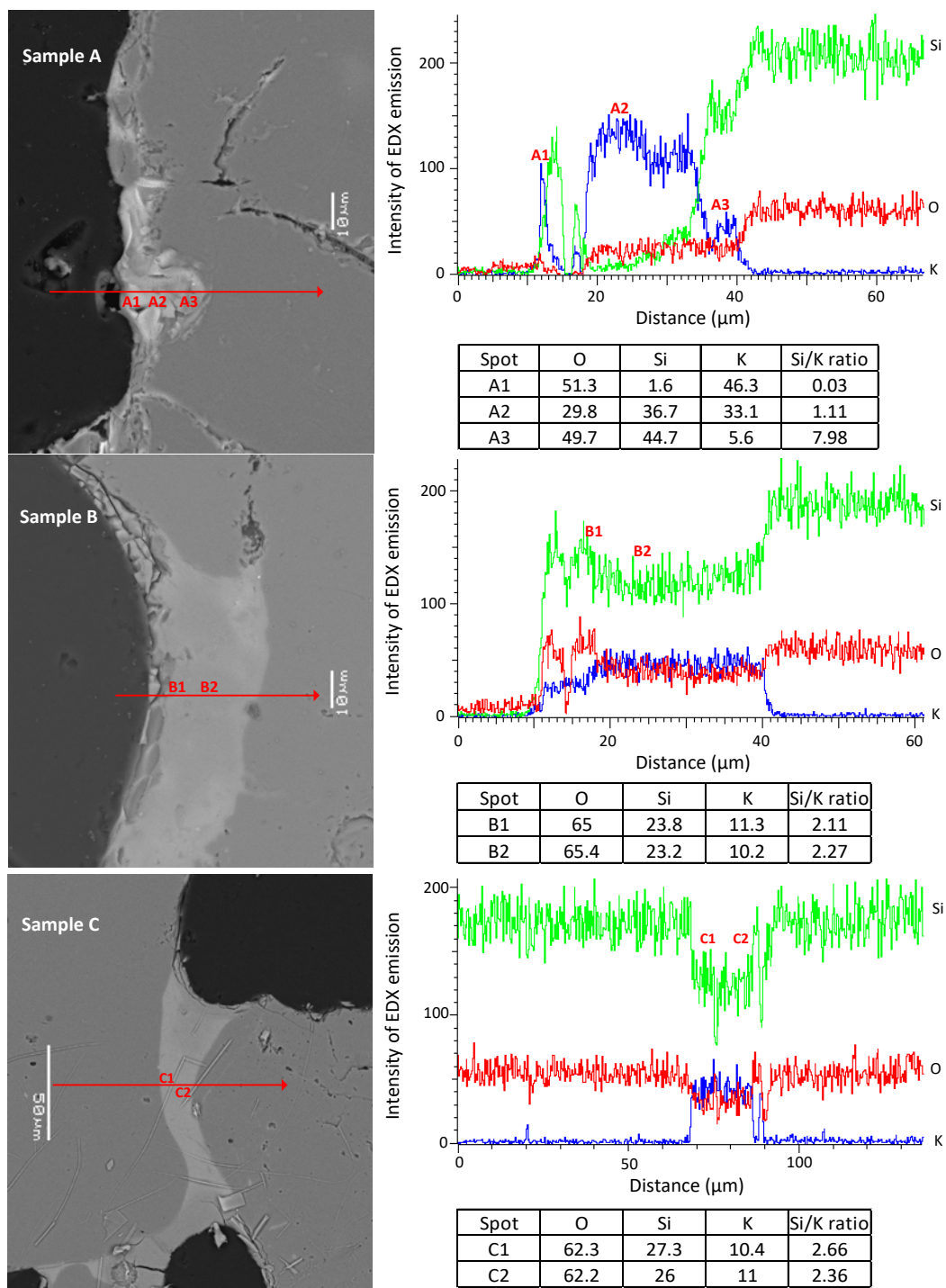


Figure 4-11: SEM-EDX analysis of imbedded samples. Sample A:  $K_2CO_3$  conversion 0.15;  $SiO_2:K_2CO_3$  molar ratio = 1:0.013;  $T = 800^\circ C$ ; pure  $CO_2$  atmosphere; residence time 10 min. Sample B:  $K_2CO_3$  conversion 0.55;  $SiO_2:K_2CO_3$  molar ratio = 1:0.013;  $T = 800^\circ C$ ; pure  $CO_2$  atmosphere; residence time 2 h. Sample C:  $K_2CO_3$  conversion 0.99;  $SiO_2:K_2CO_3$  molar ratio = 1:0.013;  $T = 800^\circ C$ ; pure  $N_2$  atmosphere; residence time 4 h.

It should be pointed out that no unreacted potassium carbonate was observed in the Sample 2 for this particular grain, meaning that its local concentration was relatively low and it was fully converted under the operating conditions. The obtained results are similar as SEM-EDX analysis of agglomerated samples from straw combustion in a lab scale fluidized bed <sup>11</sup>. Lin *et al.* reported the formation of a continuous product layer covering silica sand surface and acting as a binder of the silica grains. They observed a steep potassium concentration profile at the interphase between the layer and the grain, and concluded that the formation of the layer was main reason for agglomeration <sup>11</sup>.

Beside the described SEM-EDX analyses, XRD analysis was also performed to identify the reaction products. The only crystalline phase detected was SiO<sub>2</sub>, indicating that all of the products, including the potassium silicates detected by SEM-EDX, were present in amorphous form. The results of XRD analysis are given in Appendix B.

#### 4.3.4 Plausible reaction mechanism

A reaction mechanism, which is proposed based on the experimental results and thermodynamic calculations, is schematically presented in Figure 4-12. The reaction between K<sub>2</sub>CO<sub>3</sub> and the silica sand starts at the contact area between the reactants. Initial stage of the reaction depends on the contact areas between reactants, and it results in a relatively homogeneous molten layer of potassium silicates with a comparative low Si:K ratio (e.g. a mixture of K<sub>2</sub>Si<sub>4</sub>O<sub>9</sub> and K<sub>2</sub>Si<sub>2</sub>O<sub>5</sub>). The molten potassium silicates layer can further react with both the silica sand and K<sub>2</sub>CO<sub>3</sub>, resulting in an expanding homogeneous product layer with increasing Si:K ratios (e.g. a mixture of K<sub>2</sub>Si<sub>4</sub>O<sub>9</sub> and SiO<sub>2</sub>).

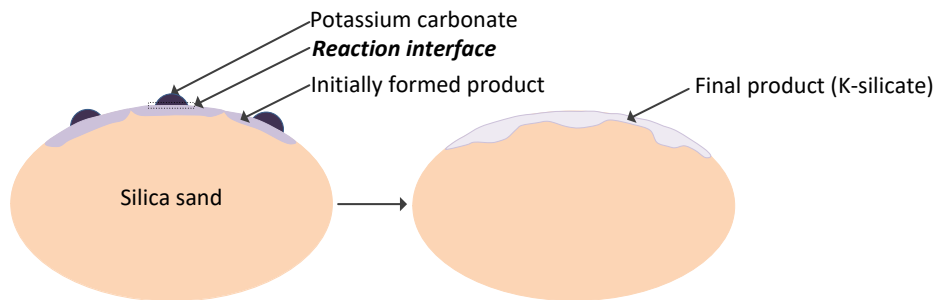


Figure 4-12: Schematic representation of the reaction mechanisms between K<sub>2</sub>CO<sub>3</sub> and silica sand

One of the possible reactions between K<sub>2</sub>CO<sub>3</sub> and potassium silicates has been illustrated in Figure 4-8. The interface between K<sub>2</sub>CO<sub>3</sub> and the product layer probably has a relatively low local Si:K ratios. Thus, according to the thermodynamic calculations in Figure 4-1, the reaction rate at the interface may be

inhibited by the presence of CO<sub>2</sub>, resulting in the experimentally observed lower reaction rate under CO<sub>2</sub> atmospheres.

#### **4.3.5 Practical implication**

The investigated mechanism of the reaction between K<sub>2</sub>CO<sub>3</sub> and SiO<sub>2</sub> can contribute to the overall understanding of agglomeration mechanisms in biomass-fired fluidized bed boilers. Potassium carbonate may be generated from conversion of char bounded potassium, as indicated by previous research<sup>31,37,38</sup>. It can come into a contact with the silica sand particles, thus initiating solid-solid state reaction that results in the formation of a molten potassium silicates product layer. The layer can further react with the attached K<sub>2</sub>CO<sub>3</sub>. As a consequence, the thickness of the product layer increases. At the same time, the formed product layer is capable of dissolving SiO<sub>2</sub>, which further increases the thickness of the formed coating layer. As the layer thickness is increasing, the particle becomes stickier and they agglomerate when a critical thickness is achieved. This may cause bed defluidization.

#### **4.4 Conclusions**

Based on the results of this work, the following conclusions can be drawn for the reaction between K<sub>2</sub>CO<sub>3</sub> and silica sand:

- Potassium carbonate can react with silica sand to release CO<sub>2</sub> at temperatures well below the decomposition temperature of potassium carbonate. The reaction occurs in solid-solid phase with a high reaction rate at temperatures relevant to fluidized bed combustors (> 800°C).
- The reaction rate increases with increasing temperature, but decreases with an increase of CO<sub>2</sub> partial pressure. Mixing of the two solid reactants has a significant impact on the reaction rate, which is much higher for the well mixed particles than for the segregated particles due to enhanced contact between the solid particles. Moreover, the reaction rate is affected in a same way by the particle size of K<sub>2</sub>CO<sub>3</sub>, i.e. smaller particle size results in a higher reaction rate.
- Based on the SEM/EDS analyses of the samples, a plausible mechanism of the reaction is proposed. The reaction is initiated by surface reaction at the contact area between K<sub>2</sub>CO<sub>3</sub> and silica sand, forming a molten homogeneous product layer. The product layer further reacts with K<sub>2</sub>CO<sub>3</sub> and silica sand.

The results obtained in this work provide a basis for understanding of potassium carbonate induced agglomeration process in fluidized bed biomass combustion.

# 5

## BIOMASS COMBUSTION IN FLUIDIZED BED REACTOR

---

This chapter is written in manuscript form and the slightly revised version will be submitted to peer-review journal soon.

### 5.1 Introduction

Agglomeration phenomena during fluidized bed biomass combustion have been studied for long time, and the impact of the most of operating parameters (superficial gas velocity, sand size, etc.) is known<sup>3</sup>, apart from air staging. Air staging is related to combustion properties and even though it is widely applied for dealing with NO<sub>x</sub> problems<sup>3</sup>, there is limited information about its impact on defluidization tendency. Moreover, it is commonly agreed that, the interaction between potassium species and silica sand is mainly responsible for defluidization<sup>3,9,14</sup>, but the impact of other inorganic components (Si, Ca, Mg, S, Cl) in the biomass fuels, has to be further considered<sup>10</sup>.

The recent study on model potassium compounds interaction with silica sand<sup>50-52,118</sup>, as well as the results presented in Chapter 3, can provide valuable information. However, the behaviour of potassium compounds may be different in actual combustion systems, due to the different conditions. In order to further evaluate the interaction between potassium compounds and silica sand, the continuous combustion experiments of potassium compound (KCl, KOH, K<sub>2</sub>CO<sub>3</sub>, and KCl/K<sub>2</sub>CO<sub>3</sub>) doped biomass (washed straw and pine wood) are conducted in a lab-scale fluidized bed reactor. The transformation of doped potassium compounds under combustion conditions is evaluated. Moreover, combustion experiments of wheat straw and sunflower husk are also conducted in a lab-scale fluidized bed reactor. The impacts of the bed temperature, bed material, fuel compositions, and air staging, on agglomeration and defluidization tendencies are evaluated by comparing the amount of fuel burned before defluidization point, which is monitored by the sudden change in pressure drop over the bed.

In addition to continuous combustion experiments of wheat straw and sunflower husk and potassium doped fuels, Scanning electron microscopy coupled with Energy-dispersive X-ray spectroscopy (SEM-EDX), X-ray diffraction (XRD), and thermodynamic calculations are carried out to understand the defluidization behaviours.

## 5.2 Experimental

### 5.2.1 Fluidized bed reactor

The experimental studies are carried out in fluidized bed reactor illustrated in Figure 5-1.

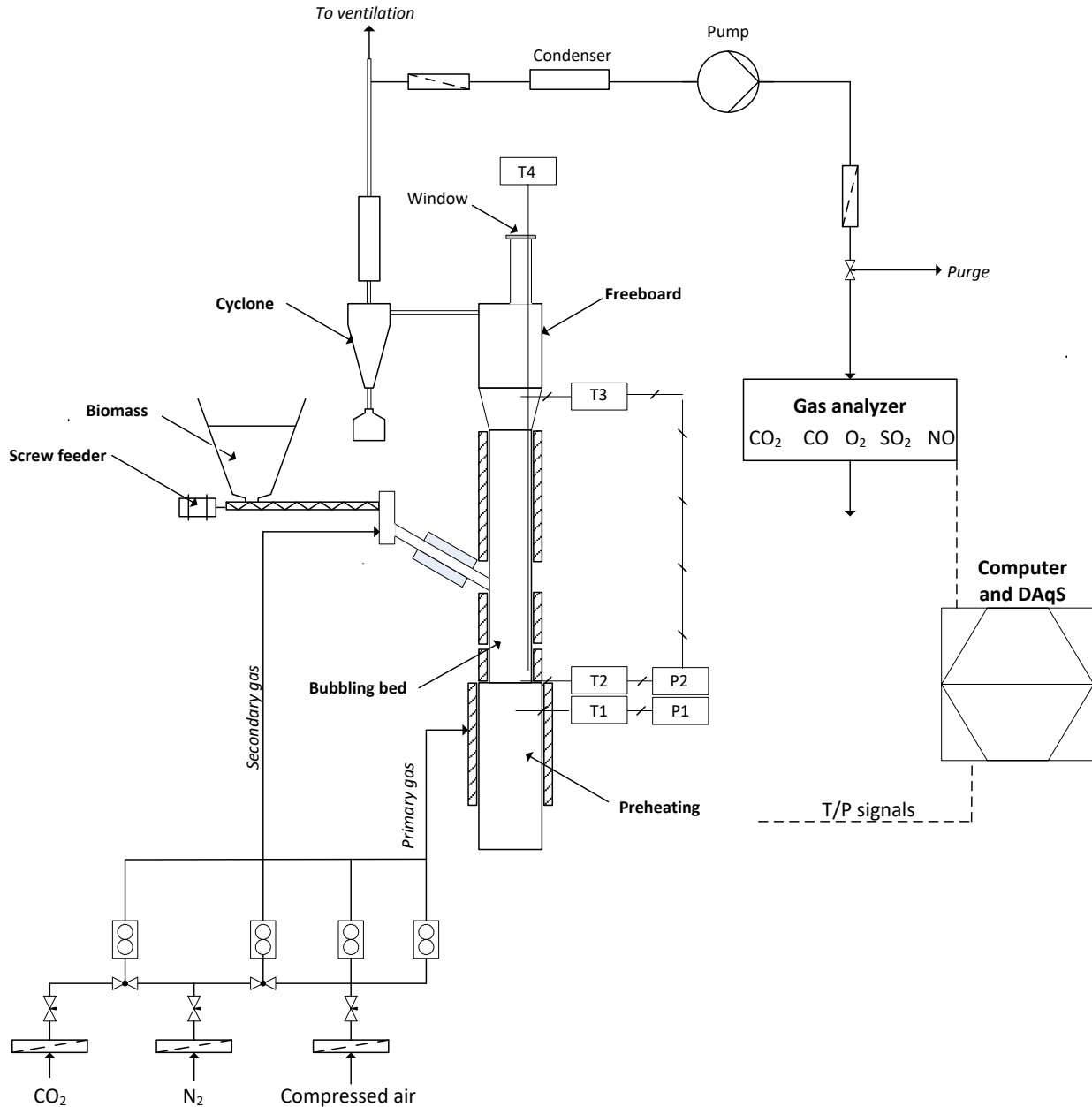


Figure 5-1: A schematic drawing of the lab-scale fluidized bed reactor used for continuous combustion experiments

The same setup has been already used for potassium induced defluidization experiments (see Chapter 3 Figure 3-1). In order to be used for continuous combustion experiments, the gas dosing system is modified to enable simultaneous feeding of air,  $N_2$ , and  $CO_2$ , to the reactor. Moreover, the gas can be fed as primary gas from the bottom of reactor, or as secondary gas through the fuel-feeding pipe. The modified setup contains also the screw particles feeder (K-Tron K-ML-KT20), which is used for

continuous feeding of biomass fuels. The fuels enter the reactor above the dense bed region (30 cm above the gas distributor). The secondary gas is fed through the fuel-feeding pipe to ensure a stable fuel feeding rate. The gas from the reactor enters a cyclone to remove the elutriated fines and it is sent to the ventilation system, as already described in Chapter 3. Similarly, a small part of gas is sampled to gas analyser Fischer-Rosemount to determine CO<sub>2</sub> (by infrared-absorption) CO (by infrared-absorption), O<sub>2</sub> (by electrochemical method), NO and SO<sub>2</sub> (by method of chemiluminescence) concentrations.

## 5.2.2 Materials

Silica sand with a size range of 200 – 300 µm and lime with a size range of 250-500 µm are used as bed materials in the experiments. The biomass fuels used are wheat straw, washed straw, sunflower husk and pine wood, with the compositions given in Table 5-1.

Table 5-1: Properties of the fuels used in the experiments

	Unit	Sunflower husk	Wheat straw	Washed straw	KCl doped straw	Pine wood	KCl doped wood	
Moisture	%	9.1	12.5	4.0	5.0	7,1	0.9	
Ash	wt.% (dry base)	3.2	4.6	3.3	3.8	0,43	1.9	
Ultimate	N	wt.% (dry base)	0.8	0.7	0.6	0.5	<0,1	0.1
	C	wt.% (dry base)	51.7	48.7	47.1	47.0	49,5	49.8
	H	wt.% (dry base)	5.7	5.8	5.9	5.7	6,1	6.1
	O	wt.% (dry base)	38.5	40.2	43.1	42.8	44.0	42.1
	Cl	wt.% (dry base)	0.04	0.18	0.02	0.58	0.02	0.66
	S	wt.% (dry base)	0.14	0.08	0.04	0.05	0.006	<0.01
	Inorganic content	Al	mg/kg (dry base)	55	230	180	150	90
Ca		mg/kg (dry base)	3700	3600	3700	3500	950	770
Fe		mg/kg (dry base)	94	180	130	110	53	12
K		mg/kg (dry base)	9600	8000	990	7700	507	8300
Mg		mg/kg (dry base)	2100	630	530	500	94	130
Na		mg/kg (dry base)	21	280	230	210	15	57
P		mg/kg (dry base)	660	750	320	210	35	25
Si		mg/kg (dry base)	290	11000	9500	8900	299	57
Ti	mg/kg (dry base)	<5	17	13	10	/	/	

The wheat straw and sunflower husk pellets are grinded and subsequently sieved to 0.6-4 mm size range. This size range is chosen because particles smaller than 0.6 mm can be easily elutriated from the reactor, while particles bigger than 4 mm can cause unsteady fuel feeding. Pine wood is received in 1-3 mm size range, thus no additional pre-treatment is performed. The washed straw is prepared in a pilot-scale mixer, where 2-4 kg of wheat straw pellets are soaked in approximately 40-80 L of water corresponding to 20mL(of water)/g(of fuel) ratio<sup>24</sup>. The straw-water slurry is mixed for 24h, and then the water is drained before the washed straw is filtered. The washed straw is dried in a vacuum oven

at 105 °C for 24 h. Gridding of washed straw is not performed, since straw pellets have been reassembled during the washing process, while the sieving of washed straw to the 0.6-4 mm size range is performed after drying. Potassium chloride, potassium carbonate, and potassium hydroxide, with purity more than 99.9 %, are used for doping of washed wheat straw and pine wood. In the case of washed wheat straw, it has been assumed that 90% of potassium in the wheat straw has been removed during the washing process<sup>22,24</sup>. The amount of the removed potassium is compensated by adding model potassium compounds, including KCl, K<sub>2</sub>CO<sub>3</sub>, KOH, and a mixture of KCl/K<sub>2</sub>CO<sub>3</sub> (15/85 wt.%). The same amount of model compounds has been added to the pine wood (based on the biomass dry basis). After the addition of model compounds, water (about 4-6 gram of water per gram of solid) is added to obtain slurry, which has been stirred for 24h. Afterwards, the doped fuels are dried (24h at 70°C followed by 24h at 105 °C) and sieved to 0.6-4 mm size range. The compositions of KCl doped washed straw and pine wood are analysed and given in Table 5-1. It can be seen that the K contents in the doped washed straw and pine wood are very close to the K content of wheat straw, which validates the doping procedure described above. Thus, it is reasonable to assume that all the doped pine fuels and doped washed straw have the same composition (apart from Cl content) as KCl doped pine wood, and KCl doped washed straw, respectively. Due to the high analysis costs, the analysis of other doped fuels was not performed to further validate the doping method, and the estimated compositions of other doped fuel are given in Table 5-2.

*Table 5-2: Estimated composition of doped fuels*

	Unit	KOH doped w. straw	K <sub>2</sub> CO <sub>3</sub> doped w. straw	KCl/K <sub>2</sub> CO <sub>3</sub> doped w. straw	KOH doped wood	K <sub>2</sub> CO <sub>3</sub> doped wood	KCl/K <sub>2</sub> CO <sub>3</sub> doped wood
Moisture	%	5.0	5.0	5.0	0.9	0.9	0.9
Ash	wt.% (dry base)	3.8	3.8	3.8	1.9	1.9	1.9
Ultimate	N	wt.% (dry base)	0.5	0.5	0.5	0.1	0.1
	C	wt.% (dry base)	47.0	47.0	47.0	49.8	49.8
	H	wt.% (dry base)	5.7	5.7	5.7	6.1	6.1
	O	wt.% (dry base)	42.8	42.8	42.8	42.1	42.1
	Cl	wt.% (dry base)	0.02	0.02	0.09	0.02	0.02
	S	wt.% (dry base)	0.05	0.05	0.05	<0.01	<0.01
	Inorganic content	Al	mg/kg (dry base)	150	150	150	11
Ca		mg/kg (dry base)	3500	3500	3500	770	770
Fe		mg/kg (dry base)	110	110	110	12	12
K		mg/kg (dry base)	7700	7700	7700	8300	8300
Mg		mg/kg (dry base)	500	500	500	130	130
Na		mg/kg (dry base)	210	210	210	57	57
P		mg/kg (dry base)	210	210	210	25	25
Si		mg/kg (dry base)	8900	8900	8900	57	57
Ti	mg/kg (dry base)	10	10	10	/	/	

### 5.2.3 Experimental procedure

0.5 kg of bed material is used in each run, which corresponds to 10 cm of static bed height. Under standard conditions, the bed temperature is 850 °C. To achieve this bed temperature, the reactor has been preheated to approximately 825 °C by heating elements before the fuel is introduced. After the fuel feeding is started, a stable bed temperature is reached within 10 min. The total amount of air supplied to the system is 11.5 NL/min in all experiments. The standard fuel feeding rate is calculated based on an overall excess air ratio ( $\lambda$ ) of 1.45, and it varied between 1.6 and 1.7 g/min, depending on the biomass composition. Under standard conditions, all the air is supplied as primary gas with the ratio between primary air and total air ( $\lambda_1/\lambda$ ) equal to 1, and 15.5 NL/min of N<sub>2</sub> is used as secondary gas in order to ensure a stable fuel feeding. The total flow of primary gas is kept equal to 11.5 NL/min in all experiments, meaning that the ratio between superficial gas velocity and minimal fluidization velocity of sand particles ( $U_g/U_{mf}$ ) is kept equal approximately to 4.5 at 850 °C.

Figure 5-2 provides an example of the flue gas composition, bed temperature, and bed pressure drop from an experiment. During experiments, the fuel has been fed continuously up to the defluidization point (DP) determined by either a sudden decrease in pressure drop along the bed (as illustrated in Figure 5-2) due to gas channelling, or by a sudden increase in the pressure drop due to cake formation. The amount of fuel fed up to defluidization point and fuel feeding time are recorded.

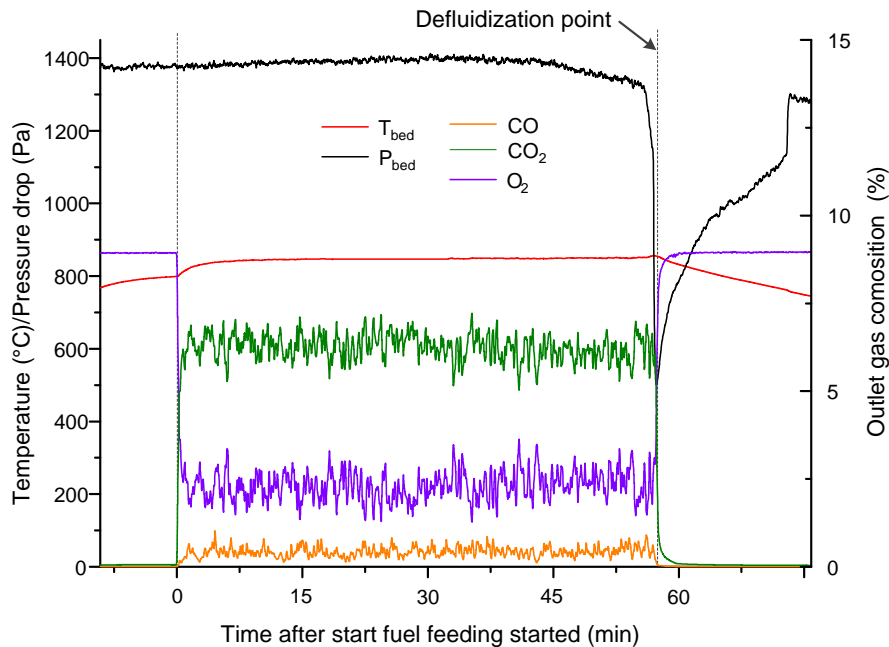


Figure 5-2: Flue gas composition, bed temperature, and bed pressure drop during wheat straw combustion under the conditions of  $T_{bed}=850$  °C;  $\lambda =1.45$ ;  $\lambda_1/\lambda = 1$ ; silica sand as bed material;  $U_g/U_{mf}$  ratio  $\approx 4.5$ .

During combustion of wheat straw, sunflower husk and doped pine wood fuels, the amount of fly ash captured by the cyclone and the amount of particles adhered to the reactor walls are negligible. Axial

temperature profiles are measured at steady state along the reactor (by stepwise pulling out the temperature sensor  $T_4$ ), and the results are given in Appendix C. The bed temperature has been relatively uniform, with only a small increase (3-5 °C) observed when approaching the top of bed, probably due to the accumulation of burning char particles. Moreover, a significant temperature decrease (100-150 °C) is observed near the fuel inlet point due to the inflow of colder secondary gas, as well as due to the absence of heating element. During combustion of washed straw and potassium doped washed straw, it is observed that a significant degree of combustion takes place near the fuel inlet point, resulting in higher temperatures in this region compared to other experiments. This is probably because of the low bulk density and the low moisture content of the washed and potassium doped washed straw, which promotes the ignition. Besides that, a significant amount of ash and partially burned char particles has been adhered to the reactor walls during combustion of washed straw and potassium doped washed straw.

The impact of bed temperature is investigated by performing experiments at different temperatures between 650 and 850 °C. The preheating temperature (by electric heaters) is set approximately 25 °C below the combustion temperature before fuel feeding is started. The impact of bed material is evaluated by replacing the silica sand with the lime. In order to investigate the impact of air staging on defluidization behaviour, experiments are performed under different  $\lambda_1/\lambda$  ratio (0.04 to 1). The  $\lambda_1/\lambda$  ratio is varied by replacing a part of the primary air with  $N_2$ , and by supplying the corresponding amount of air through the secondary gas. For instance, for  $\lambda_1/\lambda = 0.5$ , the primary gas consists of 5.75 NL/min of air and 5.75 NL/min  $N_2$ , while the secondary gas consists of 5.75 NL/min of air and 9.75 NL/min of  $N_2$ . In some experiments,  $CO_2$  is used in primary gas instead of  $N_2$ .

Stepwise combustion experiments are also performed to evaluate the impact of operation conditions on defluidization. The first step is continuous biomass feeding under  $\lambda_1/\lambda = 0$  for 180 minutes, resulting in a significant amount of char accumulated in the bed. In the second step, the biomass feeding is stopped, and 0.5 NL/min of air has been introduced to the bed to burn the accumulated char particles. Two of the stepwise combustion experiments are performed under  $N_2$  as primary gas, while  $CO_2$  is used in one of the experiments. Table 5-3 summarizes operating conditions used in the experiments. Experiments 26-28 are conducted as stepwise combustion experiments.

#### **5.2.4 Solid samples analysis**

SEM-EDX analysis (*JEOL JSM 5910 and Phenom G5 ProX*) of bed material samples removed from reactor after combustion experiments is performed to investigate particle morphology and composition. XRD analysis of biomass ashes is also performed to detect the crystalline phases in the ashes. Huber diffractometer is used for XRD analysis with a characteristic  $Cu\ K\alpha$  radiation and operation conditions of 40 kV and 40 mA (the exposure time was 30 minutes). The biomass ashes are

produced by placing the biomass (wheat straw, sunflower husk, and KCl doped pine wood and washed straw) in a ceramic crucible and fed it to a horizontal oven. The oven is heated up at 10 °C/min to 550 °C under 3 vol.% of O<sub>2</sub>, and kept at isothermal conditions for approximately 3 hours to achieve a complete burnout of biomass (monitored by CO<sub>2</sub> and CO signals). The ash is collected for XRD analysis.

Table 5-3: Experimental matrix.

Exp no.	Fuel	Temp. (°C)	Bed material	$\lambda_1/\lambda$	Primary gas
1.	Wheat straw	770	Sand	1	Air
2.	Wheat straw	810	Sand	1	Air
3.	Wheat straw	850	Sand	1	Air
4.	Sunflower husk	850	Sand	1	Air
5.	Sunflower husk	770	Sand	1	Air
6.	Washed straw	850	Sand	1	Air
7.	Wheat straw	850	Lime	1	Air
8.	KCl doped pine wood	850	Sand	1	Air
9.	K <sub>2</sub> CO <sub>3</sub> doped pine wood	850	Sand	1	Air
10.	K <sub>2</sub> CO <sub>3</sub> /KCl doped pine wood	850	Sand	1	Air
11.	KOH doped pine wood	850	Sand	1	Air
12.	KCl doped washed straw	650	Sand	1	Air
13.	KCl doped washed straw	850	Sand	1	Air
14.	K <sub>2</sub> CO <sub>3</sub> doped washed straw	850	Sand	1	Air
15.	K <sub>2</sub> CO <sub>3</sub> /KCl doped washed straw	850	Sand	1	Air
16.	KOH doped washed straw	850	Sand	1	Air
17.	Wheat straw	850	Sand	0.75	Air/N <sub>2</sub>
18.	Wheat straw	850	Sand	0.5	Air/N <sub>2</sub>
19.	Wheat straw	850	Sand	0.25	Air/N <sub>2</sub>
20.	Wheat straw	850	Sand	0.04	Air/N <sub>2</sub>
21.	Wheat straw	850	Sand	0.04	Air/CO <sub>2</sub>
22.	Sunflower husk	850	Sand	0.5	Air/N <sub>2</sub>
23.	Sunflower husk	850	Sand	0.25	Air/N <sub>2</sub>
24.	Sunflower husk	850	Sand	0.04	Air/N <sub>2</sub>
25.	Sunflower husk	850	Sand	0.04	Air/CO <sub>2</sub>
26.	Wheat straw	850	Sand	0	N <sub>2</sub>
27.	Sunflower husk	850	Sand	0	N <sub>2</sub>
28.	Wheat straw	850	Sand	0	CO <sub>2</sub>

### 5.2.5 Thermodynamic equilibrium calculations

Global equilibrium calculations are performed in the FACTSAGE 7.0 software in order to obtain information about the thermodynamically stable ash species under different fuel and reactor conditions. The databases and models are chosen according to the reference<sup>127</sup>, and they are summarized in Table 5-4 (comprehensive summary of all components considered can be found in

Appendix D). The calculations are performed for a temperature range of 550-900 °C under  $\lambda = 1.45$  and  $\lambda_1/\lambda = 1$ . 100 g of biomass is used for calculation in each run, with the C, H, N, O, S, Cl, as well as the inorganic composition considered in the calculation. Calculations are done considering only dense bed of reactor, and it is assumed that all biomass reached the bed. The bed material ( $\text{SiO}_2$ ) is not considered since the purpose of the equilibrium calculations is to investigate thermodynamically stable species in the biomass ashes without interaction with bed material, and it is difficult to estimate the amount of bed material reacting with biomass ash. The total amount of air was 735 g (secondary gas is not considered), according to  $\lambda = 1.45$  value.

*Table 5-4: Summary of databases and models used for equilibrium calculations in FACTSAGE 7.0 software<sup>127</sup>*

Phase	Database	Model
Gas	FactPS	/
Oxide slag	FToxid	SlagA
Molten salt	FTsalt	SaltF
Carbonates and sulphates	FTpulp	Hexa-HT
K and Na carbonates and sulphates	FTsalt	KSO_
Chlorides (solid)	FTsalt	ACL_B
K-Ca-carbonate	FTsalt	SCSO
Other salts	FTsalt	/
Oxides	FToxid	/
Other solids	FactPS	/

## 5.3 Results and discussion

### 5.3.1 Combustion under $\lambda_1/\lambda = 1$

The first set of experiment is performed in order to investigate the impact of bed temperatures, bed material, and fuel's composition on agglomeration and defluidization. A fixed  $\lambda_1/\lambda$  ratio = 1 is used, and the obtained results are summarized in Table 5-5. No defluidization is observed at 770 °C after combustion of approximately 0.5 kg of wheat straw and SFH. For wheat straw, defluidization is observed at 810 °C and 850 °C after 0.19 kg and 0.12 kg of fuel is burned, respectively. On the other hand, 0.30 kg of SFH is burned before defluidization at 850 °C. The obtained results indicate a significant impact of bed temperature on defluidization, which is also reported in other studies<sup>11</sup>. It is suggested that the increased defluidization tendency at higher temperatures is because of a combination of increased rate of melt formation and decreased viscosity (increased stickiness) of formed melts<sup>11</sup>. The difference between defluidization tendency of wheat straw and SFH can be attributed to different Si content, since Si and K rich fuels has higher defluidization tendency compared to only K rich fuels<sup>10</sup>. The difference in fuel properties is evaluated in further text.

Table 5-5: Summary of experimental results performed under  $\lambda_1/\lambda$  ratio = 1;  $\lambda=1.45$ ; fuel feeding rate 1.6-1.7 g/min

Fuel	Bed temp. (°C)	Bed material	Total amount of fuel utilized (kg)	Theoretical K content in bed material (wt.%)	Operation time (min)	Def.	Agglomeration
Wheat straw	770	Silica sand	0.50	0.80	300	No	Severe
Wheat straw	810	Silica sand	0.18	0.29	108	Yes	Limited
Wheat straw	850	Silica sand	0.121	0.19	56	Yes	Limited
Sunflower husk	770	Silica sand	0.51	0.98	300	No	Moderate
Sunflower husk	850	Silica sand	0.30	0.58	148	Yes	Moderate
Washed straw	850	Silica sand	0.30	0.06	180	No	Limited
Wheat straw	850	Lime	0.40	0.64	240	No	Severe
KCl doped wood	850	Silica sand	0.136	0.22	74	Yes	Limited
K <sub>2</sub> CO <sub>3</sub> doped wood	850	Silica sand	0.089	0.14	55	Yes	Limited
KCl/K <sub>2</sub> CO <sub>3</sub> doped wood	850	Silica sand	0.093	0.15	59	Yes	Limited
KOH doped wood	850	Silica sand	0.108	0.18	68	Yes	Limited
KCl doped washed straw	650	Silica sand	0.314	0.49	180	No	Limited
KCl doped washed straw	850	Silica sand	0.306	0.48	180	No	Limited
K <sub>2</sub> CO <sub>3</sub> doped washed straw	850	Silica sand	0.147	0.23	84	Yes	Limited
KCl/K <sub>2</sub> CO <sub>3</sub> washed straw	850	Silica sand	0.134	0.21	71	Yes	Limited
KOH doped washed straw	850	Silica sand	0.133	0.20	74	Yes	Limited

### 5.3.1.1 Impact of bed material

For lime bed material, no bed defluidization is observed after combustion of 0.4 kg of wheat straw at 850 °C, even though a significant amount of agglomerates is observed, when the bed material is discharged from reactor. SEM-EDX analysis of the bed material removed after combustion of wheat straw at 850 °C using both bed materials is given in Figure 5-3. Silica sand particles (Figure 5-3a) are covered by a layer consisting of K-silicates, with small amount of Ca, Mg, and Al incorporated in the layer. On the other hand, most of the lime particles are not covered by melt (coating layer) and their chemical composition indicates no interaction with potassium. Similar performance of alternative bed material has been already reported when olivine and iron blast-furnace slag are used instead of silica sand for wheat straw combustion<sup>74,128</sup>. Formation of coating layer around bed particles is not taking place, but significant number of agglomerates is observed due to the low melting temperature of ash particles<sup>74,128</sup>.

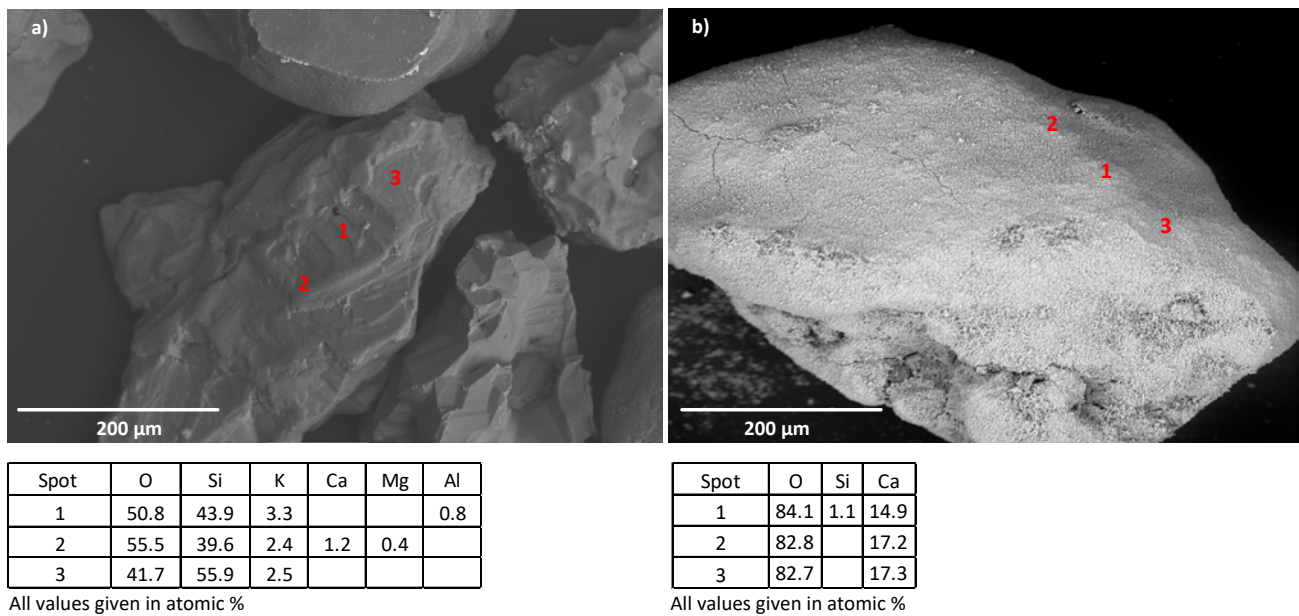


Figure 5-3: SEM-EDX analysis; wheat straw using silica sand (a) and lime (b) as bed material;  $T_{bed}=850$  °C;  $\lambda_p/\lambda$  ratio (primary air/total air) equal to 1;  $\lambda = 1.45$ ;  $U_g/U_{mf}$  ratio  $\approx 4.5$ ; sampled from cold reactor.

XRD analysis of wheat straw ash obtained at 550 °C, and thermodynamic calculations of the potassium distribution during wheat straw combustion are performed. Possible potassium compounds in the ash are identified and the results are given in Figure 5-4. The crystallinity of wheat straw ash is low and amorphous phase is dominant, based on the shape and broadness of the base peak<sup>129</sup>. The amorphous nature of the ash can be related to high K and Si content and the formation of amorphous K-silicates, which cannot be detected by XRD.

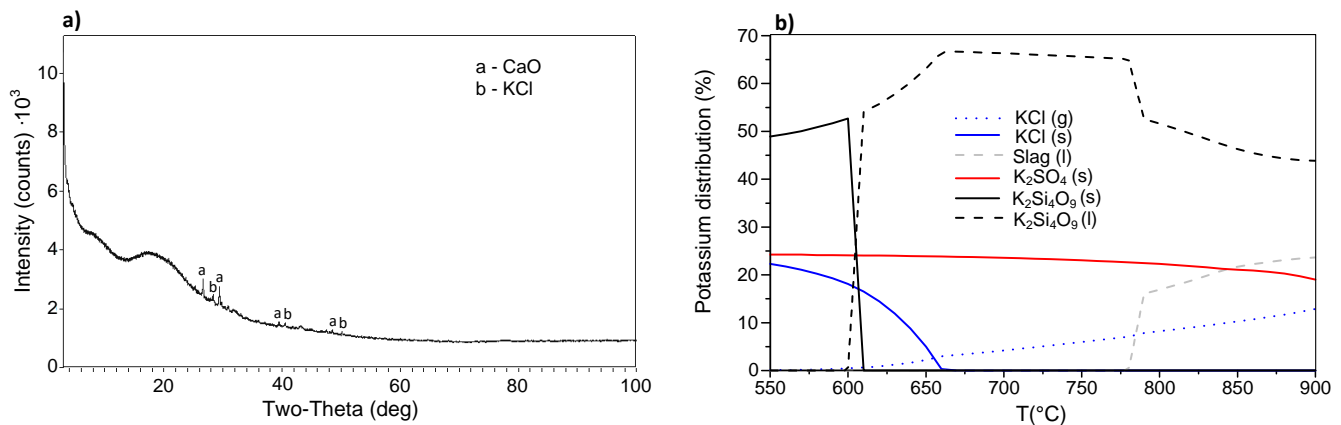


Figure 5-4: a) XRD analysis of wheat straw derived ash ( $T = 550\text{ }^{\circ}\text{C}$ ,  $3\text{ vol}\% \text{ O}_2$ ); b) and thermodynamic calculation of wheat straw ( $T = 550\text{-}900\text{ }^{\circ}\text{C}$ ,  $\lambda = 1.45$ ).

Thermodynamic calculations suggest that  $\text{K}_2\text{Si}_4\text{O}_9$  (l) is the dominant stable K-species in ash in the temperature range of 600-900 °C. It should be pointed out that Si content of wheat straw is high and some of the silica remains in form of  $\text{SiO}_2$  (since there is not enough potassium to convert it to K-silicates). Based on the results in Chapter 3, the presence of  $\text{K}_2\text{Si}_4\text{O}_9$  would not cause the formation of a coating layer responsible for the defluidization, due to the high viscosity of  $\text{K}_2\text{Si}_4\text{O}_9$  (approximately  $1 \cdot 10^4$  Pa·s at 850 °C<sup>54</sup>). Thus, the defluidization observed in straw combustion could be due to the formation of K-silicates with lower viscosity generated during straw combustion, and/or the chemical interaction between bed material and straw ash. The former is not likely since this mechanism would also cause defluidization for lime bed material. Therefore it is hypothesized that the chemical interaction between biomass ash and bed material is the main reason for the formation of the coating layer (or for transfer of melt phase over the surface of silica sand particle) and the subsequent defluidization.

### 5.3.1.2 Impact of fuel composition

Defluidization tendency of biomass fuels is mainly related to their composition, especially K, Si, Ca, Mg, Cl, and S contents. Wheat straw and washed straw have similar elemental composition apart from potassium and chlorine, which are significantly lower in washed straw. No defluidization is observed after combustion of 0.303 kg of washed straw at 850 °C, which is significantly more than amount of wheat straw burned (0.121 kg) before defluidization. It is commonly reported that water leaching is an effective way for reducing fuel potassium content<sup>70,130</sup> that, consequentially, reduces defluidization tendency. In our experiments, almost 90 % of potassium has been removed during the leaching process (as it can be seen from Table 5-1), which is the main reason why no defluidization is observed. This confirms that

agglomeration and defluidization are mainly related to fuel potassium content, under investigated temperature range <sup>3,10</sup>.

Wheat straw and SFH have similar composition apart from Si content, which is almost negligible in SFH (see Table 5-1). The amount of SFH burned before defluidization at 850 °C is much higher compared to wheat straw. The XRD analysis of SFH derived ash and thermodynamic calculations are performed in order to understand behaviour of SFH ash and to compare it with wheat straw ash. The results are given in Figure 5-5.

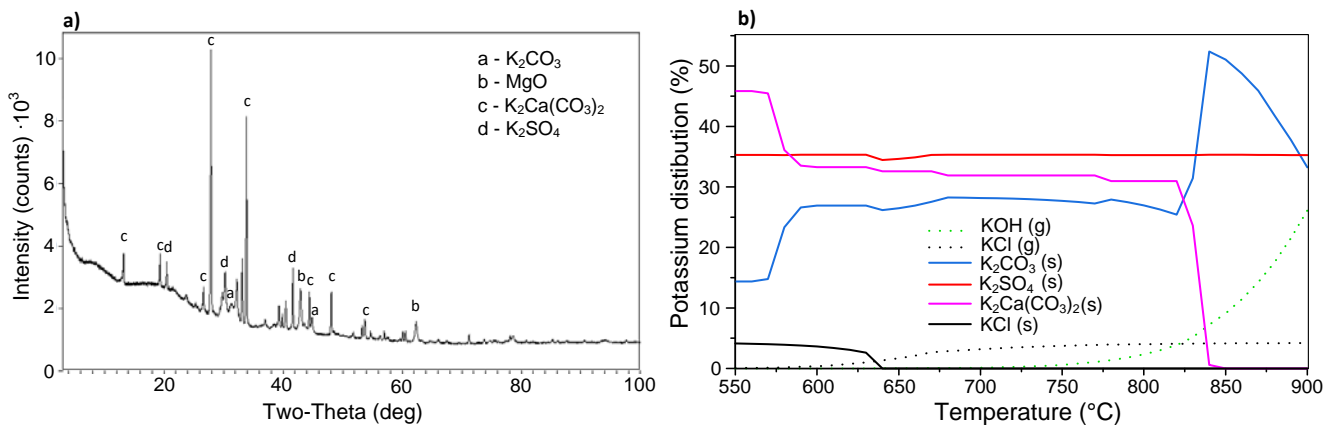


Figure 5-5: a) XRD analysis of sunflower husk derived ash ( $T = 550\text{ }^{\circ}\text{C}$ , 3 vol%  $O_2$ ); b) and thermodynamic calculation of sunflower husk ( $T = 550\text{-}900\text{ }^{\circ}\text{C}$ ,  $\lambda = 1.45$ ).

On contrary to wheat straw ash, the crystallinity of SFH is higher, most probably due to the absence of silica. K<sub>2</sub>Ca(CO<sub>3</sub>)<sub>2</sub> and K<sub>2</sub>SO<sub>4</sub> are the dominant crystalline phases in SFH ash, while a small amount of K<sub>2</sub>CO<sub>3</sub> is also identified. Thermodynamic calculations predicted the presence of potassium as K<sub>2</sub>Ca(CO<sub>3</sub>)<sub>2</sub>, K<sub>2</sub>SO<sub>4</sub>, and K<sub>2</sub>CO<sub>3</sub> at 550 °C, which is in agreement with XRD analysis. The calculation revealed that K<sub>2</sub>Ca(CO<sub>3</sub>)<sub>2</sub> decomposes above 800 °C to form K<sub>2</sub>CO<sub>3</sub>, indicating that K<sub>2</sub>CO<sub>3</sub> and K<sub>2</sub>SO<sub>4</sub> are the dominant potassium species present in biomass ash during SFH combustion at 850 °C. Compared to straw combustion, thermodynamic also revealed that a higher amount of potassium can be released to the gaseous phase in the case of SFH, as it has been already reported for silica lean fuels <sup>26</sup>. This indicates that the amount of potassium in the bed may decrease, hence contributing to reduced defluidization tendency in SFH combustion.

Beside the release of potassium, the presence of Si influences the forms of K in the biomass ash and consequentially, the further interaction with bed material. The amorphous nature of wheat straw ash indicates that formation of amorphous K-silicates can be initiated from fuel K and Si and may result in the formation of silica lean silicates (e.g. K<sub>2</sub>SiO<sub>3</sub> and K<sub>2</sub>Si<sub>2</sub>O<sub>5</sub>), instead of silica rich silicate (K<sub>2</sub>Si<sub>4</sub>O<sub>9</sub>) suggested

by equilibrium calculations. These silica lean silicates, in high viscous (glassy) molten phase, can attach and react (on contrary to  $K_2Si_4O_9$ , which cannot react) with silica bed material. The attached silicates particles can invade silica sand surface via surface diffusion (as already observed for  $K_2CO_3$  and silica sand reaction presented in Chapter 4) resulting in formation silica rich silicate ( $K_2Si_4O_9$ ), which is now smeared over silica sand due to the surface diffusion governed reaction. On the other hand, in the case of SFH, potassium salts present in the ash are directly reacting with bed material. That means that initial formation of melt is taking place between ash and bed material particles, which may be slower than formation of K-silicates from fuel K and Si due to the smaller number of contact points. Consequentially, the formation of thermodynamically stable silica rich silicate ( $K_2Si_4O_9$ ) is not as fast and the defluidization time is prolonged in the case of SFH.

For  $K_2CO_3$  doped wood and SFH, the potassium contents are comparable, while the Mg, Ca, and S content of SFH is much higher. Si is not present in a large amount in these fuels. The results show that significantly lower amount of  $K_2CO_3$  doped wood (0.089 kg) has been burned before defluidization point compared to sunflower husk (0.30 kg), indicating higher defluidization tendency of  $K_2CO_3$  doped wood. The difference in defluidization tendencies is presumably caused by the higher Mg, Ca and S content in the SFH. Mg and Ca can interact with K-silicates to form K-Mg-silicates and K-Ca-silicates, which have higher melting point compared to K-silicates. This results in reduced defluidization tendency of fuels with high Ca and Mg content<sup>12</sup>. The presence of S in sunflower husk favours the formation of  $K_2SO_4$ , which is supported by XRD analysis and thermodynamic calculations (see Figure 5-5). On contrary to  $K_2CO_3$ ,  $K_2SO_4$  does not react with silica sand under oxidizing conditions<sup>56</sup>, thus can reduce defluidization tendency. It should be pointed out that SFH and doped wood may have different distribution of potassium along the fuel particles. In the case of SFH, the potassium is evenly distributed along the fuel particles, and the interaction between potassium and bed material is taking place once the ash is formed. On the other hand, doped salts are mainly present on the other surface of fuel particles (it is most likely that K-species didn't penetrate deeper in the interior of fuel particles), indicating that K is easily interacting with bed material.

The composition of  $K_2CO_3$  and KCl doped wood is similar, apart from Cl content, which is significantly higher for KCl doped wood. The amount of fuels burned before defluidization in these two cases can be used to evaluate the impact of Cl. It is shown that a smaller amount of  $K_2CO_3$  doped wood (0.089 kg) is necessary to cause defluidization compared to KCl doped wood (0.136 kg). Under such experimental conditions (fuel feeding above the bed), it is possible that a considerable amount of KCl evaporates

before the fuel particles reaches the bed. Potassium release in a form of KCl is possible even below 800 °C<sup>25,26</sup>. In such way, the total the amount of potassium reaching the bed is decreased and defluidization tendency is decreased. It seems that presence of Cl and evaporation of KCl can reduce defluidization tendency but it may induce other problems such is deposition and corrosion. The difference in defluidization tendency of these two fuels can be also attributed to different reactivity of K<sub>2</sub>CO<sub>3</sub> and KCl toward silica sand bed material, and the interactions are evaluated in following text.

### 5.3.1.3 Combustion of doped biomasses

The amount of fuel burned in the experiments for doped pine wood, doped washed straw, and wheat straw is given in Figure 5-6 for comparison.

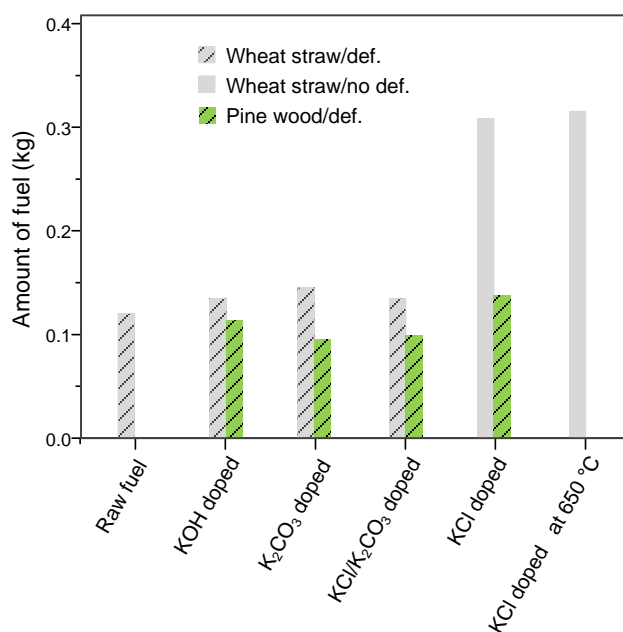


Figure 5-6: Amount of fuel burned at each experimental run for doped wood and doped washed straw, as well as the reference untreated wheat straw:  $T_{bed} = 850$  °C; fuel feeding rate 1.6-1.7 g/min;  $\lambda_v/\lambda = 1$ ;  $\lambda = 1.45$ .

Defluidization is observed during combustion of all doped sample except during combustion of KCl doped washed straw, which shows unique behavior. The amount of potassium doped wood burned before defluidization, as well as the theoretical potassium content in the bed, are generally smaller compared to wheat straw (see Table 5-5). The difference can be attributed to higher Ca content of wheat straw, which can reduce defluidization tendency as already explained. Moreover, doped salts are mainly present on the other surface of fuel particles (limited amount of K-species can penetrate to interior of pine wood particles), indicating that potassium is easily interacting with bed material, which increases defluidization tendency of doped wood samples. Figure 5-6 also indicate that higher amount of doped

washed straw fuels is necessary to cause defluidization compared to corresponding doped wood pine wood fuels and wheat straw. The difference can be attributed to the different combustion properties and the higher amount of ash particles adhered to reactor's walls observed during combustion of doped washed straw samples. Consequentially, the amount of ash particles reaching the bed and corresponding potassium contents within the bed are lower than theoretical values calculated in Table 5-5.

The amounts of  $K_2CO_3$ ,  $KCl/K_2CO_3$ , and  $KOH$  doped wood burned before defluidization are similar, while the amount of  $KCl$  doped fuel is higher. Our previous studies (results given in Chapter 4) showed that  $K_2CO_3$  reacts rapidly with silica sand at  $850\text{ }^\circ\text{C}$ <sup>120</sup> to form molten K-silicates that are responsible for defluidization, which explains the defluidization observed for  $K_2CO_3$  containing fuels. In the case of  $KOH$  doped wood, a considerable amount of  $KOH$  can be transferred to  $K_2CO_3$  during doping procedure (reaction with atmospheric  $CO_2$  in presence of moisture<sup>131</sup>) as well as during combustion in reaction with carbon in absence of air<sup>132</sup>. That means that reaction between  $K_2CO_3$  and silica sand may be responsible for defluidization in this case too.

The reaction between  $KCl$  and silica sand does not take place under oxidizing condition<sup>51,52</sup>. However,  $KCl$  may be converted to other K-species that can react with silica sand to form molten K-silicate responsible for defluidization. A previous study revealed that  $KCl$  can interact with pine wood under pyrolytic conditions to form char bonded potassium<sup>133</sup>. During the combustion process, char bonded potassium can be converted to  $K_2CO_3$ , as recently observed for  $KCl$  doped cellulose samples<sup>39</sup>. The formation of  $K_2CO_3$  from pine wood doped with  $KCl$  is investigated by XRD analysis of  $KCl$  doped pine wood derived ash, and the results are given in Figure 5-7. The results indicate the formation of a small amount of  $K_2CO_3 \cdot 1.5H_2O$ , which can explain the defluidization observed in case of  $KCl$  doped pine wood. The amount of  $K_2CO_3 \cdot 1.5H_2O$  observed in the ash is relatively small but formation of potassium carbonate may be promoted at higher temperature<sup>38</sup>.

The results obtained for doped wood samples indicate that reaction between  $K_2CO_3$  with sand is mainly responsible for defluidization. These results can be compared with defluidization experiments involving model  $K_2CO_3$  (Chapter 3). The critical  $K_2CO_3$  to sand ratio necessary to cause defluidization (up to  $850\text{ }^\circ\text{C}$ ) is 0.72 wt.%, which corresponds to 0.375 wt.% of potassium content in the bed. On the other hand, Table 5-5 indicates that defluidization is observed during combustion of  $K_2CO_3$  doped pine wood, after theoretical potassium content within the bed reached 0.14 wt.%, which is significantly lower. The difference can be partly attributed to the different gas flows used in defluidization experiments with model K-salts (23 NL/min) in Chapter 3 and in biomass combustion experiments (11.5 NL/min). A lower

gas velocity promotes defluidization, and critical conditions are reached for lower potassium content<sup>14</sup>. It is also possible the increased defluidization tendency is related to the combustion process of doped biomass and enhanced reaction between K and silica sand near burning particles, and occurrence of hot spots.

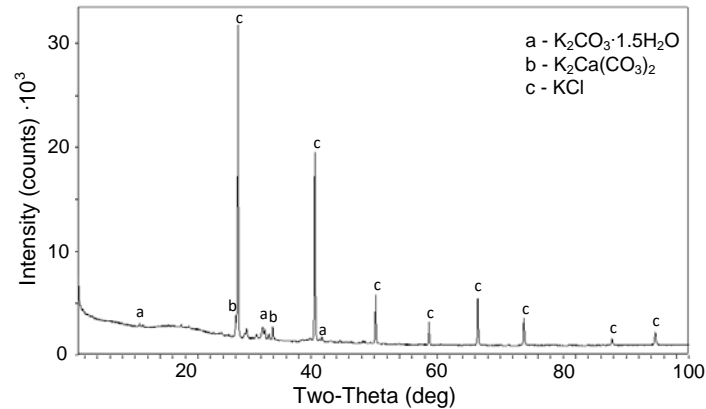


Figure 5-7: XRD analysis of KCl doped wood derived ash ( $T = 550\text{ }^\circ\text{C}$ , 3 vol%  $O_2$ )

The behavior of KCl doped washed straw is unique since defluidization is not observed in this case after combustion of 0.314 and 0.301 kg of the fuel at 650 and 850 °C, respectively. After continuous combustion experiment at 650 °C the bed temperature is increased up to 850 °C but defluidization has not been observed. In both of these experiments, the theoretical amount of potassium present in the bed (0.49 wt.%) corresponds to the critical amount of potassium (0.375 and 0.5 wt.% under different gas velocities) necessary to cause defluidization for model KCl (as observed in defluidization experiments presented in Chapter 3). The absence of defluidization is most likely related to the significant degree of combustion taking place above the bed, which causes high KCl evaporation rate. The evaporation rate should be significantly reduced at 650 °C but no defluidization is observed in this case either (even during the heat up), which indicates that local temperature of burning particles might be higher and KCl evaporation occurred even under lower bed temperature. On the other hand, the possible transformation of KCl to reactive K-species is investigated by XRD analysis of KCl doped washed straw derived ash (Figure 5-8). On contrary to KCl doped wood, formation of potassium carbonate is not taking place within the KCl doped washed straw, meaning that the transformation of KCl to the reactive potassium species is limited, most likely due to the different properties of washed straw compared to pine wood<sup>18</sup>.

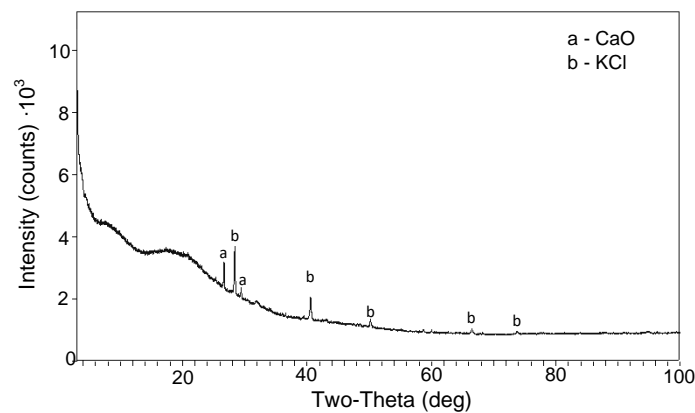


Figure 5-8: XRD analysis of KCl doped washed straw derived ash ( $T = 550\text{ }^{\circ}\text{C}$ , 3 vol%  $\text{O}_2$ )

### 5.3.2 Stage combustion

For combustions of wheat straw and sunflower husk under various  $\lambda_1/\lambda$  ratios, the amount of fuel burned in each experiment before defluidization is plotted in Figure 5-9.

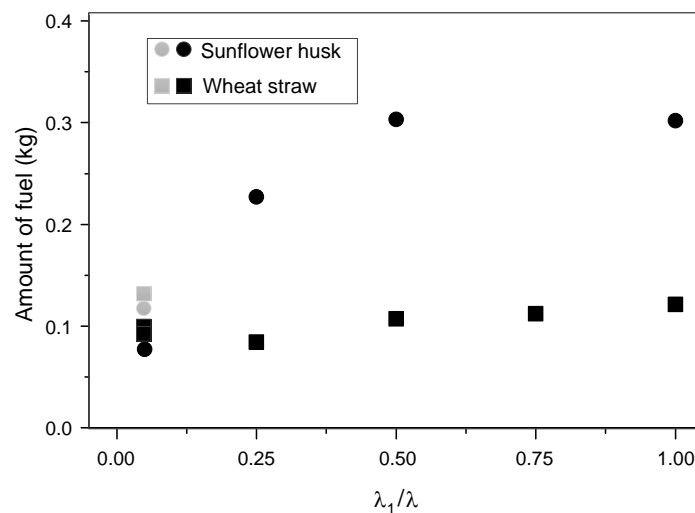


Figure 5-9: Impact of air staging on amount of fuel utilized in each experimental run; fuel feeding rate 1.6-1.7 g/min;  $T_{bed} = 850\text{ }^{\circ}\text{C}$ ;  $\lambda = 1.45$ ;  $U_g/U_{mf}$  ratio  $\approx 4.5$ ; Black symbols denote experiments performed using  $\text{N}_2$  as part of primary gas, and grey symbols denote experiments where  $\text{CO}_2$  is used as part of primary gas.

No defluidization is observed under the condition of  $\lambda_1/\lambda = 0$ , and these experimental conditions are evaluated later as stepwise combustion. For other  $\lambda_1/\lambda$  ratios, the amount of wheat straw utilized before defluidization point is decreased slightly with a decreasing  $\lambda_1/\lambda$  ratio. The difference is relatively small, but the trend is obvious and not related to the experimental error (reproducibility of results is high as seen from repeated experiment for wheat straw under  $\lambda_1/\lambda = 0.04$ ). The trend is more pronounced for sunflower husk, since the amount of fuel utilized before defluidization decreases from 0.3 kg to 0.089 kg

when the  $\lambda_1/\lambda$  ratio decreases from 1 to 0.04. For the  $\lambda_1/\lambda = 0.04$  ratio under  $\text{CO}_2$  as main primary gas, the amounts of wheat straw and sunflower husk burned before defluidization are increased (approximately by 30 %) compared to the experiments when  $\text{N}_2$  is used as main primary gas.

The impact of  $\lambda_1/\lambda$  ratio can be related to the reactivity of potassium species and silica sand under reducing conditions. Under strong reducing conditions,  $\text{H}_2$  and  $\text{CO}$  are dominant in gas phase over  $\text{H}_2\text{O}$  and  $\text{CO}_2$ , which are mainly present under oxidizing conditions. It has been already shown that reactivity of  $\text{K}_2\text{CO}_3$  toward silica sand and corresponding defluidization tendency are significantly increased under  $\text{H}_2$  atmosphere (present under reducing conditions)<sup>118</sup>. Moreover,  $\text{K}_2\text{SO}_4$  can also react with silica sand to form K-silicates under  $\text{H}_2$  atmosphere, while  $\text{K}_2\text{SO}_4$  is not reacting with silica sand under oxidizing conditions<sup>56,118</sup>. XRD analysis and thermodynamic calculations showed that these potassium species are dominant in SFH ash, which indicate that reactivity of the SFH ash, toward silica sand, is significantly increased under reducing conditions, which consequentially increases defluidization tendency. The impact of  $\lambda_1/\lambda$  ratio is not as pronounced for wheat straw combustion, since the initial reaction between K and Si is mainly taking place within the fuel particle, where the local gas concentration might be much different compared to average concentration within the bed. That is why; global  $\lambda_1/\lambda$  ratio is not playing an important role in this case. The impact of  $\lambda_1/\lambda$  ratio can be partially related to  $\text{CO}_2$  concentration (significantly higher under oxidizing conditions) and it is already shown that reaction between  $\text{K}_2\text{CO}_3$  is slower in presence of  $\text{CO}_2$ <sup>120</sup>. The impact of  $\text{CO}_2$  is also observed in the experiments with  $\lambda_1/\lambda$  ratio equal to 0.04 and  $\text{CO}_2$  as primary gas, since the defluidization tendency is reduced compared to the experiments where  $\text{N}_2$  was used as main primary gas. Overall, it can be concluded that the role of  $\text{H}_2$  is dominant in this case, but the impact of  $\text{CO}_2$  is also not negligible.

SEM-EDX analysis of bed material samples removed after combustion of sunflower husk under  $\lambda_1/\lambda = 0.04$  and  $\lambda_1/\lambda = 1$  is given in Figure 5-10. It can be seen that potassium content in the coating layer of the sample removed after combustion under  $\lambda_1/\lambda = 1$  is higher (Figure 5-10a), which should lead to a higher defluidization tendency but, at the same time, Ca and Mg are simultaneously incorporated in the layer, which increases its thickness and decreases defluidization tendency<sup>12</sup>. For the bed material removed after combustion under  $\lambda_1/\lambda = 0.04$  (Figure 5-10b), solid like particles imbedded in the thin coating layer mainly consisting of silica, potassium and calcium can be observed. It seems that Mg content at these particular spots is high, indicating that the interaction between Mg and coating layer is inhibited under reducing conditions. Consequentially, the average Mg content in the melt covering silica sand particles is lower, which increases defluidization tendency. One of the possible reasons why Mg is not interacting with

molten K-silicates can be related to the increased rate of silicate formation, meaning that critical amount and viscosity are reached before Mg interacts with the melt, but this hypothesis demands further evaluation. Based on this SEM-EDX analysis, it appears that the positive impact of Mg present in SFH cannot come to the fore under reducing conditions.

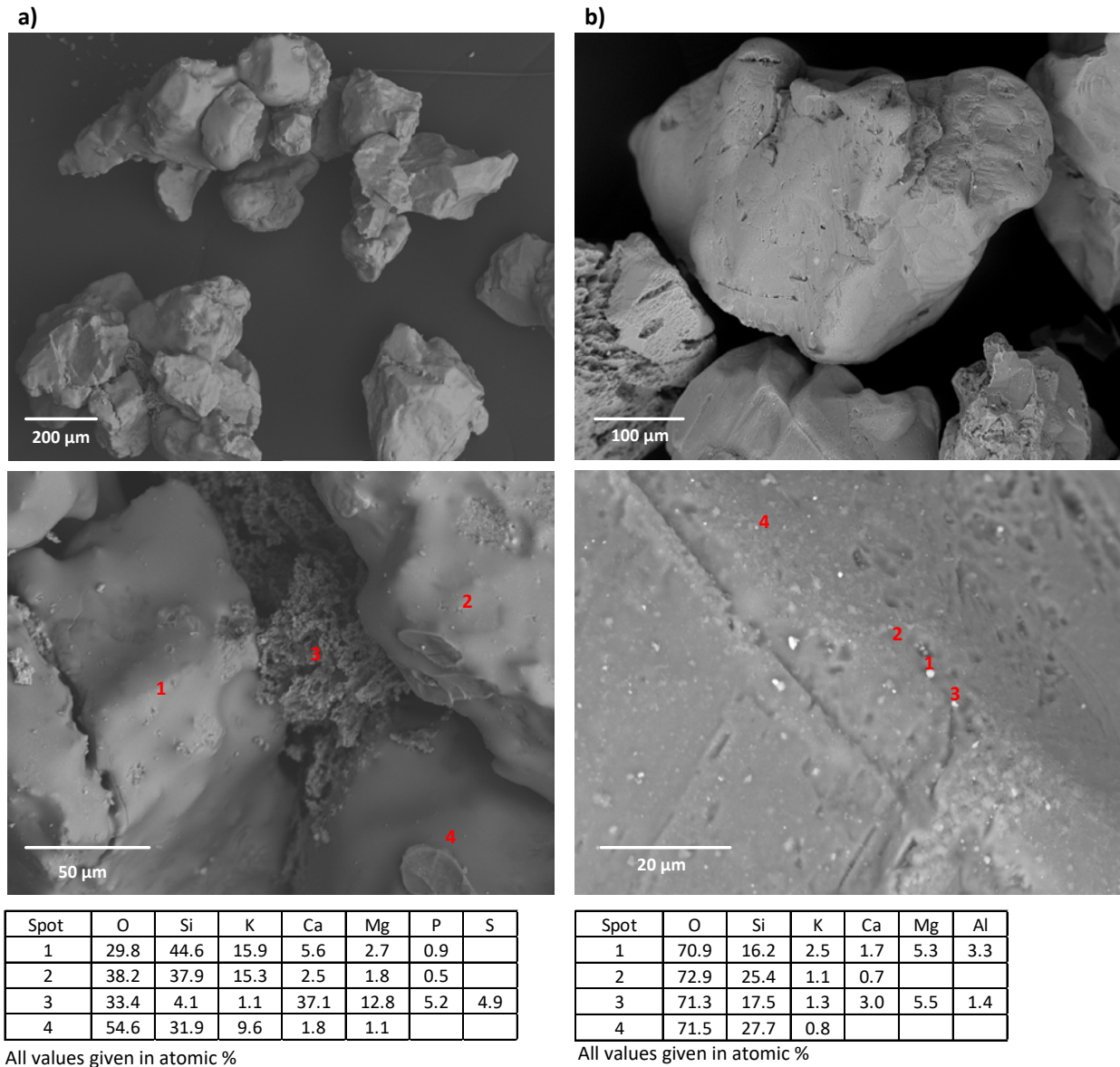


Figure 5-10: SEM-EDX analysis; SFH under (a)  $\lambda/\lambda = 1$  and (b)  $\lambda/\lambda = 0.04$ ;  $\lambda=1.45$ ; fuel feeding rate 1.6-1.7 g/min;  $T_{bed}=850$  °C; sampled from cold reactor

### 5.3.2.1 Stepwise combustion

Three stepwise combustion experiments are performed and the results are summarized in Table 5-6. 0.303 kg of wheat straw and 0.374 kg of sunflower husk are fed to the reactor at 850 °C using N<sub>2</sub> as

primary gas, while 0.304 kg of wheat straw is fed using CO<sub>2</sub> as primary gas. No signs of defluidization are observed during the first step. The bed materials are sampled from reactor after the first step of the experiments where N<sub>2</sub> has been used as primary gas and they are represented in Figure 5-11. Significant number of char particles as well as carbon coated sand particles can be observed.

Table 5-6: Experimental results for stepwise combustion experiments

Exp. No.	1	2	3
Fuel	Wheat straw	Sunflower husk	Wheat straw
Temperature (°C)	850	850	850
Primary gas (NL/min)	11.5 (N <sub>2</sub> )	11.5 (N <sub>2</sub> )	11.5 (CO <sub>2</sub> )
Amount of fuel (kg)	0.303	0.374	0.304
1 <sup>st</sup> K content in the bed (%)	0.48	0.72	0.49
Combustion time (min)	180	180	180
Defluidization	No	No	No
Primary gas (NL/min)	11.5/0.5 (N <sub>2</sub> /Air)	11.5/0.5 (N <sub>2</sub> /Air)	11.5/0.5 (CO <sub>2</sub> /Air)
2 <sup>nd</sup> Combustion time (min)	7	14	28
Defluidization	Yes	Yes	Yes

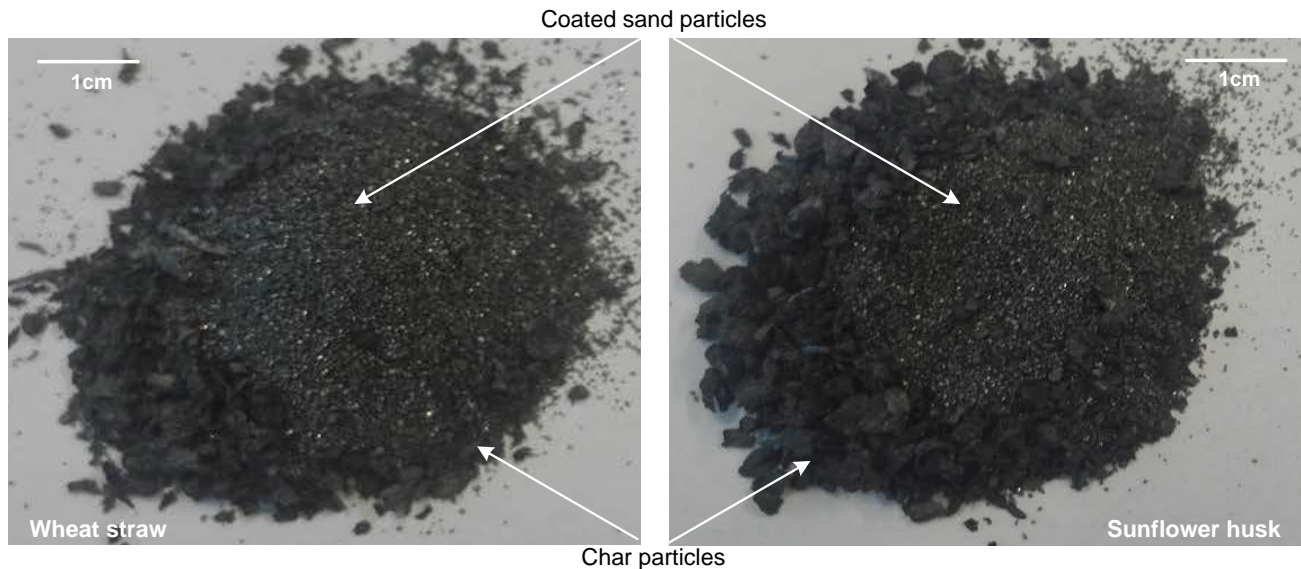


Figure 5-11: Bed material sampled at the end of 1<sup>st</sup> step of combustion experiment; pure N<sub>2</sub> as primary gas; T<sub>bed</sub>=850 °C; λ=1.45; λ<sub>1</sub>/λ =0.

The reducing conditions within the bed are stronger under λ<sub>1</sub>/λ =0 compared to λ<sub>1</sub>/λ = 0.04 and it might be expectable that defluidization tendency would be higher under such conditions. The absence of defluidization can be mainly related to the unburned char particles (Figure 5-11) that hinders the interaction between fuel K and bed material, as well as the interaction between K and Si within the fuel.

Consequentially, the formation of melt phase is not taking place and defluidization is avoided. It appears that potassium cannot leave char particle and interact with bed material, which indicates that potassium-bed material interaction is not related to gas-solid or low viscous melts-solid interaction<sup>15</sup>. Gaseous K and low viscous melts (from ionic species such as KCl, KOH) would leave the char particle easily and react with sand, but this is not the case. Instead, the interaction between potassium and silica sand probably takes place in solid/solid or high viscous liquid/solid phase once the ash particles are formed.

The second step of experiments starts by introducing 0.5 NL/min of air to the bed and defluidization is observed in all cases. For sunflower husk, under N<sub>2</sub> as primary air, defluidization occurs after 14 min, while defluidization of the wheat straw case happens after 7 min. On the other hand, the behaviour of the system with CO<sub>2</sub> as primary gas is slightly different. The comparison between the second steps of experiment for wheat straw under N<sub>2</sub> and CO<sub>2</sub> atmosphere is given in Figure 5-12. On contrary to the experiments with N<sub>2</sub> as primary gas where sudden decrease in pressure drop occurs, only small decrease in pressure drop is observed after 11-12 min in second step under CO<sub>2</sub> as primary air; indicting partial segregation of bed instead of complete defluidization. The pressure drop has been continuously decreasing and after 28 min the bed defluidization occurred.

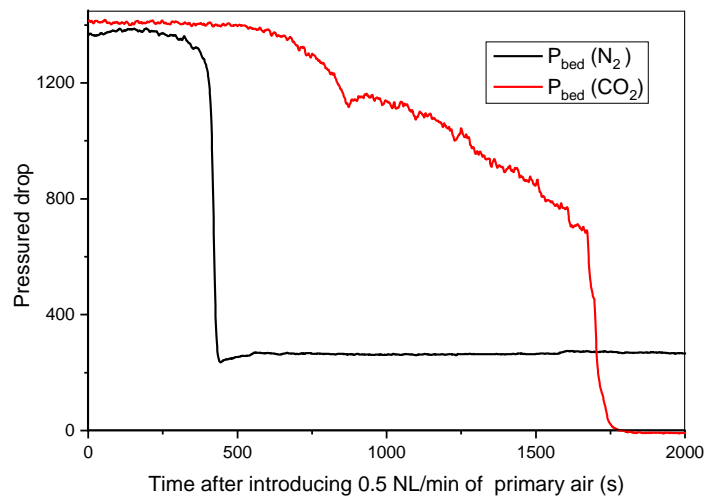


Figure 5-12: Comparison between pressure drops during 2<sup>nd</sup> step of experiments

Behaviour of all systems during the second step of these experiments indicate that as soon as the small amount of air is introduced to the bed, char conversion takes place, which enables the interaction between potassium and silica sand is possible. Besides, it is also possible that reactive potassium species (K<sub>2</sub>CO<sub>3</sub> and K<sub>2</sub>SO<sub>4</sub> under reducing conditions) are formed during char combustion phase<sup>26</sup>. Smaller char particles, adhered to the silica sand surface, are firstly utilized because of their size. Consequentially, a

rapid formation of melt is possible due to the significant number of contact points and sudden defluidization occurs. The interaction between fuel K and bed material is slower in CO<sub>2</sub> atmosphere, as already explained. That is why; defluidization time is prolonged when using CO<sub>2</sub> (exp. 3) as main primary gas, even though char conversion rate should be higher under these conditions

## **5.4 Conclusion**

Based on the results of this work, the following conclusions can be drawn for combustion of different biomass fuels under fluidized bed conditions:

- Defluidization tendency of wheat straw and sunflower husk is increased with increasing bed temperature.
- The transfer of the melt phase over the silica sand surface is governed by chemical interaction between biomass ash and silica sand, which results in formation for coating layer responsible for defluidization.
- Defluidization tendency of fuels is mainly related to their potassium content, while fuel Si also increases the tendency due to the increased rate of melt formation. On the other hand, fuel Ca and Mg reduce defluidization tendency due to the formation of melts with higher melting point and lower stickiness. Fuel S and Cl may also reduce defluidization tendency due to the formation of K<sub>2</sub>SO<sub>4</sub> and KCl, respectively, which decreases the amount of potassium available for reaction with bed material.
- For the potassium doped fuels, it is most likely that the interaction between K<sub>2</sub>CO<sub>3</sub> and silica sand is responsible for defluidization. KOH can be transferred to K<sub>2</sub>CO<sub>3</sub> during doping and combustion process. Transformation of KCl to K<sub>2</sub>CO<sub>3</sub> during char devolatilization and oxidation stage depends on fuel properties, and it is more pronounced for pine wood compared to wheat straw.
- Defluidization tendency is increasing with a decreasing  $\lambda_1/\lambda$  ratio, and the effect is especially pronounced for sunflower husk. The increased tendency under reducing conditions may be related to increased reactivity of potassium salts under reducing conditions. Moreover, it seems that positive impact of Mg present in sunflower husk cannot come to the fore under reducing conditions.
- No defluidization is observed for  $\lambda_1/\lambda = 0$ , due the absence of oxygen in the bed and presence of char matrix that hinders the interaction between inorganic species and bed material. As soon as a small amount of air is introduced to the bed, rapid defluidization occurs due the char oxidation and release of potassium species that invade silica sand surface.

# 6

## EFFECT OF ADDITIVES DURING FLUIDIZED BED COMBUSTION OF BIOMASS FUELS

---

This chapter is written in manuscript form and slightly modified version will be submitted to the peer-review journal soon.

### **6.1 Introduction**

Numerous countermeasures such as alternative bed materials, additives, co-combustion, and biomass pre-treatments have been used for reducing agglomeration problems<sup>5</sup>. All of them are either related to either additional operating costs (alternative bed material, additives and pre-treatment) or environmental problems (harmful emission during co-combustion of biomass with coal or sewage sludge), and yet the agglomeration problems during combustion of most troublesome fuels such as wheat straw cannot be completely eliminated<sup>65,70,74</sup>. The potential and effectiveness of relatively cheap additives to reduce the agglomeration problems during combustion of very troublesome fuels, such as wheat straw and sunflower husk, are studied. Kaolin, lime, magnesium carbonate, coal fly ash, clay, and ammonium sulphate are added to the fuels during continuous combustion experiments, and the agglomeration and defluidization tendency are evaluated in terms of amount of fuel burned with/or without defluidization and comparison to the experiments where no additives are applied. Moreover, fuel additives are usually added to the bed<sup>63,78,79</sup>, but in this study the additives are either mixed with fuel (4.7 wt.% of fuel) before feeding to reactor, or added to bed material (10 wt.% of bed), in order to evaluate the impact of additive dosing method. Scanning electron microscopy coupled with Energy-dispersive X-ray spectroscopy (SEM-EDX) analysis are carried out in order to investigate morphology and composition of bed material particles after continuous combustion experiments.

### **6.2 Experimental**

Continuous combustion experiments are performed in the laboratory scale fluidized bed reactor, already described in Chapter 5.

### 6.2.1 Materials

Silica sand with a size range 200-300  $\mu\text{m}$  is used as bed material. Wheat straw and sunflower husk are used in this investigation, and their composition and preparation method are already described in Chapter 5. Two size ranges of kaolin have been used: 0-85  $\mu\text{m}$  (hereafter denoted as powder kaolin), and 180-425  $\mu\text{m}$  (hereafter denoted as coarse kaolin). Two size ranges of lime particles are used too: 0-50  $\mu\text{m}$  (hereafter denoted as powder lime), and 250-500  $\mu\text{m}$  (hereafter denoted as coarse lime). Powder form of ammonium sulphate (AS) with a size range of 0-35  $\mu\text{m}$ ,  $\text{MgCO}_3$  with a size range of 0-25  $\mu\text{m}$ , coal fly ash (CFA) with a size range of 0-32  $\mu\text{m}$ , and clay with a size range of 0-35  $\mu\text{m}$  are also used. The elemental composition of all additives, as well as containing minerals is given in Table 6-1.

Table 6-1: The elemental composition and crystalline phases of all additives; elemental analysis has been determined by inductive coupled plasma – optical emission spectrometry (ICP-OES), while crystalline phases were determined by XRD.

Additive	Kaolin <sup>131</sup>	CFA <sup>134</sup>	Clay	$\text{MgCO}_3$	Lime	Ammonium sulphate
O (wt.% calculated)	56.9	46.6	54.4	50.3	31.0	48.5
Si (wt.% dry base)	22.0	22.0	28.0	/	/	/
Al (wt.% dry base)	19.0	14.0	4.2	/	/	/
Fe (wt.% dry base)	0.47	2.90	1.8	/	/	/
Ca (wt.% dry base)	0.10	4.50	8.4	/	69.0	/
Mg (wt.% dry base)	0.14	0.97	0.45	41.1	/	/
Na (wt.% dry base)	0.10	0.27	0.84	/	/	/
K (wt.% dry base)	1.10	0.87	1.9	/	/	/
P (wt.% dry base)	0.05	0.64	0.05	/	/	/
S (wt.% dry base)	0.02	0.26	/	/	/	24.2
Crystalline phases	$\text{Al}_2\text{Si}_2\text{O}_5(\text{OH})_4$ , $\text{SiO}_2$	$2\text{Al}_2\text{O}_3 \cdot \text{SiO}_2$ , $\text{SiO}_2$	$\text{CaCO}_3$ , $\text{SiO}_2$ $\text{Al}_2\text{SiO}_5$ ,	$\text{MgCO}_3$ , $\text{MgO}$	$\text{CaO}$	$(\text{NH}_4)_2\text{SO}_4$

Powder kaolin, lime, ammonium sulphate,  $\text{MgCO}_3$ , coal fly ash, and clay are added to prepared fuel (sieved to 0.6-4 mm size range) and the mixture has been continuously mixed for 2 h in rotational mixer to achieve high adhesion of powder additives to the fuel particles surface. The adhesion force between powder and fuel particles is strong enough to prevent elutriation of powder particles since only small (almost negligible) amount of particles is elutriated from reactor and captured in cyclone. Approximately 4.7 g of powder additives is added per 100 g of biomass. The amount of powder additive is chosen based on kaolin capture of potassium species at 850 °C<sup>131</sup>, and the amount of potassium present in wheat straw. Besides mixing with fuel, kaolin, lime and ammonium sulphate are also added to bed directly. 10 wt. % or total bed weight is replaced with either coarse kaolin or coarse lime. Ammonium sulphate addition to the

bed is difficult due to its low melting temperature and rapid decomposition above 350 °C<sup>135</sup>. In order to ensure that some amount of AS actually reaches the bed, AS pellets are added each 10 min. The pellet (10 mm diameter, 3 mm height) weighted approximately 0.94g and about 4.7 g of AS is added per 100 g of biomass, which corresponds to the same amount as in case of powder addition. Addition of MgCO<sub>3</sub>, coal fly ash, and clay to the bed is not considered since only powder forms of these additives are available for this investigation.

## 6.2.2 Experimental procedure

Experimental procedure is very similar to the procedure described in Chapter 5. 0.5kg of bed material is used in each experimental run. Continuous combustion experiments are performed at 850 °C. Fuel feeding rate varies between 1.60 and 1.75 g/min based on fixed air surplus amount ( $\lambda=1.45$ ), and the total amount of air supplied to the system is 11.5 NL/min in all experiments. The air is supplied as primary gas, while 15.5 NL/min of N<sub>2</sub> is used as secondary gas to ensure stable fuel feeding. Table 6-2 provides the list of all performed experiments. Fuel has been fed up to defluidization point (as described in Chapter 5 at Figure 5-2) or after all prepared fuel is burned out (approximately 0.3 kg and 0.5 kg of wheat straw and sunflower husk, respectively)

Table 6-2: Experimental matrix;  $T_{bed}=850$  °C; fuel feeding rate 1.60-1.75 g/min;  $\lambda=1.45$ ;  $\lambda_1/\lambda=1$ .

Exp no.	Fuel	Additive	Addition method
1.	Wheat straw	Kaolin	Mixed with fuel
2.	Wheat straw	Kaolin	10 wt.% added to bed
3.	Sunflower husk	Kaolin	Mixed with fuel
3.	Wheat straw	Lime	Mixed with fuel
4.	Wheat straw	Lime	10 wt.% added to bed
5.	Wheat straw	Ammonium sulphate	Mixed with fuel
6.	Wheat straw	Ammonium sulphate	Added as pellets
7.	Sunflower husk	Ammonium sulphate	Mixed with fuel
8.	Wheat straw	MgCO <sub>3</sub>	Mixed with fuel
9.	Wheat straw	Coal fly ash	Mixed with fuel
10.	Sunflower husk	Coal fly ash	Mixed with fuel
11.	Wheat straw	Clay	Mixed with fuel
12.	Sunflower husk	Clay	Mixed with fuel

During combustion of fuels mixed with additives, it is observed that the fuel particles are ignited easier compared to raw fuels. The CO level is generally lower; indicating more efficient combustion. The fuel feeding is relatively stable and the limited amount of ash and unburned char particles has been adhered to reactor's walls.

### 6.2.3 Solid samples analysis

SEM-EDX analysis (*Phenom G5 ProX*) of bed material samples removed from reactor after combustion experiments is performed in order to investigate morphology and surface composition of bed material particles.

The reaction between kaolin and  $K_2CO_3$  is investigated using TGA setup (described in Chapter 4) in order to investigate the impact of kaolin particles size on reaction rate. Powder and coarse kaolin are, respectively manually mixed for 10 minutes with powder  $K_2CO_3$  (with size range of 2.6-224  $\mu m$ , and mean diameter of 18  $\mu m$ ) in the cylindrical crucible before placing it in the TGA. 4.7 g of kaolin is mixed with 0.8 g of  $K_2CO_3$  corresponding to the amount of kaolin used as additive and amount of potassium present in wheat straw. The mixture has been heated up at 500 °C/min to 850 °C, and kept for 40 min under isothermal conditions (longer residence time is not possible due to the setup limitations) in  $N_2$  atmosphere. The reaction extent is monitored by following the mass loss related to release of  $CO_2$ , as one of the reaction product<sup>136</sup>. The  $K_2CO_3$  conversion rate is evaluated under isothermal condition, as already described in Chapter 4.

## 6.3 Results and discussion

The amount of fuel burned in each experiment is given in Table 6-3.

Table 6-3 Amounts of fuel burned in each experiment as well as the amount of untreated fuels for comparison;  $T_{bed}=850$  °C; fuel feeding rate 1.60-1.75 g/min;  $\lambda=1.45$ ;  $\lambda_1/\lambda=1$ .

Exp no.	Fuel	Additive	Addition method	Amount of fuel burned (kg)	Def.	Agg.
1.	Wheat straw	/	/	0.121	Yes	Limited
2.	SFH	/	/	0.301	Yes	Moderate
3.	Wheat straw	Kaolin	Mixed with fuel	0.307	No	Limited
3.	Wheat straw	Kaolin	10 wt.% added to bed	0.347	No	Limited
4.	SFH	Kaolin	Mixed with fuel	0.513	No	Limited
5.	Wheat straw	Lime	Mixed with fuel	0.267	No	Moderate
6.	Wheat straw	Lime	10 wt.% added to bed	0.328	Yes	Severe
7.	Wheat straw	AS	Mixed with fuel	0.195	Yes	Limited
8.	Wheat straw	AS	Added as pellets	0.190	Yes	Limited
9.	SFH	AS	Mixed with fuel	0.512	No	Moderate
10.	Wheat straw	$MgCO_3$	Mixed with fuel	0.301	No	Moderate
11.	Wheat straw	Coal fly ash	Mixed with fuel	0.199	Yes	Limited
12.	SFH	Coal fly ash	Mixed with fuel	0.491	No	Moderate
13.	Wheat straw	Clay	Mixed with fuel	0.168	Yes	Limited
14.	SFH	Clay	Mixed with fuel	0.532	No	Moderate

The effectiveness of additive addition can be evaluated by comparing the amount of fuel burned with application of additives and the amount of untreated fuels burned before defluidization.

### 6.3.1 Kaolin addition

Stable combustion of 0.307 kg of wheat straw and 0.513 kg of sunflower husk mixed with powder kaolin is done without any signs of defluidization. Moreover, 0.347 kg of wheat straw is continuously burned when 10 wt.% of coarse kaolin is added to the bed without defluidization. In all of these experiments, limited amount of agglomerates is observed after bed material is discharged from reactor. It has been already shown that meta-kaolin (dominant form in kaolin in temperature range of 650-960 °C) is reacting with various potassium species present in gaseous and aerosol form<sup>131,137</sup>, as well as with solid  $K_2SO_4$ <sup>77</sup>. Capture of potassium species released in the gaseous phase is also observed when kaolin is added in CFB boilers as the additive to reduce agglomeration and deposition problems<sup>64,78</sup>. It is also suggested that kaolin can interact with potassium silicates formed in reaction between fuel K and bed material to form K-Al-silicates, which has significantly higher melting point compared to K-silicate and, consequentially, lower defluidization tendency<sup>63</sup>. Figure 6-1 shows the SEM-EDX analysis of the bed material after the combustion of powder kaolin mixed with wheat straw and after addition of 10 wt.% of powder kaolin to the bed.

Figure 6-1a shows solid like particles rich in K and Al, which indicates formation of aforementioned K-Al-silicates. Besides that, potassium is detected (spot b1) within large kaolin particle (Figure 6-1b), indicating that reaction between fuel potassium and coarse kaolin takes place in the bed. These results indicate that reactivity of potassium toward kaolin is very high, and it is captured as soon as it reaches kaolin particles. To further evaluate the impact of kaolin particle size on K capture efficiency, TGA experiments are performed using model  $K_2CO_3$  to simulate reactive ash particles and results are given in Figure 6-2.  $K_2CO_3$  conversion rate is given as function of isothermal time. Significant amount of  $K_2CO_3$  is reacting with powder kaolin below 850 °C, which indicates that the reaction between these reactants is very fast even at lower temperatures. On the other hand, conversion of  $K_2CO_3$  mixed with coarse kaolin is taking place mainly at 850 °C, and both conversion degrees (approximately 0.8) approach each other after sufficiently long time. This analysis shows that kaolin is reactive toward solid potassium species, thus explaining high capture degree of potassium from biomass ash. It seems that both ways of kaolin addition are effective for eliminating defluidization but addition of powder kaolin might be slightly more effective since the initial reaction rate is higher and the reaction is very fast even at lower temperature.

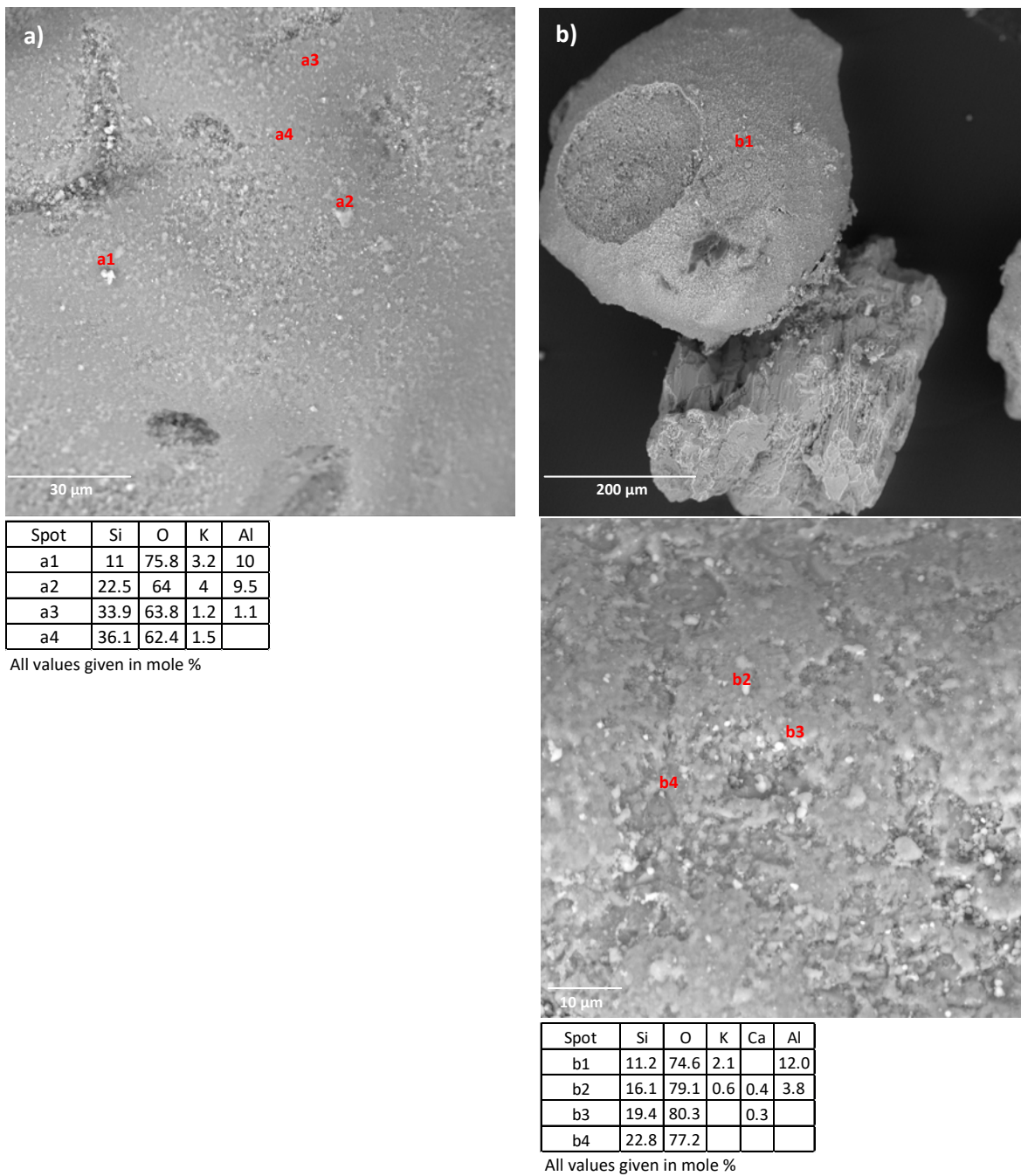


Figure 6-1: SEM-EDX analysis a) wheat straw mixed with kaolin and b) kaolin addition to bed;  $T_{bed}=850\text{ }^{\circ}\text{C}$ ;  $\lambda=1.45$ ;  $\lambda_v/\lambda=1$ ; sampled taken from cold reactor.

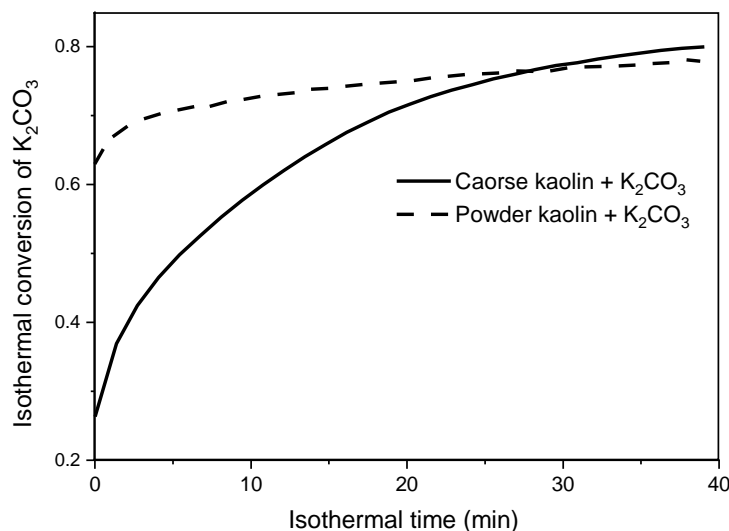


Figure 6-2: Reaction between  $K_2CO_3$  and kaolin is. 500 °C/min heating rate;  $T = 850$  °C; isothermal time 40 min;  $N_2$  atmosphere.

### 6.3.2 Lime addition

0.328 kg of wheat straw mixed with lime is continuously burned at 850 °C without defluidization. On the other hand, 0.267 kg of wheat straw has been continuously burned when 10 wt.% of bed is replaced with lime before defluidization. Significant number of agglomerates is observed after the bed material is removed from the reactor in both cases. Obtained results indicate that CaO mixing with fuel is more efficient compared to CaO addition to the bed, even though higher amount of CaO is used in later case. The impact of fuel Ca on defluidization has been already investigated and it was showed that Ca is incorporating (via dissolution) into coating layer consisting of K-silicates<sup>16</sup>, which increases layer viscosity and decreases the defluidization tendency<sup>12</sup>. The addition of Ca rich additives (such as CaO, CaCO<sub>3</sub>) during fluidized bed combustion can have a similar effect and they can reduce defluidization tendency due to formation of silicates with higher melting point<sup>66,79</sup>. Moreover, it is reported that CaO is not reacting with potassium species (on contrary to kaolin), but it is rather dissolved or incorporate into high viscous (glassy) K-silicates<sup>138</sup>. Figure 6-3 shows the SEM-EDX analysis of the bed material after the combustion of straw mixed with lime and after 10 wt.% of bed is replaced with lime.

Figure 6-3a indicates that Ca has been successfully incorporated into coating layer, which has relatively high Ca content. On the other hand, Figure 6-3b shows attachment of numerous solid particles (mainly CaO) to the continuous coating layer formed around sand particles. The small CaO (spot b2) particles originate from the bigger CaO lime particles, which are friable and can produce numerous small particles under vigorous mixing. Moreover, relatively big lime particles are observed too, without any traces of potassium, which confirms that CaO is not reacting with potassium from fuels.

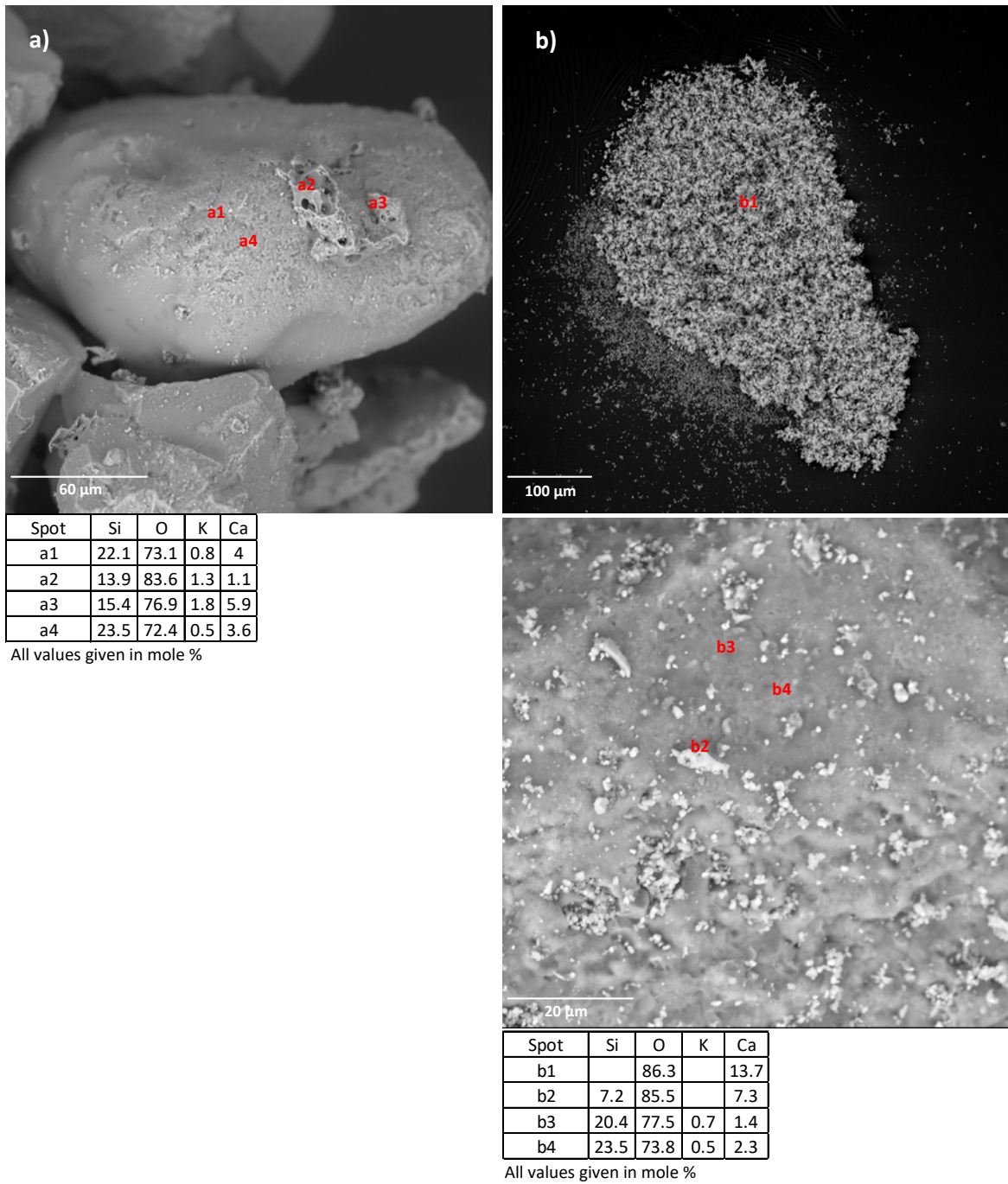


Figure 6-3: SEM-EDX analysis a) wheat straw mixed CaO b) CaO added to bed;  $T_{bed}=850\text{ }^{\circ}\text{C}$ ;  $\lambda=1.45$ ;  $\lambda_v/\lambda=1$ ; sampled taken from cold reactor.

These results indicate that effectiveness of CaO addition depends on its ability to be incorporated (dissolved) by K-Silicates melt. When the CaO is mixed with fuel, the number of contact points is significantly higher, which increases the rate of Ca incorporation. The higher contact area between fuel

and additives particles is also achieved by adding aqueous solution of  $\text{Ca}(\text{NO}_3)_2$ , which is proved to be more effective compared to addition of solid  $\text{CaO}$  <sup>79</sup>. Preparation of aqueous Ca solution is not easy due to the lower water solubility of Ca-species, which makes mixing of fuel with powder Ca-species more applicable method for enhancing the contact area between additives and fuel particles. Mixing of  $\text{CaO}$  with fuel has a potential to reduce defluidization tendency, but the effectiveness might be reduced at combustion temperatures higher than 900 °C, since some K-Ca-silicates have a melting temperature between 850 and 900 °C <sup>12</sup>.

### 6.3.3 Ammonium sulphate addition

0.195 kg of wheat straw mixed with AS has been continuously burned before defluidization, which provides an improvement compared to the combustion of wheat straw without additives (0.121 kg). No defluidization is observed during combustion of 0.512 kg of sunflower husk. It should be mentioned that elevated  $\text{SO}_2$  concentration is observed in both cases (around 400 ppm), while concentrations of other gaseous components are almost unchanged (except  $\text{NO}$ , which is reduced by 40 %). Moreover, 0.190 kg of wheat straw is continuously burned along with addition of AS pellets to the bed before defluidization. The amount of fuel fed before defluidization point is almost the same as in case of wheat straw mixed with AS, but still higher compared to wheat straw combustion without additives. The batch addition of AS influences the  $\text{SO}_2$  concentration in the flue gas. It varies between 3000 ppm (short after addition of pellet) and 150-200 ppm (right before addition of next pellet). It has been already reported that AS can react with potassium released in gaseous/aerosol form to significantly reduce deposition problems in circulating fluidized bed reactor <sup>139,140</sup>. The interaction between AS and potassium results in formation of  $\text{K}_2\text{SO}_4$ , which is less harmful compared to for example  $\text{KCl}$ . On the other hand, the impact of AS addition to agglomeration phenomena is not that pronounced due to the limited amount of AS reaching the bed <sup>78</sup>.

Figure 6-4 represents SEM-EDX analysis of bed material samples removed after continuous combustion experiments. In the case of wheat straw mixed with AS (Figure 6-4a), no sulphur is not identified on bed particles. It is most likely that the interaction between potassium species and AS is taking place near the fuel inlet point and AS is not reaching the bed due to the rapid decomposition <sup>135</sup>. The products are most probably released in aerosol form, as already suggested <sup>78</sup>. Figure 6-4b shows solid like spots consisting of K and S, indicating that formation of  $\text{K}_2\text{SO}_4$  might take place during combustion of sunflower husk mixed with AS. Sulphur present on bed particles (spots b2 and b4) can be either related to higher S content of SFH (see Table 5-1 in Chapter 5), or different interaction mechanism between AS and SFH.

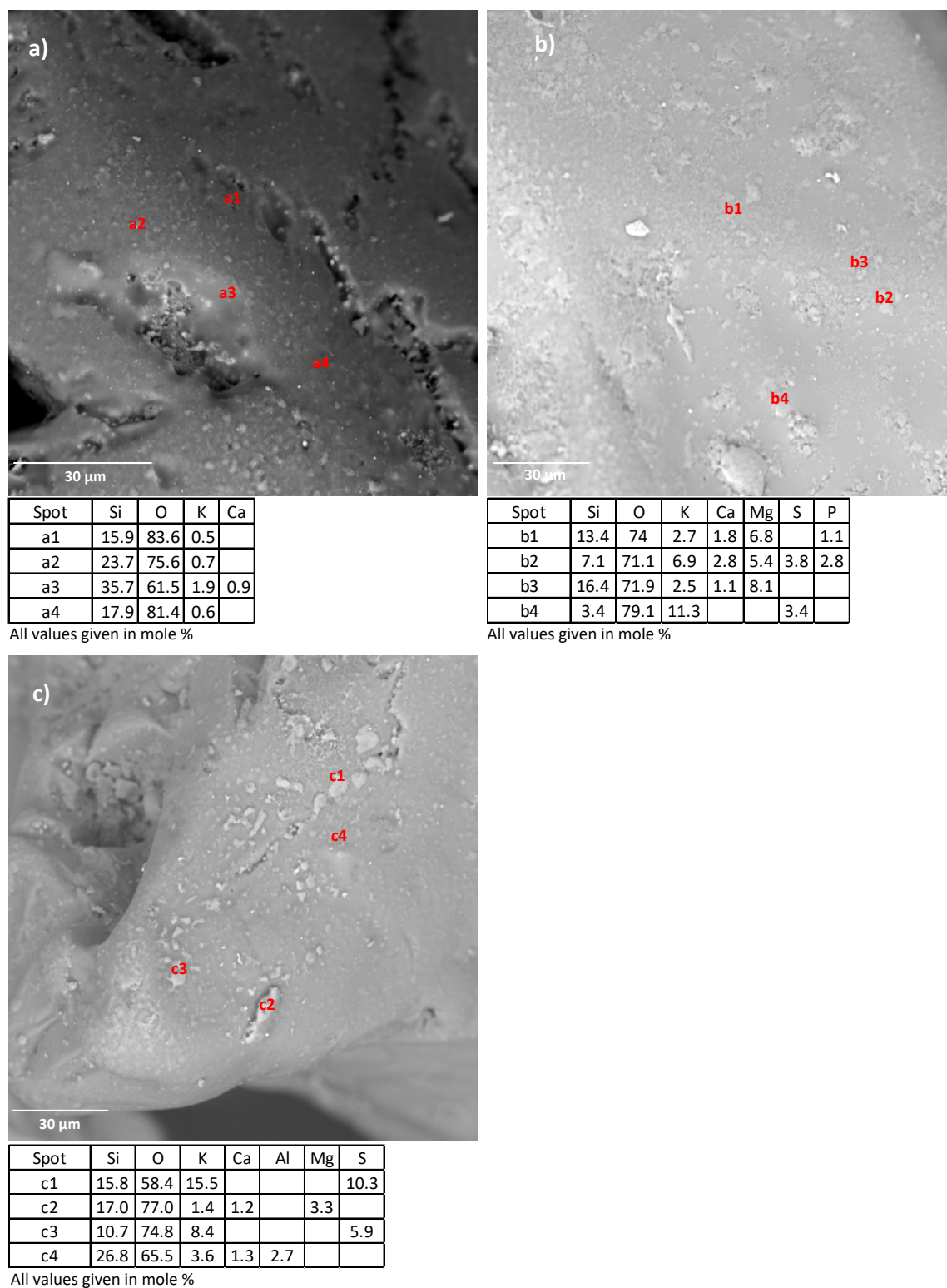


Figure 6-4: SEM-EDX analysis a) wheat straw mixed with AS, b) sunflower husk mixed with AS, c) AS addition to bed during wheat straw combustion;  $T_{bed}=850\text{ }^{\circ}\text{C}$ ;  $\lambda=1.45$ ;  $\lambda_v/\lambda=1$ ; sampled taken from cold reactor.

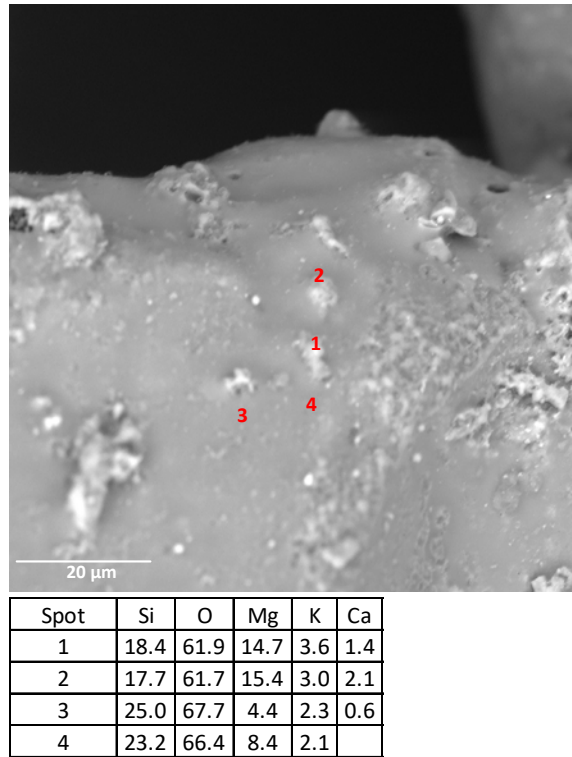
The density and shape of SFH is different compared to wheat straw and it is observed that SFH fuel particle are not as ignitable as wheat straw fuel particles. That means that some AS mixed with SFH may reach the bed due to the lower local temperature of burning particles, thus explaining sulphur presence on bed material particles. Formation of  $K_2SO_4$  limits invasion of potassium to silica sand surface, since  $K_2SO_4$  is thermodynamically stable compounds, which is not reacting with silica sand under oxidizing conditions <sup>56</sup>. When AS is added as pellets (combustion of wheat straw), formation of  $K_2SO_4$  can be assumed due to the simultaneous occurrence of K and S on the bed particles removed after combustion (Figure 6-4c). In this case some amount of AS definitely reached the bed and reacted with potassium to form  $K_2SO_4$ , which once again limits invasion of potassium to silica sand surface and reduces defluidization tendency.

Obtained results indicate that the impact of AS addition depends on fuel properties, as well as addition method. The mechanism of interaction is related to formation of thermodynamically stable  $K_2SO_4$ , which can be either retained in the bed or released in aerosol form (assumed). The effectiveness of AS addition is not as high as of kaolin and lime, since in the case of wheat straw defluidization time is only prolonged. On the other hand, even this small impact is sufficient to prevent defluidization after combustion of 0.5 kg of SFH.

#### **6.3.4 Magnesium carbonate addition**

0.301 of wheat straw mixed with powder  $MgCO_3$  is continuously burned in fluidized bed reactor without defluidization, and small amount of agglomerates is observed after the bed material is discharged from reactor. In order to understand the impact of  $MgCO_3$  addition SEM-EDX analysis (Figure 6-5) is performed.

A fused phase is covering silica sand surface, and its chemical composition (spots 3 and 4) indicates formation of K-Mg-silicates. These silicates have higher melting point compared to K-silicates, which means that formation of K-Mg-silicates is reducing defluidization tendency <sup>12</sup>. On the other hand, solid like spots, with relatively higher Mg and K content are also identified (spots 1 and 2), indicating formation of Mg-K species, apart from K-Mg-silicates. It is already suggested that K can be incorporated into MgO lattice after decomposition of magnesium precursors such as  $MgCO_3$  <sup>141,142</sup>, especially at temperature above 750 °C <sup>143</sup>.  $MgCO_3$  is in close contact with biomass particles that act as a source of potassium. In such way, some potassium might be captured and the amount invading silica sand surface is reduced.



All values given in mole %

Figure 6-5: SEM-EDX analysis; wheat straw mixed  $MgCO_3$ ;  $T_{bed}=850$  °C;  $\lambda=1.45$ ;  $\lambda_v/\lambda=1$ ; sampled taken from cold reactor;

### 6.3.5 Coal fly ash

0.199 kg of wheat straw mixed with coal fly ash is continuously burned before defluidization. On the other hand, 0.491 kg of sunflower husk is burned under same conditions, and no signs of defluidization are observed. Obtained results indicate that coal fly ash can improve combustion performance, but its effect is limited in case of wheat straw. Table 6-1 indicates similar elemental composition of coal fly ash and kaolin, but effectiveness of CFA is significantly lower compared to kaolin. The difference can be attributed to different forms of alumina-silicates present in these materials. Kaolinite, originally present in kaolin (see Table 6-1), is transferred to meta-kaolin above 650 °C, capable for effective capture of potassium species<sup>134</sup>. On the other hand, meta-kaolin is transferred to mulite above 980 °C, which has significantly lower capability for potassium capture especially below 900 °C<sup>134</sup>. Mulite is predominant form of alumina-silicates in coal fly ash (see Table 6-1), since the ash is obtained from large scale pulverized coal combustion, which occurs above 1100 °C. It is already observed that mulite is less reactive toward potassium species released in gaseous and aerosol form<sup>134</sup>, which can explain lower effectiveness of mulite (in our case coal fly ash) for reducing alkali problems during fluidized bed combustion<sup>65</sup>.

### 6.3.6 Clay soil

0.168 kg of wheat straw mixed with powder clay is continuously burned before defluidization. On the other hand, 0.523 kg of sunflower husk mixed with powder clay is burned under same conditions, and no signs of defluidization are observed. Similarly to CFA, addition of clay to fuels improves combustion performance, but the effect is limited in case of wheat straw. Table 6-1 indicates that, beside  $\text{SiO}_2$ ,  $\text{CaCO}_3$  is dominant mineral in the clay; indicating similar mechanisms of interaction as in case of CaO addition. The effectiveness of clay is significantly lower due to the lower Ca content (see Table 6-1).

### 6.3.7 Interaction mechanism

Performed analysis revealed that additives can impact agglomeration and defluidization tendencies in two ways. Firstly, they can capture potassium in thermodynamically stable compounds and limit potassium invasion to silica sand (related to formation of K-silicates and defluidization). Results presented in Chapter 5 indicate that initial stage of molten K-silicates formation is most likely taking place within the wheat straw ash particles, which further invade the surface of bed material. On the other hand, in case of sunflower husk, the formation of K-silicates is related to interaction between potassium salts present in the ash and bed material. When the biomass particles are mixed with powder additives, potassium species formed during biomass combustion have to “pass through” the additive particles in order to interact with bed material. That means that the additives are mainly influencing the interaction between K-silicates (most probably silica lean silicates) and silica sand, and between K-salts (from biomass ash) and silica sand in case of wheat straw and sunflower husk, respectively. The experiments showed that kaolin reactivity is very high in both cases and it is most likely that kaolin can rapidly react with all K-species (K-silicates, K-salts, aerosols, etc.). The driving force of formation is thermodynamically stable K-Al-silicates. On the other hand, the reactivity of CFA is reduced since mulite (dominant crystalline form in CFS) is less reactive compared to kaolin. Moreover, it appears that the reactivity of AS is lower compared to kaolin due to the rapid decomposition under combustion conditions. It might be also presumed that reactivity of CFA and AS toward K-salts is higher compared to the K-silicates, which may explain higher effectiveness when mixed with SFH. The second mechanism of interaction is related to incorporation of Mg and Ca present in additives, within high viscous K-silicates, which consequentially increases its viscosity and decreases stickiness and defluidization tendency<sup>144</sup>. The incorporation (dissolution) of these elements is dominant when lime, clay, and  $\text{MgCO}_3$  are mixed with fuels, due to the limited reaction between additives and biomass ash. The rate of incorporation depends on the number of contact points between Ca, Mg and high-viscous K-silicates, which is the reason why mixing of fuel with powder additives is more effective compared to addition to the bed, as observed in case of CaO.

Based on this investigation it might be concluded that kaolin is the most effective additive for reducing defluidization tendency of wheat straw and sunflower husk due to the very high reactivity toward all forms of potassium. It is followed by  $MgCO_3$ , which is capable to be incorporated within K-silicates, as well as to capture potassium in the crystalline lattice. Kaolin and  $MgCO_3$  are followed by lime, which is capable to increase the viscosity of formed melts and reduce defluidization tendency. The effectiveness of coal fly ash and ammonium sulphate is lower, but they also have potential (especially in case of sunflower husk) due to the lower cost (coal fly ash) and possibility to simultaneously reduce  $NO_x$  emission (ammonium sulphate). Finally, the effectiveness of clay is the lowest but it might be consider as additive for sunflower husk combustion, due to the very low cost.

The mixing of additives with fuel can be very interesting from the practical point of view since defluidization of the most troublesome fuels such as wheat straw can be avoided by using small amount of relatively cheap additives such are kaolin, lime, and  $MgCO_3$  (from dolomite stone for example). The critical amount of additives necessary to eliminate defluidization should be evaluated in detail (and for longer combustion time), and can be even less than 4.7 wt.% of fuel. Mixing of powder additives with fuel is additional operation that may need additional operating unit in practical fluidized bed power plants. On the other hand, it is possible to add the additives during grinding process of biomass.

## **6.4 Conclusion**

Kaolin, CaO,  $MgCO_3$  can potentially eliminate defluidization since stable combustion (without defluidization) of approximately 0.30 kg of wheat straw at 850 °C is achieved, while addition of coal fly ash, clay, and ammonium sulphate only prolonged defluidization time. Moreover, no defluidization is observed during combustion of approximately 0.5 kg of sunflower husk mixed with kaolin, coal fly ash, clay, and ammonium sulphate, which indicates that additives are more efficient in case of sunflower husk. Additives influence the defluidization tendency in two ways. Firstly, they can react with fuel K to form thermodynamical stable compounds and thus reduce the amount of potassium reacting with silica sand (as observed in case of kaolin addition). Secondly, they can interact with molten K-silicates (as in case of lime and  $MgCO_3$  addition) to increase its viscosity, which reduced melt stickiness and defluidization tendency. It is also showed that fuel mixing with powder additives is more efficient compared to addition of additives to the bed due to the higher contact area between fuel and additives particles. Finally, it appears that kaolin is the most efficient additive, followed by magnesium carbonate, lime, ammonium sulphate, coal fly ash, and clay in decreasing order of efficiency.

# 7

## CFD SIMULATION OF MIXING AND SEGRAGATION OF BINARY SOLID MIXTURES

---

This chapter has been written in a manuscript format. A slightly modified version of this chapter has been submitted to the peer-reviewed journal, *Canadian Journal of Chemical Engineering*.

### 7.1 Introduction

The change of bed hydrodynamics due to the segregation of formed agglomerates can be studied using CFD approach. The agglomerates have different size and density compared to initial (fresh) bed material, meaning that multi-phase modeling has to be applied. Even though CFD modeling is widely used for simulation of multi-phase systems there is no universal set of simulation models and parameters that could reproduce experimental data for wide range of operating conditions<sup>110,112,114</sup>. That is why; it is difficult to choose the simulation setting and parameters for simulation of systems where no experimental data is available for model validation. In order to obtain the optimal simulation scheme CFD simulations of binary solid phases exhibiting significantly different segregation and mixing degrees in a dense fluidized bed are investigated, and compared to the experimental data from Joseph et al.<sup>6</sup>. The impact of reactor geometry, specular coefficient, radial distribution function and solid pressure, gas-solid drag models, and solid-solid drag models is evaluated. An optimal combination of simulation parameters and a reasonable scheme that can reproduce two axial distribution profiles (mixed and segregated) are proposed.

### 7.2 Mathematical models and simulation set-up

#### 7.2.1 Experimental data

Experimental data are taken from Joseph et al.<sup>6</sup>, where the mixing and segregation of glass and polystyrene particles were experimentally studied in a fluidized bed. Two sets of data are taken for simulation: glass/polystyrene = 75:25 wt.% mixture (hereafter referred to as 75:25 mixture) that resembles good mixing, and glass/polystyrene = 50:50 wt.% mixture (hereafter referred to as 50:50 mixture) that resembles significant segregation. The physical properties of the solid phases are summarized in Table 7-1, and the relevant operating conditions are summarized in Table 7-2. The mixtures were initially well

mixed under a high gas velocity ( $U_g/U_{mf} = 3$ ), followed by a decrease of gas velocity ( $U_g/U_{mf} = 1.1$ ) in order to study the mixing and segregation behaviors. The low gas velocity was kept for 30 min and the axial mass distributions of the solid phases were determined by so-called frozen bed analysis <sup>6</sup>. This was done by turning off the gas flow and by dividing the settled particles into 12 sections. The mass fractions of both solid phases were determined in each of the sections, and presented as a function of dimensionless height (actual height divided by total bed height) <sup>6</sup>. The authors showed that the settling had a minor impact on axial distribution profiles.

Table 7-1: Physical properties of glass and polystyrene particles from Joseph et al. <sup>6</sup>

Material	$d_s(\mu\text{m})$	$\rho_s(\text{kg/m}^3)$	Sphericity	$U_{mf}$ (cm/s)
Glass	231	2476	0.944	5.6
Polystyrene	231	1064	0.981	2.9

Table 7-2: Main operating parameters of the experimental systems from Joseph et al. <sup>6</sup>

Mixture mass ratio (glass/polystyrene)	75:25	50:50
Mixture volume ratio (glass/polystyrene)	56:44	29:71
Cylinder diameter (cm)	12	12
Mass of the mixture (kg)	2	2
Minimal fluidization velocity of mixture $U_{mf}$ (cm/s)	7.1	6.9
Superficial gas velocity $U_g$ (cm/s)	7.81	7.59
$U_g/U_{mf}$ ratio	1.1	1.1
Mixture packing limit	0.585	0.572
Air density ( $\text{kg/m}^3$ )	1	1
Air viscosity (Pa·s)	$1.83 \cdot 10^{-5}$	$1.83 \cdot 10^{-5}$

### 7.2.2 Hydrodynamic model

The Eulerian multi-fluid approach was used to describe the hydrodynamics of gas-solid fluidization and Ansys® Fluent 16.2 software was employed as the solver. The relevant governing equations are given below, while more detailed explanations can be found in Ansys documentation <sup>145</sup>.

The continuity equation for gas and solid phases ( $i$ =glass, polystyrene) without consideration of mass transfer are, respectively:

$$\frac{\partial}{\partial t}(\varepsilon_g \rho_g) + \nabla \cdot (\varepsilon_g \rho_g \mathbf{u}_g) = 0 \quad (7.1)$$

$$\frac{\partial}{\partial t}(\varepsilon_{s,i} \rho_{s,i}) + \nabla \cdot (\varepsilon_{s,i} \rho_{s,i} \mathbf{u}_{s,i}) = 0 \quad (7.2)$$

$$\varepsilon_g + \sum_i \varepsilon_{s,i} = 0 \quad (7.3)$$

The momentum conservation equations for gas and solid phases ( $i$ =glass, polystyrene;  $k$ =polystyrene, glass) are, respectively:

$$\frac{\partial}{\partial t}(\varepsilon_g \rho_g \mathbf{u}_g) + \nabla \cdot (\varepsilon_g \rho_g \mathbf{u}_g \mathbf{u}_g) = -\varepsilon_g \nabla p + \nabla \cdot \boldsymbol{\tau}_g + \varepsilon_g \rho_g \mathbf{g} + \sum_i \beta_i (\mathbf{u}_{s,i} - \mathbf{u}_g) \quad (7.4)$$

$$\frac{\partial}{\partial t}(\varepsilon_{s,i} \rho_{s,i} \mathbf{u}_{s,i}) + \nabla \cdot (\varepsilon_{s,i} \rho_{s,i} \mathbf{u}_{s,i} \mathbf{u}_{s,i}) = -\varepsilon_{s,i} \nabla p - \nabla p_{s,i} + \nabla \cdot \boldsymbol{\tau}_{s,i} + \varepsilon_{s,i} \rho_{s,i} \mathbf{g} + \sum_i \beta_i (\mathbf{u}_g - \mathbf{u}_{s,i}) + \zeta_{ki} (\mathbf{u}_{s,k} - \mathbf{u}_{s,i}) \quad (7.5)$$

Kinetic theory of granular flow (KTGF) is used as solid phase stress closure in the Eulerian framework. A summary of all KTGF-based closures for solid phases and closures for the interactions of different phases is given in Table 7-3. Algebraic form of the granular temperature transport equation was used, where the diffusion and convection terms are neglected. For radial distribution and solid pressure, Lun et al. models<sup>146</sup>, and the models developed by Ma and Ahmadi<sup>147</sup> are used. Ma-Ahmadi models are particularly applicable to dense fluidized bed systems, where the particle-particle interactions are important<sup>147</sup>.

Table 7-3: KTGF-based closures for solid phases and closures for different interactions

---


$$\text{Gas stress tensor: } \boldsymbol{\tau}_g = \varepsilon_g \mu_g [\nabla \mathbf{u}_g + (\nabla \mathbf{u}_g)^T] + \varepsilon_g \left( \lambda_g - \frac{2}{3} \mu_g \right) \nabla \cdot \mathbf{u}_g \mathbf{I}, \quad \lambda_g = 0 \quad (7.6)$$


---

$$\text{Solid stress tensor: } \boldsymbol{\tau}_s = \varepsilon_s \mu_s [\nabla \mathbf{u}_s + (\nabla \mathbf{u}_s)^T] + \varepsilon_s \left( \lambda_s - \frac{2}{3} \mu_s \right) \nabla \cdot \mathbf{u}_s \mathbf{I}. \quad (7.7)$$


---

$$\text{Algebraic form of granular temperature equation: } (-p_s \mathbf{I} + \boldsymbol{\tau}_s) : \nabla \mathbf{u}_s - \gamma_s = 0 \quad (7.8)$$


---

$$\text{Total solid viscosity: } \mu_s = \mu_{s,\text{col}} + \mu_{s,\text{kin}} + \mu_{s,\text{fr}} \quad (7.9)$$


---

$$\text{Collisional viscosity using Syamlal O'Brien model }^{148}: \mu_{s,\text{col}} = \frac{4}{5} \rho_s \varepsilon_s^2 d_s g_0 (1 + e_{ss}) \sqrt{\frac{\theta_s}{\pi}} \quad (7.10)$$


---

$$\text{Kinetic viscosity Syamlal O'Brien model }^{148}: \mu_{s,\text{kin}} = \frac{\varepsilon_s d_s \rho_s \sqrt{\theta_s \pi}}{6(3 - e_{ss})} \left[ 1 + \frac{2}{5} (1 + e_{ss}) (3e_{ss} - 1) \alpha_s g_0 \right] \quad (7.11)$$


---

$$\text{Frictional viscosity using Schaeffer's model }^{149}: \mu_{s,\text{fr}} = \frac{p_s \sin \varphi}{2\sqrt{I}} \quad (7.12)$$


---

$$\text{Bulk viscosity using Lun et al. }^{146}: \lambda_s = \frac{4}{3} \varepsilon_s^2 \rho_s d_s g_0 (1 + e_{ss}) \left( \frac{\theta_s}{\pi} \right)^{1/2} \quad (7.13)$$


---

$$\text{Solid pressure: Lun et al. }^{146} \quad p_s = \varepsilon_s \rho_s \theta_s + 2\rho_s (1 + e_{ss}) \varepsilon_s^2 g_0 \theta_s \quad (7.14)$$


---

Ma and Ahmadi <sup>147</sup>

$$p_s = \varepsilon_s \rho_s \theta_s \left[ (1 + 4\varepsilon_s g_0) + \frac{1}{2} [(1 + e_{ss})(1 - e_{ss} + 2\mu_{s,fr})] \right] \quad (7.15)$$

Radial distribution function: Lun et al. <sup>146</sup>

$$g_0 = \left[ 1 - \left( \frac{\varepsilon_s}{\varepsilon_{s,max}} \right)^{1/3} \right]^{-1} + \frac{1}{2} d_l \sum_{k=1}^N \frac{\varepsilon_k}{d_k} \quad (7.16)$$

Ma and Ahmadi <sup>147</sup>

$$g_0 = \frac{1 + 2.5\varepsilon_s + 4.59\varepsilon_s^2 + 4.53\varepsilon_s^3}{\left[ 1 - \left( \frac{\varepsilon_s}{\varepsilon_{s,max}} \right)^3 \right]^{0.678}} + \frac{1}{2} d_l \sum_{k=1}^N \frac{\varepsilon_k}{d_k} \quad (7.17)$$

Solid-solid drag using Syamlal-O'Brien symmetric model <sup>150</sup>:

$$\zeta_{ik} = \frac{3(1+e_{ss})\left(\frac{\pi}{2} + C_{fr,ki}\right)\varepsilon_i \varepsilon_k \rho_i \rho_k (d_i + d_k)^2 + g_0}{2\pi(\rho_i d_i^3 + \rho_k d_k^3)} C_D \left( \frac{Re_s}{u_t} \right) |\mathbf{u}_i - \mathbf{u}_k| \quad (7.18)$$

Gas-solid drag model: Syamlal O'Brien model <sup>148</sup>

$$\beta_i = \frac{3\varepsilon_g \varepsilon_s \rho_g}{4u_t^2 d_s} C_D \left( \frac{Re_s}{u_t} \right) |\mathbf{u}_s - \mathbf{u}_g| \quad (7.19)$$

EMMS drag model <sup>151,152</sup>

$$\beta_i = H_D \frac{3}{4} C_{D0} \frac{\varepsilon_g \varepsilon_s \rho_g \varepsilon_g^{-2.65}}{d_s} |\mathbf{u}_s - \mathbf{u}_g| \quad (7.20)$$

Several gas-solid models are available in the Ansys® Fluent software. The Syamlal O'Brien drag model is a homogeneous gas-solid drag model that has been recently used for simulation of multi-phase systems <sup>113</sup>. In addition, the heterogeneous EMMS/bubbling drag model for dense fluidization is also commonly used <sup>151</sup>. In the EMMS/bubbling model, the heterogeneity indexes ( $H_D$ ), considering the disparity between the homogeneous and heterogeneous drag coefficients, are obtained by inputting operating conditions and phase parameters (gas velocity density and viscosity, maximal packing limit, mean solid density and mean solid diameter) <sup>151</sup>. The average physical properties for the two investigated solid phases are similar, so the same set of  $H_D$  (given by Eq. 21) is used for both phases.

$$H_D = \begin{cases} 1 & (\varepsilon_g < 0.4176) \\ -22980 + 211550\varepsilon_g - 727758\varepsilon_g^2 + 1118110\varepsilon_g^3 - 642017\varepsilon_g^4 & (0.4161 < \varepsilon_g < 0.446) \\ -19.75 + 153.17\varepsilon_g - 445.39\varepsilon_g^2 + 567.69\varepsilon_g^3 - 271.94\varepsilon_g^4 & (0.446 < \varepsilon_g < 0.628) \\ 1 & (0.628 < \varepsilon_g < 0.999) \end{cases} \quad (7.21)$$

### 7.2.3 Simulations settings

Figure 7-1 shows the 2D and 3D geometries of the fluidized bed, with the meshes generated by using Ansys® ICEM 17.2. For the 2D domain, the cell size is  $2 \times 4$  mm, giving a total of 9000 cells in the domain.

For the 3D domain, the total number of cells is 155375. The height of the 3D domain was reduced in order to reduce number of cells, because the 2D simulation showed that there were no solid particles above 250 mm height. The cell size was set below  $10d_s$  based on the recommendation from literature <sup>112</sup>. It has been shown that this cell size was fine enough to ensure the grid independence <sup>90</sup>, therefore the grid-dependence study was not performed. Solid mixture was initially packed (as marked in Figure 7-1) before the fluidizing air was introduced. The air inlet velocity was set to the value given in

Table 7-2. The non-slip boundary condition was prescribed for the gas phase. On the other hand, the partial-slip boundary condition with three different specular coefficients ( $\phi=0.5, 0.05, 0.0005$ ) was specified for the solid phases. Transient simulations were performed and started with 0.0001 s time step, followed by a gradual increase to 0.001s. The total simulation time was 200 s, with the last 50 s being used for data averaging. We used higher order discretization schemes in our simulations because they are commonly used for multi-phase systems <sup>112,113</sup>.

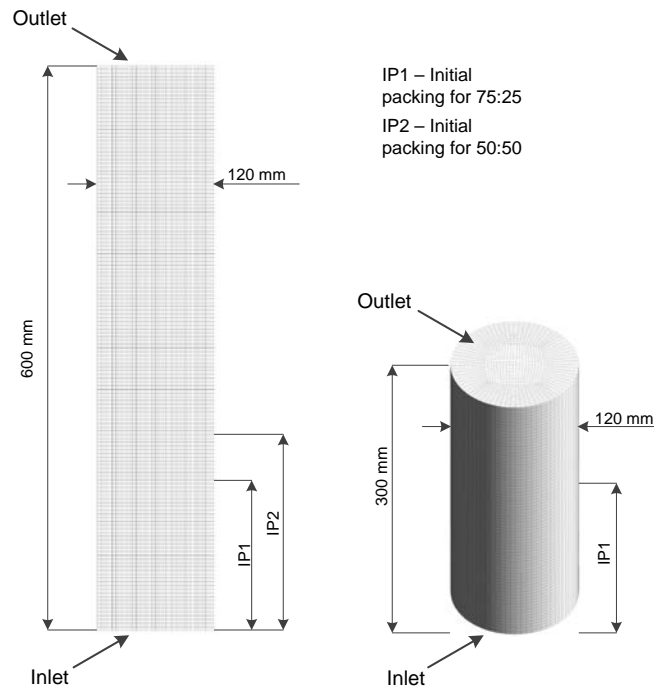


Figure 7-1: 2D and 3D geometry of the simulated fluidized bed

The parameters and models selected for all investigated simulation cases are summarized in Table 7-4. The impact of geometry was investigated because it was suggested that a 3D geometry can reproduce the behaviors of bubbles more precisely <sup>153,154</sup>, and bubbles play a significant role in mixing of solid mixtures. Furthermore, the impact of gas-solid drag model was investigated since it was already shown

that gas-solid drag model plays an important role for modelling segregation of binary solid mixtures<sup>110</sup>. The impact of boundary conditions was evaluated by modifying the specularly coefficient values, since a lower value would enable movement along the walls and, consequentially, promote the mixing<sup>113</sup>. The impact of solid stress tensor was investigated by changing solid pressure and radial distribution models, since correct modelling of solid stress tensor is extremely important in dense systems. Finally, the impact of solid-solid drag model was investigated by multiplying the solid-solid drag coefficient  $\zeta_{ki}$  with an additional constant (hereafter denoted by SS) varied between 0.25 and 4. Values higher than 1 indicate that the interaction between solid phases is enhanced, which might be important in dense systems.

Table 7-4: Summary of parameters investigated in this work

	Base case	Other investigated cases
Geometry	2D	3D
Gas-solid drag	Syamlal-O'Brien	EMMS/bubbling
Specularity coefficient	$\varphi=0.05$	$\varphi= 0.0005, 0.5$
Solid pressure	Lun et al.	Ma-Ahmadi
Radial distribution function	Lun et al.	Ma-Ahmadi
Solid-solid drag	Syamlal- O'Brien symmetric (SS=1)	Syamlal- O'Brien symmetric (SS=0.25, 2, 4)

## 7.3 Simulation results

### 7.3.1 Base case simulation

Figure 7-2 presents the comparison between the base case simulation results and the experimental data. For the 75:25 mixture, the base case simulation has a completely different axial distribution of the glass mass fraction in the solid mixture compared to the experimental data. The simulation shows that the glass and polystyrene particles are well mixed in the lower part of the bed, and the mass fraction of glass is slightly decreased as the bed height increases. In the upper part of the bed, the glass mass fraction is decreased significantly and almost no glass is present at the top of the bed. On the other hand, the experiments show that partial segregation of the glass phase only occurs in the bottom of bed, while a relatively constant mixing degree is observed in the upper part of the bed (above 0.2 dimensionless height). It should be pointed out that during transient simulation alternate mixing/segregation of two solid phases in upper part of reactor was observed. The glass mass fraction in the upper part of reactor has been following alternating scheme of lower and higher mass fraction each 4-5s (fluctuation around

the average value shown at Figure 7-2). Such behavior is less probable in actual systems, which once again indicates that the base case simulation settings cannot successfully reproduce chosen experimental data. For the 50:50 mixture, the obtained mass fraction of glass in the axial direction is closer to the experimentally observed profile. The simulation successfully reproduced the segregation trends, even though the quantitative agreement between the simulation and the experimental results is not perfect. The simulation correctly reproduced the segregation of glass in the lower part of the bed, while the upper part is polystyrene rich. Overall, the obtained mixing degree is higher compared to the experimental results.

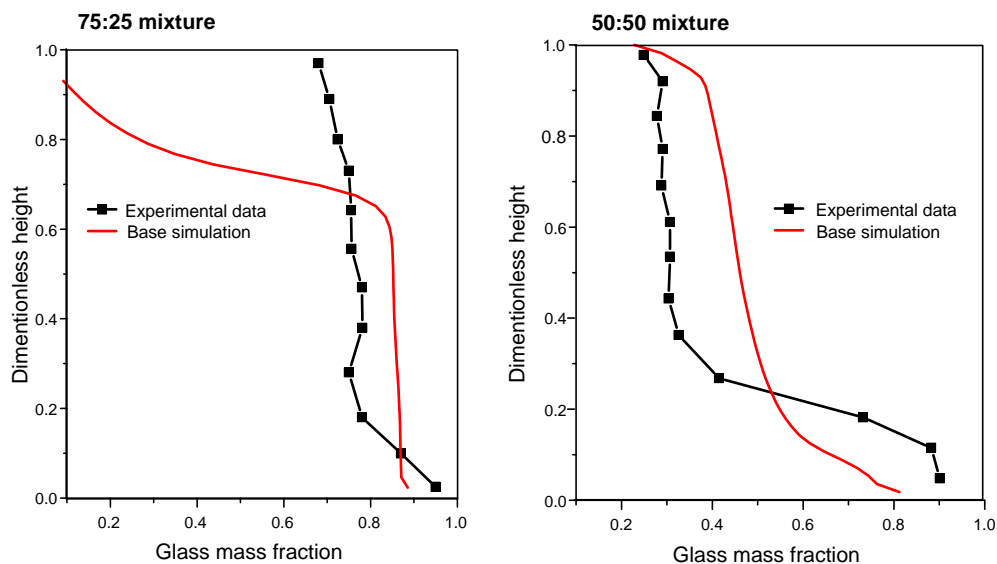


Figure 7-2: Comparison between simulation results and experimental data from Joseph et al.<sup>6</sup> for 75:25 (left) and 50:50 (right) mixtures

The simulation results in Figure 7-2 indicate that base case settings (as listed in Table 7-4) may successfully reproduce binary solid mixtures where significant phase segregation occurs, while their implementation to relatively well-mixed systems is limited.

### 7.3.2 Comparison of 2D and 3D geometry

3D simulations are performed for the 75:25 mixture and the results are presented at Figure 7-3. It is obvious that the impact of reactor geometry is minor, and that the experimental data cannot be reproduced with the base simulation settings by employing 3D geometry. It is commonly suggested that overall bed hydrodynamics and bubbles properties can be better reproduced using 3D geometry<sup>153,154</sup>, but this is not observed in our case. Due to the minor impact of reactor geometry, 2D geometry is used in further investigations because of the significantly lower computational cost.

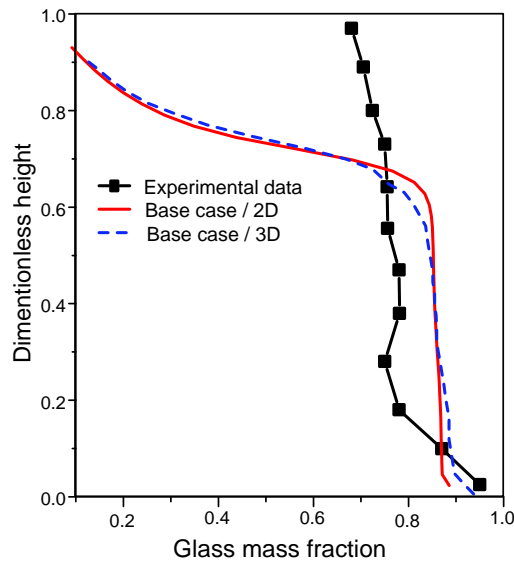


Figure 7-3: Comparison of 2D and 3D axial profiles together with experimental results from Joseph et al.<sup>6</sup> for glass/polystyrene=75:25 mixture

### 7.3.3 Impact of specular coefficient

Figure 7-4 compares the simulation results using different particle-wall boundary conditions by changing the specular coefficient.

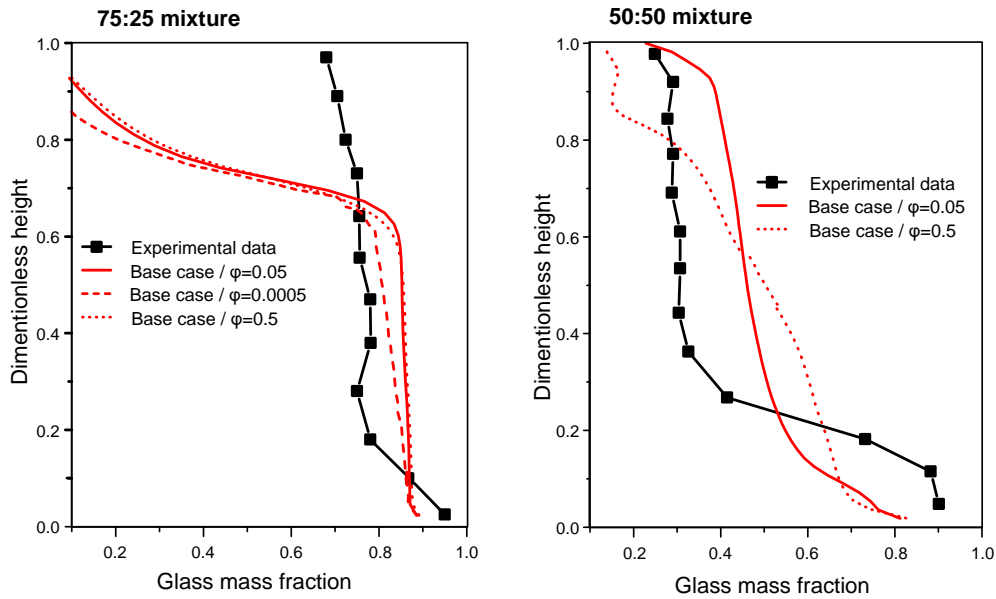


Figure 7-4: Impact of specular coefficient on simulation results and comparison with experimental data from Joseph et al.<sup>6</sup>

For 75:25 mixture, the impact of specular coefficient to the axial distribution is minor, even though a lower value promoted the mixing slightly<sup>113</sup>. For 50:50 mixture, the impact of specular coefficient seems

to be more pronounced, with the overall mixing degree decreased with a higher value of specularly coefficient (0.5). The glass mass fraction is monotonously decreasing with height for a higher value of specularly coefficient (0.5), and an almost complete segregation of polystyrene occurs at the top of the bed. This finding is in agreement with the previous studies<sup>112,113</sup>, which showed that higher values of specularly coefficient can promote phase segregation (observed only for 50:50 mixture). In our case, it is found that  $\varphi=0.05$  gives a better agreement between experimental and simulation results and thus this value is used in further simulations.

### 7.3.4 Effects of gas-solid drag model

Figure 7-5 gives a comparison of the simulation results of different gas-solid drag models. It should be pointed out that computational time to simulate the cases with EMMS/bubbling drag model is approximately 20% longer than base case simulations, since more iteration steps are necessary for convergence.

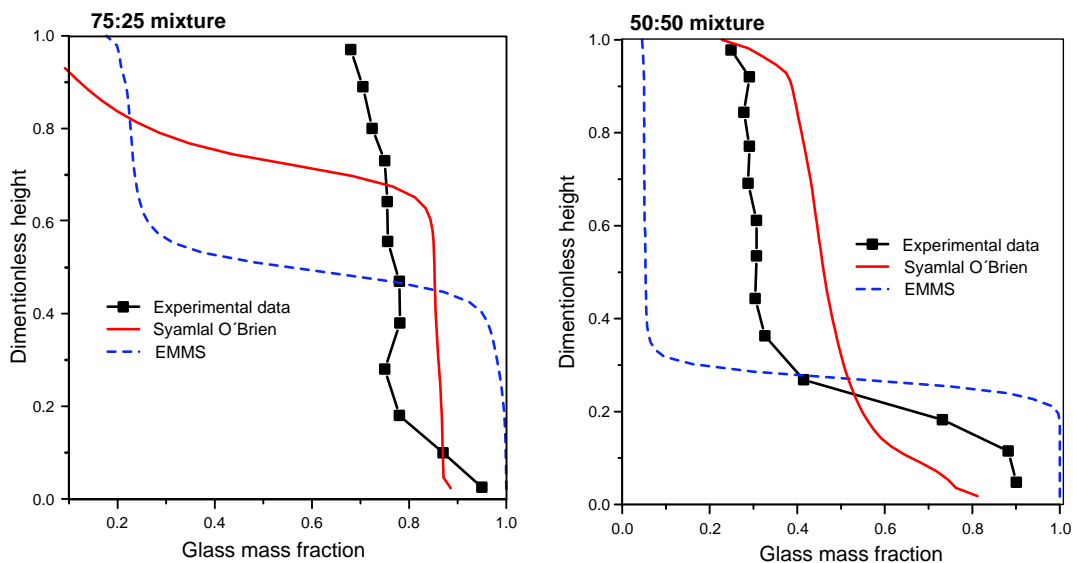


Figure 7-5: Comparison of axial profiles of glass mass fraction using Syamlal-O'Brien and EMMS/bubbling models with experimental data from Joseph et al.<sup>6</sup>

For 75:25 mixture, the gas-solid drag model has a significant impact on simulation results. When using the EMMS drag model, a significant segregation of two solid phases is observed. The glass mass fraction in the bottom part of the bed is almost equal to 1, while the solid mixture in the upper part of the bed is rich in polystyrene, with its mass fraction slightly increasing when reaching the top of the bed. There is still a significant difference between the simulation results of EMMS drag model and the experimental data. However, at least the partial segregation of heavier phase (glass) in the lower part of the bed is

captured by the simulation. On the other hand, the mixing degree of solid phases in upper part of the bed is much lower compared to experimental data. For 50:50 mixture, the overall segregation of two phases is more pronounced with the EMMS drag model. Glass can be mainly found in the lower part of the bed, with only a small amount mixed with polystyrene in the upper part. The trends of the simulation, i.e. glass rich lower part and polystyrene rich upper part of reactor, are similar to experimental results, but the agreement between experimental and simulation results is not good.

The performed analyses show that gas-solid drag model has a significant impact on simulation results in both investigated systems. However, the quantitative agreement between experimental and simulation data is bad for both drag models. Even though the EMMS/bubbling drag model can better reproduce some of the axial distribution trends, it is still hard to determine which gas-solid drag model is more appropriate to use. Thus, both of them are used in further simulations.

### 7.3.5 Impact of solid pressure and radial distribution models

Radial distribution function and solid pressure are important parameters that influence the solid stress tensor. Here, the impact of radial distribution and solid pressure models is investigated by replacing the commonly used Lun et al. models<sup>146</sup> with Ma-Ahmadi models<sup>147</sup>. The results obtained for both mixtures, using the two gas-solid drag models, are plotted at Figure 7-6 and Figure 7-7.

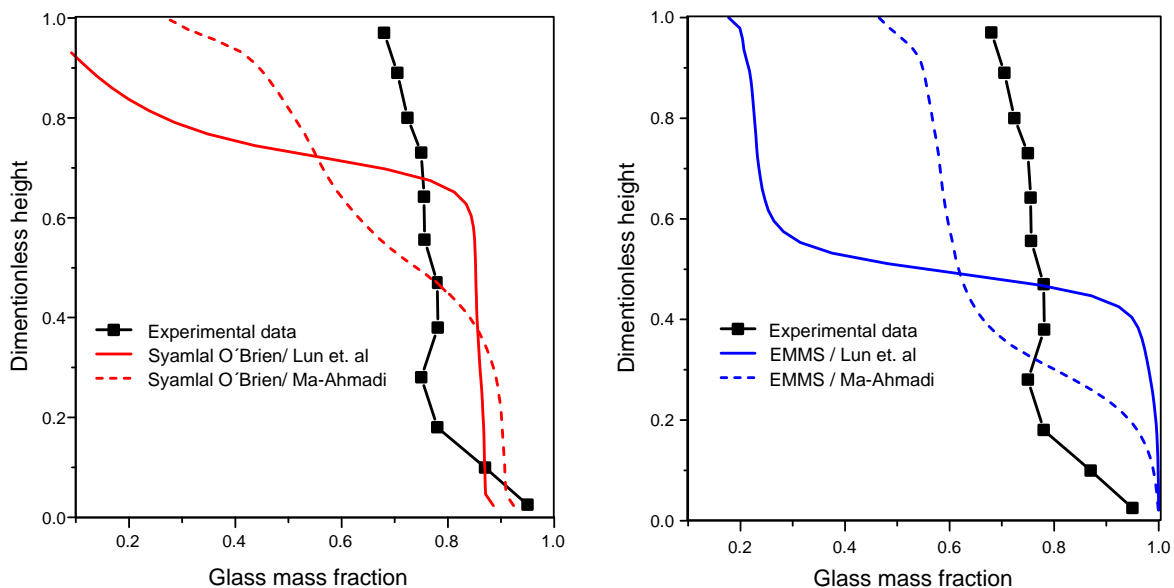


Figure 7-6: The impact of solid pressure and radial distribution models for 75:25 mixture and comparison with experimental data from Joseph et al.<sup>6</sup>

For the 75:25 mixture, the Ma-Ahmadi model increased the mixing degree of the glass and polystyrene phases for both gas-solid drag force models. Consequentially, the agreement between the simulation and experimental results is better, especially for the EMMS gas-solid drag model. Similar impact of these models is observed for the 50:50 mixture, especially when using the EMMS gas-solid drag model. In this case, the mixing degree in the upper part of the bed is increased, which improved the agreement between simulation and experimental results.

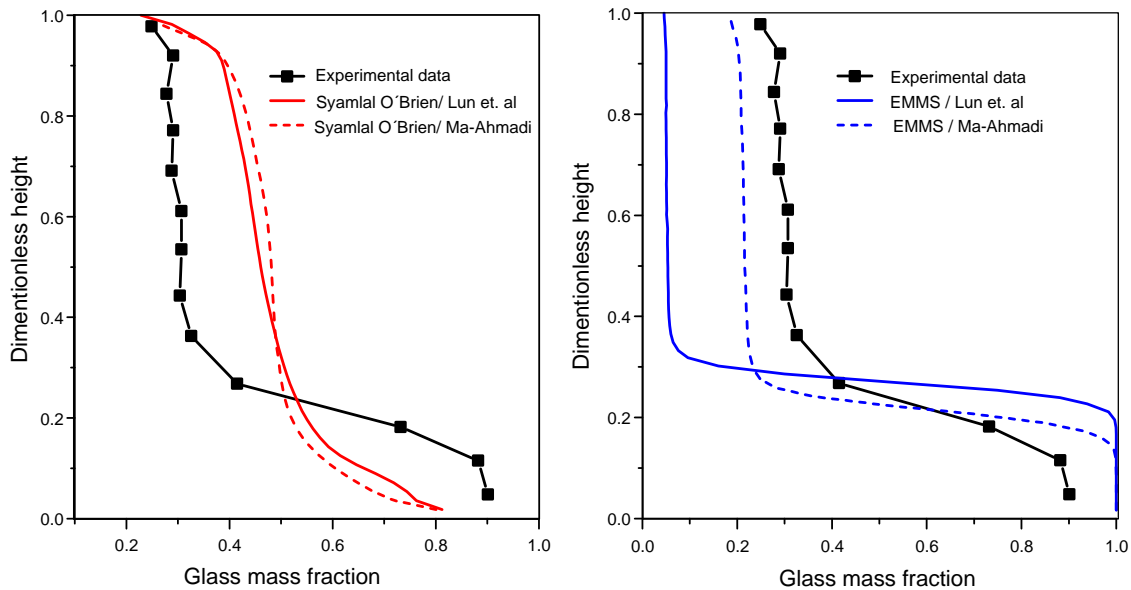


Figure 7-7: The impact of solid pressure and radial distribution models for 50:50 mixture and comparison with experimental data from Joseph et al.<sup>6</sup>

Ma-Ahmadi models take into account particulate fluctuations in kinetic energy in addition to the fluid phase fluctuations, which enables accurate predictions of solid stresses. That is why; these models are applicable to the highly dense systems, where particle collisions are important<sup>147</sup>. Since the investigated systems are dense, it is expected that the solid-solid interaction is significant or even dominant over gas-solid interactions. Implementation of the Ma-Ahmadi models for solid pressure and radial distribution together with EMMS gas solid drag model significantly improved simulation results, and the models are used for further simulations.

### 7.3.6 Impact of solid-solid drag model

Solid-solid drag models are used in order to describe the momentum transfer between the solid phases during collision. The impact of solid-solid drag model is investigated by multiplying the solid-solid drag coefficient by a constant  $SS$ . The solid-solid interaction is usually underestimated in dense systems by using Syamlal-O'Brien symmetric drag model<sup>150</sup>. In the initial derivation of solid-solid drag model<sup>150</sup>, only

the collision of one particle A (first solid phase) and one particle B (second solid phase) is considered, because considering multiple collisions is extremely complex. At the same time, the authors introduced a modification constant that should account for multiple collision between particles, and the constant was later related to radial distribution function<sup>150</sup>. In order to further enhance the impact of the multiple collisions at any given time, SS coefficients higher than 1 are considered when adjusting the solid-solid drag model. The results by adjusting the solid-solid drag for both mixtures are given in Figure 7-8.

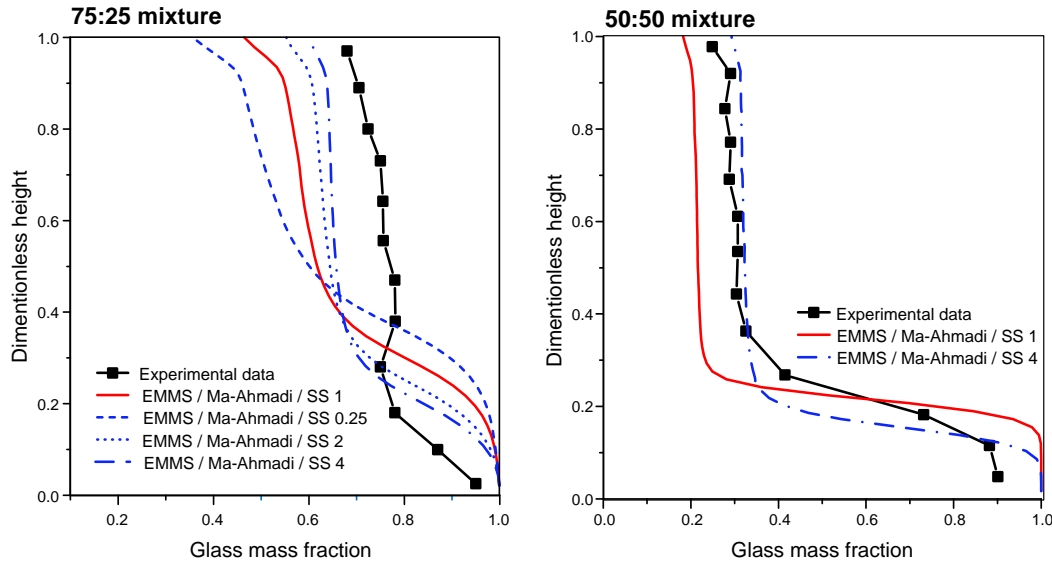


Figure 7-8: The impact of solid- solid drag modification and comparison with experimental data from Joseph et al.<sup>6</sup>

For SS equal to 4, the mixing between the solid phases is improved, which consequentially provides a better fitting between the simulation and experimental data. On the other hand, a lower value of the constant (SS=0.25) promotes segregation, as observed for 75:25 mixture. It seems that the impact of the coefficient is more significant for 75:25 mixture, probably related to the volume ratio between solid phases (almost 54:46 in this case). In this particular case, with almost equal volume of phases, solid-solid momentum exchange is significant (and dominant over gas-solid momentum exchange) and it mainly determines the flow patterns<sup>155</sup>. The modification of solid-solid drag models by adjusting relevant parameters has already been reported in literature<sup>114</sup>. The authors arbitrarily set the value of frictional coefficient ( $C_{fr,ki}$ ) in the solid-solid drag model (Eq.7-18) to 800, and achieved a significantly better agreement between the experimental and simulation results<sup>114</sup>. The multiple collisions between solid particles A and B at any given time provides the physical explanation of coefficient's values used in our case. SS values can be related to number of contact points between each particle A and each particle B in dense beds. In another words, there is certain number of particles A in contact with each particle B (and

vice-versa) at any time in the dense bed. The number of contact points depends on the volumetric ratio between particles A and B, as well as on their size, and it varies between 0 and 5<sup>156</sup>. That is why the further increment of the SS constant value may provide better fitting between simulation and experimental results although it has no specific physical interpretation. The interaction between solid phases has to be carefully considered in the future and new solid-solid drag models (in order to enhance interaction in dense multi-phase systems) have to be established. Introduction of modification coefficients is only a temporary and easy alternative.

## **7.4 Conclusion**

The gas-solid drag, solid stress tensor and solid-solid drag are important factors in CFD simulation of binary solid mixtures in dense fluidized beds. They have to be carefully chosen in order to obtain good agreement between experimental and simulation results for binary mixtures with distinguished mixing and segregation patterns. Our study showed that, compared to the commonly used Syamlal O'Brien gas-solid drag model coupled with Lun et al. solid pressure and radial distribution models, the EMMS/bubbling gas-solid drag model coupled with Ma-Ahmadi et al. solid pressure and radial distribution models can more reasonably predict the segregation and mixing behaviors of glass/polystyrene particles in dense fluidized beds. Adjustment of parameters linked to solid-solid interaction can further help to improve the simulations results. Among these factors, the choice of gas-solid drag model is important for obtaining good predictions of dense fluidization of binary mixture. The Ma-Ahmadi model for solid pressure and radial distribution function, and increasing of solid-solid friction coefficient are favorable to further improve the simulation predictions. The gas-solid and solid-solid drag considering the polydisperse features is expected to be established in the future, for improving the simulation of polydisperse fluidized system.



The thesis is the summary of three years research on mechanisms of bed agglomeration during fluidized bed combustion of biomass. This chapter provides the summary of main conclusion, as well as suggestions for future work.

### 8.1 Summary of Conclusions

The second chapter gives the overview of fluidized bed combustion of biomass, with emphasis on bed agglomeration. The impact of biomass composition, ash content, and operating conditions on the bed agglomeration is evaluated, as well as possible countermeasures for reducing agglomeration problems.

The third chapter provides the results on model potassium compounds induced defluidization in laboratory scale fluidized bed. Model potassium salts (KCl,  $K_2CO_3$ ), salt mixtures (KCl/ $K_2SO_4$ , KCl/ $K_2CO_3$ ), and potassium silicate ( $K_2Si_4O_9$ ) are mixed with silica sand and heated up at constant heating rate in the fluidized bed reactor up to defluidization point. The critical amount of potassium necessary to cause defluidization is investigated for different sand size and gas velocity. The mechanisms of interaction between different K-species and silica sand are evaluated. Based on this work, the following conclusions can be made:

- When adding KCl and a eutectic mixture of KCl- $K_2SO_4$ , defluidization is induced by molten salts, with limited reaction between salts and silica sand. Defluidization temperature is close to either KCl melting temperature (771 °C) or KCl- $K_2SO_4$  eutectic point (690 °C). A critical amount of KCl and KCl- $K_2SO_4$  eutectic increases for the higher  $U_g/U_{mf}$  ratio.
- When adding  $K_2CO_3$ , defluidization is induced by the formation of a high-viscous coating layer in the reaction between  $K_2CO_3$  and silica sand. Defluidization is related to layer thickness and viscosity. Defluidization temperature decreases with increasing amount of  $K_2CO_3$  added, reduced gas velocity, and bigger sand particles. The reaction between  $K_2CO_3$  and silica sand is promoted in presence of KCl.

## Concluding remarks

- For KCl-K<sub>2</sub>CO<sub>3</sub>-silica sand systems defluidization can occur either near KCl-K<sub>2</sub>CO<sub>3</sub> eutectic point (626 °C) or the KCl melting point (771 °C) dependent on the amount of the KCl-K<sub>2</sub>CO<sub>3</sub> salt mixture.
- Molten K<sub>2</sub>Si<sub>4</sub>O<sub>9</sub> particles act as a binder for silica sand particles. The interaction is localized at contact points. Under the investigated conditions, no defluidization is observed up to 850 °C even for potassium to sand ratio of 2.5 wt.%. Formation of a coating layer is not observed mainly due to the very high viscosity of molten particles.

The fourth chapter presents the results of reaction between K<sub>2</sub>CO<sub>3</sub> and silica sand. The experiments are performed in Thermogravimetric analyzer, which enables very high heating rate (up to 1000 °C/min). The reaction extent is monitored by release of CO<sub>2</sub> under isothermal conditions. The impact of temperature, salt to sand ratio, CO<sub>2</sub> partial pressure, mixing, and silica phase is investigated. The mechanism of reaction is evaluated and supported by SEM-EDX analysis. Following conclusions can be drawn:

- Potassium carbonate can react with silica sand to release CO<sub>2</sub> at temperatures well below the decomposition temperature of potassium carbonate. The reaction occurs in solid-solid phase with a high reaction rate at temperatures relevant to fluidized bed combustors (> 800°C).
- The reaction rate increases with increasing temperature, but decreases with an increase of CO<sub>2</sub> partial pressure. Mixing of the two solid reactants has a significant impact on the reaction rate, which is much higher for the well mixed than for the segregated particles due to enhanced contact between the solid particles. Moreover, the reaction rate is affected in a same way by the particle size of K<sub>2</sub>CO<sub>3</sub>, i.e. smaller particle size results in a higher reaction rate.
- The reaction of K<sub>2</sub>CO<sub>3</sub> with K<sub>2</sub>Si<sub>4</sub>O<sub>9</sub> occurs at approximately the same rate as with silica sand.
- The reaction between K<sub>2</sub>CO<sub>3</sub> and silica sand is initiated by surface reaction at the contact area between reactants, forming a molten homogeneous product layer. The product layer further reacts with K<sub>2</sub>CO<sub>3</sub> and silica sand.

The fifth chapter presents the results on continuous combustion experiments in laboratory scale fluidized bed reactor. Wheat straw, sunflower husk, K-compound doped washed straw and pine wood, are continuously burned under different bed temperatures, bed material, and air staging conditions. Based on this work, the following conclusions can be made:

- For wheat straw and sunflower husk, the amount of fuel burned before defluidization is decreasing at higher temperature, and no defluidization is observed after combustion of 0.5 kg of fuels at 770 °C.
- Replacing silica sand bed material with lime improves combustion performance and eliminates defluidization. Interaction between biomass ash and bed material, as well as the transfer of melt phase on bed material surface, is mainly responsible for defluidization.
- Defluidization tendency of fuels is mainly related to their potassium content, while fuel Si also increases the tendency to the increased rate of melt formation. On the other hand, fuel Ca and Mg reduce defluidization tendency due to the formation of melts with higher melting point and lower stickiness. Fuel S and Cl may also reduce defluidization tendency due to the formation of  $K_2SO_4$  and KCl, respectively, which decreases the amount of potassium available for reaction with bed material.
- For the potassium doped fuels it is most likely that the melt responsible for defluidization is formed in the reaction between  $K_2CO_3$  and silica sand. KOH can be converted to  $K_2CO_3$  during both, doping and combustion process, while transformation of KCl to  $K_2CO_3$  is likely taking place during devolatilization stage by interaction between KCl and char matrix. The transformation of KCl to  $K_2CO_3$  depends on the fuel properties and it is more pronounced for pine wood compared to washed straw.
- Defluidization tendency is influenced by air staging especially for sunflower husk. When the  $\lambda_1/\lambda$  ratio decreases from 1 to 0.04, the amount of sunflower husk burned before defluidization decreases from 0.3 to 0.089 kg. The increased defluidization tendency under reducing conditions is most likely attributed to the increased reactivity of potassium salts ( $K_2CO_3$  and  $K_2SO_4$ ) toward silica sand under these conditions. Moreover, the positive effect of Mg present in sunflower husk cannot come to the fore under reducing conditions, but this phenomena demands further investigation.
- For the  $\lambda_1/\lambda$  ratio equal to 0, no defluidization is observed even after combustion of 0.3 and 0.374 kg of wheat straw and sunflower husk, respectively. The absence of defluidization can be attributed to the char matrix, which hinders the interaction between biomass inorganic elements and bed material. As soon as the air is introduced to bed, rapid defluidization occurs because of char utilization and formation of ash particles that react with bed material.

The sixth chapter presents the results on experimental investigation on additives impact on fluidized bed combustion. Kaolin, CaO,  $MgCO_3$ , coal fly ash, clay, and ammonium sulphate are either mixed with fuel or

added to bed directly during combustion wheat straw and sunflower husk. Following conclusions can be made based on this investigation:

- Kaolin, CaO, MgCO<sub>3</sub> can potentially eliminate defluidization since stable combustion (without defluidization) of approximately 0.33 kg of wheat straw at 850 °C is achieved, while addition of coal fly ash, clay, and ammonium sulphate only prolonged defluidization time. The additives efficiency is higher when added to sunflower husk, since no defluidization is observed during combustion of approximately 0.5 kg of sunflower husk mixed with kaolin, coal fly ash, clay, and ammonium sulphate.
- The efficiency of additives can be related to the fuel properties, since additives are more effective for K rich and Si lean (SFH) fuel compared to the K and Si rich fuels (wheat straw). In case of SFH, the interaction between fuel K and silica sand is mainly responsible for melt formation, and the interaction can be significantly influenced if additives are present at the outer surface of biomass particles. On the other hand, initial formation of melt phase is taking place within the wheat straw particles, where no additives are present.
- Additives influence the defluidization tendency in two ways. They can react with fuel K to form thermodynamical stable compounds and thus reduce the amount of K reacting with silica sand. Secondly, they can interact with formed melt (K-silicates) to increase its viscosity, and hence reduce melt's stickiness and defluidization tendency.
- It appears that kaolin is the most efficient additive, followed by magnesium carbonate, lime, ammonium sulphate, coal fly ash, and clay in decreasing order of efficiency.

The seventh chapter presents the result of CFD simulations of glass/polystyrene binary solid mixtures. The impact of simulation parameters and models is investigated in order to identify the optimal simulation scheme, which can successfully reproduce experimental data for wide range of operating conditions. Based on this work, the following conclusions can be made:

- The gas-solid drag, solid stress tensor and solid-solid drag are important factors in CFD simulation of binary solid mixtures in dense fluidized beds. They have to be carefully chosen in order to obtain good fitting between experimental and simulation results for binary mixtures with two distinguished mixing and segregation patterns.
- Compared to the commonly used Syamlal O'Brien gas-solid drag model coupled with Lun et al. radial distribution and solid pressure models, the EMMS/bubbling gas-solid drag model coupled with Ma-Ahmadi radial distribution and solid pressure models can more reasonably predict the

segregation and mixing behaviors of glass/polystyrene particles in dense fluidized beds. Adjustment of solid-solid interaction can further improve the simulations results.

## **8.2 Suggestions for future work**

The presented results provide an improved understanding of bed agglomeration phenomena and the interactions between potassium species and silica sand under fluidized bed conditions. However, a considerable amount of work can be done in order to further investigate agglomeration and defluidization mechanism. These are few suggestions for future work.

### ***Interaction between model K-species and silica sand under fluidized bed conditions***

Additional experiments may be performed in order to further investigate interactions between model K-species and silica sand. Reactive K-silicates ( $K_2SiO_3$  and  $K_2Si_2O_5$ ), as well as K-salts/K-silicate mixtures, should be considered.

### ***Transformation of potassium during pyrolysis and char conversion stage***

The transformation of potassium during pyrolysis and char conversion stage should be further addressed, since the appropriate operating conditions may reduce reactivity of potassium and decrease defluidization tendency. There are indices that potassium transformations are taking place within the char during the cooling process, which have potential to reduce defluidization tendencies.

### ***Fluidized bed combustion***

The impact of most of relevant elements on defluidization tendency is evaluated, apart from Phosphorous, which should be considered in future work. Besides, the co-combustion of fuel with different elemental composition should be considered. Moreover, the impact of  $\lambda_1/\lambda$  ratio should be evaluated further, in order to understand the limited impact of fuel Mg content on defluidization tendency under reducing conditions.

### ***Proposal of effective and cheap countermeasures***

Evaluation of suitable amount of additives that should be mixed with fuel can be performed. Usage of coal fly ash from fluidized bed combustion (due to the lower operating temperature), and clay with higher Al content can be considered.

### ***Modeling***

Existing chemical engineering models for estimation of defluidization time and temperature can be improved by considering the relation to the  $U_g/U_{mf}$  ratio. Also, the formation of agglomerates can be

### *Concluding remarks*

considered through changeable  $U_g/U_{mf}$  ratio. Developed CFD scheme can be used in order to simulate sand/agglomerate system and to investigate the impact of agglomerates formation to bed hydrodynamics. Simulation may be used for manipulation of operating parameters and conditions (gas velocity, sand size) in a way to avoid partial segregation of jetsam phase (agglomerates) at the bottom of the reactor.

## REFERENCES

---

- (1) The Danish Government. *Our Future Energy*, 2011.
- (2) Gregg, J. S.; Bolwig, S.; Solér, O.; Vejlgård, L.; Gundersen, S. H.; Grohnheit, P. E. Experiences with Biomass in Denmark. Department of Management Engineering, Technical University of Denmark 2014.
- (3) Khan, A. A.; de Jong, W.; Jansens, P. J.; Spliethoff, H. Biomass Combustion in Fluidized Bed Boilers: Potential Problems and Remedies. *Fuel Process. Technol.* **2009**, *90* (1), 21–50.
- (4) Balland, M.; Froment, K.; Ratel, G.; Valin, S.; Roussely, J.; Michel, R.; Poirier, J.; Kara, Y.; Galnares, A. Biomass Ash Fluidised-Bed Agglomeration: Hydrodynamic Investigations. *Waste and Biomass Valorization* **2017**, *8* (8), 2823–2841.
- (5) Mettanant, V.; Basu, P.; Butler, J. Agglomeration of Biomass Fired Fluidized Bed Gasifier and Combustor. *Can. J. Chem. Eng.* **2009**, *87* (5), 656–684.
- (6) Joseph, G. G.; Leboireiro, J.; Hrenya, C. M.; Stevens, A. R. Experimental Segregation Profiles in Bubbling Gas-Fluidized Beds. *AIChE J.* **2007**, *53* (11), 2804–2813.
- (7) Yates, J. G.; Lettieri, P. Conversion of Biomass and Waste Fuels in Fluidized-Bed Reactors. In *Fluidized-bed Reactors: Processes and Operating Conditions*; Springer International Publishing, **2016**; 26,111–135.
- (8) Rainio, A.; Sharma, V.; Bolhàr-Nordenkamp, M.; Brunner, C.; Lind, J.; Crosher, J. Fluidized Bed Technologies for Biomass Combustion. *Am. Soc. Mech. Eng.* **2009**, *1*, 97–105.
- (9) Bartels, M.; Lin, W.; Nijenhuis, J.; Kapteijn, F.; van Ommen, J. R. Agglomeration in Fluidized Beds at High Temperatures: Mechanisms, Detection and Prevention. *Progress in Energy and Combustion Science.* **2008**, *34* (5), 633–666.
- (10) Scala, F. Particle Agglomeration during Fluidized Bed Combustion: Mechanisms, Early Detection and Possible Countermeasures. *Fuel Processing Technology.* **2018**, *171*, 31–38.
- (11) Lin, W.; Dam-Johansen, K.; Frandsen, F. Agglomeration in Bio-Fuel Fired Fluidized Bed Combustors. *Chem. Eng. J.* **2003**, *96* (1), 171–185.
- (12) Scala, F.; Chirone, R. An SEM/EDX Study of Bed Agglomerates Formed during Fluidized Bed Combustion of Three Biomass Fuels. *Biomass and Bioenergy* **2008**, *32* (3), 252–266.
- (13) Liu, H.; Feng, Y.; Wu, S.; Liu, D. The Role of Ash Particles in the Bed Agglomeration during the Fluidized Bed Combustion of Rice Straw. *Bioresour. Technol.* **2009**, *100* (24), 6505–6513.
- (14) Visser, H. J. M.; van Lith, S. C.; Kiel, J. H. A. Biomass Ash-Bed Material Interactions Leading to Agglomeration in FBC. *J. Energy Resour. Technol.* **2008**, *130* (1), 011801.
- (15) Gatternig, B.; Karl, J. Investigations on the Mechanisms of Ash-Induced Agglomeration in Fluidized-Bed Combustion of Biomass. *Energy & Fuels* **2016**, *29* (2), 931–941.
- (16) Brus, E.; Öhman, M.; Nordin, A. Mechanisms of Bed Agglomeration during Fluidized-Bed

Combustion of Biomass Fuels. *Energy & Fuels* **2005**, *19*(3), 825–832.

- (17) Öhman, M.; Nordin, A.; Skrifvars, B.-J.; Backman, R.; Hupa, M. Bed Agglomeration Characteristics during Fluidized Bed Combustion of Biomass Fuels. *Energy & Fuels* **2000**, *14*(1), 169–178.
- (18) Vassilev, S. V.; Baxter, D.; Andersen, L. K.; Vassileva, C. G.; Morgan, T. J. An Overview of the Organic and Inorganic Phase Composition of Biomass. *Fuel* **2012**, *94*, 1–33.
- (19) Vassilev, S. V.; Baxter, D.; Andersen, L. K.; Vassileva, C. G. An Overview of the Chemical Composition of Biomass. *Fuel* **2010**, *89*(5), 913–933.
- (20) Vassilev, S. V.; Baxter, D.; Andersen, L. K.; Vassileva, C. G. An Overview of the Composition and Application of Biomass Ash. Part 1. Phase–mineral and Chemical Composition and Classification. *Fuel* **2013**, *105*, 40–76.
- (21) Mason, P. E.; Darvell, L. I.; Jones, J. M.; Williams, A. Observations on the Release of Gas-Phase Potassium during the Combustion of Single Particles of Biomass. *Fuel* **2016**, *182*, 110–117.
- (22) Lane, D. J.; Zevenhoven, M.; Ashman, P. J.; van Eyk, P. J.; Hupa, M.; de Nys, R.; Lewis, D. M. Algal Biomass: Occurrence of the Main Inorganic Elements and Simulation of Ash Interactions with Bed Material. *Energy & Fuels* **2014**, *28*(7), 4622–4632.
- (23) Zevenhoven, M.; Yrjas, P.; Skrifvars, B.-J.; Hupa, M. Characterization of Ash-Forming Matter in Various Solid Fuels by Selective Leaching and Its Implications for Fluidized-Bed Combustion. *Energy & Fuels* **2012**, *26*(10), 6366–6386.
- (24) Skrifvars, B.-J.; Yrjas, P.; Kinni, J.; Siefen, P.; Hupa, M. The Fouling Behavior of Rice Husk Ash in Fluidized-Bed Combustion. 1. Fuel Characteristics. *Energy & Fuels* **2005**, *19*(4), 1503–1511.
- (25) van Lith, S. C.; Jensen, P. A.; Frandsen, F. J.; Glarborg, P. Release to the Gas Phase of Inorganic Elements during Wood Combustion. Part 2: Influence of Fuel Composition. *Energy & Fuels* **2008**, *22*(3), 1598–1609.
- (26) Knudsen, J. N.; Jensen, P. A.; Dam-Johansen, K. Transformation and Release to the Gas Phase of Cl, K, and S during Combustion of Annual Biomass. *Energy & Fuels* **2004**, *18*(5), 1385–1399.
- (27) Johansen, J. M.; Jakobsen, J. G.; Frandsen, F. J.; Glarborg, P. Release of K, Cl, and S during Pyrolysis and Combustion of High-Chlorine Biomass. *Energy & Fuels* **2011**, *25*(11), 4961–4971.
- (28) Wei, X.; Schnell, U.; Hein, K. R. G. Behaviour of Gaseous Chlorine and Alkali Metals during Biomass Thermal Utilisation. *Fuel* **2005**, *84*(7–8), 841–848.
- (29) Lindberg, D.; Backman, R.; Chartrand, P. Towards a Comprehensive Thermodynamic Database for Ash-Forming Elements in Biomass and Waste Combustion — Current Situation and Future Developments. *Fuel Process. Technol.* **2013**, *105*, 129–141.
- (30) Boström, D.; Skoglund, N.; Grimm, A.; Boman, C.; Öhman, M.; Broström, M.; Backman, R. Ash Transformation Chemistry during Combustion of Biomass. *Energy & Fuels* **2012**, *26*(1), 85–93.
- (31) Umamaheswaran, K.; Batra, V. S. Physico-Chemical Characterisation of Indian Biomass Ashes. *Fuel* **2008**, *87*(6), 628–638.
- (32) Thy, P.; Jenkins, B. M.; Grundvig, S.; Shiraki, R.; Leshner, C. E. High Temperature Elemental Losses and Mineralogical Changes in Common Biomass Ashes. *Fuel* **2006**, *85*(5), 783–795.
- (33) Wang, G.; Shen, L.; Sheng, C. Characterization of Biomass Ashes from Power Plants Firing Agricultural Residues. *Energy & Fuels* **2012**, *26*(1), 102–111.

- (34) Xiao, R.; Chen, X.; Wang, F.; Yu, G. The Physicochemical Properties of Different Biomass Ashes at Different Ashing Temperature. *Renew. Energy* **2011**, *36* (1), 244–249.
- (35) Olanders, B.; Steenari, B.-M. Characterization of Ashes from Wood and Straw. *Biomass and Bioenergy* **1995**, *8* (2), 105–115.
- (36) Vamvuka, D.; Zografos, D. Predicting the Behaviour of Ash from Agricultural Wastes during Combustion. *Fuel* **2004**, *83* (14), 2051–2057.
- (37) Wu, H.; Bashir, M. S.; Jensen, P. A.; Sander, B.; Glarborg, P. Impact of Coal Fly Ash Addition on Ash Transformation and Deposition in a Full-Scale Wood Suspension-Firing Boiler. *Fuel* **2013**, *113*, 632–643.
- (38) Zhao, H.; Song, Q.; Wu, X.; Yao, Q. Study on the Transformation of Inherent Potassium during the Fast-Pyrolysis Process of Rice Straw. *Energy & Fuels* **2015**, *29* (10), 6404–6411.
- (39) Chen, C.; Luo, Z.; Chunjiang, Y.; Wang, T.; Zhang, H. Transformation Behavior of Potassium during Pyrolysis of Biomass. *RSC advances* **2017**, *7*, 31319–31326.
- (40) Piotrowska, P.; Zevenhoven, M.; Davidsson, K.; Hupa, M.; Åmand, L.-E.; Barišić, V.; Coda Zabetta, E. Fate of Alkali Metals and Phosphorus of Rapeseed Cake in Circulating Fluidized Bed Boiler Part 1: Cocombustion with Wood. *Energy & Fuels* **2010**, *24* (1), 333–345.
- (41) Nielsen, H. P.; Baxter, L. L.; Sclippab, G.; Morey, C.; Frandsen, F. J.; Dam-Johansen, K. Deposition of Potassium Salts on Heat Transfer Surfaces in Straw-Fired Boilers: A Pilot-Scale Study. *Fuel* **2000**, *79* (2), 131–139.
- (42) Srikanth, S.; Das, S. K.; Ravikumar, B.; Rao, D. S.; Nandakumar, K.; Vijayan, P. Nature of Fireside Deposits in a Bagasse and Groundnut Shell Fired 20 MW Thermal Boiler. *Biomass and Bioenergy* **2004**, *27* (4), 375–384.
- (43) Armesto, L.; Bahillo, A.; Veijonen, K.; Cabanillas, A.; Otero, J. Combustion Behaviour of Rice Husk in a Bubbling Fluidised Bed. *Biomass and Bioenergy* **2002**, *23* (3), 171–179.
- (44) Steenari, B. M.; Karlsson, L. G.; Lindqvist, O. Evaluation of the Leaching Characteristics of Wood Ash and the Influence of Ash Agglomeration. *Biomass and Bioenergy* **1999**, *16* (2), 119–136.
- (45) Steenari, B. M.; Schelander, S.; Lindqvist, O. Chemical and Leaching Characteristics of Ash from Combustion of Coal, Peat and Wood in a 12 MW CFB - a Comparative Study. *Fuel* **1999**, *78* (2), 249–258.
- (46) Grimm, A.; Skoglund, N.; Bostrom, D.; Ohman, M. Bed Agglomeration Characteristics in Fluidized Quartz Bed Combustion of Phosphorus-Rich Biomass Fuels. *Energy & Fuels* **2011**, *25* (3), 937–947.
- (47) Pettersson, A.; Åmand, L.-E.; Steenari, B.-M. Chemical Fractionation for the Characterisation of Fly Ashes from Co-Combustion of Biofuels Using Different Methods for Alkali Reduction. *Fuel* **2009**, *88* (9), 1758–1772.
- (48) Moradian, F.; Tchoffor, P. A.; Davidsson, K. O.; Pettersson, A.; Backman, R. Thermodynamic Equilibrium Prediction of Bed Agglomeration Tendency in Dual Fluidized-Bed Gasification of Forest Residues. *Fuel Process. Technol.* **2016**, *154*, 82–90.
- (49) Billen, P.; Creemers, B.; Costa, J.; Van Caneghem, J.; Vandecasteele, C. Coating and Melt Induced Agglomeration in a Poultry Litter Fired Fluidized Bed Combustor. *Biomass and Bioenergy* **2014**, *69*, 71–79.

- (50) Montes, A.; Ghiasi, E.; Tran, H.; Xu, C. (Charles). Study of Bed Materials Agglomeration in a Heated Bubbling Fluidized Bed (BFB) Using Silica Sand as the Bed Material and KOH to Simulate Molten Ash. *Powder Technol.* **2016**, *291*, 178–185.
- (51) Sevonius, C.; Yrjas, P.; Hupa, M. Defluidization of a Quartz Bed – Laboratory Experiments with Potassium Salts. *Fuel* **2013**, *127*, 161–168.
- (52) Narayan, V.; Jensen, P. A.; Henriksen, U. B.; Glarborg, P.; Lin, W.; Nielsen, R. G. Defluidization in Fluidized Bed Gasifiers Using High-Alkali Content Fuels. *Biomass and Bioenergy* **2016**, *91*, 160–174.
- (53) US Commerce of diffence, *Phisical Properties Data Compilations Relevant to Energy Storage*, **1979**.
- (54) Bockris, J. O.; Mackenzie, J. D.; Kitchener, J. A. Viscous Flow in Silica and Binary Liquid Silicates. *Trans. Faraday Soc.* **1955**, *51* (12), 1734.
- (55) Arvelakis, S.; Jensen, P. A.; Dam-Johansen, K. Simultaneous Thermal Analysis (STA) on Ash from High-Alkali Biomass. *Energy & Fuels* **2004**, *18* (4), 1066–1076.
- (56) Ma, T.; Fan, C.; Hao, L.; Li, S.; Song, W.; Lin, W. Biomass-Ash-Induced Agglomeration in a Fluidized Bed. Part 1: Experimental Study on the Effects of a Gas Atmosphere. *Energy & Fuels* **2016**, *30* (8), 6395–6404.
- (57) Chaivatamaset, P.; Tia, S. The Characteristics of Bed Agglomeration during Fluidized Bed Combustion of Eucalyptus Bark. *Appl. Therm. Eng.* **2015**, *75*, 1134–1146.
- (58) Duan, F.; Chyang, C.-S.; Zhang, L.; Yin, S.-F. Bed Agglomeration Characteristics of Rice Straw Combustion in a Vortexing Fluidized-Bed Combustor. *Bioresour. Technol.* **2015**, *183*, 195–202.
- (59) Gatterneg, B.; Karl, J. The Influence of Particle Size, Fluidization Velocity and Fuel Type on Ash-Induced Agglomeration in Biomass Combustion. *Front. Energy Res.* **2014**, *2* (November), 1–12.
- (60) Werther, J.; Saenger, M.; Hartge, E. U.; Ogada, T.; Siagi, Z. Combustion of Agricultural Residues. *Prog. Energy Combust. Sci.* **2000**, *26* (1), 1–27.
- (61) Arromdee, P.; Kuprianov, V. I. Combustion of Peanut Shells in a Cone-Shaped Bubbling Fluidized-Bed Combustor Using Alumina as the Bed Material. In *Third International Conference on Applied Energy*, **2012**; *97*, 470–482.
- (62) Shimizu, T.; Han, J.; Choi, S.; Kim, L.; Kim, H. Fluidized-bed combustion characteristics of cedar pellets by using an alternative bed material. *Energy & Fuels* **2006**, *20* (6), 2737–2742.
- (63) Ohman, M.; Nordin, A. The Role of Kaolin in Prevention of Bed Agglomeration during Fluidized Bed Combustion of Biomass Fuels. *Energy & Fuels* **2000**, *14* (3), 618–624.
- (64) Davidsson, K. O.; Steenari, B.-M.; Eskilsson, D. Kaolin Addition during Biomass Combustion in a 35 MW Circulating Fluidized-Bed Boiler. *Energy & Fuels* **2007**, *21* (4), 1959–1966.
- (65) Olofsson, G.; Ye, Z.; Bjerle, I.; Andersson, A. Bed Agglomeration Problems in Fluidized-Bed Biomass Combustion. *Ind. Eng. Chem. Res.* **2002**, *41* (12), 2888–2894.
- (66) Billen, P.; Costa, J.; van der Aa, L.; Westdorp, L.; Van Caneghem, J.; Vandecasteele, C. An Agglomeration Index for CaO Addition (as CaCO<sub>3</sub>) to Prevent Defluidization: Application to a Full-Scale Poultry Litter Fired FBC. *Energy & Fuels* **2014**, *28* (8), 5455–5462.
- (67) Grimm, A.; Skoglund, N.; Bostrom, D.; Boman, C.; Ohman, M. Influence of Phosphorus on Alkali Distribution during Combustion of Logging Residues and Wheat Straw in a Bench-Scale Fluidized Bed. *Energy & Fuels* **2012**, *26* (5), 3012–3023.

- (68) Teixeira, P.; Lopes, H.; Gulyurtlu, I.; Lapa, N.; Abelha, P. Evaluation of Slagging and Fouling Tendency during Biomass Co-Firing with Coal in a Fluidized Bed. *Biomass and Bioenergy* **2012**, *39* (Sp. Iss. SI), 192–203.
- (69) Elled, A. L.; Davidsson, K. O.; Åmand, L. E. Sewage Sludge as a Deposit Inhibitor When Co-Fired with High Potassium Fuels. *Biomass and Bioenergy* **2010**, *34* (11), 1546–1554.
- (70) Vamvuka, D.; Zografos, D.; Alevizos, G. Control Methods for Mitigating Biomass Ash-Related Problems in Fluidized Beds. *Fuel* **2008**, *99* (9), 3534–3544.
- (71) Ninduangdee, P.; Kuprianov, V. I. Combustion of Palm Kernel Shell in a Fluidized Bed: Optimization of Biomass Particle Size and Operating Conditions. *Energy Convers. Manag.* **2014**, *85*, 800–808.
- (72) Han, J.; Kim, H.; Cho, S.; Shimizu, T. Fluidized bed combustion of some woody biomass fuels. *Energy Sources* **2008**, *30* (19), 1820–1829.
- (73) Grimm, A.; Öhman, M.; Lindberg, T.; Fredriksson, A.; Boström, D. Bed Agglomeration Characteristics in Fluidized-Bed Combustion of Biomass Fuels Using Olivine as Bed Material. *Energy & Fuels* **2012**, *26* (7), 4550–4559.
- (74) Brus, E.; Öhman, M.; Nordin, A.; Boström, D. Bed Agglomeration Characteristics of Biomass Fuels Using Blast-Furnace Slag as Bed Material. *Energy & Fuels* **2004**, *18* (4).
- (75) Corcoran, A.; Marinkovic, J.; Lind, F.; Thunman, H.; Knutsson, P.; Seemann, M. Ash Properties of Ilmenite Used as Bed Material for Combustion of Biomass in a Circulating Fluidized Bed Boiler. *Energy & Fuels* **2014**, *28* (12), 7672–7679.
- (76) Marinkovic, J. Choice of Bed Material: A Critical Parameter in the Optimization of Dual Fluidized Bed Systems; PhD Thesis, Chalmers University of Technology, **2016**.
- (77) Steenari, B. M.; Lindqvist, O. High-Temperature Reactions of Straw Ash and the Anti-Sintering Additives Kaolin and Dolomite. *Biomass and Bioenergy* **1998**, *14* (1), 67–76.
- (78) Davidsson, K. O.; Åmand, L. E.; Steenari, B. M.; Elled, A. L.; Eskilsson, D.; Leckner, B. Countermeasures against Alkali-Related Problems during Combustion of Biomass in a Circulating Fluidized Bed Boiler. *Chem. Eng. Sci.* **2008**, *63* (21), 5314–5329.
- (79) Chou, J.-D.; Lin, C.-L. Inhibition of Agglomeration/Defluidization by Different Calcium Species during Fluidized Bed Incineration under Different Operating Conditions. *Powder Technol.* **2012**, *219*, 165–172.
- (80) Skoglund, N.; Grimm, A.; Ohman, M.; Bostrom, D. Effects on Ash Chemistry when Co-firing Municipal Sewage Sludge and Wheat Straw in a Fluidized Bed: Influence on the Ash Chemistry by Fuel Mixing. *Energy & Fuels* **2013**, *27* (10), 5725–5732.
- (81) Ren, Q.; Li, L. Co-Combustion of Agricultural Straw with Municipal Sewage Sludge in a Fluidized Bed: Role of Phosphorus in Potassium Behavior. *Energy & Fuels* **2015**, *29* (7), 4321–4327.
- (82) Kumar, R.; Singh, R. I. An Investigation of Co-Combustion Municipal Sewage Sludge with Biomass in a 20kW BFB Combustor under Air-Fired and Oxygen-Enriched Condition. *Waste Manag.* **2017**, *70*, 114–126.
- (83) Varol, M.; Atimtay, A. T. Effect of Biomass-Sulfur Interaction on Ash Composition and Agglomeration for the Co-Combustion of High-Sulfur Lignite Coals and Olive Cake in a Circulating Fluidized Bed Combustor. *Bioresour. Technol.* **2015**, *198*, 325–331.

- (84) Piotrowska, P.; Grimm, A.; Skoglund, N.; Boman, C.; Öhman, M.; Zevenhoven, M.; Boström, D.; Hupa, M. Fluidized-Bed Combustion of Mixtures of Rapeseed Cake and Bark: The Resulting Bed Agglomeration Characteristics. *Energy & Fuels* **2012**, *26* (4), 2028–2037.
- (85) Vamvuka, D.; Alloimonos, N. Combustion Behaviour of Olive Pruning/Animal Manure Blends in a Fluidized Bed Combustor. *Heliyon* **2017**, *3* (9).
- (86) Bakker, R. R.; Jenkins, B. M.; Williams, R. B. Fluidized Bed Combustion of Leached Rice Straw. *Energy & Fuels* **2002**, *16* (2), 356–365.
- (87) Lasek, J. A.; Kopczyński, M.; Janusz, M.; Iluk, A.; Zuwała, J. Combustion Properties of Torrefied Biomass Obtained from Flue Gas-Enhanced Reactor. *Energy* **2017**, *119*, 362–368.
- (88) Kopczynski, M.; Lasek, J. A.; Iluk, A.; Zuwała, J. The Co-Combustion of Hard Coal with Raw and Torrefied Biomasses (Willow-Salix Viminalis), Olive Oil Residue and Waste Wood from Furniture Manufacturing). *Energy* **2016**, *140*, 1316–1325.
- (89) Andersson, B. *Computational Fluid Dynamics for Engineers*; Cambridge University Press, **2011**.
- (90) Li, T.; Gel, A.; Pannala, S.; Shahnam, M.; Syamlal, M. CFD Simulations of Circulating Fluidized Bed Risers, Part I: Grid Study. *Powder Technol.* **2014**, *265*, 2–12.
- (91) Almohammed, N.; Alobaid, F.; Breuer, M.; Epple, B. A Comparative Study on the Influence of the Gas Flow Rate on the Hydrodynamics of a Gas–solid Spouted Fluidized Bed Using Euler–Euler and Euler–Lagrange/DEM Models. *Powder Technol.* **2014**, *264*, 343–364.
- (92) Upadhyay, M.; Seo, M. W.; Nho, N. S.; Park, J.-H. Experimental and CFD Simulation Studies of Circulating Fluidized Bed Riser in the Fast Fluidization Regime. *Comput. Aided Chem. Eng.* **2015**, *37*, 695–700.
- (93) Yu, L.; Lu, J.; Zhang, X.; Zhang, S. Numerical Simulation of the Bubbling Fluidized Bed Coal Gasification by the Kinetic Theory of Granular Flow (KTGF). *Fuel* **2007**, *86* (5–6), 722–734.
- (94) Papadikis, K.; Bridgwater, A. V.; Gu, S. CFD Modelling of the Fast Pyrolysis of Biomass in Fluidised Bed Reactors, Part A: Eulerian Computation of Momentum Transport in Bubbling Fluidised Beds. *Chem. Eng. Sci.* **2008**, *63* (16), 4218–4227.
- (95) Van Buijtenen, M. S.; Deen, N. G.; Heinrich, S.; Antonyuk, S.; Kuipers, J. A. M. A Discrete Element Study of Wet Particle-Particle Interaction during Granulation in a Spout Fluidized Bed. *Can. J. Chem. Eng.* **2009**, *87* (2), 308–317.
- (96) Sutkar, V. S.; Deen, N. G.; Patil, A. V.; Salikov, V.; Antonyuk, S.; Heinrich, S.; Kuipers, J. A. M. CFD-DEM Model for Coupled Heat and Mass Transfer in a Spout Fluidized Bed with Liquid Injection. *Chem. Eng. J.* **2016**, *288*, 185–197.
- (97) Sutkar, V. S.; Deen, N. G.; Padding, J. T.; Kuipers, J. A. M.; Salikov, V.; Crüger, B.; Antonyuk, S.; Heinrich, S. A Novel Approach to Determine Wet Restitution Coefficients through a Unified Correlation and Energy Analysis. *AIChE J.* **2015**, *61* (3), 769–779.
- (98) Mikami, T.; Kamiya, H.; Horio, M. Numerical Simulation of Cohesive Powder Behavior in a Fluidized Bed. *Chem. Eng. Sci.* **1998**, *53* (10), 1927–1940.
- (99) Girardi, M.; Radl, S.; Sundaresan, S. Simulating Wet Gas-Solid Fluidized Beds Using Coarse-Grid CFD-DEM. *Chem. Eng. Sci.* **2016**, *144*, 224–238.
- (100) Che, Y.; Tian, Z.; Liu, Z.; Zhang, R.; Gao, Y.; Zou, E.; Wang, S.; Liu, B. A CFD-PBM Model Considering

Ethylene Polymerization for the Flow Behaviors and Particle Size Distribution of Polyethylene in a Pilot-Plant Fluidized Bed Reactor. *Powder Technol.* **2015**, *286*, 107–123.

- (101) Villa, M. P.; Bertín, D. E.; Cotabarren, I. M.; Piña, J.; Bucalá, V. Fluidized-Bed Melt Granulation: Coating and Agglomeration Kinetics and Growth Regime Prediction. *Powder Technol.* **2016**, *300*, 61–72.
- (102) Wu, S. Y.; Baeyens, J. Segregation by Size Difference in Gas Fluidized Beds. *Powder Technol.* **1998**, *98*(2), 139–150.
- (103) Goldschmidt, M. J. V.; Link, J. M.; Mellema, S.; Kuipers, J. A. M. Digital Image Analysis Measurements of Bed Expansion and Segregation Dynamics in Dense Gas-Fluidised Beds. *Powder Technol.* **2003**, *138*(2–3), 135–159.
- (104) Rowe, P. N.; Nienow, A. W. Particle Mixing and Segregation in Gas Fluidised Beds. A Review. *Powder Technol.* **1976**, *15*(2), 141–147.
- (105) Busciglio, A.; Vella, G.; Micale, G. On the Bubbling Dynamics of Binary Mixtures of Powders in 2D Gas-Solid Fluidized Beds. *Powder Technol.* **2012**, *231*, 21–34.
- (106) Jang, H. T.; Park, T. S.; Cha, W. S. Mixing-Segregation Phenomena of Binary System in a Fluidized Bed. *J. Ind. Eng. Chem.* **2010**, *16*(3), 390–394.
- (107) Hemati, M.; Spieker, K.; Lagurei, C.; Alvarez, R.; Riera, F. A. Experimental Study of Sawdust and Coal Particle Mising in Sand or Catalyst Fluidized Bed. *Can. J. Chem. Eng.* **1990**, *68*(5), 768–772.
- (108) Wirsum, M.; Fett, F.; Iwanowa, N.; Lukjanow, G. Particle Mixing in Bubbling Fluidized Beds of Binary Particle Systems. *Powder Technol.* **2001**, *120*(1), 63–69.
- (109) Li, J.; Luo, Z. H.; Lan, X. Y.; Xu, C. M.; Gao, J. Sen. Numerical Simulation of the Turbulent Gas-Solid Flow and Reaction in a Polydisperse FCC Riser Reactor. *Powder Technol.* **2013**, *237*, 568–580.
- (110) Leboreiro, J.; Joseph, G. G.; Hrenya, C. M.; Snider, D. M.; Banerjee, S. S.; Galvin, J. E. The Influence of Binary Drag Laws on Simulations of Species Segregation in Gas-Fluidized Beds. *Powder Technol.* **2008**, *184*(3), 275–290.
- (111) Zhou, Q.; Wang, J. CFD Study of Mixing and Segregation in CFB Risers: Extension of EMMS Drag Model to Binary Gas-Solid Flow. *Chem. Eng. Sci.* **2015**, *122*, 637–651.
- (112) Geng, S.; Jia, Z.; Zhan, J.; Liu, X.; Xu, G. CFD Modeling the Hydrodynamics of Binary Particle Mixture in Pseudo-2D Bubbling Fluidized Bed: Effect of Model Parameters. *Powder Technol.* **2016**, *302*, 384–395.
- (113) Zhong, H.; Gao, J.; Xu, C.; Lan, X. CFD Modeling the Hydrodynamics of Binary Particle Mixtures in Bubbling Fluidized Beds: Effect of Wall Boundary Condition. *Powder Technol.* **2012**, *230*, 232–240.
- (114) Chao, Z.; Wang, Y.; Jakobsen, J. P.; Fernandino, M.; Jakobsen, H. A. Investigation of the Particle-Particle Drag in a Dense Binary Fluidized Bed. *Powder Technol.* **2012**, *224*, 311–322.
- (115) Chao, Z.; Wang, Y.; Jakobsen, J. P.; Fernandino, M.; Jakobsen, H. A. Derivation and Validation of a Binary Multi-Fluid Eulerian Model for Fluidized Beds. *Chem. Eng. Sci.* **2011**, *66*(16), 3605–3616.
- (116) Johnson, P. C.; Jackson, R. Frictional–collisional Constitutive Relations for Granular Materials, with Application to Plane Shearing. *J. Fluid Mech.* **1987**, *176*, 67.
- (117) Ghiasi, E.; Montes, A.; Ferdosian, F.; Tran, H.; Xu, C. (Charles). Bed Material Agglomeration Behavior in a Bubbling Fluidized Bed (BFB) at High Temperatures Using KCl and K<sub>2</sub>SO<sub>4</sub> as Simulated Molten

Ash. *Int. J. Chem. React. Eng.* **2018**, *16* (4).

- (118) Ma, T.; Fan, C.; Hao, L.; Li, S.; Jensen, P. A.; Song, W.; Lin, W.; Dam-Johansen, K. Biomass Ash Induced Agglomeration in Fluidized Bed. Part 2: Effect of Potassium Salts in Different Gas Composition. *Fuel Process. Technol.* **2018**, *Submitted*.
- (119) Alper, A. M. *Phase Diagrams in Advanced Ceramics*; Academic Press, 1995.
- (120) Anicic, B.; Lin, W.; Dam-Johansen, K.; Wu, H. Agglomeration Mechanism in Biomass Fluidized Bed Combustion – Reaction between Potassium Carbonate and Silica Sand. *Fuel Process. Technol.* **2018**, *173*, 182–190.
- (121) Laxminarayan, Y. Formation, Sintering and Removal of Biomass Ash Deposits; PhD Thesis, Technical University of Denmark, **2018**.
- (122) Mikami, T.; Kamiya, H.; Horio, M. Numerical Simulation of Cohesive Powder Behavior in a Fluidized Bed. *Chem. Eng. Sci.* **1998**, *53* (10), 1927–1940.
- (123) Ennis, B. J.; Tardos, G.; Pfeffer, R. A Microlevel-Based Characterization of Granulation Phenomena. *Powder Technol.* **1991**, *65* (1–3), 257–272.
- (124) Modolo, R. C. E.; Tarelho, L. A. C.; Teixeira, E. R.; Ferreira, V. M.; Labrincha, J. A. Treatment and Use of Bottom Bed Waste in Biomass Fluidized Bed Combustors. *Fuel Process. Technol.* **2014**, *125*, 170–181.
- (125) Gibsons, G.; Ward, R. Reactions in Solid State: Reaction between Sodium Carbonate and Quartz. *J. Am. Ceram. Soc.* **1943**, *26* (7), 239–246.
- (126) Grynberg, J.; Gouillart, E.; Chopinet, M.-H.; Toplis, M. J. Importance of the Atmosphere on the Mechanisms and Kinetics of Reactions Between Silica and Solid Sodium Carbonate. *Int. J. Appl. Glas. Sci.* **2015**, *6* (4), 428–437.
- (127) Piotrowska, P.; Rebbling, A.; Lindberg, D.; Backman, R.; Öhman, M.; Boström, D. Waste Gypsum Board and Ash-Related Problems during Combustion of Biomass. 1. Fluidized Bed. *Energy & Fuels* **2015**, *29* (2), 877–893.
- (128) Grimm, A.; Öhman, M.; Lindberg, T.; Fredriksson, A.; Boström, D. Bed Agglomeration Characteristics in Fluidized-Bed Combustion of Biomass Fuels Using Olivine as Bed Material. In *Energy & Fuels*; **2012**; *26*, 4550–4559.
- (129) V. Dorozhkin, S. Amorphous Calcium Orthophosphates: Nature, Chemistry and Biomedical Applications. *Int. J. Mater. Chem.* **2012**, *2* (1), 19–46.
- (130) Arvelakis, S.; Gehrman, H.; Beckmann, M.; Koukios, E. G. Effect of Leaching on the Ash Behavior of Olive Residue during Fluidized Bed Gasification. *Biomass and Bioenergy* **2002**, *22* (1), 55–69.
- (131) Wang, G.; Jensen, P. A.; Wu, H.; Frandsen, F. J.; Sander, B.; Glarborg, P. Potassium Capture by Kaolin, Part 1: KOH. *Energy & Fuels* **2018**, *32* (1), 1851–1862.
- (132) Raymundo-Piñero, E.; Azais, P.; Cacciaguerra, T.; Cazorla-Amorós, D.; Linares-Solano, A.; Béguin, F. KOH and NaOH Activation Mechanisms of Multiwalled Carbon Nanotubes with Different Structural Organisation. *Carbon* **2005**, *43* (4), 786–795.
- (133) Wang, Y.; Wu, H.; Sárossy, Z.; Dong, C.; Glarborg, P. Release and Transformation of Chlorine and Potassium during Pyrolysis of KCl Doped Biomass. *Fuel* **2017**, *197*, 422–432.
- (134) Wang, G. Potassium Capture by Kaolin and Coal Fly Ash; PhD Thesis, Technical University of

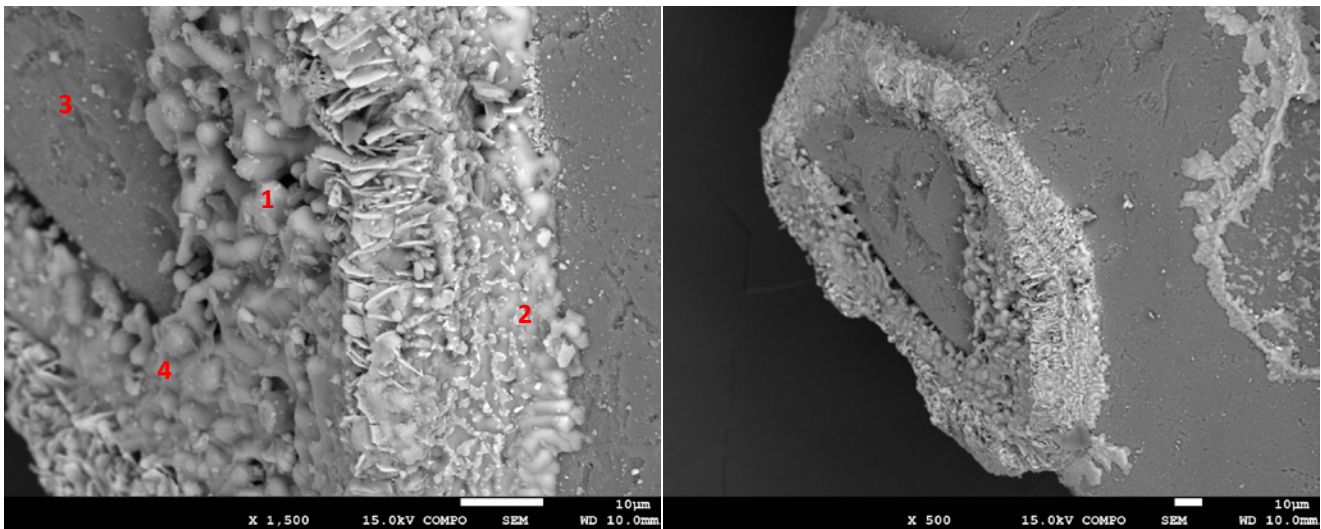
Denmark, 2018.

- (135) Kiyoura, R.; Urano, K. Mechanism, Kinetics, and Equilibrium of Thermal Decomposition of Ammonium Sulfate. *Ind. Eng. Chem. Process Des. Dev.* **1970**, *9*(4), 489–494.
- (136) Anicic, B.; Lin, W.; Dam-Johansen, K.; Wu, H. Agglomeration Mechanism in Biomass Fluidized Bed Combustion – Reaction between Potassium Carbonate and Silica Sand. *Fuel Process. Technol.* **2018**, *173*, 182-190.
- (137) Wang, G.; Jensen, P. A.; Wu, H.; Frandsen, F. J.; Sander, B.; Glarborg, P. Potassium Capture by Kaolin, Part 2: K<sub>2</sub>CO<sub>3</sub>, KCl, and K<sub>2</sub>SO<sub>4</sub>. *Energy & Fuels* **2018**, *32*, 3566–3578.
- (138) Liao, Y.; Cao, Y.; Chen, T.; Ma, X. Experiment and Simulation Study on Alkalis Transfer Characteristic during Direct Combustion Utilization of Bagasse. *Bioresour. Technol.* **2015**, *194*, 196–204.
- (139) Broström, M.; Kassman, H.; Helgesson, A.; Berg, M.; Andersson, C.; Backman, R.; Nordin, A. Sulfation of Corrosive Alkali Chlorides by Ammonium Sulfate in a Biomass Fired CFB Boiler. *Fuel Process. Technol.* **2007**, *88*(11), 1171–1177.
- (140) Kassman, H.; Pettersson, J.; Steenari, B.-M.; Åmand, L.-E. Two Strategies to Reduce Gaseous KCl and Chlorine in Deposits during Biomass Combustion — Injection of Ammonium Sulphate and Co-Combustion with Peat. *Fuel Process. Technol.* **2013**, *105*, 170–180.
- (141) Teixeira, A. P. C.; Santos, E. M.; Vieira, A. F. P.; Lago, R. M. Use of Chrysotile to Produce Highly Dispersed K-Doped MgO Catalyst for Biodiesel Synthesis. *Chem. Eng. J.* **2013**.
- (142) Rao, Y.; Wang, W.; Tan, F.; Cai, Y.; Lu, J.; Qiao, X. Influence of Different Ions Doping on the Antibacterial Properties of MgO Nanopowders. *Appl. Surf. Sci.* **2013**, *284*, 726-761.
- (143) Anicic, N.; Vukomanovic, M.; Suvorov, D. The Nano-Texturing of MgO Microrods for Antibacterial Applications. *RSC Adv.* **2016**, *6*(104), 102657–102664.
- (144) Kamyabi, M.; Sotudeh-Gharebagh, R.; Zarghami, R.; Saleh, K. Principles of Viscous Sintering in Amorphous Powders: A Critical Review. *Chem. Eng. Res. Des.* **2017**.
- (145) *ANSYS® Academic Research Manual*; 17.2; Ansys Inc., **2016**.
- (146) Lun, C. K. K.; Savage, S. B.; Jeffrey, D. J.; Chepuruiy, N. Kinetic Theories for Granular Flow: Inelastic Particles in Couette Flow and Slightly Inelastic Particles in a General Flowfield. *J. Fluid Mech.* **1984**, *140*(1), 223.
- (147) Ahmadi, G.; Ma, D. A Thermodynamical Formulation for Dispersed Multiphase Turbulent Flows-1 Basic Theory. *Multiph. Flow* **1990**, *16*(2), 323–340.
- (148) Syamlal, M.; Rogers, W.; O'Brien, T. J. *MFIX Documentation Theory Guide*; **1993**; Vol. 1004.
- (149) Schaeffer, D. G. Instability in the Evolution Equations Describing Incompressible Granular Flow. *J. Differ. Equ.* **1987**, *66*(1), 19–50.
- (150) Syamlal, M. The Particle-Particle Drag Term in a Multiparticle Model of Fluidization. *Top. Rep.* **1987**, 25.
- (151) Hong, K.; Shi, Z.; Wang, W.; Li, J. A Structure-Dependent Multi-Fluid Model (SFM) for Heterogeneous Gas-Solid Flow. *Chem. Eng. Sci.* **2013**, *99*, 191–202.
- (152) Wen, C. Y.; Yu, Y. H. Mechanics of Fluidization. *Chem. Eng. Progress, Symp. Ser.* **1966**, *62*(1), 100–111.

- (153) Xie, N.; Battaglia, F.; Pannala, S. Effects of Using Two- versus Three-Dimensional Computational Modeling of Fluidized Beds: Part I, Hydrodynamics. *Powder Technol.* **2008**, *182* (1), 1–13.
- (154) Peirano, E.; Delloume, V.; Leckner, B. Two- or Three-Dimensional Simulations of Turbulent Gas-Solid Flows Applied to Fluidization. *Chem. Eng. Sci.* **2001**, *56* (16), 4787–4799.
- (155) Li, J.; Kuipers, J. A. M. Effect of Competition between Particle-Particle and Gas-Particle Interactions on Flow Patterns in Dense Gas-Fluidized Beds. *Chem. Eng. Sci.* **2007**, *62* (12), 3249–3442.
- (156) Hao, Y. -J; Tanaka, T. Role of the Contact Points between Particles on the Reactivity of Solids. *Can. J. Chem. Eng.* **1988**, *66* (5), 761–766.

## APPENDIX A

Appendix A provides additional SEM-EDX analysis of bed material removed after model K-species defluidization experiments. Additional analyses are performed in order to observe the morphology of and composition of coating layers for KCl-K<sub>2</sub>SO<sub>4</sub>-silica sand and KCl-K<sub>2</sub>CO<sub>3</sub>-silica sand systems. The results are given at following Figures A-1 and A-2.

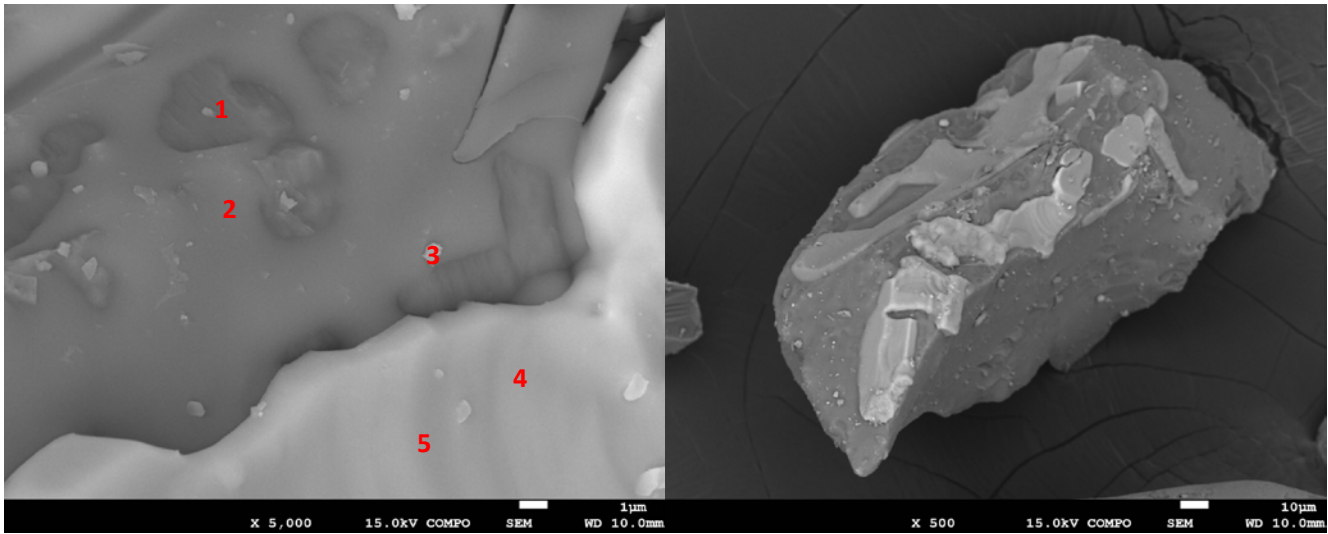


Spot	O	Si	S	Cl	K
1	80.8	5.5	0.7	4.8	7.9
2	24.4	0.6	3.7	32.5	36.8
3	84.4	11.6	0.4	1.3	1.7
4	78.6	7.7	2.2	3.4	7.26

Figure A-1: SEM-EDX analysis of the sample from KCl-K<sub>2</sub>SO<sub>4</sub>-silica sand system. Reference conditions; initial potassium to sand ratio 0.75 %; sampled from cold reactor.

Figure A-1 indicates that melt formed above KCl/K<sub>2</sub>SO<sub>4</sub> is not homogeneous since there are regions with higher S and Cl concentration. This confirms mass transfer laminations during eutectic formation since KCl and K<sub>2</sub>SO<sub>4</sub> are only mechanical mixed.

Figure A-2 shows that in the case of KCl-K<sub>2</sub>CO<sub>3</sub>-silica sand system, the reaction between K<sub>2</sub>CO<sub>3</sub> and silica sand results in formation of potassium silicates (spots 2 and 3) which are covering silica sand surface. On the other hand, KCl (spots 4 and 5) is segregated from eutectic mixture and it is present at the surface of the silica sand particles partially coated by formed K-silicates.



Spot	O	Si	Cl	K
1	81.8	18.2	0	0
2	76.6	22.7	0.1	0.6
3	71.8	24.6	1.4	2.2
4	11.3	4.6	44	40
5	15.8	4.2	42.1	37.9

Figure A-2: SEM-EDX analysis of the sample from  $KCl:K_2CO_3$ -silica sand system. Reference conditions; initial potassium to sand ratio of 0.75 %; sampled from cold reactor.

## APPENDIX B

---

Appendix B provides the results of one of the repeated experiments for  $K_2CO_3$ /silica sand systems, performed in order to evaluate the reproducibility of experimental results. In addition, results of thermodynamical equilibrium calculations for pure  $K_2CO_3$  are also given. Finally, the XRD analysis of samples removed after TGA experiments are given at Figure B-3.

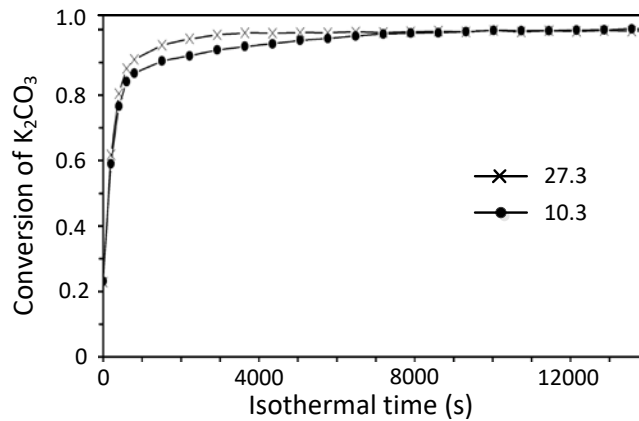


Figure B-1:  $K_2CO_3$  conversion rates of repeated experiments.  $T = 800$  °C Pure  $N_2$  environment;  $K_2CO_3:SiO_2$  ratio = 3:100; well mixed mixtures; powder  $K_2CO_3$ ; total residence time 4h.

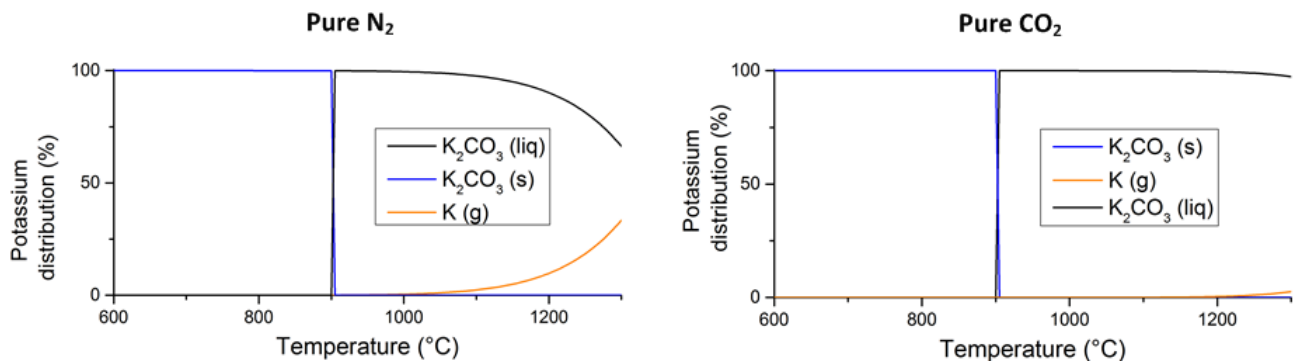


Figure B-2: Thermodynamic calculations of pure  $K_2CO_3$  under  $N_2$  and  $CO_2$  atmosphere

Figure B-1 indicates that reproducibility of experimental results is high since the average relative deviation of  $K_2CO_3$  conversion is less than 2 %. This validates the experimental procedure used in this investigation. Figure B-2 showed that thermal decomposition of  $K_2CO_3$  is taking place above 1000 °C, which is much higher compared to the highest temperature used in experiments, and it is not influenced by atmosphere below this point.

Figure B-3 indicates that silica sand is the only crystalline phase present after TGA experiments, which means that all formed products are present in amorphous phase as K-silicates.

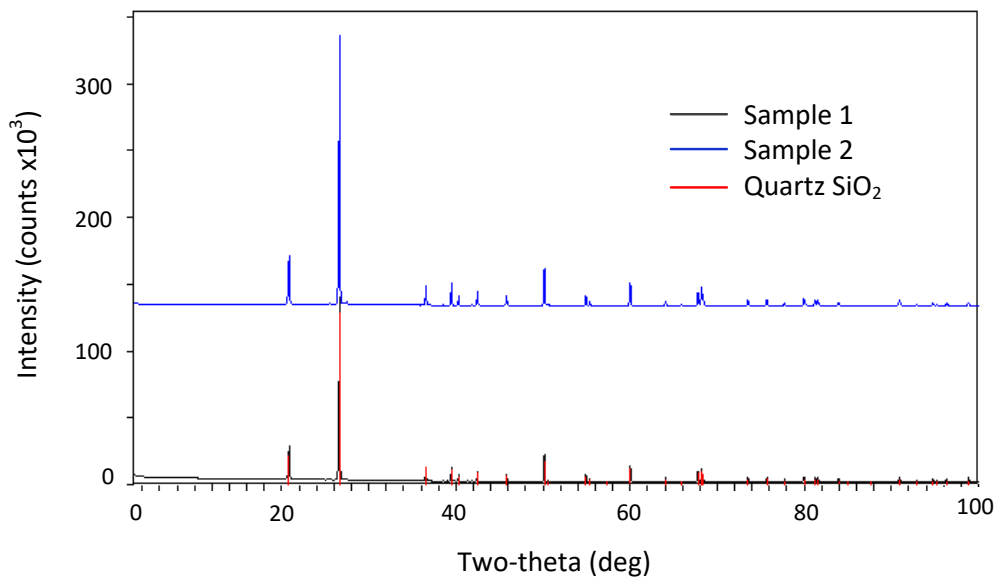


Figure B-3: XRD analysis. Sample 1:  $SiO_2:K_2CO_3$  mole ratio 1:0.013; pure  $N_2$ ; 4h residence time. Sample 2:  $SiO_2:K_2CO_3$  mole ratio 1:1; pure  $N_2$ ; 24h residence time.

# APPENDIX C

---

Appendix C summarizes the temperature profiles along the fluidized bed reactor, which were measured during continuous combustion experiments. The temperatures were measured at steady state conditions by pulling out thermocouple T<sub>4</sub> (see Figure 5-1) and changing its height. Results are plotted at following figures.

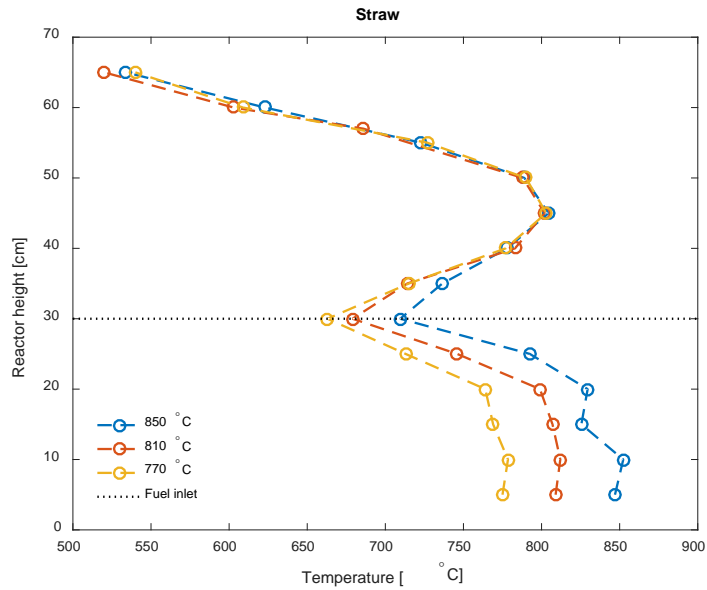


Figure C-1: Axial temperature profiles for wheat straw combustion at different temperatures.

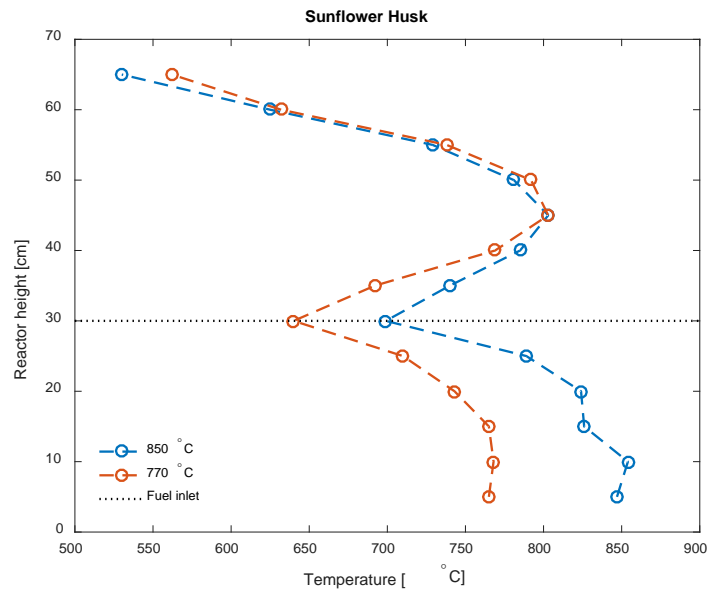


Figure C-2: Axial temperature profiles for SFH combustion at different temperatures

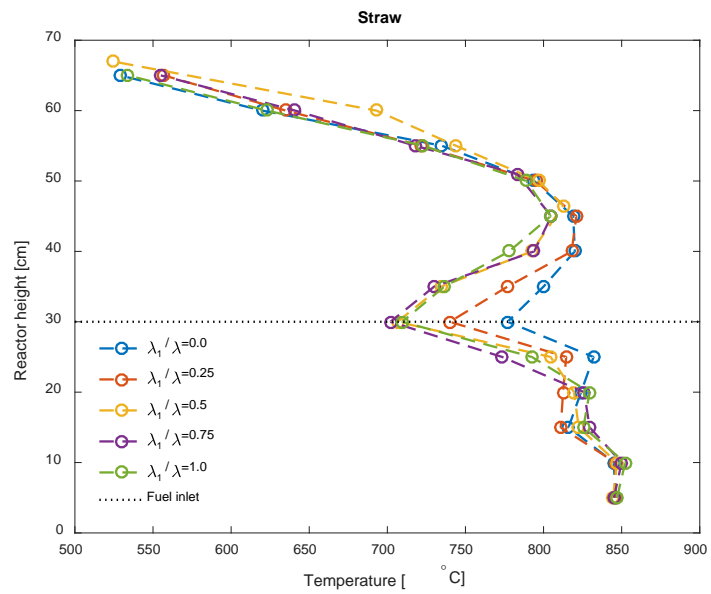


Figure C-3: Axial temperature profiles for wheat straw combustion at 850 °C under different  $\lambda_1/\lambda$  ratios

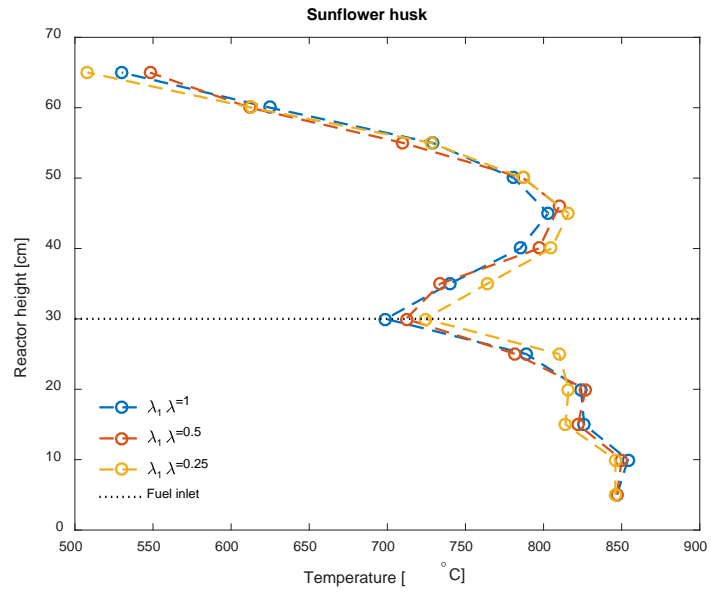


Figure C-4: Axial temperature profiles for SFH combustion at 850 °C under different  $\lambda_1/\lambda$  ratios

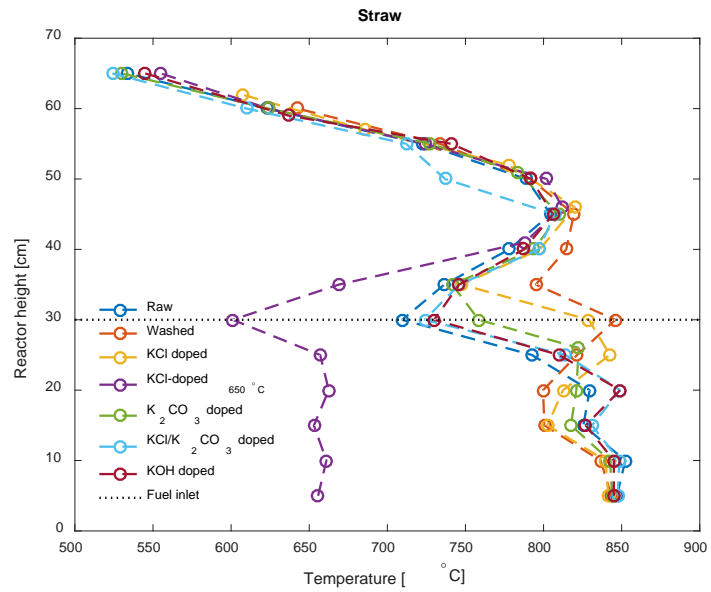


Figure C-5: Axial temperature profiles for washed and doped wheat straw combustion

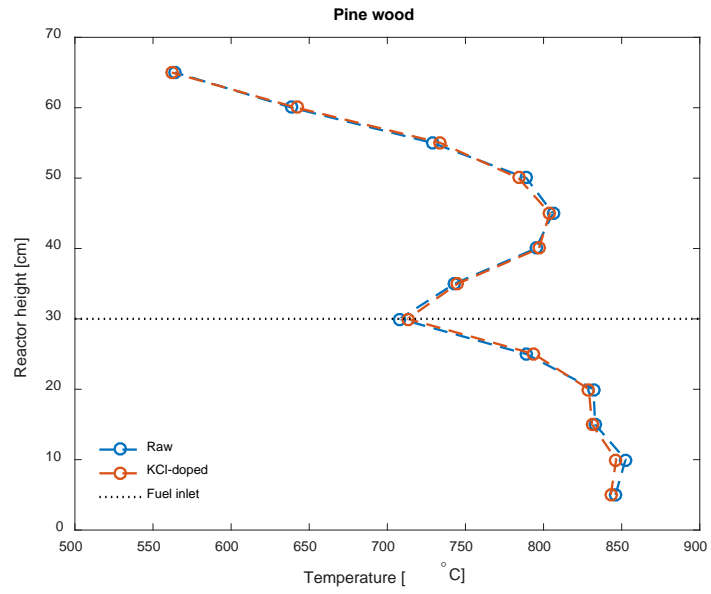


Figure C-6: Axial temperature profiles for doped pine wood combustion

## APPENDIX D

---

Appendix D provides the comprehensive summary of compounds considered in global equilibrium calculations using FACTSAGE 7.0 software. Table D-1 summarizes the compounds used thermodynamical equilibrium calculations for  $K_2CO_3$ /silica sand systems (Chapter 4), while Table D-2 provides the components considered for the equilibrium calculations of biomass combustion in fluidized bed (Chapter 5).

*Table D-1: Summary of compound used for thermodynamical equilibrium calculation  $K_2CO_3$ -silica sand system*

Phase		Database	Model
Gas	C, C <sub>2</sub> , C <sub>3</sub> , N, N <sub>2</sub> , N <sub>3</sub> , CN, C <sub>2</sub> N, CNN, (CN) <sub>2</sub> , C <sub>4</sub> N <sub>2</sub> , O, O <sub>2</sub> , O <sub>3</sub> , CO, C <sub>2</sub> O, CO <sub>2</sub> , C <sub>3</sub> O <sub>2</sub> , NO, N <sub>2</sub> O, NO <sub>2</sub> , NO <sub>3</sub> , N <sub>2</sub> O <sub>3</sub> , N <sub>2</sub> O <sub>4</sub> , N <sub>2</sub> O <sub>5</sub> , NCO, Si <sub>2</sub> , Si <sub>3</sub> , SiC, SiC <sub>2</sub> , Si <sub>2</sub> C, SiN, Si <sub>2</sub> N, SiO, SiO <sub>2</sub> , K, K <sub>2</sub> , KCN, KOH, K <sub>2</sub> O	FactPS	/
Silicates /oxide slag (liquid)	K <sub>2</sub> O, SiO <sub>2</sub>	FToxid	SlagA
Oxides (solid and liquid)	SiO <sub>2</sub> , K <sub>2</sub> SiO <sub>3</sub> , K <sub>2</sub> Si <sub>2</sub> O <sub>5</sub> , K <sub>2</sub> Si <sub>4</sub> O <sub>9</sub> , K <sub>4</sub> SiO <sub>4</sub> , K <sub>2</sub> O.	FToxid	/
Other solids	C, Si, SiC, K, KCN, K <sub>2</sub> O <sub>2</sub> , K <sub>2</sub> CO <sub>3</sub> , KNO <sub>3</sub>	FactPS	/

Table D-2: Summary of compound used for thermodynamical equilibrium calculation of biomass combustion

Phase	Database	Model
Gas	FactPS	/
Silicates /oxide slag (liquid)	FToxid	SlagA
Molten salt (liquid)	FTsalt	SaltF
Carbonates and Sulphates (solid)	FTpulp	Hexa-HT
K and Na carbonates and sulphates (solid)	FTsalt	KSO_
Chlorides (solid)	FTsalt	ACL_B
K-Ca-carbonate	FTsalt	SCSO
Other salts (solid)	FTsalt	/
Oxides (solid and liquid)	FToxid	/

$\text{Na}_2\text{Ca}_3\text{Al}_{16}\text{O}_{28}$ ,  $\text{CaSiO}_3$ ,  $\text{Ca}_2\text{SiO}_4$ ,  $\text{Ca}_3\text{SiO}_5$ ,  $\text{Ca}_3\text{Si}_2\text{O}_7$ ,  
 $\text{Na}_2\text{CaSiO}_4$ ,  $\text{CaMgSi}_2\text{O}_6$ ,  $\text{Ca}_2\text{MgSi}_2\text{O}_7$ ,  $\text{Ca}_3\text{MgSi}_2\text{O}_8$ ,  
 $\text{CaAl}_2\text{SiO}_6$ ,  $\text{CaAl}_2\text{Si}_2\text{O}_8$ ,  $\text{Ca}_2\text{Al}_2\text{SiO}_7$ ,  $\text{CaP}_4\text{O}_{11}$ ,  $\text{Ca}_2\text{P}_2\text{O}_7$ ,  
 $\text{Ca}_3\text{P}_2\text{O}_8$ ,  $\text{Ca}_4\text{P}_2\text{O}_9$ ,  $\text{Na}_2\text{CaP}_2\text{O}_7$ ,  $\text{NaCaP}_3\text{O}_9$ ,  $\text{Na}_4\text{CaP}_6\text{O}_{18}$ ,  
 $\text{Na}_2\text{Ca}_2\text{P}_2\text{O}_8$ ,  $\text{Ca}_3\text{Mg}_3(\text{PO}_4)_4$ ,  $\text{Ca}_4\text{Mg}_2\text{P}_6\text{O}_{21}$ ,  $\text{Ca}_5\text{P}_2\text{SiO}_{12}$ ,  
 $\text{Fe}_2\text{O}_3$ ,  $\text{Al}_2\text{Fe}_2\text{O}_6$ ,  $\text{FeSiO}_3$ ,  $\text{Fe}_2\text{SiO}_4$ ,  $\text{Na}_2\text{FeSiO}_4$ ,  $\text{NaFeSi}_2\text{O}_6$ ,  
 $\text{Na}_5\text{FeSi}_4\text{O}_{12}$ ,  $\text{Fe}_3\text{Al}_2\text{Si}_3\text{O}_{12}$ ,  $\text{FeP}_2\text{O}_6$ ,  $\text{CaFe}_2\text{O}_4$ ,  $\text{Ca}_2\text{Fe}_2\text{O}_5$ ,  
 $\text{CaFe}_4\text{O}_7$ ,  $\text{CaFeSi}_2\text{O}_6$ ,  $\text{Ca}_2\text{FeSi}_2\text{O}_7$ ,  $\text{Ca}_3\text{Fe}_2\text{Si}_3\text{O}_{12}$ .

$\text{C}$ ,  $\text{NaCN}$ ,  $\text{NaO}_2$ ,  $\text{Na}_2\text{O}_2$ ,  $\text{NaHCO}_3$ ,  $\text{Mg}$ ,  $\text{MgC}_2$ ,  $\text{Mg}_2\text{C}_3$ ,  
 $\text{Mg}_3\text{N}_2$ ,  $\text{Mg}(\text{OH})_2$ ,  $\text{MgCO}_3$ ,  $\text{Mg}(\text{NO}_3)_2$ ,  $\text{Al}$ ,  $\text{Si}$ ,  $\text{SiC}$ ,  $\text{Mg}_2\text{Si}$ ,  
 $\text{Mg}_3\text{Si}_2\text{O}_5(\text{OH})_4$ ,  $\text{Mg}_3\text{Si}_4\text{O}_{10}(\text{OH})_2$ ,  $\text{Mg}_7\text{Si}_8\text{O}_{22}(\text{OH})_2$ ,  
 $\text{Al}_2\text{SiO}_5$ ,  $(\text{Al}_2\text{O}_3)(\text{SiO}_2)_2(\text{H}_2\text{O})_2$ ,  $\text{Al}_2\text{Si}_4\text{O}_{10}(\text{OH})_2$ ,  
 $\text{NaAlSi}_2\text{O}_6\text{H}_2\text{O}$ ,  $\text{NaAl}_3\text{Si}_3\text{O}_{12}\text{H}_2$ ,  $\text{Mg}_5\text{Al}_2\text{Si}_3\text{O}_{10}(\text{OH})_8$ ,  
 $\text{Mg}_2\text{Al}_4\text{Si}_5\text{O}_{18}(\text{H}_2\text{O})$ ,  $\text{Na}_2\text{Mg}_3\text{Al}_2\text{Si}_8\text{O}_{22}(\text{OH})_2$ ,  $\text{P}$ ,  $\text{P}_3\text{N}_5$ ,  
 $\text{Mg}_3\text{P}_2$ ,  $\text{SiP}$ ,  $(\text{NH}_4)_2\text{SO}_4$ ,  $(\text{NH}_4)_2\text{SO}_4(\text{NH}_3)_3$ ,  $\text{Na}_2\text{S}_3$ ,  
 $\text{Na}_2\text{SO}_4(\text{H}_2\text{O})_{10}$ ,  $\text{MgS}$ ,  $\text{MgSO}_4(\text{H}_2\text{O})$ ,  $\text{Al}_2\text{S}_3$ ,  $\text{Al}_2(\text{SO}_4)_3$ ,  
 $\text{Al}_2(\text{SO}_4)_3(\text{H}_2\text{O})_6$ ,  $\text{NH}_4\text{Al}(\text{SO}_4)_2$ ,  $\text{NH}_4\text{Al}(\text{SO}_4)_2(\text{H}_2\text{O})_{12}$ ,  $\text{SiS}_2$ ,  
 $\text{P}_2\text{S}_3$ ,  $\text{P}_4\text{S}_3$ ,  $\text{P}_2\text{S}_5$ ,  $\text{NH}_4\text{Cl}$ ,  $\text{NaClO}_4$ ,  $\text{Mg}(\text{OH})\text{Cl}$ ,  $\text{MgCl}_2(\text{H}_2\text{O})$ ,  
 $\text{AlCl}_3(\text{H}_2\text{O})_6$ ,  $\text{KCN}$ ,  $\text{KO}_2$ ,  $\text{K}_2\text{O}_2$ ,  $\text{KHCO}_3$ ,  $\text{K}_4\text{C}_2\text{O}_6(\text{H}_2\text{O})_3$ ,  
 $\text{KAl}_3\text{Si}_3\text{O}_{10}(\text{OH})_2$ ,  $\text{KAl}_7\text{Si}_{11}\text{O}_{30}(\text{OH})_6$ ,  $\text{KMg}_3\text{AlSi}_3\text{O}_{10}(\text{OH})_2$ ,  
 $\text{KH}_2\text{PO}_4$ ,  $\text{K}_2\text{HPO}_4$ ,  $\text{KAl}(\text{SO}_4)_2$ ,  $\text{KAl}(\text{SO}_4)_2(\text{H}_2\text{O})_3$ ,  
 $\text{KAl}(\text{SO}_4)_2(\text{H}_2\text{O})_{12}$ ,  $\text{KClO}_4$ ,  $\text{KClO}_4(s2)$ ,  $\text{Ca}$ ,  $\text{CaC}_2$ ,  $\text{CaO}_2$ ,  
 $\text{CaC}_2\text{O}_4(\text{H}_2\text{O})$ ,  $\text{Ca}(\text{NO}_3)_2$ ,  $\text{Ca}(\text{NO}_3)_2(\text{H}_2\text{O})_2$ ,  $\text{Mg}_2\text{Ca}$ ,  
 $\text{CaMg}(\text{CO}_3)_2$ ,  $\text{Al}_2\text{Ca}$ ,  $\text{Al}_4\text{Ca}$ ,  $(\text{CaO})_3(\text{Al}_2\text{O}_3)(\text{H}_2\text{O})_6$ ,  $\text{CaSi}$ ,  
 $(\text{CaO})(\text{SiO}_2)_2(\text{H}_2\text{O})_2$ ,  $\text{Ca}_2\text{Mg}_5\text{Si}_8\text{O}_{22}(\text{OH})_2$ ,  
 $\text{CaAl}_2\text{Si}_2\text{O}_7(\text{OH})_2(\text{H}_2\text{O})$ ,  $\text{CaAl}_4\text{Si}_2\text{O}_{10}(\text{OH})_2$ ,  
 $\text{CaAl}_{14}\text{Si}_{22}\text{O}_{60}(\text{OH})_{12}$ ,  $\text{Ca}_2\text{Al}_3\text{Si}_3\text{O}_{12}(\text{OH})$ ,  
 $(\text{CaO})_2(\text{Al}_2\text{O}_3)_2(\text{SiO}_2)_8(\text{H}_2\text{O})_7$ ,  $\text{Ca}_3\text{P}_2$ ,  $\text{CaHPO}_4$ ,  $\text{Ca}_5\text{HO}_{13}\text{P}_3$ ,  
 $\text{CaS}$ ,  $\text{CaSO}_3$ ,  $\text{CaSO}_3(\text{H}_2\text{O})_2$ ,  $\text{CaCl}_2(\text{H}_2\text{O})_6$ ,  $\text{K}_4\text{Ca}(\text{NO}_3)_6$ ,  $\text{Fe}$ ,  
 $\text{Fe}_3\text{C}$ ,  $\text{Fe}(\text{OH})_2$ ,  $\text{Fe}(\text{OH})_3$ ,  $\text{Fe}_2\text{O}_3(\text{H}_2\text{O})$ ,  $\text{FeCO}_3$ ,  $\text{FeAl}_3$ ,  $\text{FeSi}$ ,  
 $\text{FeSi}_2$ ,  $\text{Fe}_7\text{Si}_8\text{O}_{22}(\text{OH})_2$ ,  $\text{FeP}$ ,  $\text{FePO}_4(\text{H}_2\text{O})_2$ ,  $\text{FeS}$ ,  $\text{FeSO}_4$ ,  
 $\text{Fe}_2(\text{SO}_4)_3$ ,  $\text{FeSO}_4(\text{H}_2\text{O})_7$ ,  $\text{KFe}_3\text{AlSi}_3\text{O}_{10}(\text{OH})_2$

Other solids

FactPS /